Potentiation of Cancer Therapy by Novel Pharmacological Inhibitors of DNA Repair

Joanne Clancy

Cancer Institute

University College London

A thesis submitted

in fulfilment of the requirements for the degree of

Doctor of Philosophy

January 2023

Declaration

I, Joanne Clancy, confirm that the work presented in this thesis is my own. Where information has been derived from other sources, I confirm that this has been indicated in the thesis.

Abstract

DNA-dependent protein kinase (DNA-PK) has a central role in the repair of DNA damage induced by radiotherapy of cancer. As such, the combination of DNA-PK inhibitors and radiotherapy are under investigation in cancer clinical trials. While much of this efficacy is attributed to cancer-cell intrinsic mechanisms, little is known about the immunological ramifications. This thesis evaluates the immunological effects of a novel inhibitor of DNA-PK, M3814 (peposertib), in combination with radiotherapy.

Here, M3814 is shown to radiosensitise a panel of cancer cell lines. Furthermore, in KP.B6.F1 cells, a murine non-small cell lung carcinoma model, this cell death is accompanied by markers of immunogenic cell death including translocation of calreticulin to the cell-surface membrane and release of high mobility group box 1 (HMGB1). Additionally, treatment with radiotherapy and M3814 in MC38 cells increased expression of *Interferon-β* (*Ifnβ)*, an anti-viral cytokine induced by the cGAS-STING pathway. In contrast, KP.B6.F1 cells failed to express IFNβ, despite evidence of increase formation of cGAS positive micronuclei following combination treatment. This was found to be due to a deficiency of STING which could be restored by the hypomethylating agent decitabine.

In a syngeneic murine tumour model, addition of decitabine to combination treatment improved KP.B6.F1 tumour control and increased survival. Analysis of the immune compartments of KP.B6.F1 tumours determined increased infiltration of active T effector cells, active $CD8^+$ T cells, inflammatory monocytes and M1 macrophages in mice treated with a combination of decitabine, M3814 radiotherapy.

Together, this work demonstrates that addition of M3814 to radiotherapy not only increases cancer cell death but also increases the immunogenicity of tumour cells. Furthermore, it provides a potential therapeutic strategy to overcome cGAS-STING downregulation in cancer.

Impact Statement

In all but six countries, cancer is the first or second leading cause of premature mortality [1]. In 2020, the number of cancer-related deaths worldwide was an estimated 10 million [1] and is forecasted to exceed 30 million in 2030 [2-4]. Primarily, the burden of cancer weighs heavily on the patients and those surrounding. However, the projected growth in cancer burden also puts health infrastructures and economies at serious risk on a global scale. There is, therefore, an urgent need for research and innovation to improve therapeutic options and patient outcomes.

DNA-damaging agents, including radiotherapy, represent one of the most widely used cancer treatment modalities. While radiotherapy is often effective initially, many patients go on to relapse and develop resistance. Developing strategies to increase the efficacy of radiotherapy presents an opportunity decrease this risk. One way this can be done is using pharmacological inhibitors of DNA damage repair. Tumour cells can be sensitised to DNA damage by inhibitors of DNA damage repair pathways. Here, this thesis evaluates the effect of combining radiotherapy and M3814, a novel inhibitor of the DNA damage repair protein DNA-PK. In particular, this work focuses on the effects of this therapeutic combination on tumour immunogenicity.

Despite representing the most widely used cancer treatment modalities, it is only recently that we are beginning to understand the implications of DNA damaging agents on the immune system. For decades, the success of DNA damaging agents has been attributed solely on their direct cytotoxic effects. However, their effects to go far beyond the cancer cells, altering the immune tumour microenvironment. For the first time, this thesis reports that cell death following combination of M3814 and radiotherapy is indicative of immunogenic cell death. Furthermore, it is demonstrated that treatment triggers the innate anti-viral pathway, cGAS-STING. These findings

provide a rationale for future preclinical and clinical investigation into combining this approach with immunotherapy in the hopes of improving patient outcomes.

While induction of the cGAS-STING pathway by radiotherapy and M3814 could improve patient outcomes in patients receiving efficacy, it is limited by the frequency of patients with loss of cGAS-STING pathway function [5, 6]. This thesis identified a strategy to restore cGAS-STING pathway in a STING deficient model using the FDA approved cancer drug decitabine and demonstrated its in vivo effect on the efficacy and the tumour immune microenvironment. This preclinical validation warrants further study and could form the foundation of further clinical trials, not just in combination with M3814 and radiotherapy, but combined with any other DNA damaging agent.

Acknowledgements

I would like to thank everyone who supported me and made my time at UCL so rewarding and enjoyable. Firstly, I would like to thank my supervisors, Prof. Daniel Hochhauser, Prof. Sergio Quezada and Dr Lyubomir Vassilev. Daniel, I will always be grateful that you gave me the opportunity to work in such a stimulating environment. Thank you for all the support, but also the freedom and confidence to pursue my own ideas. Thank you, Sergio for welcoming me into the world of immunology and always suggesting interesting ideas for my project. Thank you, Lubo for our chats where I always left feeling so much more knowledgeable than I started.

A big thank you for all my colleagues who helped teach me the techniques needed for this project. Thanks to Dafne, Isabelle and Marcos for all your help and patience in training me with the immune analysis and to work with mice. Certainly not something that came naturally to me but we got there in the end! Thank you to Rebecca Carter in the preclinical radiotherapy facility and the BSU for help with my treatments.

I would also like to thank my colleagues in the lab for all the advice and assistance over the years. Juanjo who was a constant source of guidance throughout my years in the lab and for the writing of my thesis. To my PhD buddy, Avigayil. I am so grateful I had you next to me to navigate the highs and lows of PhD life. Thank you also to Arman, Simon, Arola, Sylvie, Shiran, Valenti and Jose for all your advice over the years.

Thank you, all my CI friends who made my PhD so enjoyable, you played such a huge role in my time there. Thank you to all my Friday pub friends; Adi, Itzy, Diego, Manolo, York, Valenti, Sarah, Meg and truly anyone I manged to drag there. I have been so fortunate to make some amazing friends during my time at UCL. Thank

you, Dhruva, Cate, Ellie, Haley, Katie, Callum and Dimitris, for all the good times! A special thank you to Dimitris and of course, my partner in crime, Maria. From my first friend at the Cancer Institute, to my best friend, flat-mate and my mums emergency contact (as flawed as that logic may be). I would struggle to think of many of the good times at the CI without you by my side, nor can I think of any of the bad where you weren't there for me.

A big thank you to my uni girls, Emma and Holly. Thank you for always hyping me up and for being so forgiving when I inevitably turned up late due to some obscure lab-related emergency.

Thank you, George. Thank you for being so patient, understanding, and supportive. You (just about) kept me sane through the writing process.

Most importantly, thank you to my family. Thank you to my parents for all your constant love and support all throughout my life. I don't know where I would be without you both in my corner.

Table of Contents

Table of Figures

Table of Tables

Abbreviations

ADC	Antibody drug conjugate
Alt-EJ	Alternative end joining
ACK	Ammonium Chloride Potassium
AMP	Adenosine monophosphate
APC	Antigen presenting cell
ATM	Ataxia-telangiectasia mutated
ATP	Adenosine triphosphate
BMDMs	Bone marrow-derived macrophage
BSA	Bovine serum albumin
CBCT	Cone beam computed tomography
cDC1	Type 1 conventional DCs
cDNA	copy DNA
cGAS	Cyclic GMP-AMP
cGAMP	Cyclic guanosine monophosphate–adenosine
CML	Chronic myeloid leukaemia
CT	Computed tomography
CRT	Calreticulin
CTLA-4	Cytotoxic T-lymphocyte associated protein 4
DAMPs	Damage-associated molecular patterns
DAPI	4′,6-diamidino-2-phenylindole
DC	Dendritic cell
DDR	DNA damage response
DMSO	Dimethyl sulfoxide
DNA-PK	DNA-dependent protein kinase
DNA-PKcs	DNA-dependent protein kinase catalytic subunit
DNA-PKi	DNA-dependent protein kinase inhibitor
DMXAA	Dimethyloxoxanthenyl acetic acid
DSB	Double strand break
dsDNA	Double strand DNA
EDTA	Ethylenediaminetetraacetic acid
ELISA	Enzyme-linked immunosorbent assay
ER	Endoplasmic reticulum

FBS	Foetal bovine serum
GI_{50}	50% growth inhibition
GMP	Guanosine monophosphate
GzmB	Granzyme B
H3K9	Histone H3 lysine 9
HCC	Hepatocellular carcinoma
HMGB1	High mobility group box 1
HR	Homologous recombination
HRP	Horseradish peroxidase
HRR	Homologous recombination repair
ICD	Immunogenic cell death
ICI	Immune checkpoint inhibitor
ICOS	Inducible T-cell costimulator
IFN	Interferon
IFNAR	Interferon alpha receptor
IFNβ	Interferon β
IL	Interleukin
IR	Ionising radiation
IRF3	Interferon regulatory factor 3
IRF9	Interferon regulatory factor 9
ISD	Interferon stimulatory DNA
ISG	Interferon stimulated genes
JAK	Janus kinase 1
LG	L-Glutamine
LPS	Lipopolysaccharide
M1	Classically activated mac
M2	Alternatively activated macrophage
MDC1	Mediator of DNA damage checkpoint protein 1
MHC	Major histocompatibility complex
MyD88	Adaptor myeloid differentiation primary response 88
MRN	Mre11 Rad50 Nbs1
MTT	3-(4,5-dimethylthiazol-2-yl)-2,5-diphenyl-2H-tetrazolium bromide
Mx1	MX Dynamin Like GTPase 1

NHEJ	Non-homologous end joining
NER	Nucleotide excision repair
NK cells	Natural killer cells
NSCLC	Non-small cell lung carcinoma
PAMPs	Pathogen-associated molecular patterns
PBS	Phosphate-buffered saline
PCR	Polymerase Chain Reaction
PD-1	Programmed cell death 1
PD-L1	Programmed cell death ligand
PI3K	Phosphoinositide 3-kinase
PIKK	Phosphoinositide 3-kinase related kinase
P/S	Penicillin-Streptomycin
PS	Phosphatidylserine
qRT-PCR	Quantitative real-time reverse transcription PCR
ROS	Reactive oxygen species
RPA	Replication protein A
SARRP	Small animal radiotherapy research platform
SCID	Severe combined immunodeficiency
SRB	Sulforhodamine B
SSA	Single strand annealing
ssDNA	Single strand DNA
STAT1	Signal transducer and activator of transcription 1
STAT2	Signal transducer and activator of transcription 2
STING	Stimulator of interferon genes
TAM	Tumour associated macrophages
TBK1	TANK-binding kinase 1
TBS	Tris-buffered saline
TBST	Tris-buffered saline tween
TCR	T cell receptor
TDLN	Tumour-draining lymph nodes
TIME	Tumour immune microenvironment
TLR	Toll-like receptor
TME	Tumour microenvironment
TOPO1	Topoisomerase 1

TREX1	Three Prime Repair Exonuclease 1
XLF	Xrcc4-like-factor
XRCC4	X-ray repair cross complementing 4

1. Introduction

1.1. DNA damage repair and cancer

1.1.1. Genomic instability and cancer

During the development of cancer, normal cells evolve and gain certain attributes which make them tumorigenic and malignant. The diversity and complexity of these changes is vast but can be summarised by the core cancer hallmarks. Currently, there are 8 acquired core hallmarks of cancer including sustaining proliferative signals, evading growth suppressors, resisting cell death, inducing angiogenesis, initiation invasion and metastasis, enabling replicative mortality, reprogramming of energy metabolism and evasion of immune destruction [7]. During tumorigenesis, the attributes are acquired as part of a multi-step process. Importantly, there is one particularly prominent enabling hallmark which enables and promotes cells to gain the acquired hallmarks. This is genomic instability. When cells lose genomic instability, they gain a mutator phenotype, exhibiting high rates of mutations resulting in defects in oncogenes and tumour suppressors and causing transformation of cells [8]. This makes maintenance of genomic instability critical for normal cell physiology and health of the organism.

1.1.2. The DNA damage response

DNA provides the instructions for cells to be able to produce the proteins necessary for their function, failure to maintain integrity of DNA is incompatible with normal cell functioning and forms the basis cancer. To preserve genomic integrity, cells rely on a complex network of overlapping pathways to repair DNA damage as it arises, quickly and accurately. This is the DNA damage response (DDR) [9]. The DDR detects the presence and nature of DNA damage, amplifies, and transduces this signal, and can

trigger a range of cellular responses such as cell-cycle arrest, DNA repair and apoptosis [9, 10].

1.1.3. Types of DNA damage

An important factor determining which DDR pathway will be activated is the type of DNA aberration present. There is a variety of forms of DNA damage, including base alterations, base substitution during replication, and strand breaks [11]. DNA damage can arise from endogenous or exogenous sources. For example, spontaneous hydrolysis can cause base deamination, resulting the conversion of one base to another, for example cytosine to uracil. Further chemical changes to nucleotide bases include alkylation and methylation, which alters the chemical structure of bases modifying their binding affinity and specificity. During DNA replication, this increases the risk of a base substitutions, which is mutagenic [10, 12].

Another form of DNA damage are DNA strand breaks. These may occur on just one DNA strand, a single strand break (SSB), or both strands of the duplex, a double strand beak (DSB). Two endogenous sources for SSBs are cellular metabolism and replication. During adenosine triphosphate (ATP) generation in the mitochondria, reactive oxygen species (ROS) are formed as a by-product. At high levels, free radicals cause DNA oxidation and hydrolysis, resulting in the formation of SSBs. However, while some DSBs and SSBs are examples of DNA damage, others are necessary for the normal functioning of cell. For example, the formation of SSBs are critical for DNA replication. DNA typically exists in a highly coiled state which must be relaxed during replication for the replication machinery to gain access. As the replication fork moves down the DNA during replication, it separates the strands. In doing so, the DNA ahead of the replication machinery becomes under increasingly intense torsional strain. Therefore, enzymes called DNA Topoisomerases (TOPO) are necessary to cut the DNA strands, either as a SSB (TOPOI) or DSB (TOPOII) to

permit controlled rotation of the DNA strand to relieve the tension and undo tangles. Once the DNA is relaxed, the SSBs or DSBs are resolved. If repair of these intentional DNA strand breaks is prevented, such as through the use of TOPO1 poisons for cancer therapy, the DNA becomes damaged [13].

DSBs are the most deleterious form of DNA damage and must be repaired quickly and accurately to protect genomic integrity. Failure to do so risks mutations such as translocations, inversions, or deletions when incorrect ends of a DSBs undergo ligation together. An example of a deleterious chromosomal translocation is the translocation of chromosome 9 and 22 resulting in the oncogenic fusion gene *BCR-ABL1*. This translocation produces an 'always-on' tyrosine kinase and is present in all cases of chronic myeloid leukaemia (CML) [14]. Furthermore, the presence of DSBs during anaphase risks mis-segregation of chromosomes and subsequent loss of genetic information [15].

1.1.4. The DNA damage response in tumorigenesis

This network plays a critical role in preserving genomic integrity as such, dysregulation of the DDR forms the basis of a range of diseases. Ataxia telangiectasia is another inherited disorder wherein patients carry mutations in the ataxia telangiectasia mutated (ATM) gene, a central component of the homologous recombination repair pathway which is an important pathway in the repair of DSBs. These patients suffer and have an increased risk of cancer.

Genomic instability has a direct causal role in tumorigenesis [7, 8]. Dysregulation of the DDR results in cells gaining a mutator phenotype, in which the mutation rate exceeds that of normal cells [8]. As these cells accumulate more mutations, they escape the normal constraints of cell growth and avoid programmed cell death, becoming tumorigenic. Germline mutations of genes in the DDR, such as those in patients with ataxia telangiectasia, compromises genomic stability, leaving carriers

predisposed to cancer development. Many major components of the DDR were first discovered in patients with a familial predisposition to certain cancers. For example, germline BRCA1 and BRCA2 mutations which reduce a DNA strand repair pathway, homologous recombination repair (HRR), leave female carriers 40-80% more susceptible to developing breast and ovarian cancer [16].

Studies investigating the frequency of DDR mutations in patients using data from The Cancer Genome Atlas across 15 cancer types found that patients had on average 3.12 DDR mutations per cancer patient [17]. This varied greatly between cancer types, with colorectal having the highest with 11.44 DDR mutations on average per patient [17]. One of the most widely mutated genes in tumorigenesis is P53, which orchestrates the cell cycle arrest necessary for DNA repairs. In sporadic cancers, P53 is mutated in 38-50% of all cancers [18]. Furthermore, another study found 52% of patients with stage III lung adenocarcinoma carried somatic P53 mutations, and of those not harbouring a P53 mutation, 15% had ATM mutations [19]. Such findings highlight how intricately DDR and tumorigenesis are linked.

1.1.5. Cancer cells are sensitive to DNA damage

While dysregulation of the DDR is a driver of tumorigenesis, it also renders tumour cells vulnerable to high levels of DNA damage. This principle underlies the rationale for DNA damaging agents as cancer therapy. Success of this approach relies on the proliferative nature of tumour cells and their inability to repair DNA damage appropriately. One such class of chemotherapeutic drugs that induce DNA damage are platinum salts, including cisplatin, carboplatin and, oxaliplatin [20]. These chemicals form interstrand and intrastrand crosslinks in DNA which are inhibitory to DNA replication. If left unresolved, these result in stalling of the replication fork and formation of DSBs. Patients those carrying mutations in BRCA1/2 or ATM have deficiencies in HRR, an important DSB DNA repair pathway, and typically respond

better to platinum-based therapies than those with proficient HRR [21, 22]. Another important DNA damaging agent is radiotherapy. The radiation used for radiotherapy can be grouped into two main groups: external-beams or internal. Internal radiotherapy includes treatments with radioisotopes and radionuclides liquids or the implantation of a solid radioactive source. In contrast, external beams deliver a beam of ionising radiation (IR) from an external source to the target. The energy source for this can come in multiple sources, such as proton beams or X-rays. X-ray is the most used form of radiotherapy, and therefore will be the subject of this thesis.

1.1.6. Ionising radiation induces DNA double strand breaks

When cells are exposed to high energy X-rays, energy is transferred causing ionisation. This ionisation damages cellular molecules either directly through the disruption of covalent bonds or indirectly through the production of free radicals from water [23]. While ionising radiation damages all components of the cells, the most severe consequences are a result of DNA damage. Disruption of the covalent bonds linking the phosphodiester backbone of DNA leads to the instantaneous formation of DSBs. Furthermore, hydroxyl free radicals react with DNA causing chemical alterations leading to the generation of oxidative lesions and abasic sites. These may develop into SSBs, which if in close proximity to another SSB on opposing DNA strands or left unresolved, can also develop into DSBs [23]. Interstrand crosslinks may also be formed. If the cells progress through the cell cycle without repair of SSBs or crosslinks, DSBs are generated due to replication fork collapse. DSBs are the most lethal form of DNA damage and if left unrepaired will result in cell death. 1Gy of radiation has been found to induce 35 DSBs per cell while 2Gy nearly doubles this number to 50 [24, 25].

1.1.7. Mechanisms of DNA double strand break repair

To resolve DSBs, there are four main pathways: non-homologous end joining (NHEJ), homologous recombination repair (HRR), alternative end joining (alt-EJ) and single strand annealing (SSA) [23]. The majority of DSBs are resolved by NHEJ and HRR, while alt-EJ and SSA typically acts as backups. These auxiliary mechanisms are more prone to insertion and deletion events, making them more mutagenic than NHEJ and HRR.

A key determinant of pathway selection is the cell cycle stage. As implied by the name, HRR requires the presence of a sister chromatid containing at least 100bp of homology. Using a sister chromatid as a template to repair damage makes HRR largely error free, however, it also restricts HRR to the S and G2 phase. This makes cell cycle arrest essential [26]. This is the preferred mechanism for repair of DSBs formed from replication fork collapse, at which point there is both the presence of a sister chromatid in proximity and sufficient time to conduct repairs. In contrast, DSB induction from exogenous sources, such as ionising radiation, can occur at any point in the cell cycle and must be resolved rapidly. In such circumstances DNA repair is predominately carried out by NHEJ. Failure to repair these breaks, especially if DSB frequency is high, is highly mutagenic due to the risk of translocations or deletions. NHEJ allows for the rapid ligation of DSBs and, as NHEJ does not require a sister chromatid, can occur at any point in the cell cycle. Real-time monitoring of fluorescent reporters in human cells show NHEJ can be completed in 30 minutes; in contrast, HRR takes over seven hours [27]. The ability of NHEJ to resolve DSBs quickly and at any stage in the cell cycle makes it critical in the DDR to ionising radiation. However, due to the lack of homologous template, NHEJ is more error prone than HRR [26]. Despite this, even in during S and G2 phases, NHEJ is responsible for approximately 80% of DSBs repair in these phases. Outside of S phase and G2, NHEJ accounts for all DSB repair [28, 29].

1.1.6.1. The Recognition of Double Strand Breaks

Following the formation of a DSB, Histone H3 lysine 9 (H3K9) on the chromatin adjacent to the DSBs undergoes methylation to form H3K9me3. This modification is recognised by TIP60 acetyltransferases, resulting in the acetylation and consequent activation of ataxia telangiectasia mutated (ATM). This protein is a member of the Phosphoinositide 3-kinase related kinase (PIKK) kinase family and is a key orchestrator of DSB repair.

Following ATM activation, histone H2AX undergoes rapid phosphorylation at the Ser-139 residue, forming γH2AX. This occur minutes after ionising radiation, peaking between 25 and 60 minutes and is a commonly used marker of DSB [30, 31]. Mediator of DNA damage checkpoint protein 1 (MDC1) binds γH2AX and is subsequently phosphorylated by ATM, resulting in its activation [32]. This promotes recruitment of the RING finger E3 ligases RNF8 and RNF168, which ubiquitylate histones H2A and H2AX. Subsequent removal and degradation of these chromatin structures permits the DNA structure to relax and open, offering access to repair molecules. At this point HRR and NHEJ compete for substrate through pMDC1 mediated recruitment of the Mre11-Rad50-Nbs1 (MRN) complex and 53BP1[33]. HRR is promoted by the MRN complex but inhibited by 53BP1 or Ku70/80.

1.1.6.2. Homologous Recombination Repair

The MRN complex consists of three subunits, Mre11, Rad50 and Nbs1[34]. Rad50 contains a zinc loop, through which DNA is threaded, and a globular domain with dynamic ATP DNA binding sites to facilitate the shuttling of the MRN complex up and down the DNA, while Mre11 recognises the free DNA ends to promote binding. Mre11 is also a nuclease which conducts end resection of the free DNA ends in a 5’ to 3’ direction to form a long 3’ single strand DNA (ssDNA) overhang [34]. Replication

protein A (RPA) coats this ssDNA, promoting the recruitment and subsequently replacement by the ATP-dependent DNA recombinase RAD51. Multiple RAD51 molecules nucleate together to form a helical filament which stretches the ssDNA to 150% its' typical length. The RAD51 bound DNA filament then searches for its sister chromatid [35]. Once a homologous DNA strand is located, the invading 3' ssDNA anneals to the complementary strand, displacing the original homologous strand to form the D-loop. Extension occurs both at the 3' end of the invading strand, using the complementary strands as a template, and at the 5' end of the DSBs using the displaced strand as template. Holiday junctions are formed where the strands crossover, which undergo HR. At the end of this process are two homologous double stranded DNA strands (dsDNA strands) [36, 37].

As mentioned, HRR is strictly constrained to S and G2 phase. Important factors necessary for HRR progression, including CtIP, necessary for Mre11 mediated end resection, and RAD51 loading require phosphorylation by S and G2 specific cyclin-dependent kinases (CDK), in particular CDK1 [35]. Furthermore, CtIP undergoes ubiquitination and subsequent proteasomal degradation during G1. This temporal control ensures that HRR does not commence in the absence of a homologous sister strand; especially important as HR cannot easily be aborted due to the incompatibility between processed ends and NHEJ. Not only is HR limited by cell cycle, but also by direct competition for substrate by 53BP1 or the DNA binding complex, Ku70/80 [38]. This mechanism is shown in Figure 1.1.

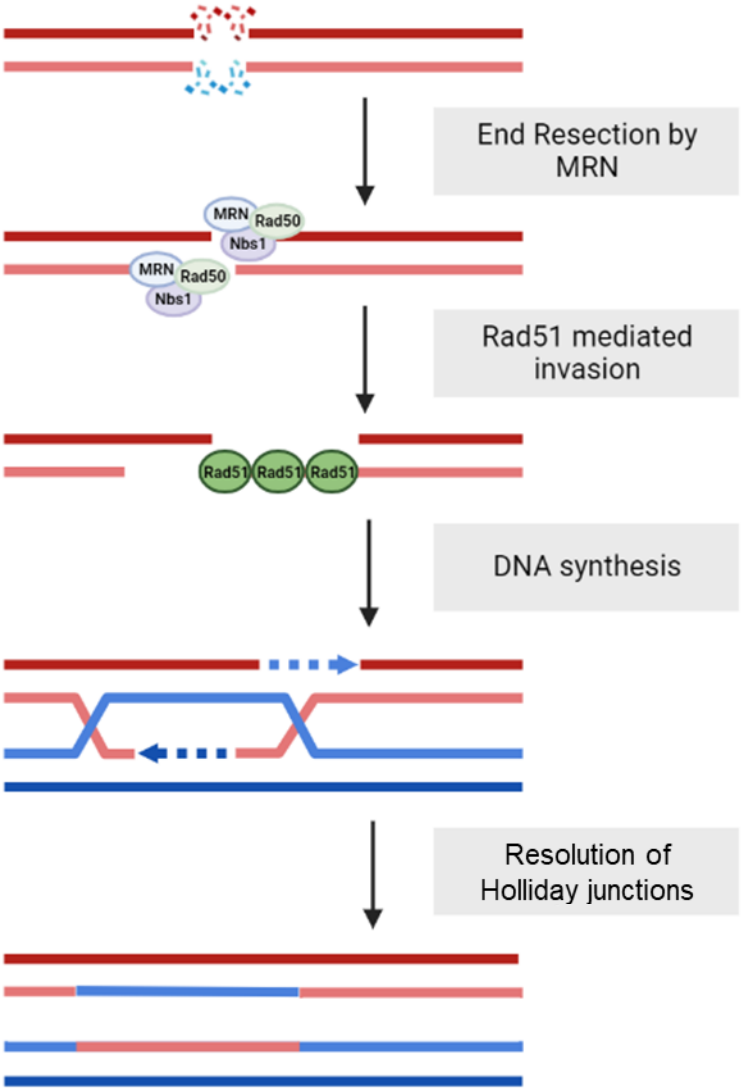

Figure 1. 1. Homologous Recombination Repair of DSBs

Diagram showing the homologous recombination repair pathway of DSBs. DSB ends are resected by the MRN complex. RPA coated DNA strand bound is stretched and Rad51 binds. This strand invades a homologous sister chromatid. DNA synthesis and resolution of holiday junction then completes the DSB resolution. Made in BioRender.

1.1.6.3. Non-Homologous End Joining

While HRR is an important pathway for DSB repair, NHEJ accounts for the DSB resolution under normal physiology and this preference is only enhanced in instances of pathological DNA damage, such as that induced by radiotherapy.

NHEJ is initiated by the binding of Ku heterodimer. This complex consists of two subunits: Ku70 and Ku80. Together, these subunits join to form a ring which binds to the open unresected ends of a DSB. The Ku70/80 heterodimer is threaded onto the DNA and forms dynamic bonds between the central domains of both Ku70 and Ku80 and phosphates on the DNA backbone in a sequence independent manner [39]. The inside channel of Ku70/80 is positively charged enabling it to move along the DNA backbone [39]. Unlike MRN, Ku70/80 is not tethered to the DNA during normal state. Instead, it moves freely around the cytoplasm and nucleus at a high concentration, which is maintained throughout the cell cycle [39, 40]. Once bound, the DNA strands are protected, impeding MRN complex end resection and thus inhibiting HRR.

Upon induction of a DSB, the heterodimer Ku70/80 is rapidly recruited to the site due to its high abundance within the cell and strong affinity to DNA ends. This recruitment can occur within seconds of damage [41]. However, while Ku70/80 DNA docking occurs very rapidly, dissociation is slower, typically only occurring following complete repair.

Another key player in the NHEJ is a member of the PIKK family called DNA-dependent protein kinase (DNA-PK) [26]. DNA-PK consists of two subunits, Ku70/80 and the DNA-PK catalytic subunit (DNA-PKcs) [26, 29]. The interaction between Ku70/80 and DNA increases the binding affinity of DNA-PKcs to DNA. Binding occurs between Ku70/80 and the C-terminal end of DNA-PKcs in the presence of DNA, while the N-terminal forms a pincer-shape structure around a central cavity through which the DNA is threaded [42]. This binding promotes the translocation of Ku70/80 along the DNA backbone and away from the DSB site. The two opposing DNA-PKcs

molecules bind together to form a bridge, bringing the DSB ends together into a synaptic complex. At this point, autophosphorylation of DNA-PKcs occurs at Ser2056 and DNA-PK is now active, triggering a signal cascade. While DNA-PK has a large array of phosphorylation targets, this autophosphorylation event is arguably the most important regarding DNA repair [43, 44]. Active DNA-PK phosphorylates key downstream components of the NHEJ, but another interesting phosphorylation event is the phosphorylation of GOLPH3 which in turn triggers fragmentation of the Golgi apparatus [45]. This will be explained in further detail in Section 3.1.1.

The presence of Ku70/80 may impede extensive end resection, such as that required for HR. However, minimal end-processing can be performed by the nuclease Artemis to make them compatible for ligation. Minimal end resection by Artemis often occurs in during the repair of ionising radiation induced DSBs which are frequently in proximity to oxidised and alkylated bases [29]. Nucleotide excision and reliance on microhomology, rather than extensive homology, makes NHEJ more error prone than HR. Once the ends are NHEJ compatible, polymerisation and ligation commence.

Ligation is initiated by the recruitment of DNA ligase IV in complex with x-ray repair cross-complementary 4 (XRCC4) to Ku70/80 on either side of the DSB. XRCC4 molecules on either side of the break homodimerize, providing a scaffold holding the two ends together [46]. Once the DSB ends are stabilised, the DNA polymerase Pol λ fills the gaps on the ssDNA regions on either side and XXRC4-like factor (XLF) completes the ligation [29]. Upon the formation of covalent bonds between the opposing DNA ends, Ku70/80 is removed via ubiquitin-proteasomal degradation [47]. A diagram showing this process is shown in Figure 1.2.

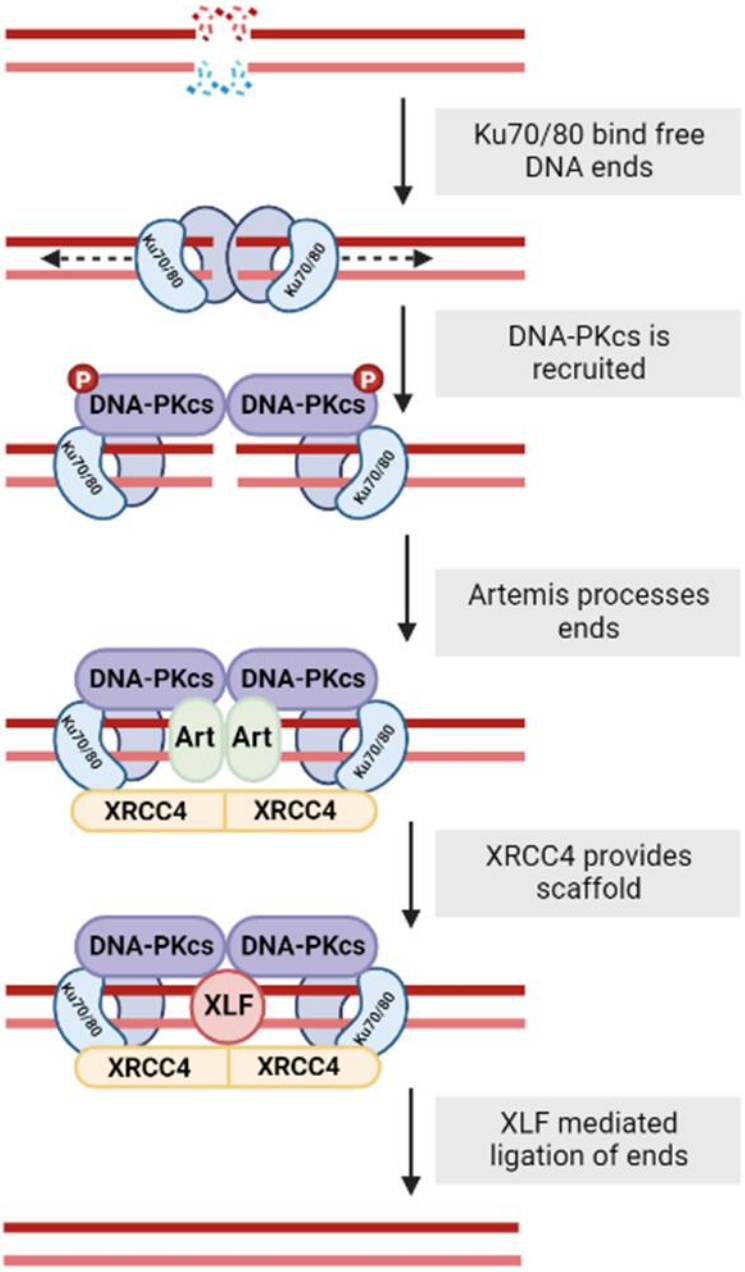

Figure 1. 2. Non-homologous end joining repair of DSBs

Diagram showing the non-homologous end joining repair pathway. Ku70/80 is recruited to free DSB DNA ends and DNA-PKcs is recruited. Following DNA-PKcs activation, end processing and ligation factors artemis, XRCC4 and XLF are recruited and the DSB is resolved. Made in BioRender.

1.1.8. Targeting DNA damage response to improve radiotherapy

The therapeutic ratio is the relationship between the dose required for tumour control and the risk of normal tissue damage which results in toxicity. Over the years, improvements have been developed to help widen this window. Advances in imaging technology have improved the accuracy of radiotherapy administrations. It has also become standard practice to divide the planned dose into fractions which has multiple benefits. Breaks in between doses offers normal cells the chance to repair between sub-lethal doses while malignant cells accumulate the damage instead. Efficacy of radiotherapy relies on certain factors such as cell cycle phase and cell oxygenations, therefore irradiating at different times increases the chance of the therapy being successful [48]. There are two other important strategies to optimise the therapeutic ratios, that will be the focus of this thesis. First, the use of pharmacological inhibitors of DSB repair, and secondly, the activation of an anti-tumour immune response. The latter of which will be discussed in more detail in Section 1.2.

The prevention of DSB repair after radiotherapy preferentially targets cancer due to their proliferative nature and dysregulated DDR. NHEJ is the most important pathway in the repair of ionising radiation-induced DNA breaks. As a critical component of NHEJ-mediated repair, DNA-PK presents an attractive therapeutic target to potentiate radiotherapy for the treatment of cancer.

1.1.9. DNA-PK inhibitors as radiosensitisers in cancer

The earliest compounds targeting DNA-PK inhibition were non-specific inhibitors of PI3K. The first was the naturally occurring fungal metabolite, Wortmannin [49]. While Wortmannin demonstrated significant radiosensitising properties, it had significant limitations such as poor stability in solution and significant off-target effects [49]. In 1994, Lilly Pharmaceuticals developed LY294002, which was a much more selective PI3K inhibitor [50]. This compound inspired the development of more selective

compounds, with improved properties. The next generation were Nu7427, Nu72056 and Nu7441. These compounds are DNA-PK specific and much more potent in comparison to LY294002. Nu7441 potentiates the effects of DNA damaging agents including chemotherapy [51, 52] and radiotherapy [53] in a variety of cancers [54, 55].

Nu7441 remains the most used DNA-PK inhibitor (DNA-PKi) for *in vitro* studies [56]. However, despite promising early studies, upon translation into mice, poor solubility of the compound and limited oral bioavailability restricts its use *in vivo* but their promising activity encouraged further development [55]. Since then, using high throughput screening methods, compounds have been developed with higher specificity and favourable properties. Currently, there are four compounds undergoing clinical trials, M3814, CC-115, VX-984 and AZD-7648 [56, 57]. Details of these clinical trials are shown are shown in Table 1. Currently, the outcomes of only two of the trials are reported. Including a first-in-man study reporting the maximum tolerated dose, safety, and preliminary efficacy of M3814 in advance solid tumours. This trial found M3814 to be well tolerated and offer moderate efficacy [58]. Another first-in-man study reported the safety, pharmacokinetics pharmacodynamic profile and preliminary efficacy of the dual mTOR and DNA-PK inhibitor, CC-115. This study reported CC-115 to be well tolerated and reported moderate efficacy [59].

Table 1. 1. Clinical trials investigating DNA-PK inhibitors for cancer therapy. Table showing all clinical trials investigating DNA-PKi. Data from clinicaltrials.gov and accurate as of 04/01/2022.

DNA-PKi	Phase	Tumour Type	Combination Treatment	Results/Recruitment Status	Registration No.	Year
M3814	I	Advanced solid tumours or Chronic Lymphocytic Leukaemia		Well tolerated and moderate efficacy [58]	NCT02316197	2014
	I	Advanced solid tumours	Radiotherapy Cisplatin.	Study completed but not reported	NCT02516813	2015
	Ib/II	Small cell lung cancer	Cisplatin, Etoposide.	Recruitment terminated due to recruitment issues	NCT03116971	2017
	I	Solid tumours	Avelumab, radiotherapy	Study completed but not reported	NCT03724890	2018
	I/II	Locally Advanced Rectal Cancer	Capecitabine, Radiotherapy	Study completed but not reported.	NCT03770689	2019
	I	Relapsed or refractory acute myeloid leukaemia	Cytarabine, Etoposide, Mitoxantrone	Suspended for interim monitoring	NCT03983824	2019
	I/II	Advanced prostate cancer not responsive to hormonal therapy	Avelumab, Radium	Recruiting	NCT04071236	2019
	I/II	Advanced/Metastatic solid tumours and Hepatobiliary malignancies	Avelumab, Radiotherapy	Recruiting	NCT04068194	2019
	I	Ovarian cancer	Doxorubicin	Recruiting	NCT04092270	2020
	I/II	Localised pancreatic cancer	Radiotherapy	Recruiting	NCT04172532	2020
	I	Glioblastoma or Gliosarcoma	Radiotherapy, resection, temozolomide	Recruiting	NCT04555577	2020
	I	Advanced Head and Neck Cancer	Radiotherapy	Suspended, accrual met	NCT04533750	2020
	I	Neuroendocrine tumours	Lutetium	Recruiting	NCT04750954	2021
	I	Healthy		Study completed but not reported.	NCT04702698	2021
CC-115 (dual mTOR and DNA-PM inhibitor)	I	Advanced solid tumours and hematologic malignancies	Alone	Well tolerated and moderate efficacy [59]	NCT01353625	2011
	I	Castration-resistant prostate cancer	Enzalutamide	Active, not recruiting.	NCT02833883	2016
VX-984	I	Advanced solid tumours	Doxorubicin	Study completed but not reported.	NCT02644278	2016
AZD-7648	I/II	Advanced malignancies	Doxorubicin	Active, not recruiting.	NCT03907969	2019
	I	Soft tissue Sarcoma	Radiotherapy	Recruiting	NCT05116254	2022

1.1.10. M3814: a novel inhibitor of DNA-PK

M3814 (peposertib/nedisertib) is currently the subject of many current clinical trials as shown in Table 1. As a DNA-PKi of clinical interest, and the focus of this thesis, M3814 will be discussed in further detail. M3814 is an ATP-competitive inhibitor. Recent structural analysis investigating the binding of DNA-PKcs and ATP or DNA-PK inhibitors show that while the older compound, Wortmmannin, competes for ATP binding in the ATP binding domain, M3814 binds in a pocket near the ATP binding groove. This induces a conformational change which closes the ATP binding site. This specific binding to DNA-PK improves the specificity of M3814 [60]. The structure and binding to DNA-PK is shown in Figure 1.3.

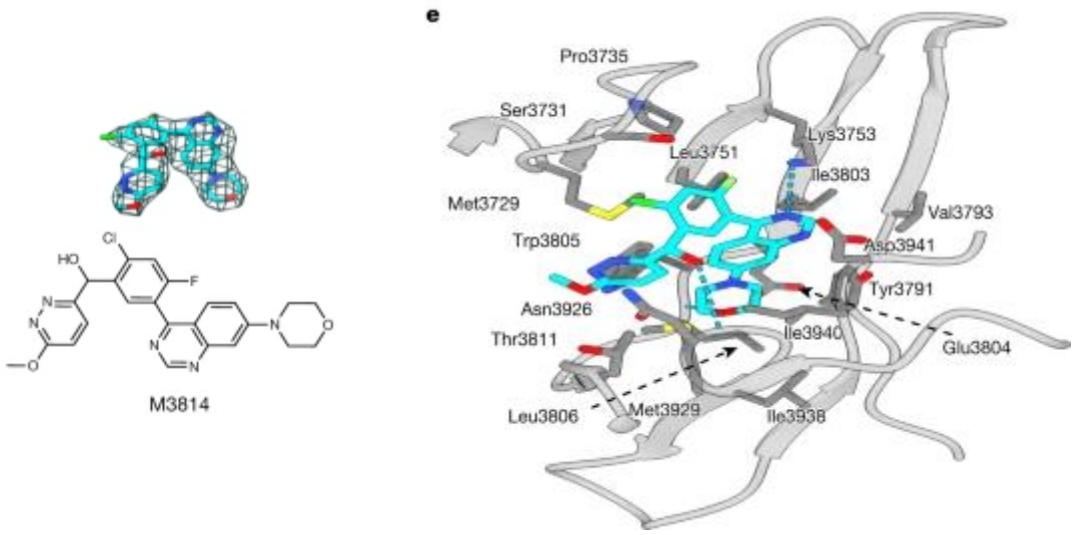

Figure 1. 3. M3814 structure and binding to DNA-PKcs.

Structure of M3814 and binding pocket in DNA-PK. M3814 binds in a pocket close to the ATP binding site of DNA-PKcs. Adapted from Liang *et al.,* (2022) *Nature.*

The first clinical trial using M3814 commenced in 2014. This first-in-man study demonstrated M3814 to be well tolerated in humans with advanced solid tumours [61]. As shown in Table 1, there are many trials investigating M3814 in combination with a variety of DNA damaging agents, and immunotherapy. However, these studies are yet to report their findings.

In preclinical studies, however, M3814 has shown synergy with a variety of DSB inducing agents. This includes docetaxel in prostate cancer [62] and TOPO II inhibitors such as doxorubicin and etoposide in ovarian cancer [63] and etoposide and paclitaxel in NSCLC [64]. In acute myeloid leukaemia xenograft models, M3814 synergised with daunorubicin and cytarabine [65] and gemtuzumab ozogamicin, a CD33 antibody drug conjugate (ADC) with calicheamicin (DSB inducer) [66]. A mouse model of rectal cancer also showed synergistic effects of M3814 when combined with 5-fluorourcil or radiotherapy [67]. Furthermore, M3814 radiosensitised tumours in cervical cancer mouse models [68] and xenograft mouse models [69].

Therefore, preclinical experiments demonstrate M3814 has potential for sensitising cells to DNA damaging agents. However, while the ability of M3814 to potentiate radiotherapy and induced cytotoxicity through cancer-cell intrinsic mechanisms are important, it is of great interest to investigate how treated cells interact with the tumour immune microenvironment.

1.2. Cancer and the Immune Response

1.2.1. Immunoediting in tumorigenesis

Cancer immunosurveillance is defined by the ability of the immune system to recognise and eliminate tumours [70, 71]. When this was first proposed, it was somewhat controversial as the role of the immune system was defined by its ability to recognise non-self from self. Now, however, evasion of the immune surveillance is a known turning point in tumorigenesis. Understandably, the theory of immunosurveillance now exists under the wider umbrella of immunoediting. Rather than focusing on the ability of the immune system to detect and eliminate tumour cells, immunoediting also describes the strategies tumours express to evade control. This is a dynamic process in which the more immunogenic tumour cells are more

readily detected. At times, however, this exerts a selective pressure on the developing lesions resulting in the expansion of the less immunogenic cells. This results in resistant tumour cells which can evade the immune system and grow into a tumour. There are three stages of immunoediting: elimination, equilibrium, and escape [70, 72]. A diagram showing these this process is shown in Figure 1.4.

1.2.1.1. Immune elimination of premalignant lesions

A cancerous lesion stimulates release of inflammatory signals which recruits innate immune cells including natural killer (NK) cells, macrophages, and dendritic cells. Tumour cells release pathogen associated molecular patterns (PAMPs) and damage-associated molecular patterns (DAMPs). This stimulates recruitment and activation of antigen presenting cells (APCs) which engulf tumour cells and tumour debris. APCs degrade the tumour debris and migrate to a nearby lymph node. Here, the degraded tumour peptide fragment is presented in complex with major histocompatibility complex (MHC) molecules. These APCs then prime and activate complementary naïve T cells in a two-signal system. Signal one is the binding of tumour-antigen loaded MHC molecules to the complementary TCR, while signal two is the binding of costimulatory molecules such as CD80/86 on dendritic cells to CD28 on the T cell. Both signals together stimulate survival, differentiation, and proliferation of the recipient T cell, which migrate to the tumour site. Upon exposure to cells bearing the same tumour antigen, $CD8^+$ T cells can launch a potent anti-tumour response by the production of granzyme B and perforin which perforates the target cell membrane. CD4+ T cells increase the antitumour release through the release of cytokines, including IFNγ. As such, the presence of $CD8^+$ T cells within a tumour are a positive predictor of good prognosis in many cancers [73, 74]. MHC Class II for $CD4^+$ T cells activation and MHC Class I for the cross priming of $CD8^+$ T cells. This process is shown in Figure 1.4.

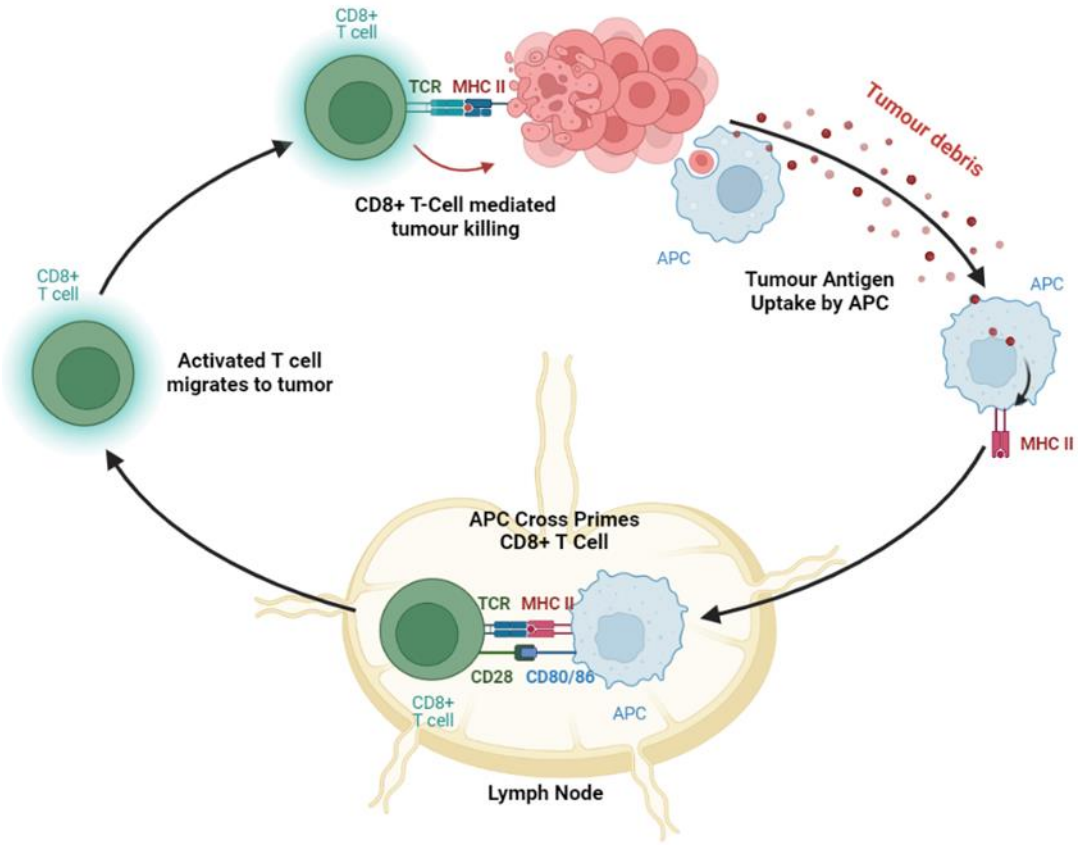

Figure 1. 4. CD8+ T Cell Mediated Tumour Clearance

Diagram showing the crossing-priming of tumour reactive T cells by APC. Tumour debris and tumour cells is engulfed by APC and degraded. Tumour peptide fragments are presented on APC which then migrate to the lymph nodes where complementary $CD8^+$ T Cells and activates them. Primed $CD8^+$ T cells migrate to the tumour where they mediate tumour killing. Made in BioRender.

1.2.1.2. Equilibrium and tumour immune evasion

Due to the dynamic and heterogeneous nature of tumour cells, tumour subclones develop which avoid immune-mediated elimination. During this stage the immune system and the tumour are in equilibrium. Tumour cells can avoid immune elimination through a variety of mechanisms. These include downregulation of MHC Class I and tumour associated antigens, the creation of an immunosuppressive tumour microenvironment (TME) through the release of anti-inflammatory chemokines, and induction of T cell tolerance by changes in expression of immune modulatory molecules [70, 72, 75]. The persistence of resistant subclones leads to an evolutionary race between tumour cells and the immune system. Immune evasion

confers a strong selective advantage and soon these immune resistant clones can grow. If the immune system becomes unable to control the developing tumours, there is a period of rapid tumour growth termed tumour escape [70, 72, 75].

1.2.2. Tumour immunogenicity

For successful elimination of tumour cells by cytotoxic $CD8^+$ T cells, there must be antigen uptake by the innate arm and subsequent antigen presentation to adaptive arm. Once primed, these T cells then must recognise their target and receive signal two. Tumours can evade immune elimination by shutting down adaptive immune response through upregulation of inhibitory immune checkpoint molecules. Tumours with high levels of tumour-reactive T cell infiltration and markers indicating a pre-existing anti-tumour response, and therefore antigen presentation, can be described as immunogenically 'hot' [73, 74, 76, 77]. In contrast, those lacking immune infiltration and evidence of a previous immune response are deemed 'cold'. Cold tumours lack antigen presentation [73, 74, 76, 77]. The development of pharmacological inhibitors of inhibitory immune checkpoint molecules, called immune checkpoint inhibitors (ICIs) has drastically improved the clinical landscape. These lift the inhibitory signals sent to T cells, to restore tumour elimination. However, their success is limited to 'hot' tumours making strategies to increase tumour immunogenicity appealing both to facilitate an anti-tumour immune response, but also to increase the proportion of patients that can benefit from ICIs. Whether the use of radiotherapy combined with the DNA-PKi M3814 might increase tumour immunogenicity is the focus of this thesis.

1.2.3. Radiotherapy and the immune system

The clinical success of radiotherapy lies in the induction of DNA DSBs which are not repaired by cancer cells, resulting in their death. However, in recent years it has become clear that radiotherapy is also capable of stimulating a systemic anti-tumour

immune response including increased dendritic cell activity and subsequent cross-priming of $CD8^+$ T cells. This has been demonstrated in syngeneic tumour model models to result in $CD8^+$ T cell dependent anti-tumour response [78-82]. The ability of radiotherapy to promote and anti-tumour immune response is not limited to the treatment field can extend to other distant tumour sites. This is termed the 'abscopal effect'. However, while radiotherapy is known to be capable of promoting an anti-tumour immune response, the consensus on the optimal conditions to do so remain unclear. For example, preclinical studies have demonstrated the importance of dosing and scheduling of radiotherapy in invoking and anti-tumour immune response but which approach is more favourable is yet to be determined. In a syngeneic mouse breast cancer model, in combination with CTLA-4 treatment, when a fractionated radiotherapy regimen (3x8Gy) was administered to a tumour on one flank, tumour control was observed both at the irradiated flank, but also of the tumour on the contralateral flank. This did not occur upon treatment with a single large dose (1x30Gy) [83, 84]. In contrast, in the colorectal syngeneic mouse tumour models, a single 30Gy was found to induce immune mediated tumour elimination, increased tumour infiltration of $CD8^+$ T cells and protect mice from future tumour rechallenge, while those receiving 10x3Gy did not [85]. In a melanoma mouse model, a single dose of 15Gy was also more effective in promoting an anti-tumour adaptive immune response than treatment with 5x3Gy [78]. The immunoregulatory ability of radiotherapy is more apparent when used in combination with immunotherapy and with the emergence of ICIs, the abscopal effect has been observed in human patients. This was first reported during a clinical trial investigating the efficacy of the ICI ipilimumab (anti-CTLA4) for metastatic melanoma in which a patient receiving radiotherapy to treat spinal metastases had tumour regression not just in irradiated sites, but also at distant metastatic regions [86]. This synergy with ICIs points at the ability of radiotherapy to increase the immunogenicity of tumours.

While the administration of radiotherapy will have effects on the entire irradiated TME, in this thesis the cancer cell intrinsic response to radiation will be focused on. Two important mechanisms linking radiotherapy and immunogenicity, which will be focused on, are immunogenic cell death (ICD) and the cGAS-STING pathway.

1.2.4. Immunogenic cell death

Programmed cell death, apoptosis, is a process which is required for normal physiology and frequently an outcome of cell death induces by DNA damaging agents. Apoptosis is non-inflammatory, however, in recent years a classification of apoptosis, known as immunogenic cell death (ICD), has been established [87]. ICD is apoptosis resulting in the release of specific damage associated molecular patterns (DAMPs) which can invoke an immune response. In doing so, the potential for antigen presentation from these cells is enhanced [87-90].More specifically, ICD increases dendritic cell activation and subsequent priming and cross-priming of T cells. It is, therefore, a strategy to determine how cancer therapies that kill cells, can do so in this highly immunogenic manner. There are three key immunostimulatory events that are determinants of ICD [88]. These include translocation of Calreticulin (CRT) to the cell surface membrane, secretion of ATP, and HMGB1 release.

1.2.4.1. Markers of immunogenic cell death

Under normal conditions, CRT is localised in the lumen of the endoplasmic reticulum (ER) and is important in MHC Class I peptide loading. In the early stages of apoptosis, CRT is translocated to the cell surface membrane [89]. Cell surface CRT is an ‘eat me’ signal for dendritic cells and, to a lesser extent, macrophages [91, 92]. CRT binds CD91 on dendritic cells or Macrophages and encourages phagocytosis and antigen processing [90]. The timing of CRT translocation is important for immunogenicity. While CRT translocation occurs during the early phases of cell death, the late-stage

marker of apoptosis, extracellular phosphatidylserine (PS), stimulates macrophage clearance in an immunogenically silent manner. This prevents engulfment and subsequent antigen presentation by dendritic cells [93, 94].

During ICD, ATP is released. ATP is chemotactic to dendritic cells and T cells and increases T cell priming [95]. HMGB1 is also released during ICD and binds toll-like receptor 4 (TLR4) and adaptor myeloid differentiation primary response 88 (MyD88) receptor on dendritic cells, promoting dendritic cell maturation and increasing antigen presentation to T cells [96]. In addition to this, HMGB1 provide direct stimulation to T cells to promote their proliferation [97]. This is shown in Figure 1.5.

If a cancer cell releases DAMPs during ICD, tumour antigen processing and presentation is increased, mobilising a potent anti-tumour immune response. Presence of these DAMPs are important for therapy-induced anti-tumour immune response. For example, injection of anthracycline-treated dying CT26 tumour cells into mice invokes an immune response into mice and protects the mouse from future rechallenge with naïve CT26 cells. This effect was abrogated by inhibition of CRT translocation to the CT26 cell surface membrane [89]. Furthermore, loss of the HMGB1/TLR4 signalling axis using $TLR4^{-/-}$ mice prevented a similar vaccination response to Doxorubicin treated tumour cells [96].

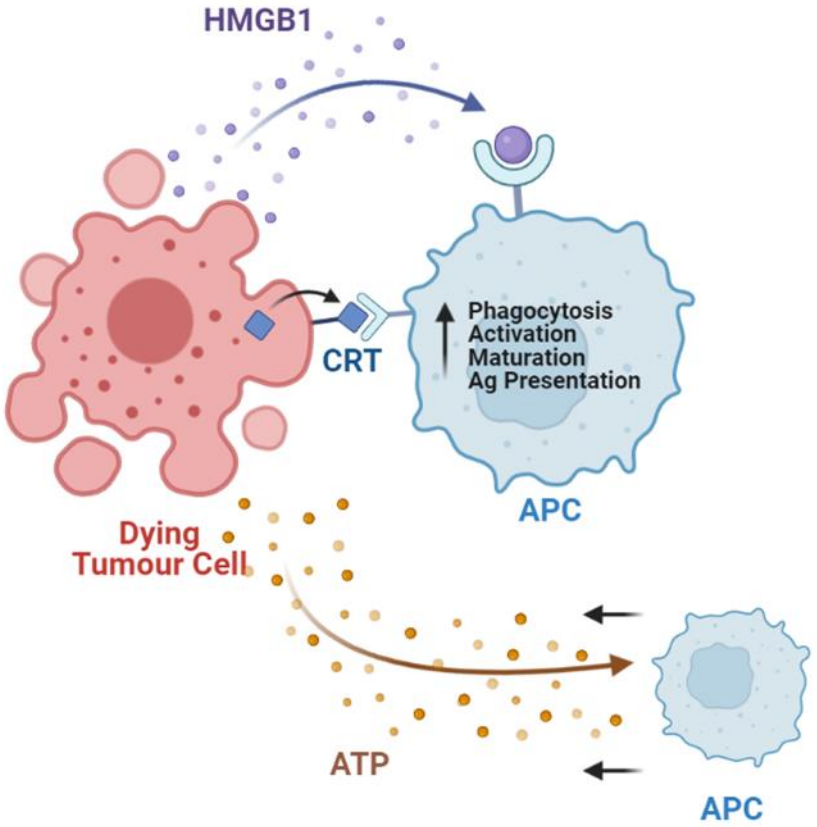

Figure 1. 5. Immunogenic Cell Death

There are three main markers of ICD including translocations of CRT to the cell surface membrane and release of HGMB1 and ATP. This increases APC mediated phagocytosis of tumours and APC activation and maturation. Made in BioRender.

A variety of pharmacological agents used in clinic such as mitoxantrone, doxorubicin and oxaliplatin are well-established inducers of ICD [98, 99]. Radiotherapy may also induce ICD and result in tumour rejection [91, 100]. In TSA murine cancer cells, CRT translocation, HMGB1 expression and ATP secretion increased following radiotherapy in a dose dependent manner [100]. Radiation-induced ICD was further enhanced upon addition of chemotherapeutics including oxaliplatin, paclitaxel and carboplatin, which resulted in increased CRT translocation [100]. This was observed both *in vitro* and *in vivo* [100].

1.2.5. cGAS-STING sensing of cytosolic DNA in cancer

A further mechanism linking radiotherapy and immunity is the cytosolic DNA sensing cGAS-STING pathway [101-103]. DNA is not present in the cytosol under physiological conditions. Upon viral infection, however, DNA can be released into the cytoplasm either following direct transfection from a DNA virus or due to the loss of viral capsid integrity containing reverse transcribed cDNA from retroviruses. Cytosolic DNA is a PAMP, the recognition of which alerts the cell to a viral infection and enables the innate immune system to mount an antiviral response through the transcription and release of type I IFNs and inflammatory cytokines [104-106].

1.2.5.1. The cGAS-STING pathway

The cGAS-STING pathway is an anti-viral innate pathway which is triggered by cytosolic dsDNA. A diagram of this pathway can be found in Figure 1.6. Upon the accumulation of double stranded DNA (dsDNA) in the cytosol, dsDNA can bind to cyclic GMP-AMP synthase (cGAS). This may occur at either the N-terminal nucleotidyltransferase domain, or the C-terminal dsDNA recognition domain. Binding is sequence independent, although it has been shown that longer dsDNA strands bind more readily [107, 108]. Upon binding, cGAS-dsDNA complexes dimerise with another cGAS-dsDNA complex. Oligomerisation of these cGAS-dsDNA continues, forming high order complexes. These complexes form dense-phase liquid droplets, concentrating activated cGAS to amplify the signal and sequester potentially harmful viral DNA [109]. Following oligomerisations, cGAS undergoes a conformational change, opening its active site. ATP and GMP can then enter the active site to be converted into 2',3'cyclic GMP-AMP (cGAMP).

cGAMP binds to a transmembrane protein located on the ER called Stimulator of Interferon Genes (STING) promoting its dimerisation and subsequent translocation to the Golgi apparatus [104-106]. Here, STING is palmitoylated, resulting in the

recruitment and subsequent phosphorylation of TANK binding protein (TBK1). TBK1 undergoes self-phosphorylation at Ser 172, and then phosphorylates STING at Ser 366, triggering the recruitment of transcription factor interferon regulatory factor (IRF3). TBK1 phosphorylates IRF3 at Ser 396, resulting in the formations of a IRF3 homodimer which leaves the Golgi to enter the nucleus wherein it induces expression of type I IFN, in particular IFNβ, and inflammatory cytokines [104-106].

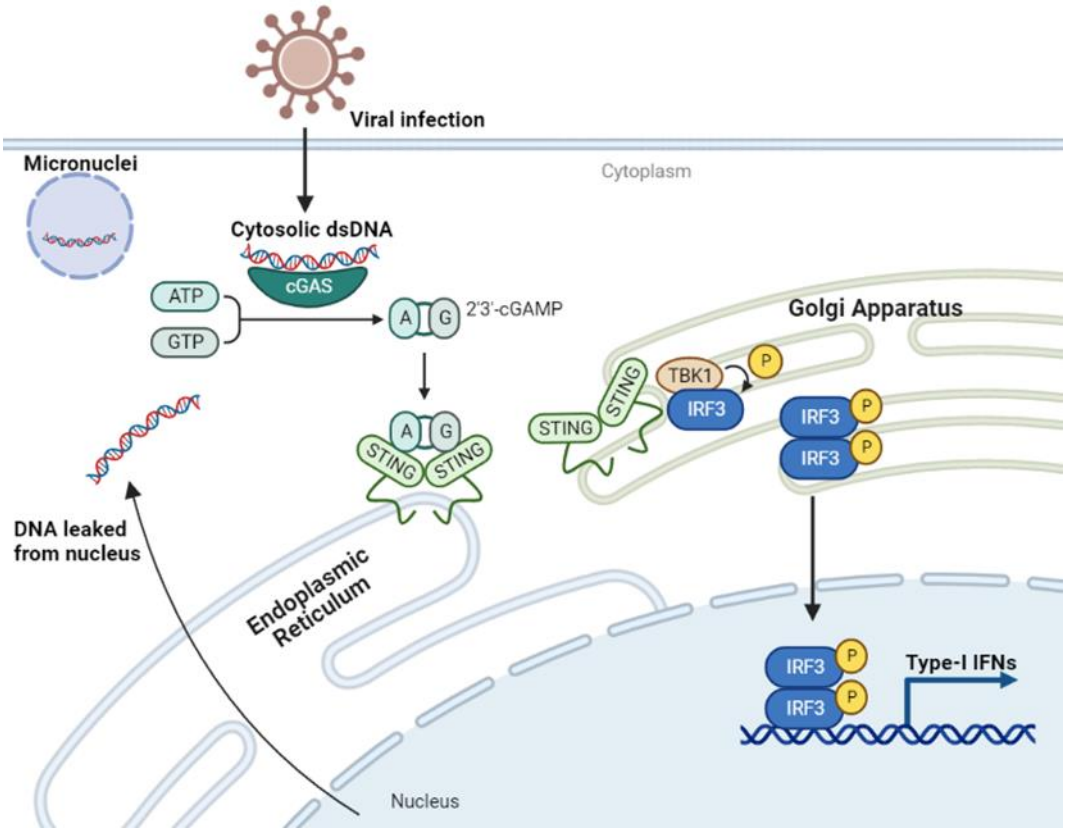

Figure 1. 6. The cGAS-STING Pathway

Cytosolic dsDNA can arise from degradation of micronuclei, leaking from the nucleus or during viral infection. cGAS binds DNA which triggers cGAS mediated conversion of ATP and GMP to cGAMP. cGAMP binds to STING on the ER, promoting translocation to the Golgi. TBK1 phosphorylated by STING and in turn phosphorylates IRF3. IRF3 homodimerises and enters the nucleus where it promotes the transcription of type I IFNs. Created in BioRender.

1.2.5.2. Interferon-β is an immunostimulatory molecule

Extracellular IFNβ binds IFN alpha receptor 1 (IFNAR1) or IFNAR2, which activates Janus kinase 1 (JAK) and tyrosine kinase 2 (TYK2), which in turn results in the recruitment and activation of signal transducer and activator of transcription (STAT)

proteins 1 and 2. STAT1 homodimerises or forms a complex with STAT2 and IRF9 [110, 111]. These complexes translocate to the nucleus and promote the transcription of IFN stimulated genes (ISGs). The genes promoted by STAT1 homodimer are involved in the antiviral response, such as Mx1 and Trex1, while those promoted by the STAT1 STAT2 IRF9 complex are involved in inflammation, including CCL2 and CXCL10 [111]. Both STAT complexes trigger almost promote cGAS transcription, forming a positive feedback mechanism [104, 106, 111]. The kinases involved in the response to IFNβ are widely expressed by all cells, meaning a rapid anti-viral response can be mounted in any receiving cell type. However, other IFNβ induced effects depend on the receiving cell type. IFNβ recruits dendritic cells to the site of inflammation and provide a stimulatory signal to dendritic cells, promoting their activation and maturation. This results in upregulation of MHC molecules, CD80 and CD86, which in turn, promotes the priming and activation of complementary T cells [112, 113].

1.2.5.3. Targeting the cGAS-STING pathway for cancer treatment

Activation of the cGAS-STING pathway produces an inflammatory response and can drive antigen uptake and presentation by dendritic cells to $CD8^+$ cytotoxic T cells. This makes it an attractive pathway to stimulate anti-tumour immune responses. Strategies to do so range from novel cyclic dinucleotides and direct STING agonists and delivery of cGAMP to the tumour [114]. The first cGAS-STING targeted therapy was reported in 2002 upon the development of dimethyloxoxanthenyl acetic acid (DMXAA). When first synthesised, DMXAA was not known to be a STING agonist. However, it later became clear that anti-tumour effects in mice were dependent on IFNβ induced $CD8^+$ T cell response due to increased activity of the cGAS-STING pathway [115, 116]. Unfortunately, the use of this compound failed to translate into success in human clinical trials due to differences in interactions between DMXAA

and human STING compared to the mouse counterpart [117]. Despite this setback, there is much interest in developing therapeutic approaches to target the cGAS-STING pathways, ranging from agents such as novel cyclic dinucleotides and direct STING agonists, to improving delivery of the cyclic dinucleotides [114].

1.2.5.4. The cGAS-STING pathway is activated by DNA damage

While therapies directly stimulating the cGAS-STING pathway are of interest, there are other approaches which aim to activate the cGAS-STING pathway indirectly. The cGAS-STING pathway was originally described as a response to viral infection. However, it is now apparent that self-DNA can also trigger the cGAS-STING pathway. Following genotoxic stress in cancer cells, either due to their inherent genomic instability or from exogenous sources such as radiotherapy or chemotherapeutics such as cisplatin, doxorubicin and etoposide, dsDNA can accumulate in the cytoplasm. This occurs as dsDNA leaks from the nucleus or the formation of micronuclei [118-120]. Micronuclei form when a cell harbouring DNA damage fails to prevent entry into mitosis resulting in chromosomal mis-segregation [15, 121]. During telophase, nuclear membranes form around DNA material. Typically, this results in two identical daughter nuclei. However, nuclear envelopes will also form around the DNA not attached to a centrosome, known as lagging DNA creating micronuclei [15, 121]. These micronuclei are then either excluded from the cell, reincorporated into the main nuclei, degraded, or can persist in the cytoplasm [122]. A diagram showing the formation of micronuclei can be found in Figure 1.7 A. Evidence shows that following radiotherapy, micronuclei are formed [118-120]. Micronuclei which lose their integrity during degradation offers cGAS access to the dsDNA within, triggering pathway activation, this is shown in Figure 1.7 B [118-120]. The induction of DSBs in cancer cells during radiotherapy creates chromosomal abnormalities resulting in fragments of DNA, and subsequently micronuclei formation and the successful

triggering of an IFNβ driven inflammatory response via the activation of the cGAS-STING pathway [104-106]. The link between genomic instability and micronuclei is has been proposed as a biomarker for cancer predisposition and malignancy for [123]. However, the proposal that their presence may also initiate an immune response is more novel.

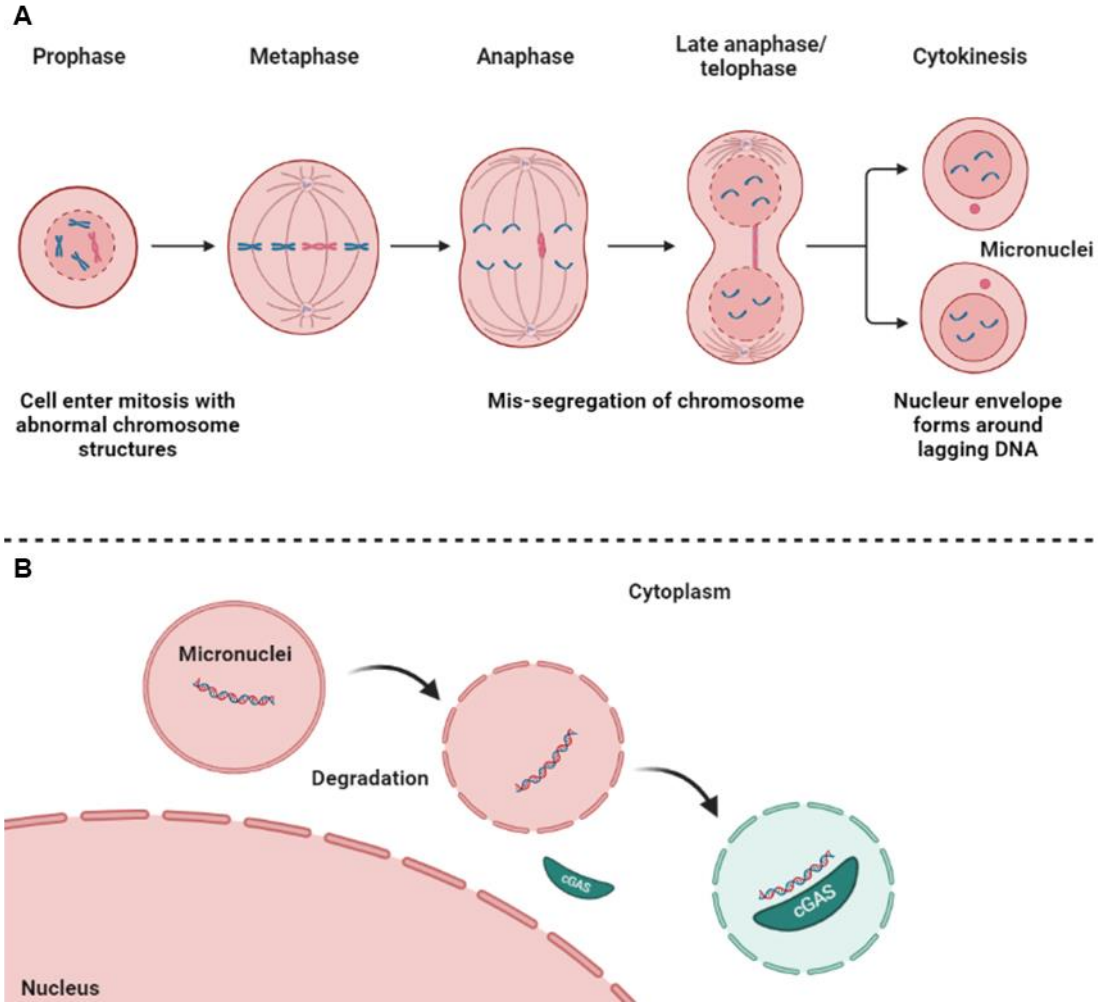

Figure 1. 7. Micronuclei formation and initiation of the cGAS-STING pathway

(A) Diagram showing the formation of micronuclei following chromosomal mis-segregation during mitosis. **(B)** Diagram showing degradation of micronuclear membrane resulting which triggers the cGAS-STING pathway. Drawn in BioRender.

1.2.5.5. Downregulation of the cGAS-STING pathway in cancer by hypermethylation

As DNA damage and aberrant mitosis are triggers of the cGAS-STING pathway, cancer cells, which have inherently higher degrees of genomic instability and DDR dysregulation than normal cells, are more visible to the immune system and thus, prone to immune mediated elimination. However, as previously discussed, immunoediting is a dynamic and evolutionary process. Therefore, cells with downregulation of the cGAS-STING pathway are therefore less visible to the immune system, making them more likely to survive and escape immune detection. Loss of the cGAS-STING pathway function provide a method of immune evasion and has recently been reported to occur frequently in cancer. A study on gastric cancer reported that 90.5% of patients had decreased STING expression and that this correlated with shorter overall survival [5]. A study on human colorectal cell lines found 10 of 11 cell lines assessed had defective cGAS-STING signalling [124]. Analysis of 32 types of The Cancer Genome Atlas (TCGA) tumour types identified higher levels of methylation in the promotor regions of both *cGAS* and *STING* in tumour tissue resulting the STING silencing [6]. DNA methylation is an example of an epigenetic mechanism, a process through which cells regulate gene expression without changing the nucleotide sequence. For DNA methylation to occur, DNA methyltransferase (DNMT) transfers a methyl group to a cytosine residue to form 5-methylcytosine. The addition of a methyl group prevents the binding of transcriptional proteins and recruits' factors involved in chromatin remodelling. Together, this inhibits transcription resulting in gene silencing [125]. Gene promoters are often rich in CpG sites and are particularly sensitive to DNA methylation. Epigenetic reprograming, of which aberrant DNA methylation is an example, is associated with cancer and has recently been proposed as another hallmark of cancer [7]. Given this, hypomethylating agents are of interest for cancer therapy due to their ability to correct some of the epigenetic reprograming that occurs during tumorigenesis. Decitabine (5-

aza-2'-deoxycytidine) is a hypomethylating agent which is FDA and EU approved for use as a cytotoxic agent in AML [126-128]. Decitabine is a cytidine nucleoside analogue which is incorporated in the place of cytosine of rapidly proliferating cells during S phase. If DNMT1 interacts with incorporated decitabine with the aim of transferring a methyl group, it becomes irreversibly bound. This limits the enzymatic activity of DNMT1 resulting in hypomethylation and restoration of previously silenced genes. An illustration of this process can be found in Figure 1.8. In cancer, this includes tumour suppressors such as those involved in apoptosis and cell cycle, but in addition, hypomethylation can undo the epigenetic reprograming which enabled the developing tumour to evade the immune system. An example of this is STING, which has been reported to be silenced in cancer cells by hypermethylation [6]. In a preclinical study on triple-negative breast can provided evidence that STING is suppressed by DNMT1. This suppression was lifted with decitabine treatment and increased *in vivo* sensitivity to anti-PD-1 therapy [129]. This has also been demonstrated in a KRAS-drive LKB1 mutant lung cancer. Using the TCGA lung cancer dataset, a correlation was reported between the LKB1 mutation, commonly seen in patients with NSCLC, and loss of Type 1 IFN signalling [130]. These LKB1 mutant tumours were associated with poor immune infiltration and resistance to ICI. Mechanistically, this was due to LKB1 mediated hypermethylation of the STING promoter [130].Treatment with decitabine restored STING and cGAS-STING functionality, consequently improving response to anti-PD-1 antibody [130]. The frequency of cGAS-STING pathway downregulation presents an obstacle to therapies targeting this pathway but also provide a rationale for combination of therapies which initiate the cGAS-STING pathway and hypomethylating agents such as decitabine.

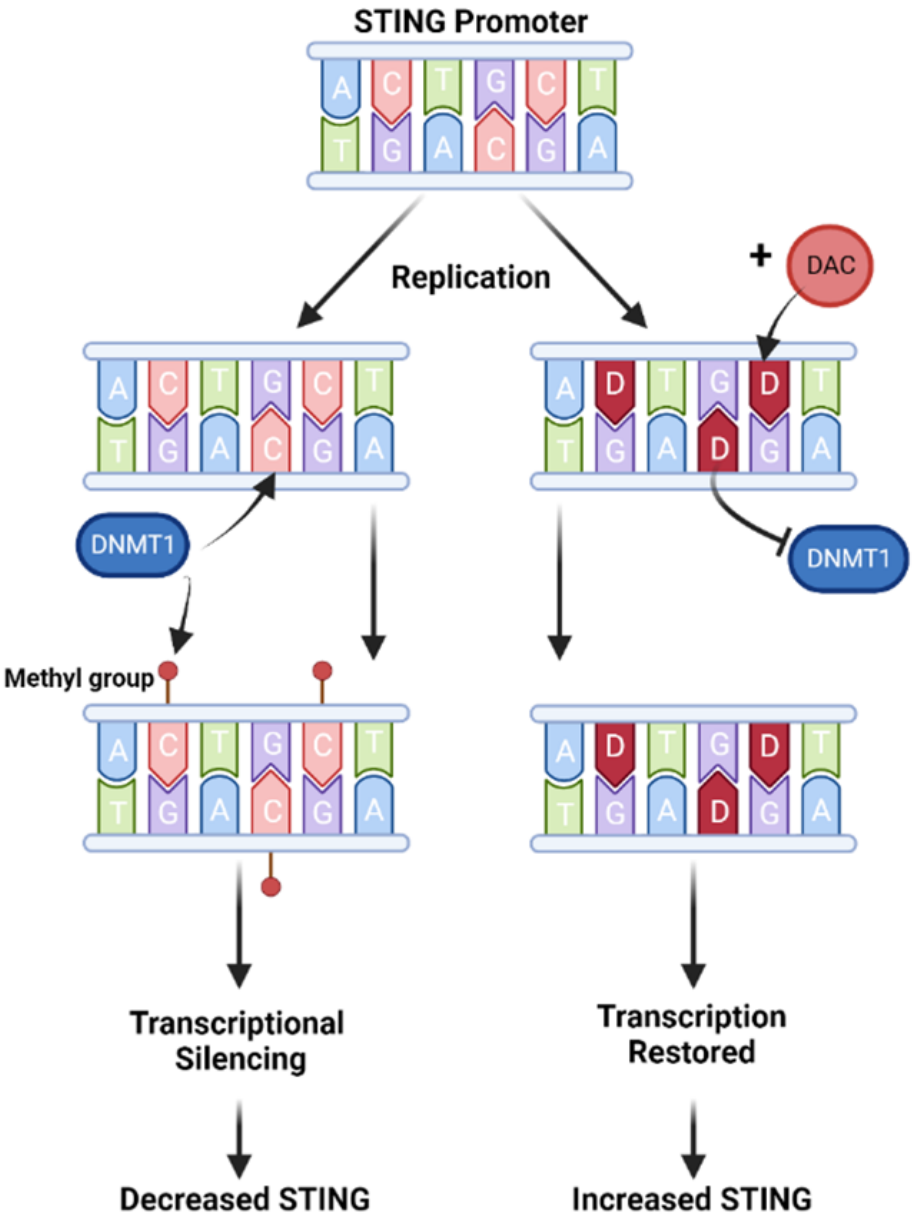

Figure 1. 8. Illustration showing the mechanism of decitabine induced hypomethylation

DNMT1 catalyses the transfer of a methyl group to a cytosine residue, resulting in gene silencing. Decitabine is a cytidine nucleoside analogue which is incorporated in the place of cytosine during replication. If a DNMT1 engages with decitabine to transfer a methyl group, it becomes irreversibly bound. This inhibits DNMT1 activity resulting in gene expression of previously silenced regions. For example, this can lead to restoration of STING. Adapted from Navada et al., (2014) *Journal of Clinical Investigation*.

1.2.5.7. Radiotherapy and the cGAS-STING pathway

While the formation of micronuclei during mitosis of cells with genomic instability can activate the cGAS-STING pathway, this is exacerbated with induction of DNA damage. There is a strong link between DSBs induced by radiotherapy and the activation of cGAS-STING pathway. For example, STING knockout has been demonstrated to abrogate radiotherapy induced abscopal tumours control in syngeneic mouse tumours models [103, 119]. Administration of IFNβ rescued tumour control following STING knockout in the CT26 model [103].

There is a clear link between DNA damage induced by radiotherapy and activation of the cGAS-STING pathway but this relationship is not linear. While increased x-ray doses correlates to increased DNA damage, this does not directly correlate with cGAS-STING pathway activity. In TSA, MC38 and 4T1 cells, the accumulation of cytosolic dsDNA increased in a dose dependent manner up to 12Gy. Dose over 12Gys stimulated expression of the endonuclease Three Prime Repair Exonuclease 1 (TREX1). This correlated with loss of cytosolic dsDNA due to TREX1 mediated degradation and consequently a loss of cGAS-STING pathway activity [83, 131]. These findings translated into syngeneic tumour mouse models in which 3x8Gy induced a cGAS-STING-dependent $CD8^+$ T cell response, while 1x20Gy failed to do so [83, 84]. Therefore, there is a careful balance between causing enough DNA damage to increase cytosolic dsDNA, triggering the cGAS-STING pathway, while not activating TREX1 [83, 84, 131].

1.2.5.7. The DDR and the cGAS-STING Pathway

In addition to the link between DNA damage and cGAS-STING pathway activity, there is also evidence that loss of DNA repair proteins correlates with increased levels of cytosolic dsDNA and subsequently cGAS-STING pathway activity. Patients with Ataxia Telangiectasia hereditary cancer syndromes, characterised by loss of ATM,

and $ATM^{-/-}$ mice have increased levels of spontaneous DSB lesions and enrichment of genes involved in the IFNβ response [132]. Cell obtained from Ataxia Telangiectasia cancer patients were resistant to HSV1 infection, indicating increased anti-viral response. This anti-viral protection was lost with silencing of IFNAR1 [132]. Loss of BRCA1 and BRCA2 in breast cancer cell lines also results in the spontaneous accumulation of cytosolic dsDNA and increased cGAS-STING pathway activity [133]. Mouse models of triple-negative breast cancer found that the PARP inhibitor Olaparib increased infiltration of $CD8^+$ T cells in the tumour but following STING knockout, this effect was lost [134]. In NSCLC cell lines and patient derived samples, treatment with PARP inhibition increased formation of micronuclei, which in turn activated the cGAS-STING pathway [135].

To date, there have been few studies investigating the immune implications of combining DNA-PKi and radiotherapy for cancer treatment. In 2022, the first study investigating this relationship was published [136]. In this study, MC38 cells treated with radiotherapy and M3814 had persistent chromosomal abnormalities. This results in the formation of micronuclei and activation of the cGAS-STING pathway, as measured by IRF3 and TBK1 phosphorylation and increased gene expression of ISGs. In mice bearing the MC38 tumour model, the combination of M3814, 3x5Gy and bintrafusp alfa (bifunctional fusion protein targeting TGFβ and PD-L1) improved tumour control, both at the irradiated tumour and at an abscopal site and survival [136]. As the subject of numerous clinical trials, M3814 is of significant clinical interest and therefore, improving our understanding of the immunological effects of combining M3814 and radiotherapy will be critical to the success of this approach.

1.3. Research Aims

DNA-PK inhibitors are known to sensitise cells to radiotherapy via cancer-cell intrinsic mechanisms but little is known about the immunological implications. Considering the capability of radiotherapy alone to stimulate an anti-tumour, the aim of this thesis is to determine the effects of radiotherapy and the newly developed DNA-PKi, M3814, on the immunogenicity of cancer cells.

Chapter 3

This chapter will investigate the effects of M3814 and radiotherapy combination treatment on the DDR and cell death in a variety of cancer cell lines. In addition, whether the cell death accompanying treatment is characteristic of ICD will also be determined.

Chapter 4

The focus of this chapter is the effect of combination treatment on the cGAS-STING pathway. By exploring the response in both cGAS-STING proficient and cGAS-STING deficient cancer cells, this chapter also aims to develop an approach to restore cGAS-STING pathway functionality.

Chapter 5

In this chapter, the findings from Chapters 3 and 4 will be translated into immunocompetent mouse models to explore the therapeutic efficacy and immune response to combination treatment of M3814, radiotherapy and decitabine.

2. Materials and Methods

2.1. Materials

2.1.1. Cell lines

B16 WT, MC38 and LCC were obtained from Professor Quezada. CT26 was donated by Dr Martin Pule. HCT-116 was provided by Professor Bert Vogelstein. CMT-167 was purchased from Sigma-Aldrich (Catalogue number - 10032302). KP.B6.F1 was previously generated by Dr Fred Arce Vargas in the Quezada laboratory at UCL. To do so, $Kras^{LSL/G12D}$;$Trp53^{flox/flox}$ C57BL/6 mice were treated with intranasal Cre-expressing adenovirus, resulting in the formation of lung tumours. Resulting tumour-bearing lungs were harvested and cultured, from this the KP.B6.F0 was generated. Wildtype C57BL/6 were challenged with KP.B6.F0 cells intravenously and left to form lung tumours. The resulting tumours-bearing lungs were harvested and cultured to obtain the KP.B6.F1 line. More details regarding cell lines and their culturing can be found below in Table 2.1.

2.1.2. Therapeutic agents

2.1.2.1. *In vitro* experiments

A 10mM stock solution of Nu7441 (Generon, HY-11006) was prepared in dimethyl sulfoxide (DMSO) and stored at -20ºC. M3814 (provided by Merck EMD Serono) was prepared as a 5mM stock solution in DMSO at -20ºC. Mitoxantrone dihydrochloride (Sigma-Aldrich, M6545) was prepared as a 10mM stock in DMSO. Decitabine (Abcam, ab120842) stock was prepared at 10mM in DMSO and stored at -20ºC. Recombinant mouse IFN-γ (BioLegend, 575302) was prepared as a 100µg/mL stock in phosphate buffers solution (PBS) and stored at -20ºC. A 100µg/ml polyinosinic–polycytidylic acid potassium salt (Poly(I:C) (Sigma-Aldrich) was prepared in PBS and stored at -20ºC. Interferon Stimulatory DNA (ISD) naked (InvivoGen) 100µg/ml stock

was prepared in endotoxin-free water (InvivoGen) and stored at -20ºC. A 500µM cGAMP sodium salt (Sigma-Aldrich, SML1232) was prepared in sterile water and stored at -20ºC. Cells were transfected with Poly(I:C), ISD or cGAMP using Lipofectamine 3000 as per manufacturer's instructions (Invitrogen). In vitro radiotherapy was administered using the A.G.O. HS 321 kV X-ray system.

2.1.2.2. *In vivo* experiments

For mouse experiments, a 1mg/mg M3814 solution was prepared the night before treatment and stored in the dark at 4ºC. M3814 was dissolved in 0.5% Methocel (Sigma-Aldrich), 0.25% Tween (Sigma-Aldrich), 300mM Na-Citrate (Sigma-Aldrich) sterile water at pH2.5. A 50mM decitabine (Abcam, ab120842) stock was prepared in DMSO and stored at -20ºC. At the beginning of each mouse experiment, this was diluted to 1mg/ml in sterile water and stored at 4ºC for a week.

2.2. Methods

2.2.1. Cell line maintenance

All cell lines were cultured in T75 flasks and maintained at a 37ºC; 5% CO_2 humidified atmosphere. Detail regarding the cell lines used and their maintenance can be found in Table 2.1. All media for cell culture was supplemented with 10% Foetal bovine serum (FBS)(Gibco), 1% penicillin/streptomycin (P/S)(Sigma Aldrich) and 2nM L-Glutamine (LG)(Sigma Aldrich) to make 'Complete' media. Cells were passaged prior to reaching confluency, typically this occurs 3 times a week. To do so, cells were washed with PBS (Gibco) and incubated with 3mL Trypsin EDTA (Sigma Aldrich) for 3-5 minutes at 37ºC. Once detached, 7mL of complete media was added and aspirated to mix. Cells were added to a fresh flask with complete media in the ratios indicted in Table 2.1. Lines were maintained until they reached passage 30, at which they were replaced by a fresh aliquot of cells maintained in liquid nitrogen.

Table 2. 1. Cancer Cell Line Maintenance

Cell Line	Species	Cancer Type	Medium
B16	Mouse	Melanoma	DMEM (Sigma Aldrich), 10% FBS (Gibco), 1% P/S (Sigma Aldrich), 2nM LG (Sigma Aldrich)
CMT-167	Mouse	Lung	DMEM (Sigma Aldrich), 10% FBS (Gibco), 1% P/S (Sigma Aldrich), 2nM LG (Sigma Aldrich)
CT26	Mouse	Colorectal	RPMI (Sigma Aldrich), 10% FBS (Gibco), 1% P/S (Sigma Aldrich), 2nM LG (Sigma Aldrich)
HCT-116	Human	Colorectal	McCoys 5A (Sigma Aldrich), 10% FBS (Gibco), 1% P/S (Sigma Aldrich), 2nM LG (Sigma Aldrich)
KP.B6.F1	Mouse	Lung	IMDM (Gibco), 10% FBS (Gibco), 1% P/S (Sigma Aldrich), 2nM LG (Sigma Aldrich)
LLC	Mouse	Lung	DMEM (Sigma Aldrich), 10% FBS (Gibco), 1% P/S (Sigma Aldrich), 2nM LG (Sigma Aldrich)
MC38	Mouse	Colorectal	RPMI (Sigma Aldrich) 10% FBS (Gibco), 1% P/S (Sigma Aldrich), 2nM LG (Sigma Aldrich)

2.2.3.1. Cell line storage and retrieval

For long-term storage, cells were maintained in liquid nitrogen. To freeze cells, cell suspension in complete media was obtained as detailed above and cells counted. The suspension was centrifuged a 1200rpm for 3 minutes to form a pellet which was resuspended at 1-2 x 10^6 cells/mL in Freezing Media (90% FBS and 10% DMSO (Sigma Aldrich)). This suspension was transferred to cryotubes (Thermo Scientific) and stored at -80^{o}C for 24-72 hours, at which point they were stored at liquid nitrogen. To thaw cells, cryotubes were incubated in a 37^{o}C until they could be transferred to 10mL of pre-warmed complete media.

2.2.2. Mice

2.2.3.1. Mouse handling and welfare

Female C57BL/6 mice aged 6 to 8-weeks old were purchased from Charles Rivers Laboratories UK. Mice were maintained under a 12-hour light/12-hour dark cycle in ventilated cages and pathogen-free conditions in the UCL Biological Service Unit. All animal procedures were pre-approved and in accordance with the UK Home Office Animal Scientific Procedures Act. Pre-approved humane endpoints included signs of severe discomfort, loss of >20% body weight and tumour diameter over 150mm, at which point mice were euthanised using Schedule One approved methods. No mice exceeded these endpoints.

2.2.3.2. Mouse tumour models

The KP.B6.F1 orthotopic lung model was established by intravenous injection of 80,000 KP.B6.F1 cells on day 0. On day 6, radiotherapy treatment began as indicated and mice were sacrificed on day 17 post tumour challenge. Details regarding mouse irradiation can be found below in Section 2.2.3.3. Lungs were collected for qRT-PCR analysis.

To establish subcutaneous tumours in mice, first the right flank of the mouse was shaved. The next day, mice were anaesthetised using isoflurane (UCL Hospitals) and $5x10^5$ KP.B6.F1 cells or MC38 cells were injected subcutaneously on the right flank. When tumours reached approximately $100mm^3$, mice were randomised and treatment began. Treatment began on day 5 for the KP.B6.F1 subcutaneous mouse model and day 6 for MC38. Mice receiving decitabine were then treated for 5 consecutive days, from days 5-10 for KP.B6.F1 and days 6-11 for MC38. For KP.B6.F1 decitabine alone experiment, mice were sacrificed, and tumours collected for western blot analysis on days 10 and 15. Mice received M3814 and/or

radiotherapy on day 11 for KP.B6.F1 and day 12 for MC38. More details regarding mouse treatment can be found below in Section 2.2.3.3. For the tumour growth and survival experiments, tumours were measured with a calliper three times a week. When tumour diameter reached 150mm or tumours became ulcerated, the mice was sacrificed. For statistical analysis of survival experiments, only cancer-related death is included as an event but when a mouse is sacrificed due to ulceration, this is denoted on the figure. these counted as an event Tumour-free mice were defined as those with no palpable tumour for 30 days, at which point $5x10^5$ cells KP.B6.F1 were subcutaneously implanted on the left flank and monitored. Tumour volume was calculated as an ellipsoid using the following formula:

$$Tumour\ Volume = \frac{\pi}{6} \times width \times length \times depth$$

For immune characterisation of the tumour immune microenvironment experiment, mice were sacrificed on day 18 and tumour draining lymph nodes and tumours collected for flow cytometry analysis.

2.2.3.3. Mouse treatment

For decitabine treatment, mice were intraperitoneally injected with 20µg decitabine (Merck) for 5 consecutive days. Treatment with 2µg M3814 (Merck) was administered via oral gavage 1 hour prior to radiotherapy. Radiotherapy was performed in collaboration with Dr Rebecca Carter at UCL Cancer Institute using an Xstrahl Small Animal Research Radiotherapy Platform (SARRP) irradiator. Mice were placed on a 3D-printed bed under anaesthesia (Isoflurane, UCL Hospitals) and cone-beam computed tomography (CBCT) images were obtained using a 60kVp 0.8mA primary uncollimated primary beam with 1mm Al filtration and a digital flat-panel detector. The resulting CBCT slices were rendered using the FDK® algorithm with a voxel size between 0.01 and 5mm to generate a 3D image reconstruction of each mouse. Using

Muriplan software, dose calculations were determined using the Monte Carlo simulation superposition-convolution dose algorithm. This enabled the planning of radiotherapy beams to specifically target the tumour or lung while avoiding damage to nearby important tissues.

2.2.3. Statistical analysis

Statistical analysis was performed using GraphPad Prism V9. For comparison between multiple groups, the ANOVA test was performed with Bonferroni multiple comparison test. When comparing two groups, the student 2-tailed t-test was used. The statistical analysis for each experiment is denoted in the corresponding figure legend.

2.2.4. Cell proliferation assays

Cells were seeded in flat-bottom 96-well plates. Seeding density was dependent on the doubling rate of cells with the aim of 80% confluency in untreated wells at the end of experiment. One day after seeding, cells were treated with corresponding compound. Radiotherapy was administered one hour after treatment with Nu7441 or M3814. Cell proliferation was determined by performing the Sulforhodamine B (SRB) and the 3-(4,5-dimethylthiazol-2-yl)-2,5-diphenyl-2H-tetrazolium bromide (MTT) assays. Growth inhibition was calculated as the percentage of inhibition relative to DMSO alone treated control.

2.2.4.1. SRB assay

To determine cell proliferation using the SRB assay, at the end of the experiment, cells were fixed with 50µL Carnoy's fixative (3:1 ratio of methanol and acetic acid) and stored at 4^{o}C. Plates were washed 5 times in water and dried at 80^{o}C for 3 hours,

at which point cells were stained with 100µL 0.4% SRB (Sigma Aldrich) for 1 hour at room temperature. Cells were washed with 1% acetic acid 5 times. Plates were dried again at 80^{o}C for 3 hours. Once dried, the stain was solubilised with 100µL per well of 10mM Tris-HCL (pH10.5). Using Varioskan LUX plate reader, optical absorbance at 570nm was measured.

2.2.4.2. MTT assay

To determine cell proliferation using the MTT assay, MTT solution was added to the media in the 96-well plate to make a final concentration of 0.5mg/mL in the well and incubated at 37^{o}C for 4 hours. Plate was centrifuges at 2000rpm for 3 minutes. Media was then carefully aspirated from the wells, leaving behind the MTT crystals which were then solubilised in 200µL DMSO. Using Varioskan LUX plate reader, optical absorbance at 570nm was measured.

2.2.5. Clonogenics

Cells were seeded at low density in 6-well plate and incubated overnight to allow cells to adhere. Cells were treated with corresponding compound and radiotherapy was administered one hour after treatment with Nu7441 or M3814. One day later, cells were washed to remove dead cells and fresh media was added. KP.B6.F1 cells were incubated for 6 days and MC38 cells for 7 days to enable growth of visible colonies without overgrowing. At this point, cells were washed with PBS and fixed with Carnoy's fixative (3:1 ratio of methanol and acetic acid). The fixative was removed, and cells were stained with 0.5% crystal violet (Sigma Aldrich). Once stained, plates were thoroughly washed with water and left to dry overnight. Images were taken of plates and colonies counted. The clonal viability was calculated as number of clone

relative to number of cells seeded, multiplied by 100. This was then normalised to DMSO treated control well.

2.2.6. Immunoblotting

To obtain lysate from tumours tissue samples, shavings of snap-frozen tumours samples were taken using a scalpel. Lysis buffer (0.0625M Tris-HCL, 10% glycerol, 2% SDS) was added to the shaving and tissue was homogenised using a syringe. To obtain lysate from cells in culture, wells were first washed with cold PBS and lysis buffer added to the wells. Cells were scraped using a cell scraper and the lysates collected. Subsequently, lysates obtained from tumour tissue or cell cultures were heated to 90^{o}C for 10 minutes to denature the proteins. Samples were placed on ice and sonicated to disrupt the nucleus. Samples were stored at -20^{o}C.

The RC-DC protein assay (Bio-Rad) was used to determine protein concentration. To do so, samples were diluted 1 in 10 and added to the wells of a flat-bottom 96-well plate. Reagents S and A were combined in a ratio of 1 to 50 and 25µL added to each well. Reagent B was added 200µL and well was incubated at room temperature on a shaking platform for 10 mins. Using the Varioskan LUX plate reader, optical absorbance at 750nm was measured. The protein concentration was determined by plotting against a standard curve generated by Bovine Serum Albumin (BSA)(Sigma-Aldrich) samples of known concentrations (100µg/ml, 200µg/ml, 400µg/ml, 600µg/ml, 800µg/ml, 1000µg/ml) which were ran on the same plate each time.

Once the concentration was known, samples were diluted in PBS to obtain the same concentration. Typically, this was typically 30µg in 1x Sample Buffer and PBS per well (15µL). The sample was mixed and incubated at 95^{o}C for 10 minutes. Samples and Dual Colour MV ladder (Bio-Rad) were loaded on a pre-cast 4-15% Criterion TGX gel (Bio-Rad) or 4-15% Mini-PROTEAN TGX (Bio-Rad), depending on number of wells

required. Gels were run in electrophoresis tank at an initial constant voltage of 80V for 10 minutes followed by 140V for one hour. Proteins ran on Criterion TGX gels were transferred to pre-packed 0.2µM Trans-Blot Turbo Midi Nitrocellulose Transfer Packs while those on Mini-PROTEAN TGX gels were transferred to pre-packed 0.2µM Trans-Blot Mini Nitrocellulose Transfer Packs (both Bio-Rad). Transfers were performed using the Trans-Turbo-Blot Transfer System (Bio-Rad). Resulting membranes were blocked in 5% BSA or 5% milk in tris buffered saline with tween (TBST)(20mM Tris-base (Sigma Aldrich), 150mM NaCl (Sigma Aldrich), 0.1% Tween 20 (Sigma Aldrich).

Membranes were incubated overnight at 4^{o}C with primary antibodies in 5% BSA or 5% Milk TBST with 0.01% Sodium Azide (Severn Biotech). Information regarding primary antibodies can be found in Table 2.2. Following incubation, membranes were washed at least 3 times in TBST and incubated at room temperature for 1 hour with anti-rabbit or anti-mouse IgG horse radish peroxidase (HRP)- linked secondary antibodies (Cell Signalling Technology). Information regarding the primary and secondary antibodies used and their dilutions can be found in Table 2.2. Membranes were washed again at least 3 times in TBST and HRP-conjugated antibody bound to the membrane was visualised using Enhanced Chemiluminescence Substrate (Amersham) chemiluminescence on X-ray films (Kodak X-Omat).

Table 2. 2. Primary Antibodies for Immunoblotting.

Antibody	Vendor	Catalogue number	Dilution
pSer139 H2AX	Millipore	05-636	1:1000
Calnexin	Abcam	Ab22595	1:5000
STING	Cell Signaling Technology	13647	1:500
cGAS	Cell Signaling Technology	31659	1:1000
TBK1	Cell Signaling Technology	3504	1:1000
IRF3	Cell Signaling Technology	4302	1:1000
DNMT1	Cell Signaling Technology	5032S	1:1000
A-tubulin	Sigma-Aldrich	A1978	1:1000

2.2.7. Immunofluorescence

2.2.7.1. cGAS micronuclei

KP.B6.F1 cells were seeded on glass coverslips in a 24-well plate at $3x10^5$ cells per well and left to adhere overnight. The next day, cells were treated with DNA-PKi and 1 hour later, radiotherapy. Plates were incubated for 24 hours, at which point cells were washed once in cold PBS and fixed in 4% paraformaldehyde (PFA)(Thermo Fisher) at room temperature for 15 minutes. Cells were washed 3 times in PBS 1% FBS and permeabilised with 0.1% Triton x-100 (Sigma Aldrich) at room temperature for 10 minutes. Cells were washed 3 times in cold PBS and blocked for one hour at room temperature in IF Blocking Buffer (1xPBS, 5% BSA, 10% FBS). Cells were incubated in primary unconjugated rabbit cGAS antibody (Cell Signaling Technology – 31659) for 1 hour. Following 3 washes with PBS 1% FBS, cells were incubated in Anti-rabbit secondary Alexa Fluor 488 1:320 (Invitrogen) and 1:50 Phalloidin 568 (Invitrogen) in PBS 1% FBS for 30 minutes at room temperature. Cells were then washed 3 times in PBS and incubated for 15 minutes at room temperature in 0.1% Hoechst (Invitrogen), after which cells were washed twice in cold PBS.

2.2.7.2. Golgi dynamics

KP.B6.F1 cells were seeded on glass coverslips in a 24-well plate at $3x10^5$ cells per well and left overnight to adhere. The next day, cells were treated with DNA-PKi and radiotherapy an hour later. Plates were incubated for 24 hours, at which point cells were washed once in cold PBS and fixed and permeabilised in ice-cold methanol for 5 minutes at -20^{o}C. Cells were washed 3 times in cold PBS and incubated in IF Blocking Buffer (1xPBS, 5% BSA, 10% FBS) for one hour at room temperature. Cells were incubated in primary unconjugated rabbit GOLPH3 (ab264406) 1:200 and mouse GM130 (ab169276) 1:200 for 1 hour at room temperature. Subsequently, cells were washed 3 times in cold PBS and incubated in anti-rabbit secondary Alexa Fluor-

488 (Invitrogen) 1:320 and anti-mouse secondary Alexa Fluor-568 (Invitrogen) 1:320 in PBS for 30 minutes at room temperature. Cells were then washed 3 times in PBS and incubated at room temperature in 0.1% Hoechst (Invitrogen) for 15 minutes. Following this, cells were washed a further 2 times.

2.2.7.3. Immunofluorescence mounting and confocal microscopy

Once stained, coverslips were mounted on glass slides using ProLong Gold Antifade mounting media (Invitrogen) and left to dry overnight in the dark. The next day, coverslips were sealed with nail varnish and once dry, stored slides were stored at 4^{o}C in the dark.

Confocal microscopy of stained slides was performed using Zeiss LSM 880 with AiryScan. At least three slides were taken per slide and every day of image acquisition non-primary stained control was imaged. AiryScan images were processed and exported. Image analysis was performed using ImageJ Software. For the micronuclei experiment this involved counting the micronuclei and cGAS positive micronuclei per cell. Micronuclei were defined as nuclear bodies that were separate from the main nuclear body and <1/3 the size of the main nuclear body. cGAS positive staining was defined as staining greater than the main nuclear body. For Golgi experiment, for each cell the nucleus area and the area of GM130 and GOLPH3 was quantified.

2.2.8. Flow cytometry

2.2.8.1. Flow cytometry of cells in culture

Cells were seeded in 6-well plates and left to adhere overnight. Cells were treated with indicated treatments. For a positive control of CRT translocation, cells were treated with 1µM of mitoxantrone for 24 hours. For a positive control of MHC Class I and PD-L1, cells were treated with 1µg/mL of IFN-γ for 24 hours Cells were incubated for 24, 48 or 72 hours.

At the end of treatment, cells were washed in PBS and trypsinised. The collected cells from media, wash and adherent were collected and washed in FACs buffer (PBS, 2% FBS, 2mM Ethylenediaminetetraacetic acid (EDTA)) and plated in duplicate a round bottomed 96-well plate. For each sample, an unstained control was generated. Cells were incubated in primary antibodies diluted in FACs buffer (Table 2.3) in the dark at 4ºC. Following this, cells were washed 3x in FACs buffer by centrifuging plate at 2000rpm for 5 minutes. When using non-conjugated antibodies such as anti-Calreticulin, cells were then incubated in Goat anti-rabbit PE (Thermo Fisher) in the dark, at 4ºC for 30 minutes. Next, cells were washed in FACs buffer twice. To detect apoptosis, the Annexin V Apoptosis Detection FITC kit was used (Thermo Fisher). To do so, cells were washed in 1x Annexin V Binding Buffer and then incubated in 1µg/mL Annexin V primary antibody (Invitrogen) and 1µg/mL DAPI (Invitrogen) for 5 minutes at room temperature. Cells were then washed 1x in Annexin V binding buffer. DAPI was used instead of the Propidium Iodide supplied in the Apoptosis detection kit to avoid overlapping fluorescence with the chosen primary antibodies. For the decitabine cell surface marker experiment, dead cells were stained using 1:1000 Fixable Viability Dye eFluor 780 (eBiosciences). Cells were washed once in FACs Buffer and resuspended in FACs Buffer 1% PFA. Samples were stored at 4ºC in the dark and ran on LSR-Fortessa X20 (BD Biosciences) within 48 hours. More details on data acquisition can be found below in Section 2.2.8.3.

Table 2.3. Primary Antibodies for in vitro flow cytometry

Target	Fluorophore	Vendor	Catalogue Number	Dilution
Annexin V (1µg/mL)	FITC	Invitrogen	331200	1:100
Calreticulin	None	Abcam	Ab2907	1:100
CD40	PE	eBiosciences	15298519	1:200
CD80	BV605	eBiosciences	15882469	1:200
CD86	FITC	eBiosciences	11-0862-82	1:200
MHC Class I	APC	eBiosciences	17-5958-82	1:200
MHC Class II	AF700	eBiosciences	56-5321-80	1:200
PD-L1	PE-Cy7	Invitrogen	25-5982-80	1:200
Anti-rabbit 2º	PE	Invitrogen	P-2771MP	1:500
Viability	eFluor780	eBiosciences	65-0865-18	1:1000
DAPI (1mg/ml)	V450	Invitrogen	D1306	1:1000

2.2.8.2. Flow cytometry of mouse tissues

Tumours and tumour draining lymph nodes (TDLNs) were harvested from mice at the end of the experiment. Tumour tissue was chopped up and digested for 30 minutes at 37ºC in a 300µg/mL Liberase TL (2oche), 2µg/mL DNAse (Roche) mix. Unprocessed TDLNs and digested tumours were individually passed through a 70µM cell strainer to obtain a single cell suspension. Tumour cell suspension was centrifuged at 2000rpm for 3 minutes and resuspended in 3mL RMPI. Room temperature Histopaque 1119 (Sigma-Aldrich) was added in a 1:1 ratio beneath the cell suspension using a glass Pasteur pipette to form a single density gradient. Samples were centrifuged at 700g, 25ºC for 25 minutes, with the brake set to low. The cells at the gradient interface were collected, washed and resuspended in FACs Buffer. Tumour and TDLN samples were plated in a round-bottom 96-well plate for staining.

Samples were stained first with cell-surface antibodies and viability dye diluted in Superblock (PBS, 2% FBS, 5% rat serum, 5% mouse serum, 5% rabbit serum, 25µg/mL anti-FcγR monoclonal antibody) and incubated on ice, in the dark for 30 minutes. Following this, samples were washed twice in FACs Buffer. To enable intracellular staining, cells were fixed and permeabilised using the Foxp3/Transcription Factor Staining Buffer Set (eBioscience) as per manufacturer's instructions. To do so, cells were incubated on ice in the dark for 25 minutes in Fixation/Permeabilization Concentrate diluted in Fixation/Permeabilization Perm Diluent. Samples were then washed twice with PermWash (1x Permeabilisation Buffer in water). Antibody mix containing all secondary and intracellular antibodies was made in PermWash 10% SuperBlock and added to samples which were then incubated on ice in the dark for 30 minutes. Information regarding antibodies used for the Lymphoid and Myeloid panels can be found in Tables 2.4 and 2.5 respectively. At the end of staining, samples were washed twice in PermWash and resuspended in 1% PFA FACs buffer. Samples were run on the FACSymphony (BD Biosciences) within 72 hours.

Table 2.4. Antibodies for flow cytometry characterisation of tumour and TDLNs lymphoid compartment.

Target	Fluorophore	Vendor	Catalogue Number	Dilution
Extracellular				
4-1BB	Biotin	Invitrogen	13-1371-82	1/200
CD11b	BUV661	BD Biosciences	565080	1/300
CD25	BB515	BD Biosciences	564424	1/200
CD4	BUV496	BD Biosciences	564667	1:300
CD45	BUV563	BD Biosciences	565710	1/300
CD8	BUV805	BD Biosciences	564920	1/300
CTLA-4	BV605	BioLegend	106323	1/100
GITR	BV510	BD Biosciences	740192	1/200
ICOS	PE-CY7	BioLegend	313520	1/200
LAG3	BV650	BioLegend	125227	1/200
NK1.1	BUV395	BD Biosciences	564144	
OX40	BV786	BD Biosciences	740945	1/200
PD-1	PECF594	BD Biosciences	562523	1/200
TIGIT	BB700	Thermo Fisher	20210402	1/200
TIM-3	PE	BioLegend	119704	1/200
Viability dye	eFluor780	eBiosciences	65-0865-18	1/1000
Intracellular				
CD3	BUV737	BD Biosciences	564380	1/300
FOXP3	BV421	Thermo Fisher	20210613	1/100
Granzyme B	APC	Invitrogen	GRB05	1/100
KI67	AF700	Invitrogen	56569882	1/400
Strep 2º	BV711	BioLegend	405231	1:1000

Table 2.5. Antibodies for flow cytometry characterisation of tumour and TDLNs myeloid compartment.

Target	Fluorophore	Vendor	Catalogue Number	Dilution
Extracellular				
41BBL	Per-CP-eFluor 710	eBioscience	46-5901-80	1/100
CD103	APC	BioLegend	121414	1/200
CD11b	BUV661	BD Biosciences	565080	1/400
CD11c	BV786	BD Biosciences	117336	1/100
CD19	BUV737	BD Biosciences	564296	1/100
CD24	BUV496	BD Biosciences	564664	1/400
CD45	BUV805	BD Biosciences	624287	1/400
CD86	FITC	eBioscience	11-0862-82	1/100
ICOSL	PE	Invitrogen	12-5985-82	1/100
F4/80	AF700	BioLegend	123130	1/100
GITRL	BV510	BD Biosciences	563367	1/100
LY6C	BV605	BD Biosciences	563011	1/200
LY6G	BUV563	BD Biosciences	565707	1/100
MHC Class II	BV711	BioLegend	107643	1/800
NK1.1	BUV395	BD Biosciences	564144	1:300
OX40L	PE-CY7	BioLegend	108813	1/100
PD-L1	PE-DAZZLE	BioLegend	124324	1/400
Viability dye	eFluor780	eBioscience	65-0865-18	1/1000
Intracellular				
CD3	BUV737	BD Biosciences	564380	1/300
CD206	BV650	BioLegend	141723	1/100
CD68	BV421	BioLegend	137017	1/100

2.2.8.3. Flow Cytometry data acquisition and analysis

Flow cytometry data acquisition was performed on the LSR-Fortessa for in vitro experiments, and the FACSymphony for *in vivo* experiments. All data was acquired within 72 hours of staining. For all experiments, the optimal voltages were determined using single fluorescence compensation controls mad from UltraComp eBeads (BioLegend) and the antibody with the corresponding fluorophore. Doublets and dead cells were excluded.

Data analysis was performed using FlowJo v10.8.1. In FlowJo, samples were down sampled using the DownSampleV3.3.1 plugin. The FlowSOM plugin was used to generate and visualise clusters. Statistical analysis was performed using GraphPad Prism 9.0.

2.2.9. Enzyme-linked immunosorbent assay (ELISA)

Cells were plated in 24-well plates and left to adhere overnight, at which point they were treated with their respective treatments. At the end of treatment, conditioned media was collected and centrifuged at 2000rpm for 10 minutes at 4^{o}C to obtain the supernatant. Resulting supernatant was stored at -80^{o}C. HMGB1 was quantified using HMGB1 ELISA Kit (Tecan, ST51011) and IFNβ was quantified using LEGEND MAX^{TM} Mouse IFN-β ELISA Kit (BioLegend, 439407). Both kits were performed as per the manufacturer's instructions.

2.2.10. Quantitative real-time polymerase chain reaction (qRT-PCR)

RNA was extracted using the RNeasy kit (Qiagen) as per manufacturer's instructions. The source of RNA was either cells grown to a confluency of 80% and treated in culture, or from frozen mouse tumour-bearing lungs. Quantification of mRNA was performed using Nanodrop One (Thermo Fisher) and mRNA was stored at -80^{o}C. Samples were made to a concentration of 200µg/mL and reverse transcription was performed using the High-Capacity cDNA Reverse Transcription Kit (Thermo Fisher) as per manufacturer's instructions. Reverse transcription was performed in a ThermoCycler using the program denoted in Table 2.6. The resulting cDNA was stored at -20^{o}C.

Table 2. 6. Reverse transcription steps

Step	Temperature (ºC)	Duration
Primer annealing	25	10 minutes
DNA polymerisation	37	3 minutes
Enzyme deactivation	85	5 minutes
Maintain	4	∞

qRT-PCR was performed using 1x Fast SYBR™ Green Master Mix (Applied Biosystems), 50ng cDNA and 1x PrimePCR™ PCR Primers (BioRad, 10025636). Primers used were mouse Ccl2 (qMmuCED0003785), Cxcl10 (qMmuCED0049500), Ifnαr1 (qMmuCID0020191), Isg20 (qMmuCID0008251), IFNβ (qMmuCED0050444), Mx1 (qMmuCID0023356), cGas (qMmuCID0025813), Sting (qMmuCID0016081), Trex1 (qMmuCED0061616) and the B-Actin (qMmuCED0027505). Reactions were performed in MicroAmp Fast Optical 96-well Reaction Plates (Applied Biosystems) using the QuantStudio 5 Real-Time PCR System (Thermo Fisher) to run the program detailed in Table 2.7. Analysis was performed using the ΔΔCT method by subtracting the housekeeping (B-actin) cycle threshold (CT) from the gene of interest to obtain the ΔCT. The ΔCT of untreated samples were then subtracted from the treated samples ΔCT to obtain the ΔΔCT.

Table 2. 7. qRT-PCR steps

Step	Temperature (ºC)	Duration	No. Cycles
Initial denaturation	95	20 seconds	Hold
Denaturation	95	3 seconds	X50
Anneal/Extend	60	20 seconds	
Maintain	4	∞	Hold

2.2.10. Isolation of mouse bone marrow derived monocytes (BMDMs)

To obtain murine bone marrow derived monocytes (BMDMs), untreated mice were sacrificed, and the femurs harvested for processing. The ends of the bones were removed, and bone marrow flushed out using a syringe with Complete RPMI (Sigma-Aldrich). Resulting marrow was aspirated to make a cell suspension, washed in Complete RPMI and resuspended in Ammonium-Chloride-Potassium (ACK) lysing buffer (Gibco) for 5 minutes. Cells were washed in Complete RPMI and plated at $3x10^5$ cells/mL in Complete RPMI with 100ng/mL murine colony growth factor (M-CSF) (2BScientific). Cells were incubated for 7 days prior to their use.

3. DNA-PK Inhibition Alters the DNA Damage Response to Radiotherapy

3.1. Introduction

While aberrant dysregulation of the DNA damage response makes cancer cells less able to recover from damage in comparison, loss of NHEJ pathway functionality is uncommon [137]. Therefore, NHEJ provides a means for cancer cells to repair the DSBs induced by radiotherapy and thus, survive. However, this reliance on NHEJ presents an opportunity to widen the therapeutic window through inhibition of DNA-PK. Accordingly, combination of radiotherapy and DNA-PKi has been the subject of investigation since the earliest generations of DNA-PK into present day, with 8 clinical trials currently investigating the efficacy of M3814 in combination with radiotherapy (Table 1.1). This Chapter focuses on establishing the effect of combining M3814 and radiotherapy on cell viability in multiple cancer cell lines. In addition, it will explore the events preceding cell death, including changes to the DNA damage response, expression of cell-surface immunomodulatory markers and whether the resulting cell death is accompanied with the release of DAMPs associated with ICD.

3.1.1. DNA-PK inhibitions alters the DNA Damage response following radiotherapy

Upon the induction of DSBs by radiotherapy H2AX undergoes rapid Ser139 phosphorylation to generate γH2AX. During the early stages of NHEJ, there is further amplification of γH2AX mediated by DNA-PKcs [31, 138]. Following treatment with X-ray, γH2AX amplification can be abrogated by DNA-PK inhibition using Nu7026 or Wortmannin [30, 139]. In addition, although DNA-PKcs is central to NHEJ, its role in the DDR is not limited to DNA damage repair pathways. Another aspect of the DDR which is mediated by DNA-PKcs is Golgi dispersal via the phosphorylation of GOLPH3 [45, 140, 141]. Activation of GOLPH3 on the Golgi increases tensile forces

between the cells actin cytoskeleton and the Golgi apparatus resulting in Golgi dispersal [142]. Dispersal of the Golgi triggers the release of vesicles associated with tumour cell survival and migration [143-145]. As such, abrogation of radiotherapy-induced Golgi dispersal can mitigate this effect and presents an attractive strategy to improve the efficacy of radiotherapy [45].

3.1.2. The induction of DNA damage alters the immunogenicity of cancer cells

Using syngeneic mouse tumour models, a recent study demonstrated that the anti-tumour effect of DNA-PK inhibitor AZD7648 and radiotherapy was in part $CD8^+$ T cell dependent [146]. Indicating that while inhibition of DNA-PK may sensitise cells to radiotherapy via cancer-cell intrinsic mechanisms, the immune system also plays an important role. While the cancer-cell intrinsic mechanisms of radiosensitisation by DNA-PKi have been studied, very little is known about the effect of the combination in the context of the tumour microenvironment. In this Chapter, the effect of DNA-PKi and radiotherapy treatment on cell surface expression of immunomodulatory markers and the induction of ICD will be explored.

3.1.2.1. Radiation alters the expression of immune-modulatory markers

During normal physiology, the immune system is under tight regulation to detect and eliminate potential threats, while not triggering a response to non-threats. These regulatory pathways can be altered by tumour cells to avoid elimination. One immune escape mechanism is the downregulation of the MHC Class I complex, which is necessary for recognition by $CD8^+$ T cells [147, 148]. Another is the upregulation of PD-L1, which delivers an inhibitory signal upon its activation following successful binding of MHC Class I molecules to a corresponding TCR. Loss of this signalling could trigger an oversensitive T cell response, while chronic PD-L1/PD-1 signalling results in T cell exhaustion and dysfunction, enabling immune escape. Understanding

of the importance of immune checkpoints in the tumour microenvironment has culminated in the development of pharmacological inhibitors which have revolutionised cancer treatment in the clinic [149].

Radiotherapy-induced DNA damage has been shown to alter the expression of both molecules. In the case of MHC Class I, radiotherapy stimulates TAP, resulting in an enhanced peptide pool and subsequently increase peptide loading to the MHC complexes. This increases the presentation of tumour neoantigens, resulting in T cell recognition of tumour cells and $CD8^+$ mediated tumour elimination [147, 150, 151]. DNA damage induced by IR also increases mRNA and cell surface expression of PD-L1 [152, 153]. In the case of IR, knock-down of Ku70/80 or DNA-PK inhibition using Nu7441 further increased the upregulation of PD-L1 [152]. However, a study exploring the effect of DNA-PKi (Nu7441) on PD-L1 and MHC Class I expression in 27 human melanoma cell lines found that Nu7441 alone reduced PD-L1 expression in 20 of the 27 cell lines tested, while MHC Class I expression was unchanged [154]. To better understand how DNA-PKi may alter the expression of these important immune-modulatory molecules in response to radiotherapy, flow cytometry experiments will be performed as part of the results in this Chapter.

3.1.2.2. Determining whether cell death is immunogenic

As discussed further in section 1.2.4., ICD is a form of regulated cell death which is characterised by the release of DAMPs, resulting in an immunostimulatory effect [88]. It has been demonstrated that radiotherapy induces ICD, however, the extent to which this occurs is influenced by numerous factors including radiation modality, dose, fractionation, and combination with other agents such as chemotherapy [91, 100, 155]. In contrast, the effect of combination with DNA-PKi is not known and will be investigated in this chapter.

3.2. Research Aims

The aim of this chapter is to characterise the effects of combining M3814 and radiotherapy to improve the therapeutic window of radiotherapy. This will begin with establishing the treatment regimen and determining the effects of the combination in cancer cell viability and the DDR, including γH2AX formation and Golgi dynamics. Following this, ways in which this combination may alter the expression of immunomodulatory molecules and the release of DAMPs during cell death will be determined.

3.3. Results

3.3.1. Cancer cells lines are not sensitive to DNA-PK inhibitors as a single agent

To establish an appropriate treatment regimen, a dose-escalation study was performed to determine the toxicity of the DNA-PK inhibitors Nu7441 and M3814 in a variety of murine, and one human, cancer cell lines. Information regarding the cell lines used can be found in Table 3.1. Information regarding these cell lines used throughout this project can be found in Table 3.1.

Table 3.1. Cancer cell line characteristics.

Cell Line	Species	Cancer type	Key mutations
CMT-167	Murine	Metastatic alveogenic lung carcinoma	KRAS G12V, P53 wt
CT26	Murine	Colon carcinoma	KRAS G12D, P53 wt
HCT-116	Human	Colon carcinoma	KRAS G12D, P53 loss of function
KP.B6.F1	Murine	Non-small cell lung carcinoma	KRAS G12D, p53 null
LLC	Murine	Squamous-cell carcinoma	KRAS G12C, P53 wt
MC38	Murine	Colon adenocarcinoma	KRAS wt, P53 mut

To perform the dose escalation study, CMT-167, CT26, HCT-116, KP.B6.F1, LLC and MC38 cells were treated with 0.01µM, 0.1µM, 1µM, 10µM or 100µM of Nu7441 or M3814 for 72 hours (Figure 3.2 A-F respectively). Half-maximal growth inhibition (GI_{50}) was calculated based on results from cell growth inhibitions measured using the SRB assay. The growth inhibition curves in are shown in Figure 3.1 and the calculated GI_{50} from these experiments in Table 3.2. As shown, cancer cell lines were not sensitive to Nu7441 and M3814. Of the two inhibitors, cells were consistently less sensitive to M3814.

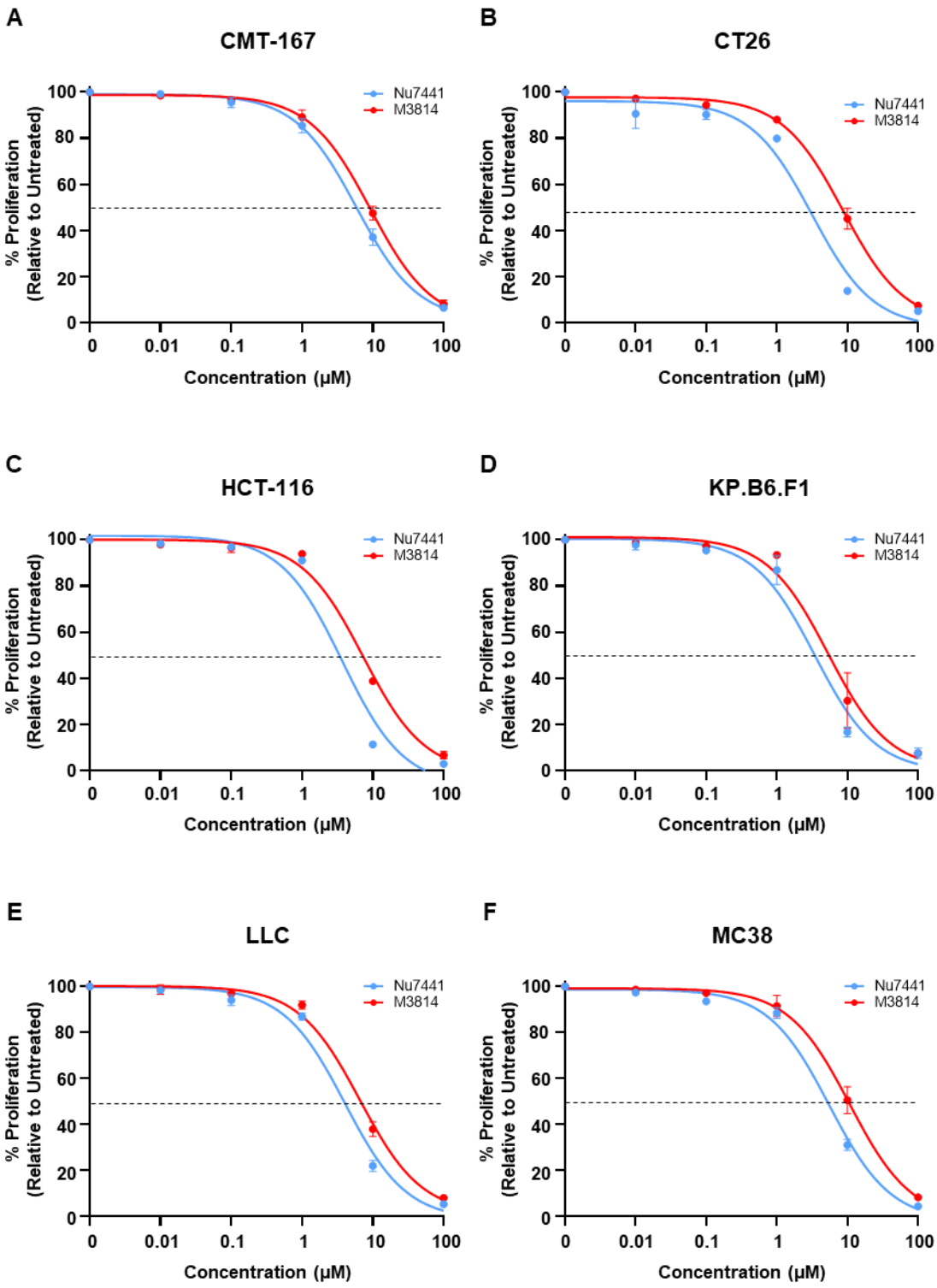

Figure 3.1. Cancer lines are not sensitive to DNA-PK inhibitors alone.

Cancer cells were treated with DMSO (untreated control), 0.01μM, 0.1 μM, 1 μM, 10 μM or 100 μM of Nu7441 or M3814 for 72 hours. Cell proliferation was measured using the SRB assay and % proliferation calculated relative to untreated cells. This was performed in a variety of cells **(A)** CMT-167 **(B)** CT26 **(C)** HCT-116 **(D)** KP.B6.F1 **(E)** LLC **(F)** MC38. Dashed line indicates 50%. Joint data of three independent experiments are presented as average±SEM with line of nonlinear regression.

Table 3. 2. GI50 of cancer cells treated with Nu7441 or M3814

	GI_{50} (μM)	
Cell Line	**Nu7441**	**M3814**
CMT-167	5.896 (±0.8)	9.274 (±1.2)
CT26	3.151 (±1.0)	8.673 (±1.3)
HCT-116	3.700 (±1.3)	7.291 (±1.5)
KP.B6.F1	3.459 (±1.1)	5.342 (±1.7)
LLC	4.045 (±1.0)	6.577 (±1.2)
MC38	5.554 (±1.1)	10.80 (±1.9)

3.3.2. Combination of radiotherapy and DNA-PK inhibition reduces cancer cell proliferation

As NHEJ is a major repair pathway activated following the induction of DSBs after treatment with IR, the combination of DNA-PKi and X-ray was evaluated. There has been extensive published work demonstrating the radiosensitising effects of Nu7441 [53-55], and more recent on the novel compound M3814 [67-69, 156, 157]. The combination of Nu7441 and M3814 with IR was evaluated in HCT-116, CMT-167, CT26, KP.B6.F1, LLC and MC38. To do so, cells were treated with 0.5μM or 1μM of Nu7441 or M3814, and 60 minutes later 4Gy, 8Gy or 12Gy X-ray was administered. The SRB and MTT assays were performed 72 hours later and calculated as percent inhibition relative to untreated cells. The MTT assay measures cell metabolic activity by NAD(P)H dependent reduction of MTT, while SRB gives a readout correlating to the number of cells present by binding to cellular protein.

The data from SRB and MTT assays demonstrated that addition of DNA-PK radiosensitised cells in all tested cell lines, addition of DNA-PK inhibitors decreases cell proliferation. This is shown in Figure 3.2 for CMT-167, CT26 and HCT-116 and Figure 3.3 for KP.B6.F1, LLC and MC38 cells. 12Gy alone induced substantial cell loss and due to this, will be excluded from future viability experiments. In all cell lines, radiotherapy was determined to have had a statistically significant on cell proliferation.

Addition of DNA-PKi to IR had the greatest, and most consistent, effect on KP.B6.F1 and MC38 cells, whereas combination had the least effect on CMT-167. A significant interaction between the X-ray and DNA-PKi indicates that any change to proliferation is not due to the independent effects of X-ray and DNA-PKi, rather there is some degree of synergism between the two. In KP.B6 cells, there was a significant interaction between X-ray and DNA-PKi treatments (two-way ANOVA, SRB $p=0.0017$; MTT $p=0.0017$). The largest effect of adding DNA-PKi was observed when combined with 8Gy. Using the SRB assay, proliferation was reduced from 8Gy alone at 36.2% (±1.6) proliferation down to 9.5% (±3.8)(Bonferroni's, $p=0.0064$) when combined with 0.5μM M3814 and 6.9% (±2.8) with the addition of 1μM M3814 (Bonferroni's, $p=0.0018$)(Figure 3.3 A). Similarly, there was a significant interaction between X-ray and DNA-PKi in MC38 cells, indicating synergy (two-way ANOVA, SRB $p<0.0001$; MTT $p<0.0001$)(Figure 3.3 B). Addition of DNA-PKi had the greatest effect in combination with 8Gy. Using the SRB assay, compared to 33.8% (±0.83) proliferation with 8Gy alone, addition 0.5μM decrease proliferation down to 10.4% (±3.6) with (Bonferroni's, $p<0.0001$) and finally down to 8.5% (±3.0) with 1μM M3814 (Bonferroni's, $p<0.0001$)(Figure 3.3 B). In contrast to KP.B6.F1 and MC38, CMT-167 was less sensitive to radiotherapy and DNA-PKi. Therefore, these cell lines will be the focus of further studies.

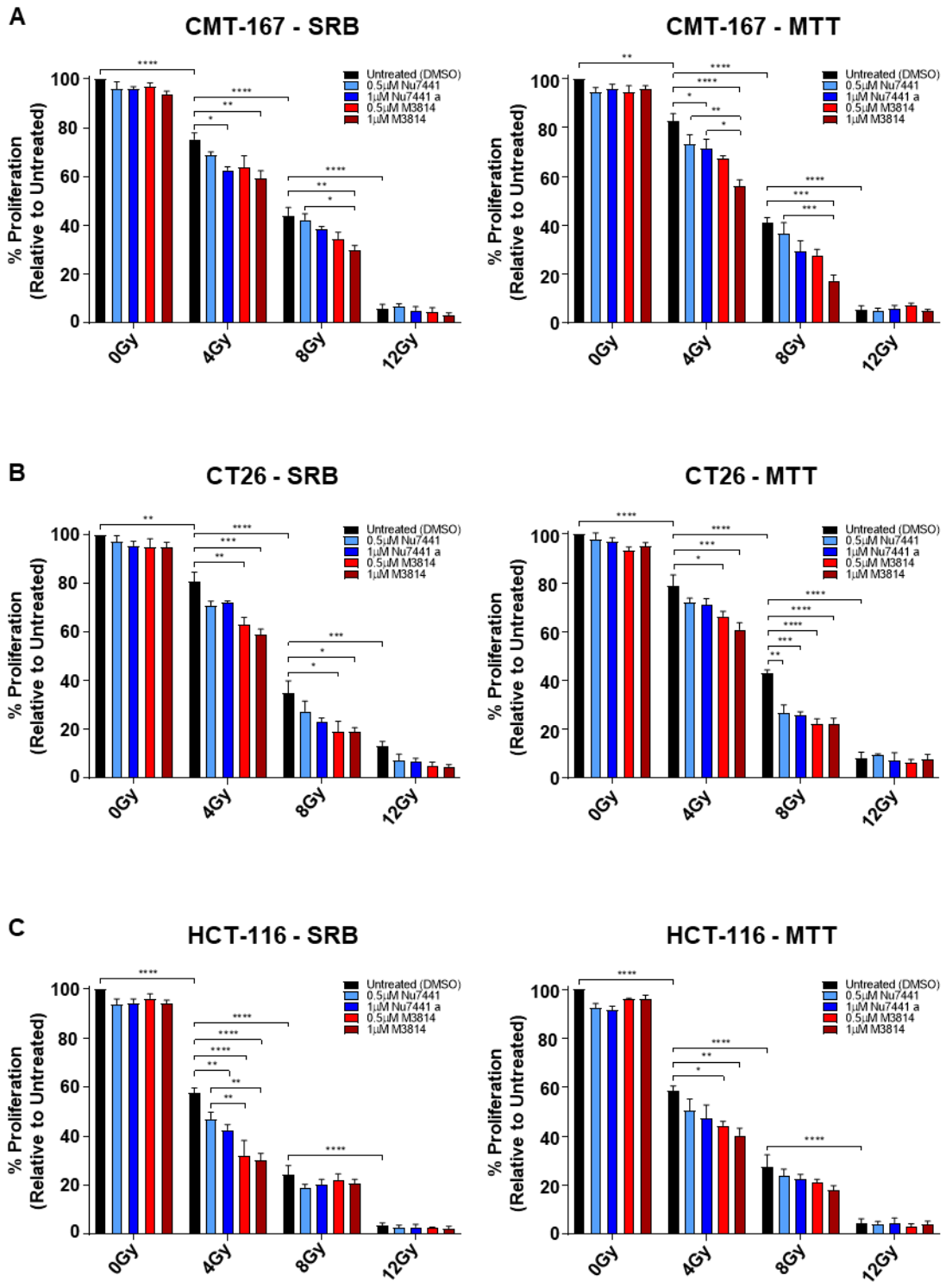

Figure 3.2. DNA-PKi radiosensitises CMT-167, CT26 and HCT-116 cells.

Cells were treated with 0.5μM, 1μM Nu7441 or M3814. 60 minutes later cells were irradiated with 4Gy, 8Gy or 12Gy X-ray. 72 hours later the % proliferation relative to untreated was determined using the SRB and MTT assay. Performed using **(A)** CMT-167 **(B)** CT26 and **(C)** HCT-116 cells. Joint data of three independent experiments are presented as average±SEM and analysed by two-way ANOVA performed followed by Bonferroni's multiple comparison test: *p<0.05, **p<0.01, ***p<0.001 ****p<0.0001. Significance shown between adjacent X-ray doses and within X-ray groups.

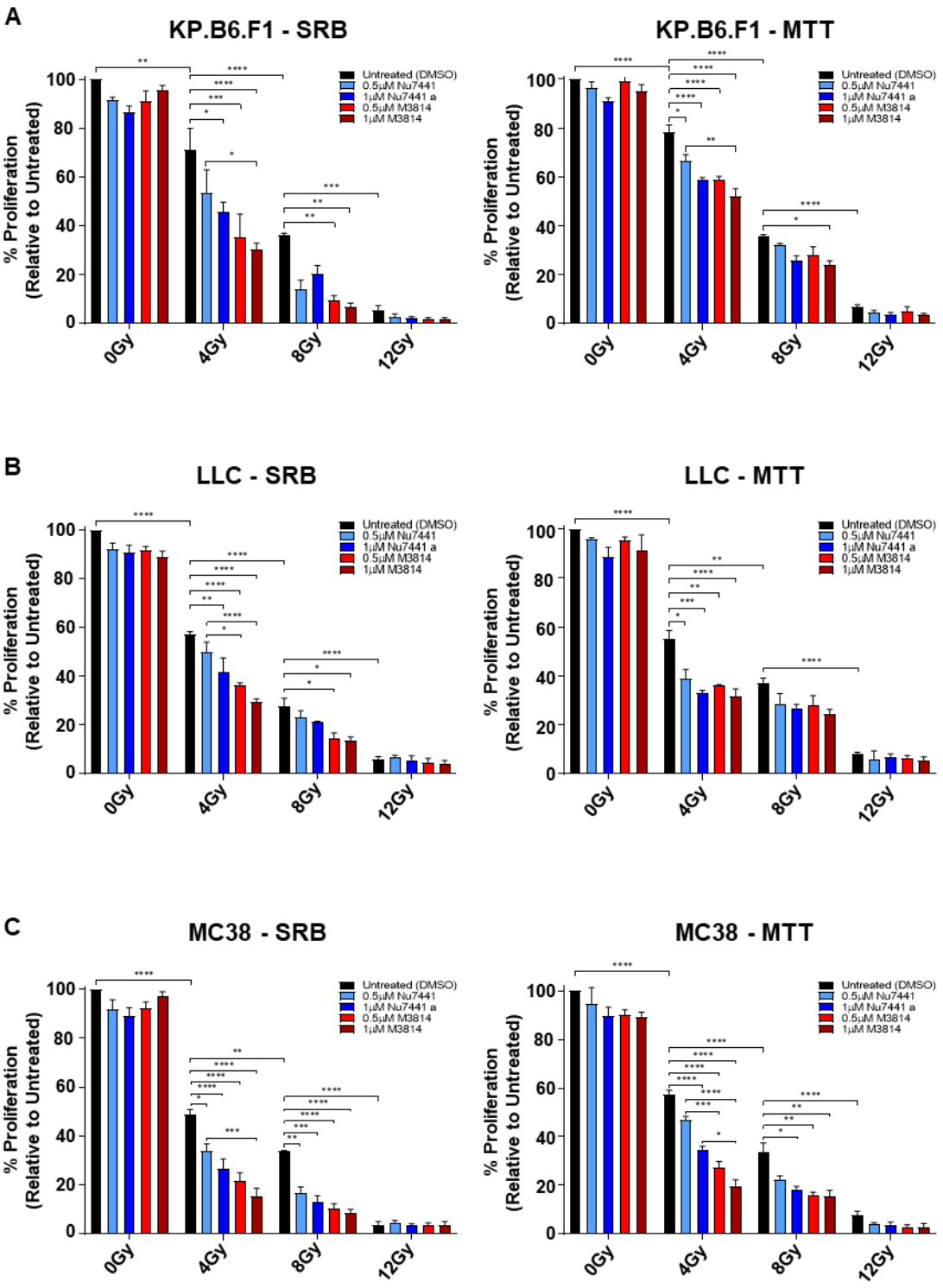

Figure 3.3. DNA-PKi radiosensitises KP.B6.F1, LLC and MC38 cells.

Cells were treated with 0.5μM, 1μM Nu7441 or M3814. 60 minutes later cells were irradiated with 4Gy, 8Gy or 12Gy X-ray. 72 hours later the % proliferation relative to untreated was determined using the SRB and MTT assay. Performed using **(A)** KP.B6.F1 **(B)** LLC and **(C)** MC38 cells. Joint data of three independent experiments are presented as average±SEM and analysed by two-way ANOVA performed followed by Bonferroni's multiple comparison test: *p<0.05, **p<0.01, ***p<0.001 ****p<0.0001. Significance shown between adjacent X-ray doses and within X-ray groups.

3.3.3. Combination of radiotherapy and DNA-PK inhibition reduces cancer cell survival.

The previous assays indicate that addition of DNA-PKi to IR reduced cell proliferation. It is, however, important to understand how combination treatment effects long term cell survival and the ability of treated cells to reproduce and form clones. To do so, the clonogenic assay was performed using KP.B6.F1 and MC38 cells. These cell lines were chosen as both KP.B6.F1 and MC38 demonstrated synergy between X-ray and DNA-PKi. Cells were seeded at low density and 24 hours later treated with 0.5μM or 1μM of Nu7441 or M3814 in combination with 4Gy or 8Gy X-ray. KP.B6.F1 cells were then incubated for 6 days and MC38 for 7 days to allow for optimal growth of clones, at which point the resulting colonies were fixed, stained with crystal violet, and counted to determine clonal viability.

The clonal viability of KP.B6.F1 cells was significantly affected by both X-ray and DNA-PKi (two-way ANOVA, $p<0.0001$ both)(Figure 3.4 A). There was also a significant interaction between the two treatments, indicating synergy (two-way ANOVA, $p=0.0017$). Treatment with 4Gy alone reduced clonal viability to 54.8% (±0.80)(Bonferroni's, $p<0.0001$) and 8Gy further to 21.1%(±5.1)(Bonferroni's, $p<0.0001$). When combined with 4Gy, M3814 decreased clonal viability from 54.8%(±0.80) to 32.9%(±5.3) with 0.5μM M3814 (Bonferroni's, $p>0.0001$) and to 23.7%(±2.8) with 1μM M3814 (Bonferroni's, $p>0.0001$). Clonal viability of cells treated with 4Gy+0.5μM M3814 was significantly lower than 4Gy+0.5μM Nu7441 at 45.3% (±9.2) (Bonferroni's, $p=0.0134$), while 4Gy+1μM M3814 was lower than both 4Gy+0.5μM Nu7441 (Bonferroni's, $p=0.0029$) and 4Gy+1μM Nu7441, 42.7% (±4.0) (Bonferroni's, $p=0.0131$). In combination with 8Gy, 1μM Nu7741 significantly decreased viability to 5.9% (±3.7) (Bonferroni's, $p=0.0044$). To a similar extent, 8Gy+0.5μM M3814 decreased viability to 6.1% (±2.9) (Bonferroni's, 0.0074) while 8Gy+1μM M3814 reduced viability to just 0.97% (±0.43) (Bonferroni's, $p=0.0001$) (Figure 3.4 A).

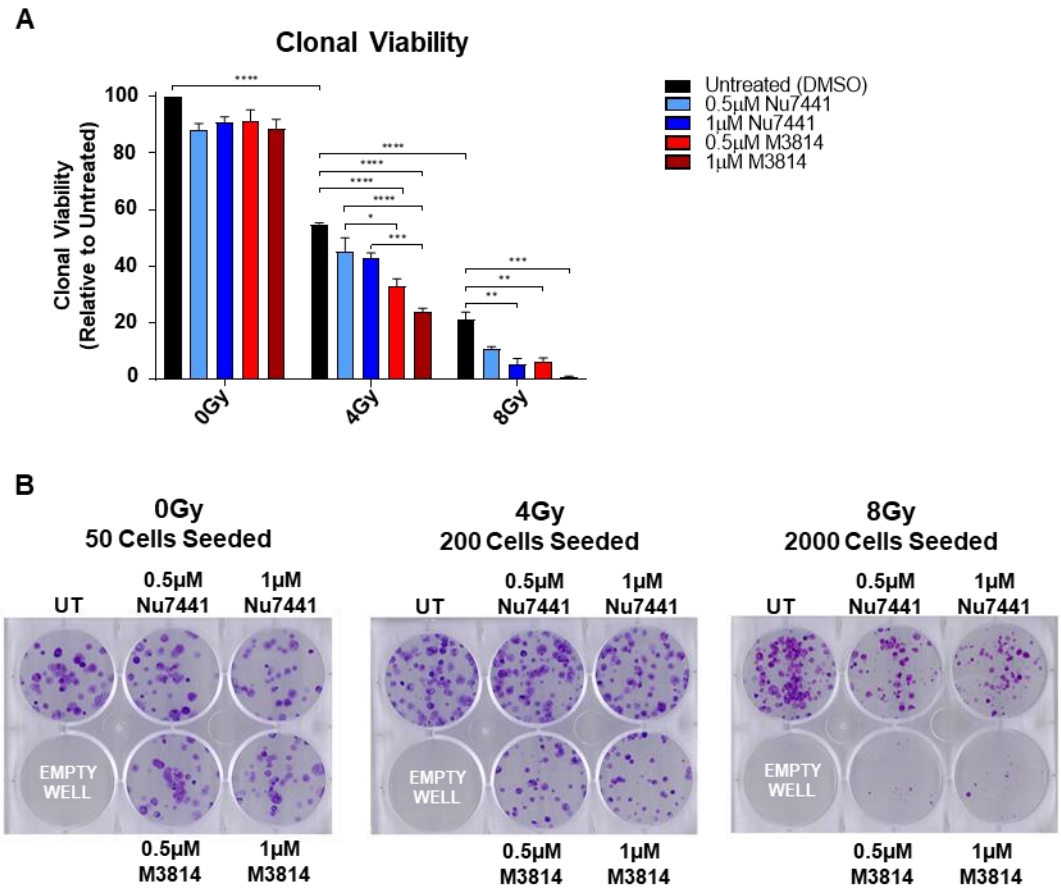

Figure 3. 4. Combination of X-ray and DNA-PKi decreases KP.B6.F1 survival.

KP.B6.F1 cells were seeded at low density and treated with 4Gy or 8Gy irradiation and 0.5µM, 1µM Nu7441 or M3814. After 24 hours the media was replaced, and the cells were left for an additional 5 days to allow clones to grow . Resulting clones were fixed, stained with crystal violet and counted. The clonal viability is the proportion of seeded cells which formed a clone, normalised to untreated cells. **(A)** Clonal viability **(B)** Representative images of clonogenic experiment. Joint data of three independent experiments are presented as average±SEM and analysed by two-way ANOVA performed followed by Bonferroni's multiple comparison test: *p<0.05, **p<0.01, ***p<0.001 ****p<0.0001. Significance shown between adjacent X-ray doses and within X-ray groups.

Next, the clonogenic assay was performed on MC38 cells. There was a significant interaction between X-ray and DNA-PKi (two-way ANOVA, p<0.0001), as well as independently (two-way ANOVA, p<0.0001 both)(Figure 3.5 A). Upon administration of 4Gy alone, clonal viability decreased to 16.0% (±3.7)(Bonferroni's, p<0.0001). This fell to 2.6% (±1.8) with 8Gy (Bonferroni's, p<0.0001). Addition of 0.51µM M3814 to 4Gy decreased clonal viability to 1.3% (±1.2) (Bonferroni's, p<0.0001) and 1µM M3814 to 0.30%(±0.3)(Bonferroni's, p<0.0001). The clonal viability of MC38 cells

treated with 4Gy+0.5μM M3814 or 4Gy+1μM M3814 were also significantly lower than those treated with 4Gy+0.5μM Nu7441, 8.3% (±2.2)(Bonferroni's, p=0.0134 and p=0.0029, respectively). Cells treated with 4Gy+1μM M3814 also had significantly lower clonal viability than cells treated with 4Gy+1μM Nu7441, 7.4% (±2.2) (Bonferroni's, p=0.0131). These experiments demonstrate that not only does combination of radiotherapy and DNA-PKi decrease short-term proliferation, but also long-term survival. They also determine that of the two DNA-PKi's investigated, M3814 is the more potent sensitizer.

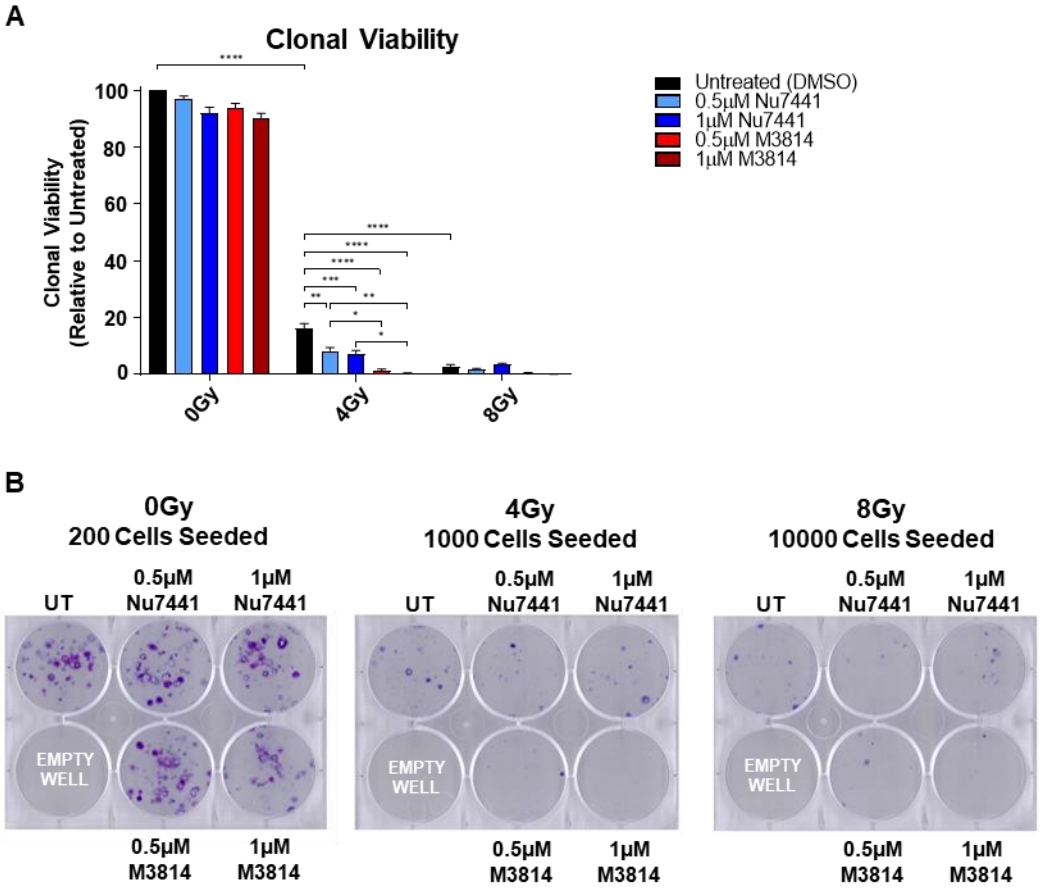

Figure 3. 5. Combination of X-ray and DNA-PKi decreases MC38 survival.

MC38 cells were seeded at low density and treated with 4Gy or 8Gy irradiation and 0.5μM, 1μM Nu7441 or M3814. After 24 hours the media was replaced, and the cells were left for an additional 6 days to allow clones to grow . Resulting clones were fixed, stained with crystal violet and counted. The clonal viability is the proportion of seeded cells which formed a clone, normalised to untreated cells. **(A)** Clonal viability **(B)** Representative images of clonogenic experiment. Joint data of three independent experiments are presented as average±SEM and analysed by two-way ANOVA performed followed by Bonferroni's multiple comparison test: *p<0.05, **p<0.01, ***p<0.001 ****p<0.0001. Significance shown between adjacent X-ray doses and within X-ray groups.

3.3.4. DNA-PK inhibition affects IR-induced DDR.

To better understand the effect of DNA-PK inhibition on the DDR to radiotherapy, immunoblotting was performed on lysates of KP.B6.F1 cell treated with X-ray and DNA-PKi's to determine the levels of γH2AX (Figure 3.6). Treatment with 4Gy, 8Gy or 12Gy increased the levels of γH2AX compared to untreated. However, addition of 0.5μM Nu7441 or 0.5μM M3814 abrogated the increase induced by 4Gy and 8Gy but not 12Gy (Figure 3.6).

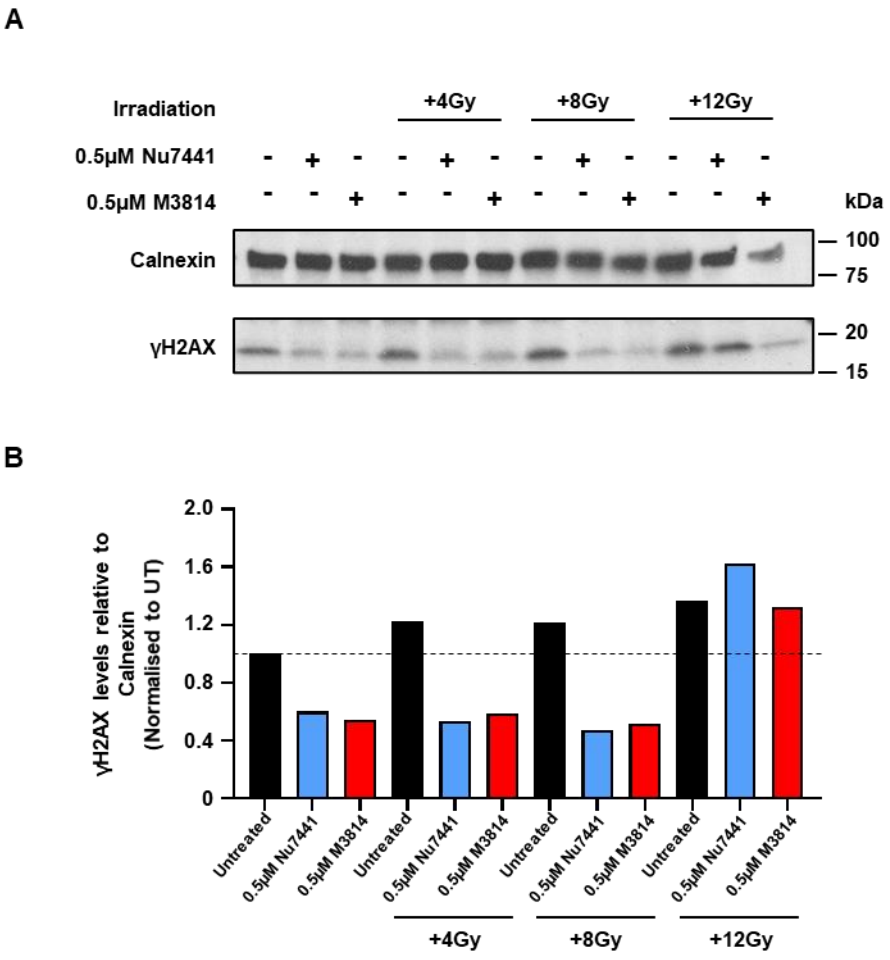

Figure 3. 6. DNA-PKi abrogates radiotherapy induces γH2AX accumulation.

KP.B6.F1 cells were treated with 0.5μM Nu7441 and 0.5μM M3814 and 60 minutes later irradiated with 4Gy, 8Gy or 12Gy. Ten hours later, protein was extracted, and immunoblot performed for Calnexin (loading control) and γH2AX. **(A)** Immunoblot **(B)** Levels of γH2AX normalised to Calnexin (loading control) levels. Normalised to UT. Blots are representative images of 3 biological repeats.

Another way in which DNA-PK can orchestrate the DDR is through changing the morphology of the Golgi apparatus. In response to DNA damage, the Golgi become dispersed resulting in increased cell survival following DNA-damaging agents [45]. Therefore, the effect of DNA-PKi and X-ray on the Golgi structure was investigated using confocal microscopy.

KP.B6.F1 cells were treated with 0.5μM Nu7441 or 0.5μM M3814 and 60 minutes later, irradiated with 4Gy. After 24 hours, the cells were fixed and stained DNA with Hoechst and antibodies for Golgi markers GM130 and GOLPH3. GM130 is localised within the Cis and Medial Golgi, whereas GOLPH3 localises in the Trans Golgi Network [45]. Confocal microscopy was performed and for each cell, the area of the nuclei and Golgi apparatus (defined as the sum of GM130 and GOLPH3) was calculated. From this, the nuclei to Golgi area ratio was calculated. Figure 3.7 A&B show examples of images obtained and how the area was determined. The cell in Figure 3.7 A shows a typical compact Golgi, whereas Figure 3.7 B shows an example of a larger, more dispersed Golgi. Treatment significantly altered the relative Golgi area (one-way ANOVA, $p=0.0008$).The relative Golgi area in cells treated with 4Gy were 1.50-fold greater than those in untreated cells (Bonferroni's, $p=0.004$). However, Golgi dispersal was significantly abrogated in cells treated with 4Gy+0.5μM Nu7441 (Bonferroni's, $p=0.0288$) or 4Gy+0.5μM M3814 (Bonferroni's, $p=0.0074$). The relative Golgi area in cells treated with 4Gy+0.5μM Nu7441 were 1.13-fold greater than those in untreated cells, while in those treated with 4Gy+0.5μM M3814 were just 1.08-fold larger, both of which were not significant differences (Figure 3.7 C). Representative images are shown in Figure 3.7 D. These findings indicate that the treatment with DNA-PKi altered the DDR to radiotherapy.

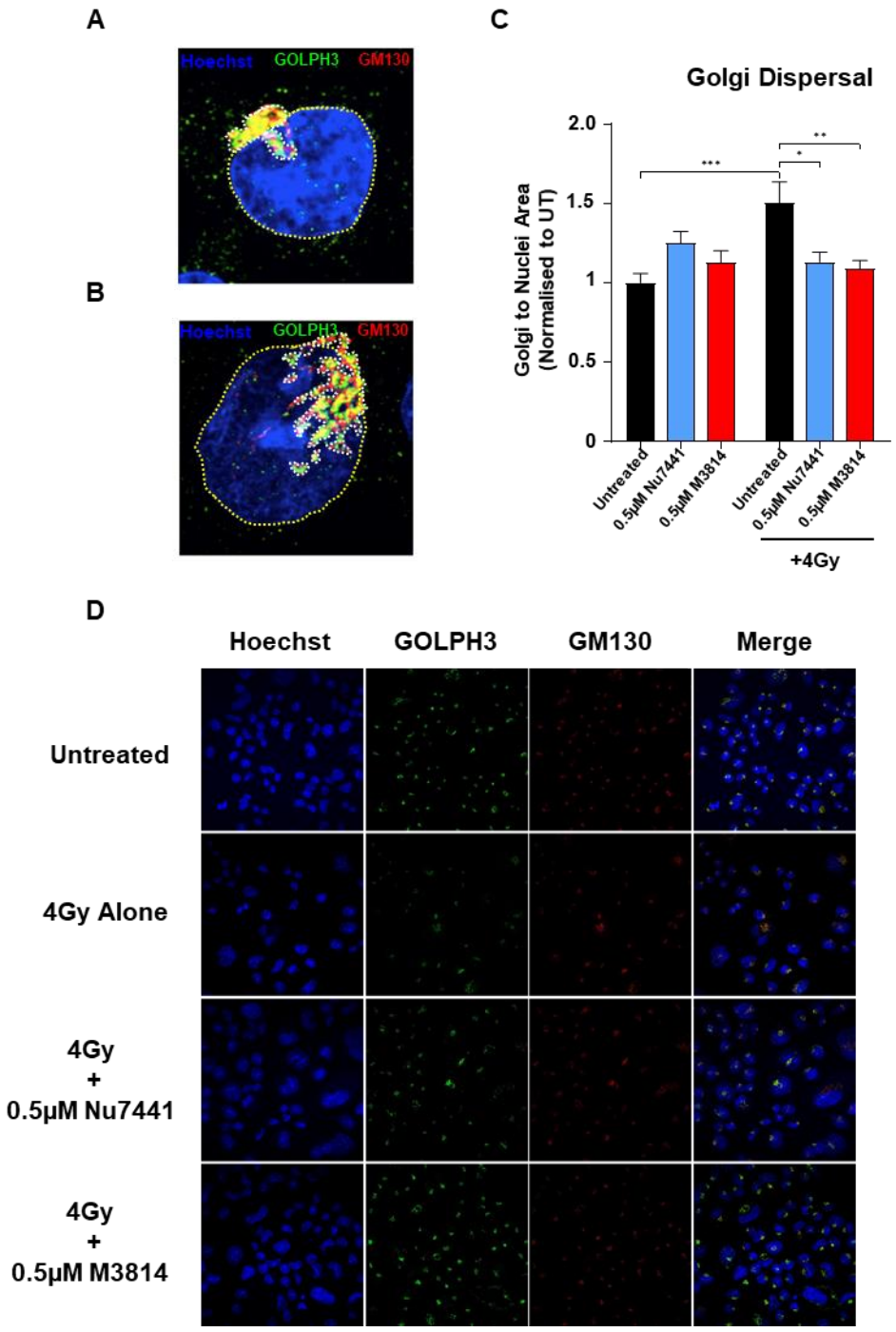

Figure 3. 7. DNA-PKi abrogates X-ray induced Golgi fragmentation.

KP.B6.F1 cells were mounted on coverslip and treated with 0.5μM Nu7441 or 0.5μM M3814 and 60 minutes later irradiated with 4Gy X-ray. Cells were fixed 24 hours after treatment and stained for GM130, GOLPH3 and Hoechst and imaged using confocal microscopy. Golgi area was defined as the sum of GM130 and GOLPH3 signal. Golgi area relative to nuclei area was calculated per cell. **(A)** Representative image of compact Golgi **(B)** fragmented Golgi. **(C)** Golgi area relative to nuclei. **(D)** Representative images. Joint data of three independent experiments are presented as average±SEM and analysed by one-way ANOVA performed followed by Bonferroni's multiple comparison test: *p<0.05, **p<0.01, ***p<0.001 ****p<0.0001.

3.3.5. Combination of X-ray and DNA-PKi induces apoptosis

To identify immunogenic cell death, first it needed to be determined whether dying cells are undergoing apoptosis, secondly the timing of this death needs to be better understood to enable further study on events occurring immediately prior to death [158].

A flow cytometry time course experiment was performed on KP.B6.F1 and CMT-167 cells to determine the expression of immunomodulatory markers in response to X-ray and DNA-PK inhibition. Firstly, the viability markers annexin V and DAPI were used to identify the presence of apoptotic cells and at which time this may occur. Annexin V binds phosphatidyl serine (PS) which is flipped from the internal side of the cell surface membrane to external side during the early phases of apoptosis. Therefore, Annexin V^+ cells are committed to apoptosis while DAPI signifies a cell is already dead. Accordingly , Annexin V^+DAPI^- were characterised as 'apoptotic' cells.

At 24 hours after treatment, while X-ray treatment had a significant effect on the proportion of viable KP.B6.F1 cells (two-way ANOVA, $p<0.001$)(Figure 3.8 A). DNA-PKi had no significant effect on this population of cells. Furthermore, Bonferroni's multiple comparison test found no significant differences between adjacent X-ray doses nor with the addition of DNA-PKi to any X-ray dose. 48 hours post treatment, both X-ray treatment and DNA-PKi had a significant effect on the proportion of apoptotic cells (two-way ANOVA, X-ray $p<0.0001$ and DNA-PKi $p=0.0002$)(Figure 3.8 B). There was also a significant interaction between X-ray and DNA-PKi, indicating synergy (two-way ANOVA, $p=0.0394$). At this timepoint, the greatest increase in cell death occurred with the addition of 0.5μM M3814 to 12Gy wherein the % of apoptotic cells increased from 7.6% (±1.0) to 13.5% (±4.6)(Bonferroni's, $p<0.0024$). This pattern was also observed at 8Gy wherein addition of 0.5μM M3814 increase the frequency of apoptotic cells from 3.7% (±0.5) to 8.5% (±1.1)(Bonferroni's, $p=0.0228$)(Figure 3.8 B).

At 72 hours there was a significant interaction together (two-way ANOVA, p=0.0104), indicating synergy. The frequency of apoptotic cell significantly increased from 8.0% (±1.9) with 8Gy irradiation to 26.5% (±6.0) with 12Gy. Similarly, to that seen at 48 hours, addition of 0.5μM M3814 to 8Gy increased the frequency of apoptotic cells, but to a greater extent, increasing 3.7-fold from 8% (±1.9) with 8Gy alone up to 30.5% (±9.7) with 8Gy+0.5μM M3814 (Bonferroni's, p=0.003). 8Gy+0.5μM M3814 was also 14.1% greater than 0.5μM Nu7441+8Gy at 16.4% (±6.4)(Bonferroni's, p=0.0449)(Figure 3.8 C).

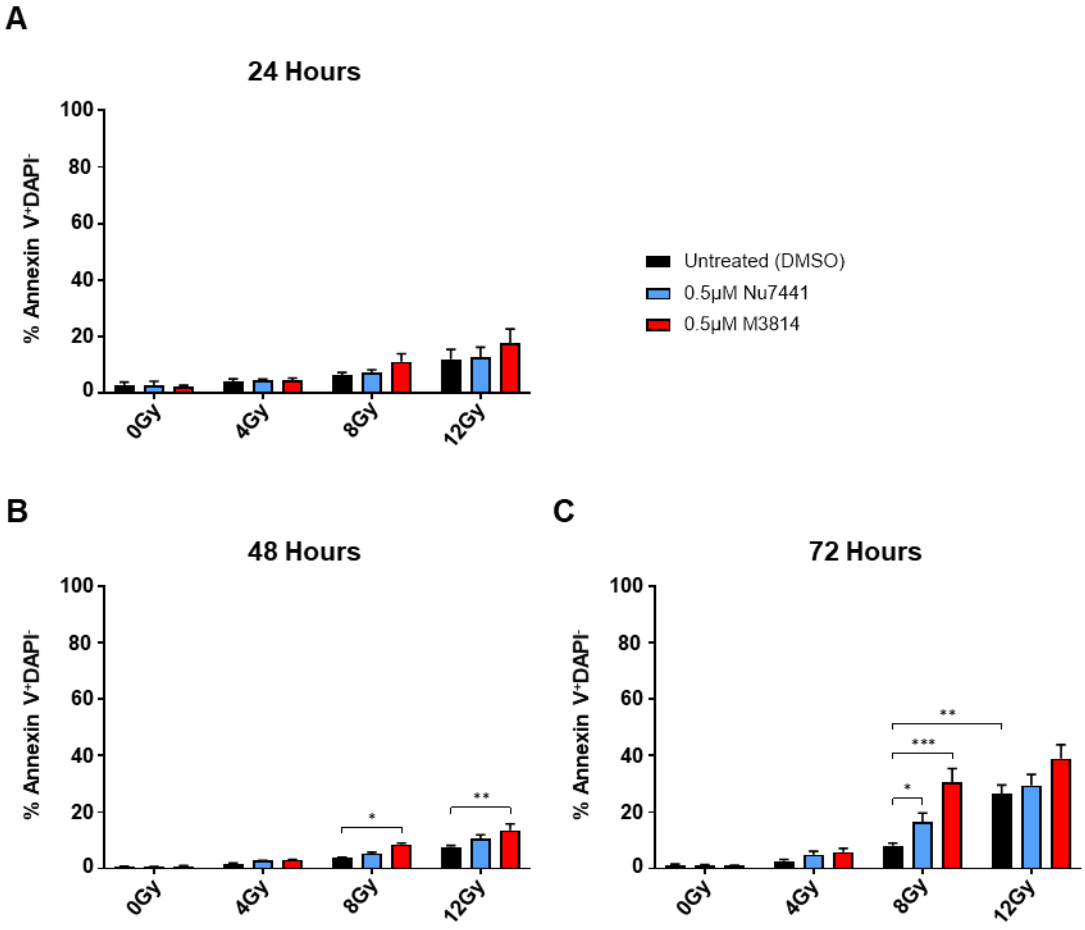

Figure 3. 8. Combination of M3814 and X-ray increases of apoptosis in KP.B6.F1 cells.

KP.B6.F1 cells were treated with 0Gy, 4Gy, 8Gy or 12Gy X-ray, either alone or in combination with 0.5μM Nu7441 or 0.5μM M3814. Cells were collected 24, 48 and 72 hours after treatment and analysed by flow cytometry. **(A)** % of annexin V^+DAPI^- KP.B6.F1 cells 24 hours following treatment. **(B)** % of annexin V^+DAPI^- KP.B6.F1 cells 48 hours following treatment. **(C)** % of annexin V^+DAPI^- KP.B6.F1 cells 72 hours following treatment. Joint data of three independent experiments are presented as average±SEM and analysed by two-way ANOVA followed by Bonferroni's multiple comparison test: *p<0.05, **p<0.01, ***p<0.001 ****p<0.0001.

In CMT-167 the % of apoptotic cells 24 hours post treatment was significantly influenced by X-ray treatment only (two-way ANOVA, $p<0.0001$)(Figure 3.9 A). Addition of DNA-PKi did not have a significant effect, nor was there an interaction between the two factors. The only significant change between adjacent X-ray doses or within X-ray groups was seen between 8Gy with 6.0% (±1.6) of apoptotic cells up to 12.5% (±3.5) in cells treated with 12Gy (Bonferroni's, $p=0.0349$)(Figure 3.9 A).

At 48 hours post treatments, both X-ray treatment and DNA-PKi had significant altered on the apoptotic cell population (two-way ANOVA, X-ray $p<0.0001$ and DNA-PKi $p<0.0001$)(Figure 3.9 B). There was also a significant interaction between the two, indicating synergy (two-way ANOVA, $p=0.0003$). Increasing the X-ray dose from 8Gy to 12Gy resulted in a significant increase in the % of apoptotic cells from 6.6% (±1.0) to 26.9% (±1.7) respectively (Bonferroni's, $p<0.0001$). Furthermore, addition of either 0.5μM Nu7441 or 0.5μM M3814 to 8Gy resulted in a significant increase compared to 8Gy alone. Addition of 0.5μM Nu7441 to 8Gy increased the % of apoptotic cells to 17.2% (±3.1)(Bonferroni's, $p=0.0336$) while 0.5μM M3814 increased it to 28.8% (±2.7)(Bonferroni's, $p<0.0001$). The proportion of apoptotic cells following 8Gy+0.5μM M3814 treatment was significantly greater than those treated with 8Gy+0.5μM Nu7441 (Bonferroni's, $p=0.0158$)(Figure 3.9 B).

Both X-ray treatment and DNA-PKi had significant influences on the frequency of apoptotic cells (two-way ANOVA, X-ray $p<0.0001$ and DNA-PKi $p<0.0001$)(Figure 3.9 C). There was, however, no interaction between the two. The % apoptotic cells increase in an X-ray dose dependent manner, from 4Gy with 5.2% (±2.0) to 17.9% (±0.9) with 8Gy (Bonferroni's, $p=0.0082$). Administration of 12Gy alone further increased this to 38.6% (±8.1)(Bonferroni, $p<0.0001$). Addition of 0.5μM M3814 to

8Gy significantly increased the apoptotic population to 31.1% (±6.4) compared to 8Gy alone (Bonferroni's, p=0.0052)(Figure 3.9 C).

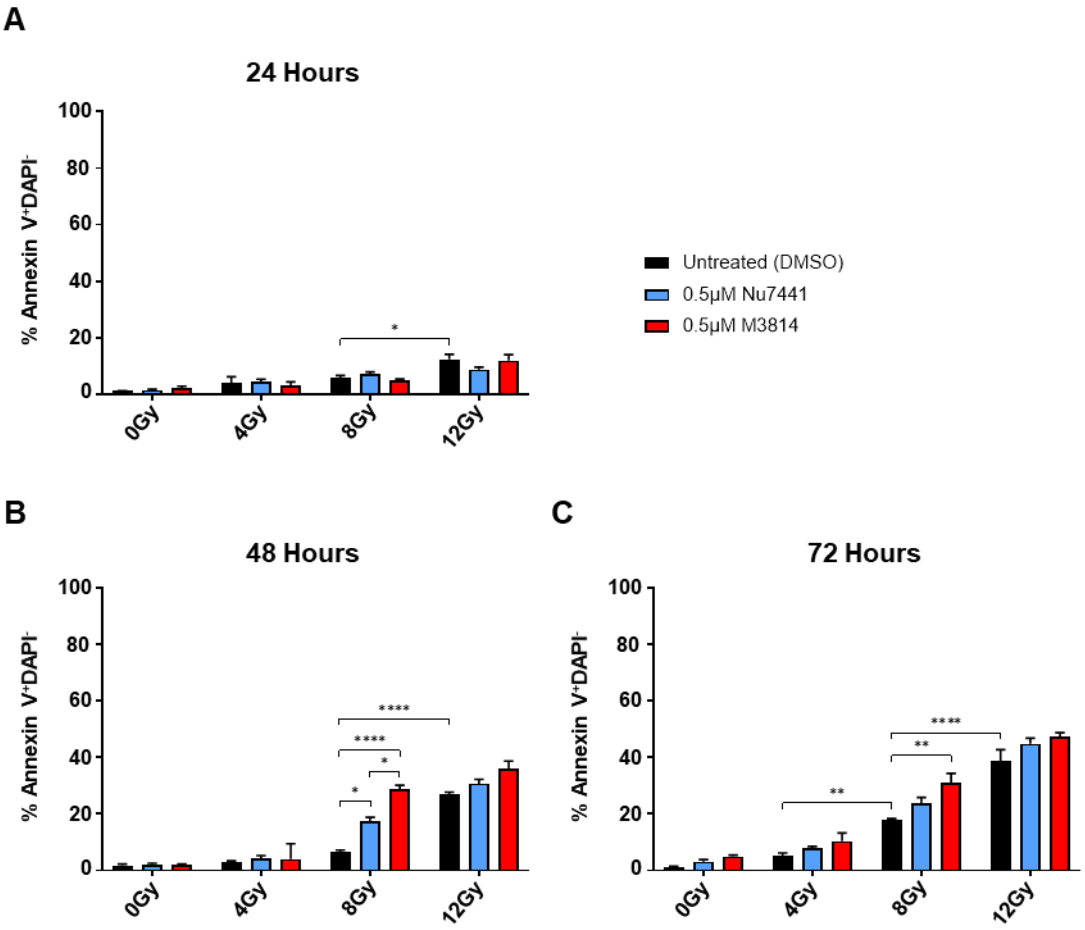

Figure 3. 9. Combination of M3814 and X-ray increases apoptosis in CMT-167 cells.

CMT-167 cells were treated with 0Gy, 4Gy, 8Gy or 12Gy X-ray, either alone or in combination with 0.5μM Nu7441 or 0.5μM M3814. Cells were collected 24, 48 and 72 hours after treatment and analysed by flow cytometry. **(A)** % of annexin V^+DAPI^- CMT-167 cells 24 hours following treatment. **(B)** % of annexin V^+DAPI^- CMT-167 cells 48 hours following treatment. **(C)** % of annexin V^+DAPI^- CMT-167 cells 72 hours following treatment. Joint data of three independent experiments are presented as average±SEM and analysed by two-way ANOVA followed by Bonferroni's multiple comparison test: *p<0.05, **p<0.01, ***p<0.001 ****p<0.0001.

3.3.6. DNA-PKi and X-ray increases cell surface level of PD-L1.

DNA damaging agents have been demonstrated to alter expression of PD-L1 expression in cancer cells [152, 159]. Loss of components of the HRR, NHEJ and BER pathways have been shown to further augment this effect. Therefore, the cell surface level of PD-L1 following treatment with X-ray and DNA-PKi was evaluated using flow cytometry.

KP.B6.F1 and CMT-167 cells were treated with 0.5μM Nu7441 or 0.5μM M3814 for 60 minutes, at which point cells were irradiated with 4Gy, 8Gy or 12Gy. Cells were collected 24, 48 and 72 hours after treatment and stained with the viability markers DAPI and annexin V, as wells as antibodies for MHC Class I, PD-L1 and CRT. Flow cytometry was subsequently performed on these stained cells. As previously mentioned, $DAPI^+$ cells were characterised as dead and therefore excluded from the analysis.

At 24 hours, both X-ray (two-way ANOVA, $p<0.001$) and DNA-PKi (two-way ANOVA, $p<0.001$) had a significant impact on the frequency of $PD\text{-}L1^+$ cells (Figure 3.10). The addition of M3814 to 4Gy irradiation further increased the frequency of $PD\text{-}L1^+$ cells from 36.8% (±5.4) to 52.8%, (±3.2)(Bonferroni's, $p=0.0127$). This was also 15% greater than those treated with 4Gy+0.5μM Nu7441 at 37.4% (±7.2)(Bonferroni's, $p=0.0212$)(Figure 3.10 A). However, the greatest difference was seen at 48 hours wherein both DNA-PKi and irradiation had significant effects (two-way ANOVA, $p=0.007$, $p<0.001$ respectively), and had a significant interaction with one another (two-way ANOVA, $p=0.0091$)(Figure 3.10 B). The addition of M3814 to 4Gy significantly increased $PD\text{-}L1^+$ KP.B6.F1 cells from 35% (±5.4) to 51% (±2.8)(Bonferroni's, $p=0.0228$), which was also greater than those treated with Nu7441 in combination with 4Gy (Bonferroni's, $p=0.0099$)(Figure 3.14 B). At 72 hours, X-ray dose or addition of DNA-PKi did not alter the size of the $PD\text{-}L1^+$ population to a statistically significant degree (Figure 3.10 C).

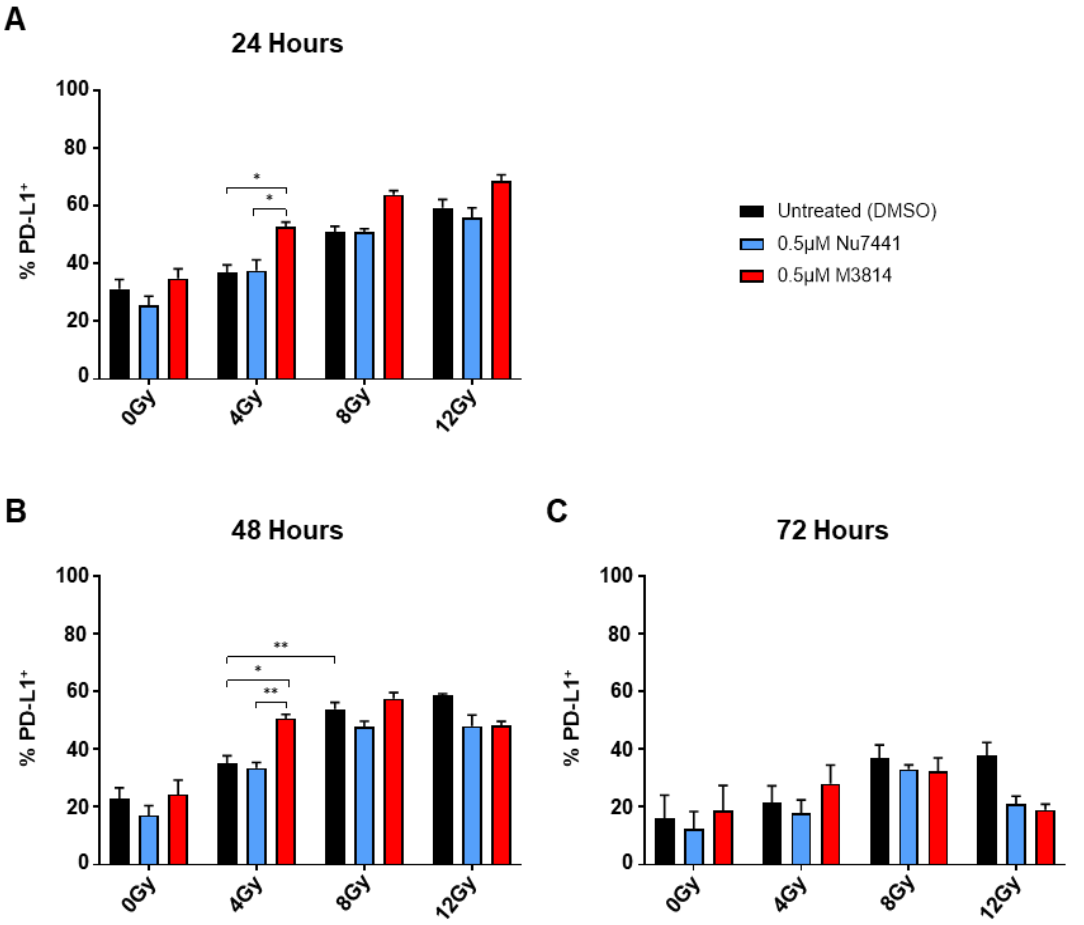

Figure 3. 10. The frequency of PD-L1+ KP.B6.F1 cells is increased 48 hours following treatment with X-ray and M3814.

KP.B6.F1 cells were treated with 0Gy, 4Gy, 8Gy or 12Gy X-ray, either alone or in combination with 0.5μM Nu7441 or 0.5μM M3814. Positive control for PD-L1 expression was achieved with 1μg/mL IFNγ treatment (see Figure 4.6B). Cells were collected 24, 48 and 72 hours after treatment and analysed by flow cytometry. Cells were gated on $DAPI^-$ cells. **(A)** % of $PD\text{-}L1^+$ KP.B6.F1 cells 24 hours following treatment. **(B)** % of $PD\text{-}L1^+$ KP.B6.F1 cells 24 hours following treatment. **(C)** % of $PD\text{-}L1^+$ KP.B6.F1 cells 72 hours following treatment. Joint data of three independent experiments are presented as average±SEM and analysed by two-way ANOVA followed by Bonferroni's multiple comparison test: *p<0.05, **p<0.01, ***p<0.001 ****p<0.0001.

While alterations in the proportion of $PD\text{-}L1^+$ are of interest, it is important to note that the actual level of cell surface PD-L1 per positive cell, as measured by fluorescence, was only moderately increased. As shown in the histograms in Figure 3.11 A, the $PD\text{-}L1^+$ cells following X-ray and M3814 form a 'shoulder' of cells. This contrasts with those treated with IFN-γ which show a clear bimodal population (Figure 3.11 B).

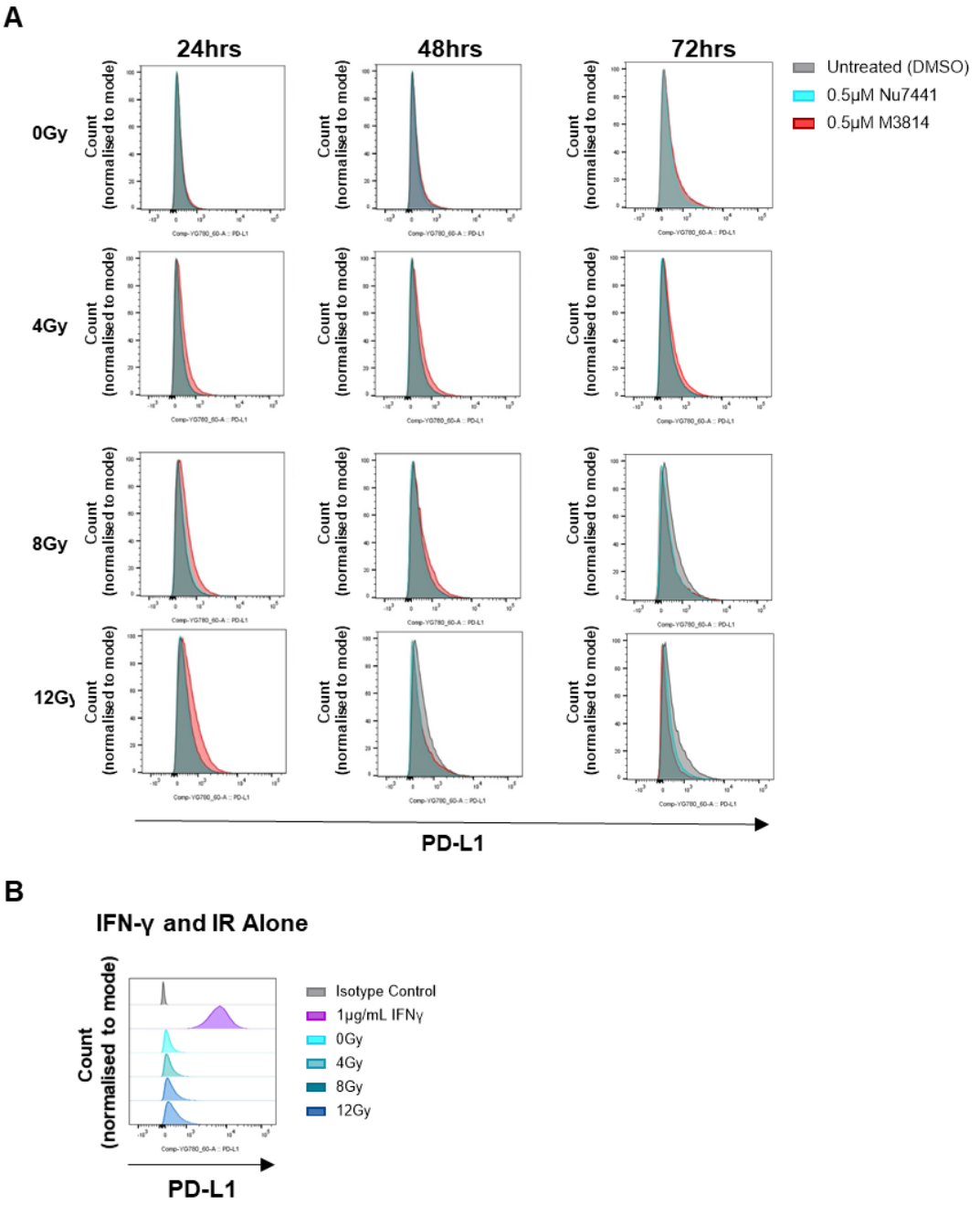

Figure 3. 11. Representative histograms of PD-L1 expression in KP.B6.F1 cells after treatment with X-ray and DNA-PKi.

KP.B6.F1 cells were treated with 0Gy, 4Gy, 8Gy or 12Gy X-ray, either alone or in combination with 0.5μM Nu7441 or 0.5μM M3814. Positive control for PD-L1 expression was achieved with 1μg/mL IFNγ treatment. Cells were collected 24, 48 and 72 hours after treatment and analysed by flow cytometry. Representative histograms showing PD-L1 expression in $DAPI^-$ KP.B6.F1 cells treated with **(A)** X-ray and DNA-PK inhibitors **(B)** X-ray alone and 1μg/mL IFNγ.

The frequency of PD-L1$^+$ CMT-167 cells was significantly influenced by treatment with X-ray at 24, 48 and 72 hours (two-way ANOVA, $p<0.0001$ at all timepoints), but not significantly influenced by the addition of DNA-PKi (Figure 3.12 A-C). At 24 hours the increase in PD-L1$^+$ cells were most prominent, rising from 4% (±6.7), to 25% (±13.8) with 4Gy, 50% (±13.9) with 8Gy and 62% (±11.2) with 12Gy (Figure 3.12 A). Over time this pattern became less pronounced, indicating this response may be transient.

As with KP.B6.F1 cells, the PD-L1$^+$ population at 24 and 48 hours resembles a small shoulder rather than the distinct bimodal population seen following IFNγ treatment (Figure 3.13 A&B). However, 72 hours following treatment with 12Gy in combination with Nu7441 or M3814, there was a more distinct separate population in the histogram measured as fluorescence intensity of PD-L1 molecules in the cell surface (Figure 3.13 A).

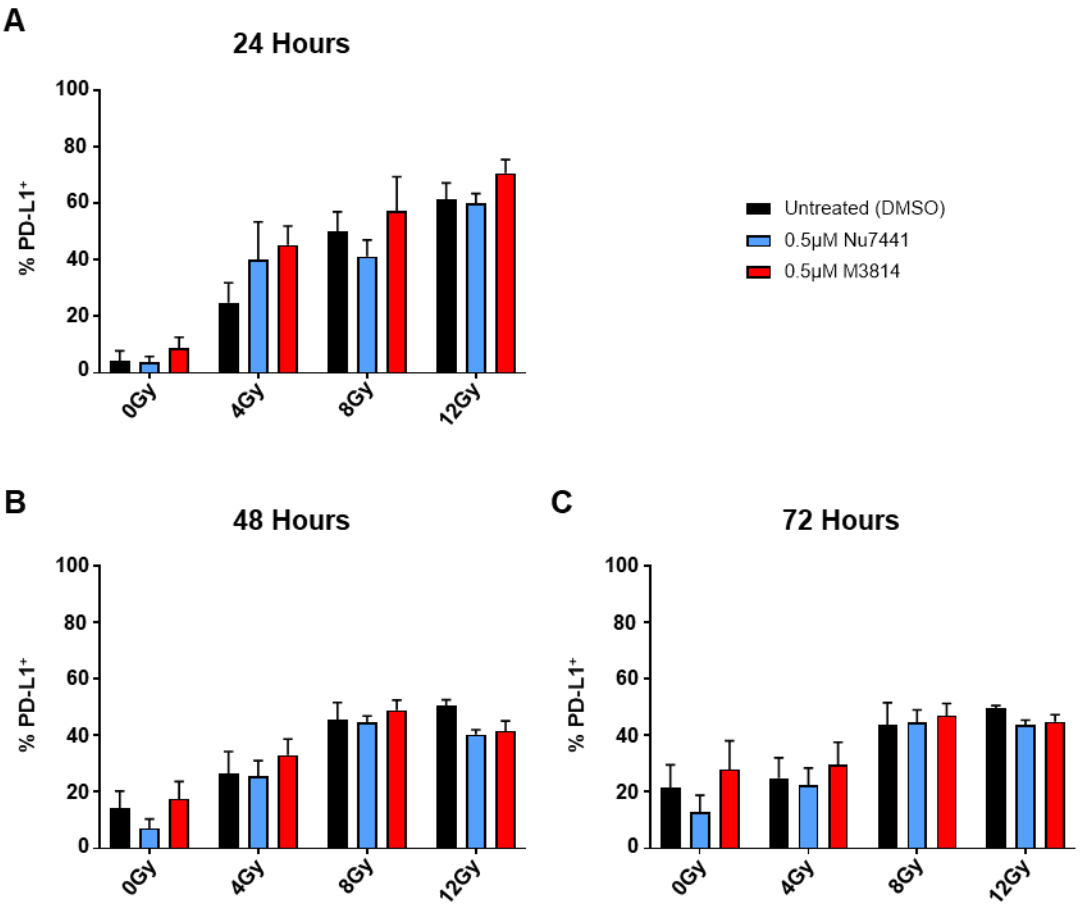

Figure 3. 12. The frequency of PD-L1+ CMT-167 cells is increased 24- and 48-hours following treatment with IR.

CMT-167 cells were treated with 0Gy, 4Gy, 8Gy or 12Gy X-ray, either alone or in combination with 0.5μM Nu7441 or 0.5μM M3814. Positive control for PD-L1 expression was achieved with 1μg/mL IFNγ treatment. Cells were collected 24, 48 and 72 hours after treatment and analysed by flow cytometry. Cells were gated on $DAPI^-$ cells. **(A)** % of $PD\text{-}L1^+$ CMT-167 cells 24 hours following treatment. **(B)** % of $PD\text{-}L1^+$ CMT-167 cells 24 hours following treatment. **(C)** % of $PD\text{-}L1^+$ CMT-167 cells 72 hours following treatment. Joint data of three independent experiments are presented as average±SEM and analysed by two-way ANOVA followed by Bonferroni's multiple comparison test: *p<0.05, **p<0.01, ***p<0.001 ****p<0.0001.

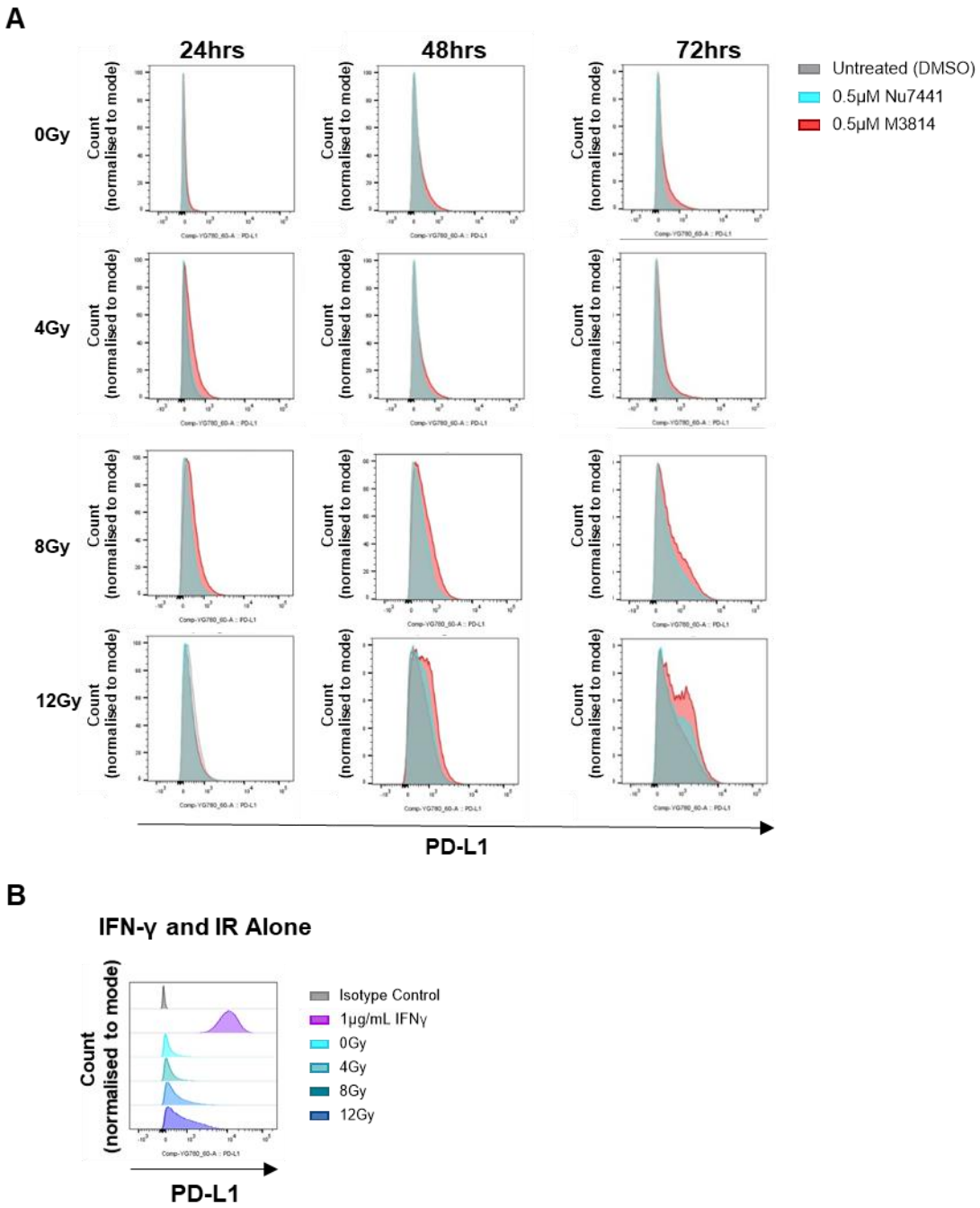

Figure 3. 13. Representative histograms of PD-L1 expression in CMT-167 cells after treatment with IR and DNA-PKi.

CMT-167 cells were treated with 0Gy, 4Gy, 8Gy or 12Gy X-ray, either alone or in combination with 0.5μM Nu7441 or 0.5μM M3814. Positive control for PD-L1 expression was achieved with 1μg/mL IFNγ treatment. Cells were collected 24, 48 and 72 hours after treatment and analysed by flow cytometry. Representative histograms showing PD-L1 expression in $DAPI^-$ CMT-167 cells treated with **(A)** IR and DNA-PK inhibitors **(B)** IR alone and 1μg/mL IFNγ.

3.3.7. MHC Class I cell surface levels are not increased by treatment with X-ray and DNA-PKi.

Previous studies have shown that irradiation alone can increase the level of MHC Class I [151, 160, 161]. Therefore, the levels of MHC Class I was investigated in KP.B6.F1 and CMT-167 following treatment with X-ray and DNA-PK inhibition. There was little change to the levels of MHC Class I in KP.B6.F1 cells treated with X-ray and DNA-PKi (Figure 3.14). X-ray had a significant influence on MHC Class I^+ cells at 72 hours (two-way ANOVA, p=0.0014)(Figure 3.14 C). MHC I levels were low, ranging from 1.9% (±3.4) of untreated cell to 8.0% (±2.4) of cells after 72 hours of 12Gy+M3814, however, this was not significant. X-ray had a significant effect on the frequency of MHC Class I^+ CMT-167 cells 24 hours (two-way ANOVA, p=0.0163), 48 hours (two-way ANOVA, p<0.0001) and 72 hours after treatment (two-way ANOVA, p<0.0001)(Figure 3.15). At 72 hours, the percentage of MHC Class I^+ cells rose significantly from 1% (±1.0) in untreated, up to 4.5% (±1.9) with 12Gy (Bonferroni's, p=0.0137) and 5.6% (±1.5) with 12Gy+M3814 (Bonferroni's, p=0.0006)(Figure 3.15 C).

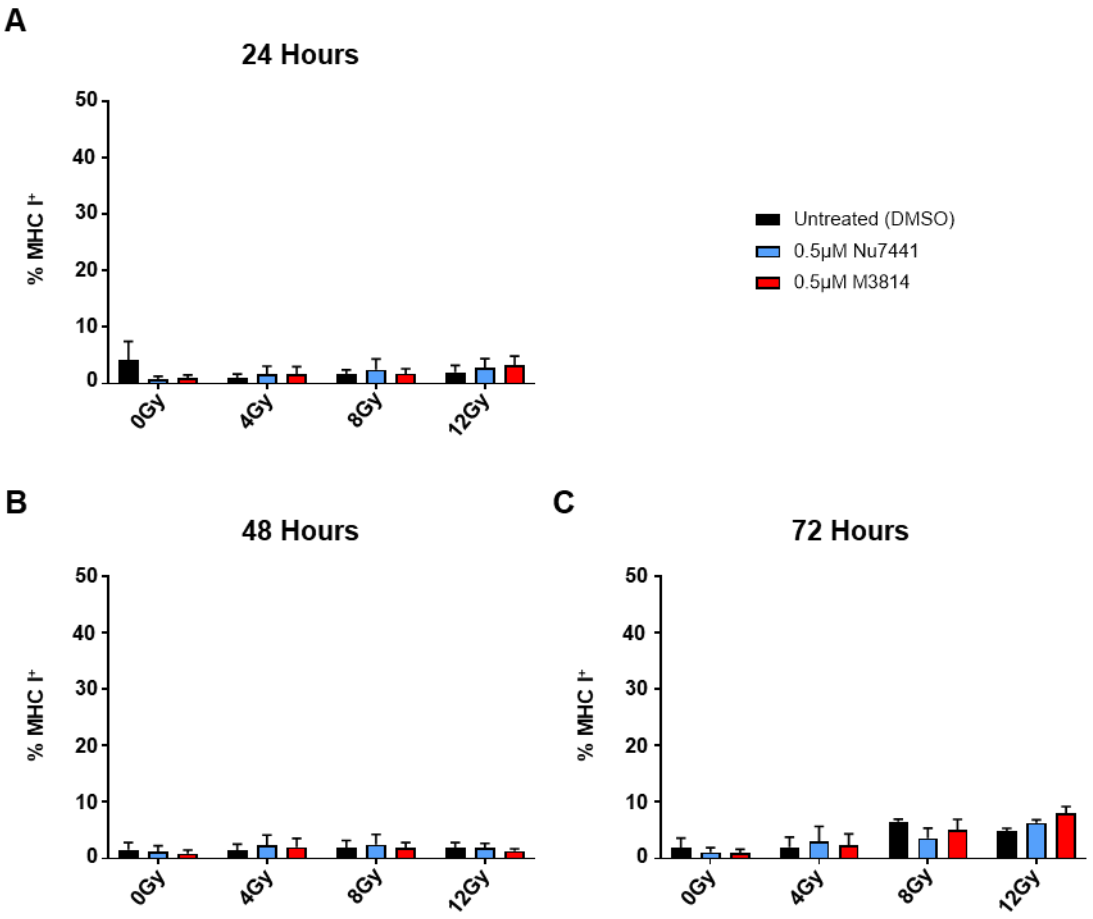

Figure 3. 14. The frequency of MHC Class I+ KP.B6.F1 cells is increased 72 hours following treatment with IR and M3814.

KP.B6.F1 cells were treated with 0Gy, 4Gy, 8Gy or 12Gy X-ray, either alone or in combination with 0.5μM Nu7441 or 0.5μM M3814. Cells were collected 24, 48 and 72 hours after treatment and analysed by flow cytometry. Cells were gated on $DAPI^-$cells. **(A)** % of MHC Class I^+ KP.B6.F1 cells 24 hours following treatment. **(B)** % of MHC Class I^+ KP.B6.F1 cells 24 hours following treatment. **(C)** % of MHC Class I^+ KP.B6.F1 cells 72 hours following treatment. Joint data of three independent experiments are presented as average±SEM and analysed by two-way ANOVA followed by Bonferroni's multiple comparison test.

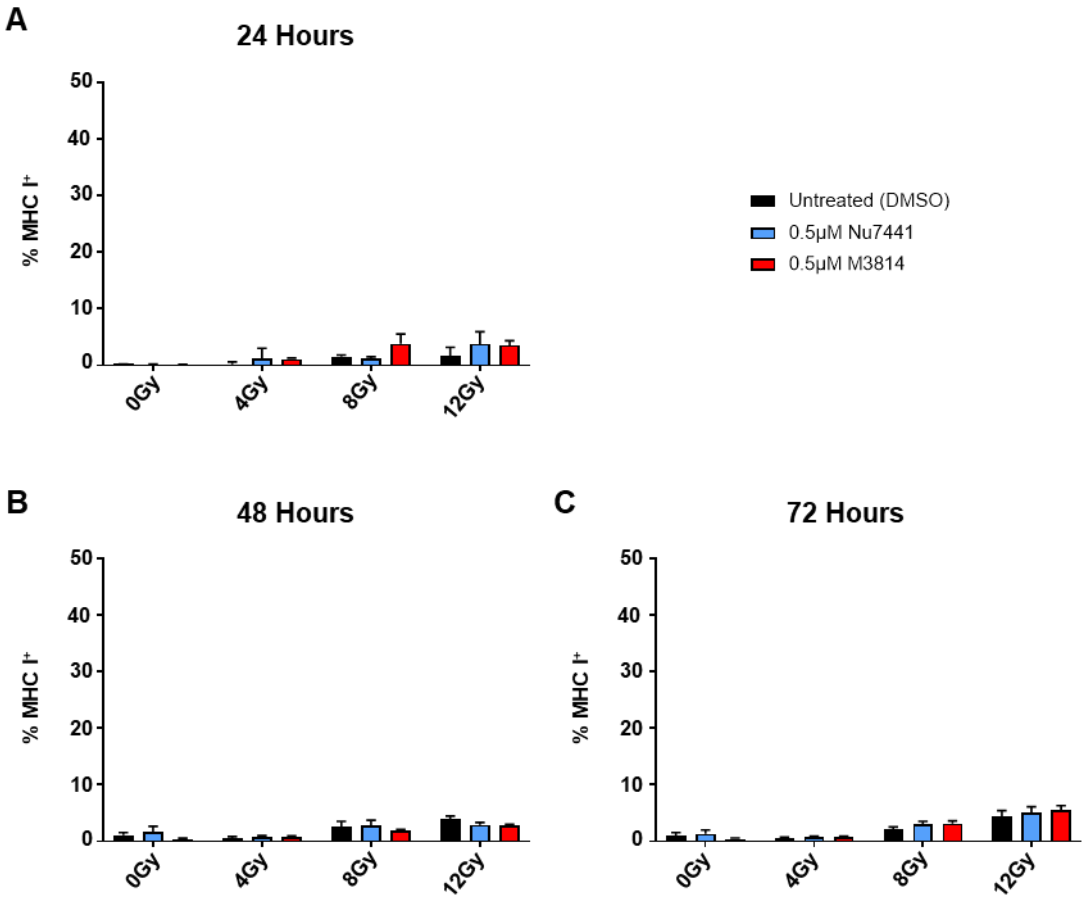

Figure 3. 15. The frequency of MHC Class I+ CMT-167 cells increase with radiotherapy.

CMT-167 cells were treated with 0Gy, 4Gy, 8Gy or 12Gy X-ray, either alone or in combination with 0.5μM Nu7441 or 0.5μM M3814. Cells were collected 24, 48 and 72 hours after treatment and analysed by flow cytometry. Cells were gated on $DAPI^-$cells. **(A)** % of MHC Class I^+ CMT-167 cells 24 hours following treatment. **(B)** % of MHC Class I^+ CMT-167 cells 24 hours following treatment. **(C)** % of MHC Class I^+ CMT-167 cells 72 hours following treatment. Joint data of three independent experiments are presented as average±SEM and analysed by two-way ANOVA followed by Bonferroni's multiple comparison test.

3.3.8. Combination of DNA-PKi and X-ray induces immunogenic cell death in KP.B6.F1 cells.

While there are many markers of ICD, Calreticulin (CRT) translocation from the ER to the cell surface membrane is one of the most studied and is deemed necessary for ICD classification [90, 162]. The presence of CRT on the cell surface membrane was analysed on cells treated as described in the previous sections.

The frequency of CRT^+ cells increased with X-ray alone in a dose dependent response at all time points (two-way ANOVA, $p>0.001$ at all timepoints). This response was modest at 24 hours however was much more pronounced at 48 hours and greater still after 72 hours (Figure 3.16 A-C). At 48 hours, DNA-PK inhibition had a significant role in CRT translocation (two-way ANOVA, $p=0.0003$) and both X-ray and DNA-PK inhibition had a significant interaction (two-way ANOVA, $p=0.0345$)(Figure 3.16 B). Importantly, addition of 0.5μM M3814 to 8Gy significantly increased cell surface CRT from 7.4% (±1.6) to 34.3% (±24.5)(Bonferroni's, $p=0.0098$). This was also seen at 12Gy in which the frequency of CRT^+ cells rose from 25.5% (±6.1) to 51.2% (±14.5) upon addition of 0.5μM M3814 (Bonferroni's, $p=0.0152$)(Figure 3.16 B).

The greatest change to CRT translocation was observed at 72 hours, wherein there was a significant interaction between X-ray and treatment with DNA-PKi (two-way ANOVA, $p=0.0002$) and both had significant effects individually (two-way ANOVA, $p>0.0001$)(Figure 3.16 C). Addition of 0.5μM M3814 caused the % of CRT^+ KP.B6.F1 cells to increase from 11.2% (±5.9) in 8Gy alone to 57.2% (±14.0) in combination (Bonferroni's, $p>0.0001$). This 5-fold increase in CRT^+ cells is a strong indicator of ICD. In cells treated with 12Gy, 48.0% (±5.8) were CRT^+, this increased to 72.3% (±1.6) in cells treated with 12Gy+0.5μM M3814 (Bonferroni's, $p=0.0142$).

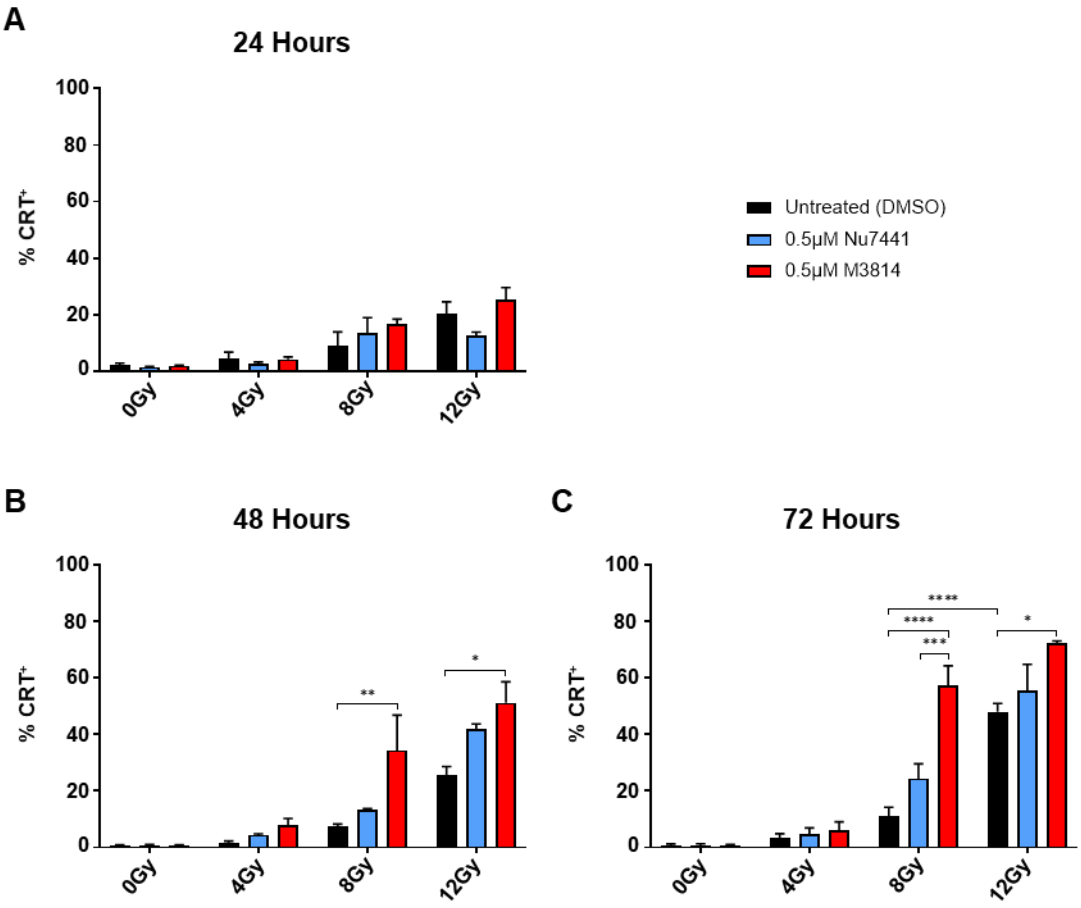

Figure 3. 16. The frequency of CRT+ KP.B6.F1 cells is increased following treatment with IR and DNA-PKi.

KP.B6.F1 cells were treated with 0Gy, 4Gy, 8Gy or 12Gy X-ray, either alone or in combination with 0.5μM Nu7441 or 0.5μM M3814. Positive control for Calreticulin expression was achieved by 24 hours treatment with 1μM Mitoxantrone. Cells were collected 24, 48 and 72 hours after treatment and analysed by flow cytometry. CRT^+ cells were gated on $DAPI^-$ cells. **(A)** % of $Calreticulin^+$ KP.B6.F1 cells at 24 hours **(B)** 48 hours and **(C)** 72 hours. Joint data of three independent experiments are presented as average±SEM and analysed by two-way ANOVA followed by Bonferroni's multiple comparison test: *p<0.05, **p<0.01, ***p<0.001 ****p<0.0001.

Furthermore, as shown on the representative histograms in Figure 3.17, this increase proportion of CRT^+ cells formed a distinct bimodal population. This distribution was similar to that observed after treatment with 1μM Mitoxantrone, a well-studied and known inducer of ICD [162].

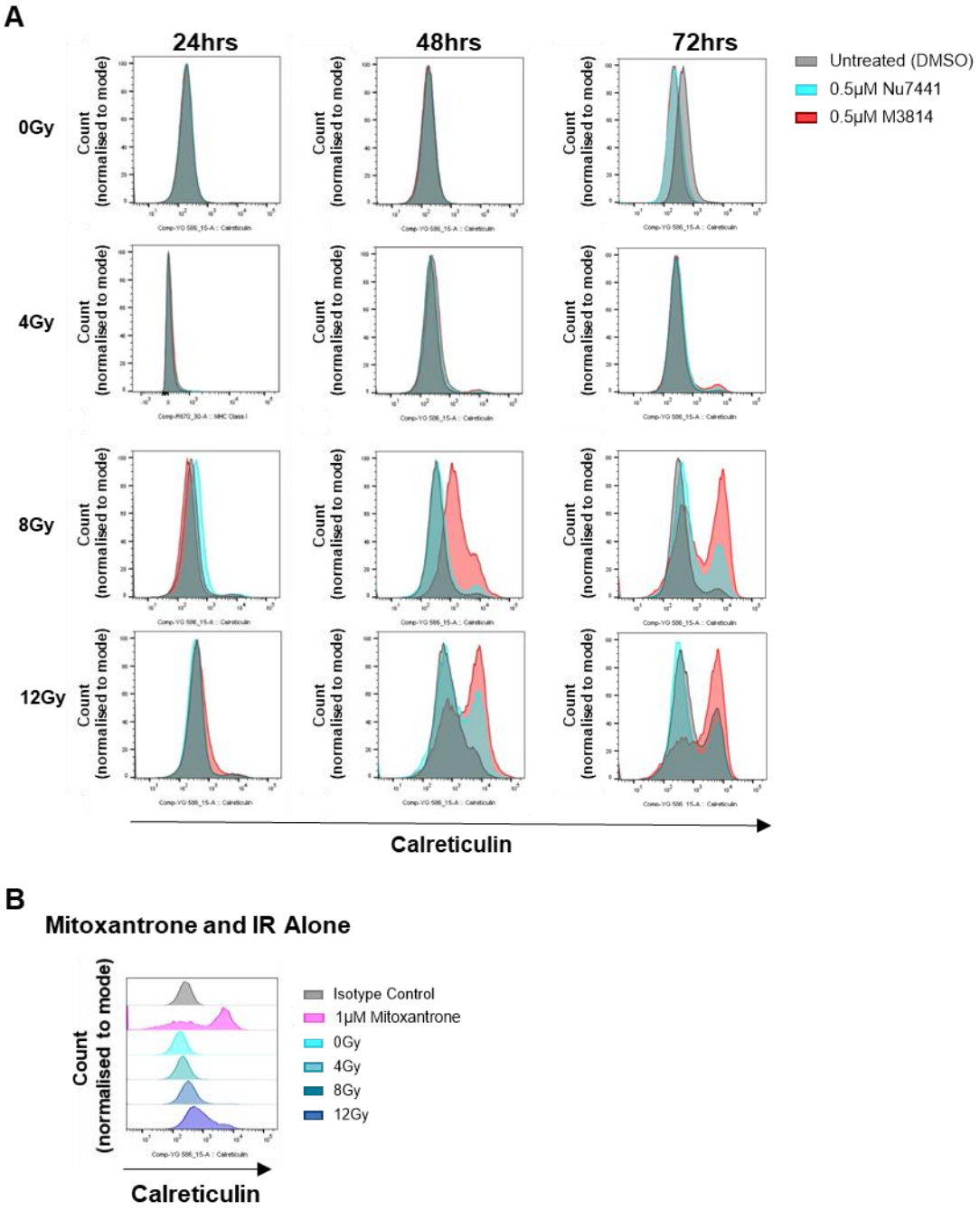

Figure 3. 17. Representative histograms of CRT+ KP.B6.F1 cells following treatment with IR and DNA-PKi.

KP.B6.F1 cells were treated with 0Gy, 4Gy, 8Gy or 12Gy X-ray, either alone or in combination with 0.5μM Nu7441 or 0.5μM M3814. Positive control for cell surface CRT expression was achieved by 24 hours treatment with 1μM Mitoxantrone. Cells were collected 24, 48 and 72 hours after treatment and analysed by flow cytometry. Representative histograms showing cell surface levels of CRT in $DAPI^-$ KP.B6.F1 cells treated with **(A)** IR and DNA-PK inhibitors **(B)** IR alone and 1μM Mitoxantrone.

Similarly, to KP.B6.F1 cells, 24 hours following treatment, cell surface CRT on CMT-167 cells was significantly altered by both X-ray (two-way ANOVA, p=0.0001) and DNA-PKi (two-way ANOVA, p=0.0032)(Figure 3.18 A). The frequency of CRT^+ CMT-167 cells significantly increased from 2.8% (±0.7) in untreated to 16.0% (±5.4) following 12Gy (Bonferroni's, p=0.0009), however, unlike KP.B6.F1 the addition of DNA-PK inhibition abrogated this increase. For example, addition of M3814 to CMT-167 cells treated with 8Gy significantly decreased the proportion of CRT^+ cells from 11.5% (±2.9) to 2.6% (±5.4)(Bonferroni's, p=0.05) and similar was observed at 12Gy wherein the addition of Nu7441 decreased the frequency of CRT^+ from 15.9% (±5.4) to 5.6% (±2.4)(Bonferroni's, p=0.014)(Figure 3.18 A). Furthermore, contrary to the results seen in KP.B6.F1 cells, no significant change to CRT translocation is seen at 48 or 72 hours (Figure 3.18 B&C). Of note, while a CRT^+ population of CMT-167 cells is present after Mitoxantrone treatment (Figure 3.19 B), it is markedly less than observed in KP.B6.F1 treated cells (Figure 3.17 B) indicating that treatment does not induce ICD in CMT-167. Due to this, KP.B6.F1 was selected for further study.

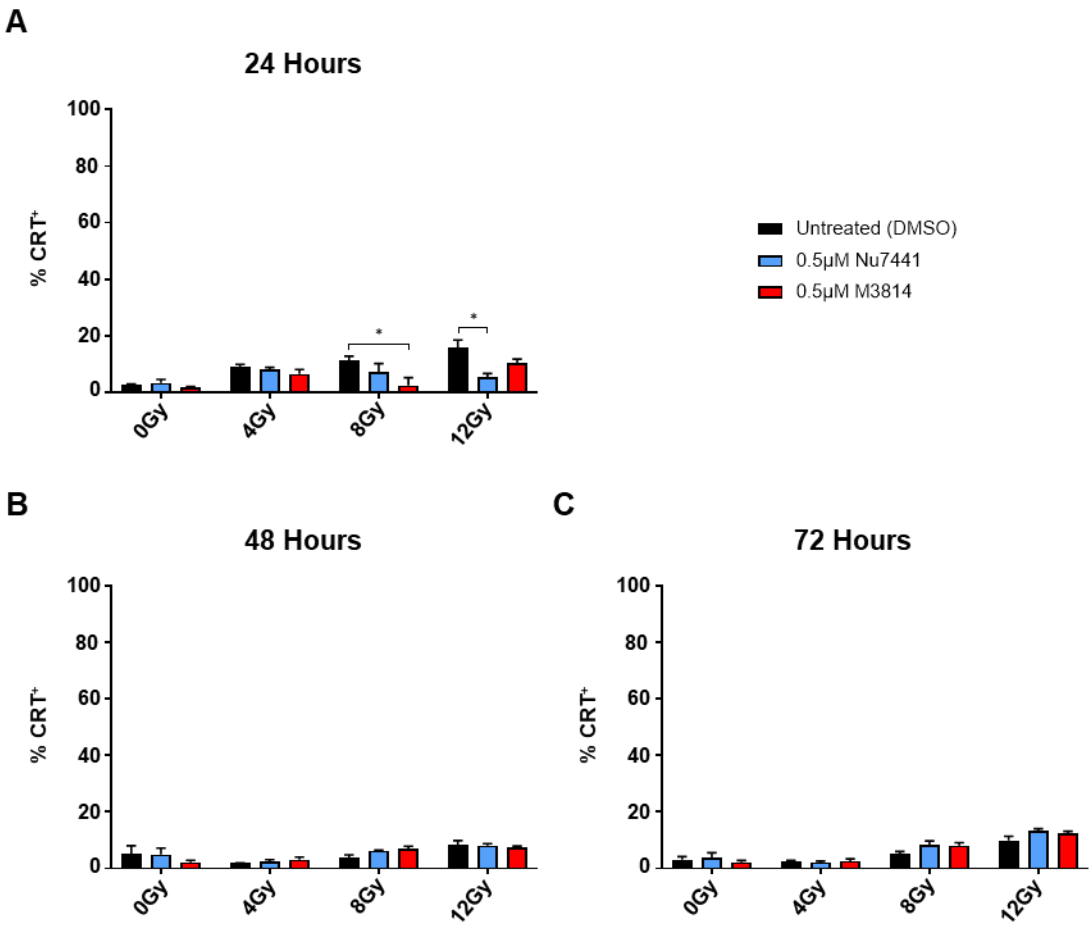

Figure 3. 18. The % of CRT+ CMT-167 cells is increased following treatment IR and DNA-PKi.

CMT-167 cells were treated with 0Gy, 4Gy, 8Gy or 12Gy X-ray, either alone or in combination with 0.5µM Nu7441 or 0.5µM M3814. Positive control for cell surface CRT was achieved by 24 hours treatment with 1µM Mitoxantrone. Cells were collected 24, 48 and 72 hours after treatment and analysed by flow cytometry. CRT^+ cells were gated on $DAPI^-$ cells. **(A)** % of CRT^+ CMT-167 cells at 24 hours **(B)** 48 hours and **(C)** 72 hours. Joint data of three independent experiments are presented as average±SEM and analysed by two-way ANOVA followed by Bonferroni's multiple comparison test: *p<0.05, **p<0.01, ***p<0.001 ****p<0.0001.

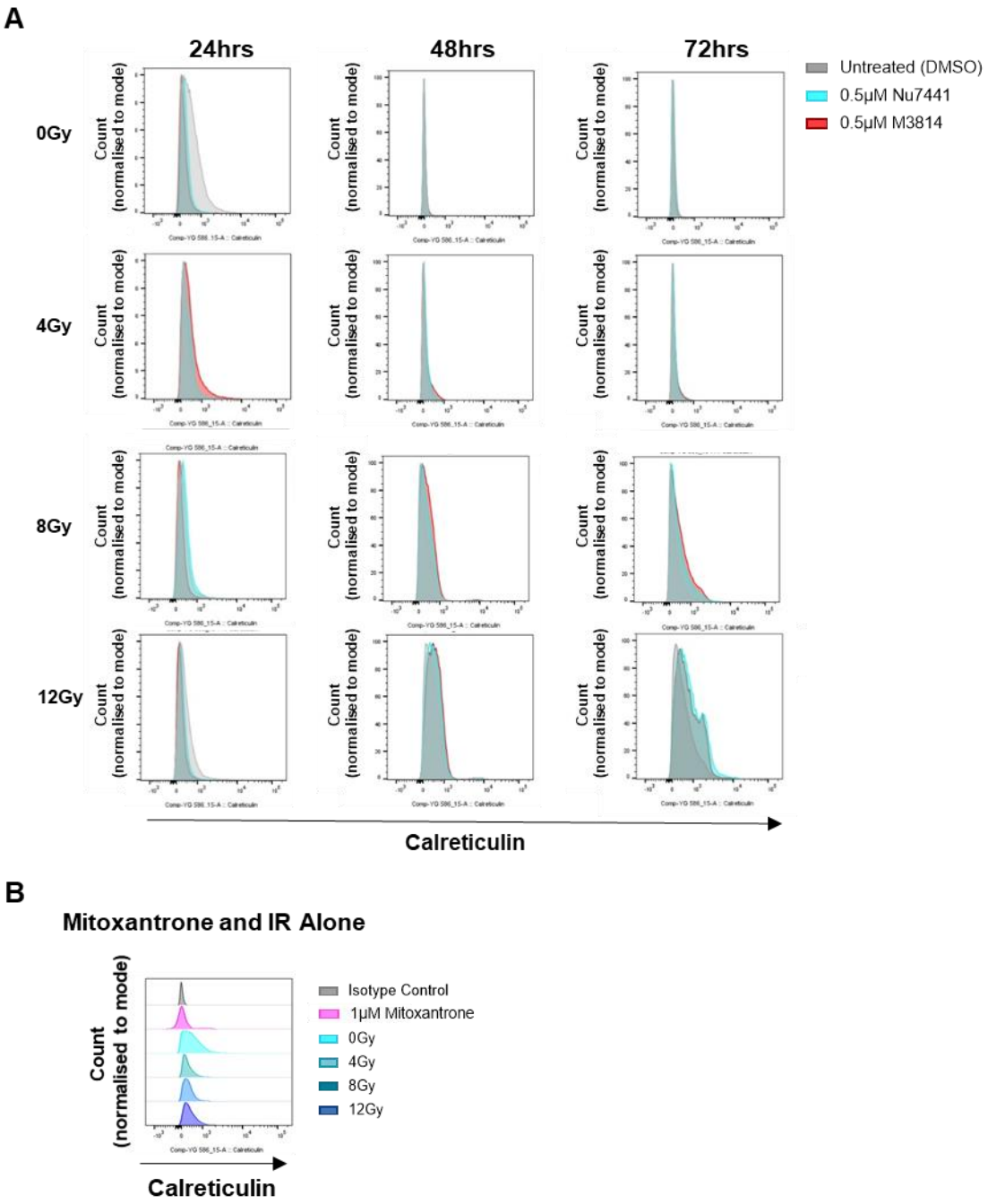

Figure 3. 19. Representative histograms of CRT+ CMT-167 cells following treatment with IR and DNA-PKi.

CMT-167 cells were treated with 0Gy, 4Gy, 8Gy or 12Gy X-ray, either alone or in combination with 0.5μM Nu7441 or 0.5μM M3814. Positive control for cell surface CRT expression was achieved by 24 hours treatment with 1μM Mitoxantrone. Cells were collected 24, 48 and 72 hours after treatment and analysed by flow cytometry. Representative histograms showing cell surface levels of CRT in $DAPI^-$ CMT-167 cells treated with **(A)** IR and DNA-PK inhibitors **(B)** IR alone and 1μM Mitoxantrone.

Having established that the combination of X-ray and M3814 significantly increased translocation of CRT to the cell surface membrane, another marker of ICD, the secretion of HMGB1 [88], was investigated in KP.B6.F1 cells. To do so, an ELISA assay was performed on the conditioned media of KP.B6.F1 cells 72 hours after treatment with 4Gy or 8Gy in combination with 0.5μM or 1μM Nu7441 or M3814. As seen in Figure 3.20, X-ray played a significant role in HMGB1 secretion (two-way ANOVA, p>0.0001). Cells treated with 8Gy alone released the most HMGB1 at 2.8ng/mL (±0.4), significantly greater than 4Gy alone at 1.8ng/mL (±0.4)(Bonferroni's, p=0.0061) and the 1.3ng/mL (±0.1) released by untreated KP.B6.F1 cells (Bonferroni's, p>0.0001). Unlike the CRT translocation, the addition of DNA-PKi had no significant effect on HMGB1 release (Figure 3.20).

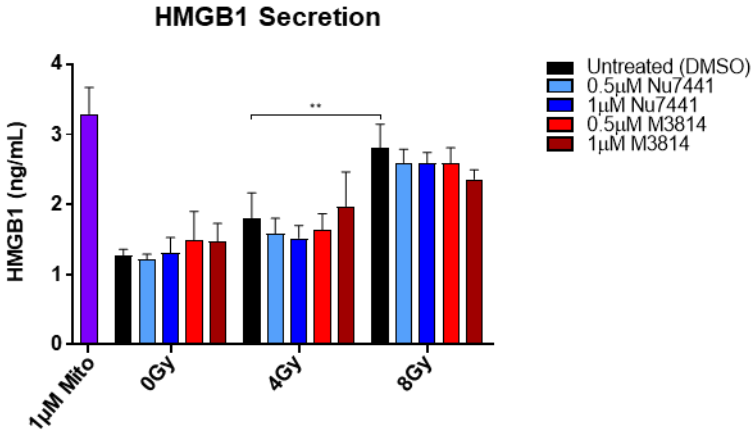

Figure 3. 20. IR increases HMGB1 secretion in KP.B6.F1 cells.

KP.B6.F1 were treated with 0Gy, 4Gy or 8Gy X-ray, either alone or in combination with 0.5μM or 1 μM Nu7441 or M3814. Conditioned media was collected 72 hours after treatment and an ELISA for HMGB1 performed. Joint data of three independent experiments are presented as average±SEM and analysed by two-way ANOVA followed by Bonferroni's multiple comparison test: *p<0.05, **p<0.01, ***p<0.001 ****p<0.0001.

3.4. Discussion

3.4.1. DNA-PK inhibition radiosensitises cancer cells and alters the DNA damage response

The radiosensitising effect of M3814 has previously been reported in a range of cancer models [67-69, 136, 156, 157] and is the subject of eight ongoing clinical trials (see Table 1.1). In this Chapter, the radiosensitising properties of DNA-PKi has been further corroborated. When used as a single agent, M3814 and Nu7441 had little effect on cell viability, but enhanced the loss of cell viability in combination with radiotherapy. M3814 consistently had a greater effect than Nu7441. The radiosensitising effect was more pronounced at a later timepoints, as demonstrated by clonogenic assay. Recently, it has been demonstrated that P53 status is an important factor in response to radiotherapy and DNA-PKi. Those cells either lacking P53 or with loss of function mutations continue to proliferate despite DSBs, resulting in the accumulation of damage until they undergo mitotic catastrophe [157]. However, at the shorter time point, 72 hours, there was no clear difference in response between those with wildtype P53, HCT-116 and CT26, in comparison to P53 mutant or null cell lines (CMT-167, KP.B6.F1, MC38 or LLC)(further information regarding cell line characteristics can be found in Table 1.2). Both cell lines used in the clonogenic experiment are P53-null, therefore, it would be interesting to determine whether long-term response is associated with P53 status.

In cancer cells, DDR to radiotherapy was also altered by the addition of DNA-PK inhibition. Treatment with X-ray increased the level of γH2AX 60 minutes after treatment, which could be abrogated upon addition of a DNA-PKi. In combination with 4Gy and 8Gy, both 0.5μM M3814 and 0.5μM Nu7441 restored γH2AX levels back to untreated levels. This indicates that 0.5μM of either DNA-PKi is sufficient to alter the cells response to damage. With the higher dose, 12Gy, Nu7441 did not abrogate the increase, while M3814 did. At this early timepoint, loss of γH2AX indicates that repair

has been inhibited [31, 138]. The finding that DNA-PK inhibition decreases γH2AX induced by radiotherapy agrees with the literature [30, 139]. Early γH2AX accumulation was used to determine NHEJ inhibition due to difficulties measuring phDNA-PK due to the lack of reliable antibodies for murine phDNA-PK (Ser2056). Using longer timeframes, the repair kinetics of DSBs can be determined by the quantification of γH2AX foci using immunofluorescence. In both cell lines [69, 157] and mouse models [68], the addition of M3814 to radiotherapy has been shown to increase the persistence of γH2AX foci over time indicating inhibition of DNA damage repair. The ability of DNA-PKi to alter the DDR was also apparent in regard to Golgi dynamics in response to radiotherapy. Treatment with 4Gy alone resulted in Golgi dispersal, and this was abrogated upon the addition of 0.5μM M3814 or Nu7441. This, too, is in accordance with the published literature [45, 140, 141] and indicates that 4Gy induces sufficient damage to trigger the DDR, while 0.5μM Nu7441 or M3814 was enough to inhibit this response. Higher X-ray doses were not used as the degree of damage to the cell made quantification of Golgi area compared to nuclear area unreliable, due to the accumulation of apoptotic cells with complete disruption of Golgi architecture [163]

3.4.2. Radiotherapy and DNA-PK inhibition induces immunogenic cell death.

The radiosensitising effect of DNA-PK inhibition has been extensively studied in the context of cancer-cell extrinsic mechanisms, however, much less is understood about how treated cells may interact with the surrounding TME. While we know that the addition of DNA-PKi to radiotherapy increases cell death, it is currently unknown whether the resulting death is accompanied by the release of DAMPs associated with ICD. This Chapter presents evidence that both X-ray alone induces ICD, and that addition of M3814 potentiates this effect. The levels for CRT translocation increased in an X-ray dose-dependent manner and accumulated over time, in line with

increasing frequency of apoptotic cells. This effect was drastically enhanced upon addition of M3814. At 72 hours, 57% of cells treated with 8Gy+0.5μM M3814 and 72% of those with 12Gy+0.5μM M3814 were CRT positive (Figure 3.16). Interestingly, KP.B6.F1 secretion of HMGB1 increased with X-ray dose, but addition of M3814 had no significant effect (Figure 3.20).

While this is not the first time that radiotherapy has been shown to induce ICD [91, 100, 164], it is the first time the addition of DNA-PK has been shown to increase CRT translocation. Cell-surface membrane expression of CRT binds CD91 expressed on APCs, DCs primarily but also macrophages, and triggers antigen processing and maturation [90-92, 162]. Similarly, HMGB1 enhances DC maturation and increase antigen presentation to T cells [96, 97]. These APCs can then prime and cross prime tumour specific $CD4^+$ and $CD8^+$ T cells respectively and mobilise an anti-tumour adaptive immune response. Of note, while both KP.B6.F1 and CMT-167 had a similar frequency of apoptotic cells following treatment, apoptosis in CMT-167 was not accompanied by CRT translocation. Mitoxantrone, a known inducer of ICD [98, 99] also failed to elicit CRT translocation, indicating that this response is not universal. Further work in a wider range of cell lines would help better understand the underlying cause for this discrepancy.

3.4.3. DNA-PKi and IR increases cell surface level of PD-L1.

Increased cell surface CRT and HMGB1 indicate that cancer cells treated with X-ray and M3814 may be capable of eliciting an immunostimulatory effect, however, the frequency of PD-$L1^+$ cells also increased following treatment. In both CMT-167 and KP.B6.F1 cells, the size of this population was greatest at 24 hours post 12Gy+0.5μM M3814 treatment . This increase appeared to be transient, falling back to a similar level of untreated by 48 hours. There is evidence that X-ray increases PD-L1 expression, and that this is enhanced by loss of NHEJ through Ku70/80 knockdown

[152]. Interestingly, the use of Nu7441 as a single agent has been shown to reduce PD-L1 expression in melanoma cancer cell lines [154]. It is important to note however, that while the proportion of PD-L1$^+$ KP.B6 increased, expression remained low in comparison to those treated with IFNγ. As such, it is difficult to determine how biologically relevant this increase may be.

3.5. Conclusions

The results presented in this Chapter support that the addition of DNA-PKi to radiotherapy is an attractive strategy to widen the therapeutic window of radiotherapy. All the cell lines investigated exhibited a decrease in cell viability with X-ray plus DNA-PKi. Of note, M3814 had a greater sensitizing effect than Nu7441, and was better tolerated. This work determined a suitable dosing regimen for use in further experiments. With 4Gy and 8Gy being high enough to trigger γH2AX formation and Golgi dispersal, without being too cytotoxic as single agents. Similarly, 0.5μM Nu7441 or M3814 were found to be enough to both alter the DDR and sensitise cells to radiotherapy. These findings lay the foundation for the rest of this Thesis.

The fate of these treated cells was cell death, identified as apoptosis, which was accompanied by HMGB1 release and translocation of CRT to the cell surface membrane. Both of which are DAMPs released during ICD which increase DC uptake of tumour antigen and subsequent presentation to T cells. However, treatment also increased the frequency of PD-L1$^+$ cells, which would have a more immunosuppressive effect. To better understand how these opposing effects may change tumour cell immunogenicity and in turn whether this may improve response to radiotherapy, in vivo experiments must be done. This aspect is explored in Chapter 5.

4. Radiotherapy and DNA-PK inhibition activates the cGAS-STING pathway

4.1. Introduction

While the direct effects of radiotherapy induced DNA damage is responsible for most of its efficacy, its ability to mobilise an anti-tumour immune response also plays an important part. There is, therefore, a need to improve our understanding and develop strategies to maximise the immune benefits of a radiotherapy. As discussed in the Chapter 3, in response to stress, cells can alter expression of immunomodulatory cell-surface markers or undergo ICD, increasing antigen presentation. Another way radiotherapy can stimulate the innate immune response is through nucleic acid sensing pathways which trigger the release of Type I IFNs [101, 102]. The cGAS-STING pathway is an innate immune anti-viral pathway which is initiated by cytosolic dsDNA and results in the secretion of IFN-β to potentiate an anti-viral response. Recently, radiotherapy has been shown to increase the levels of cytosolic double stranded DNA (dsDNA), providing a link between DNA damage and genomic instability with the mobilisation of an anti-tumour response. This makes the cGAS-STING pathway an attractive therapeutic target for cancer therapy. This Chapter investigates the effect of DNA-PK inhibition with radiotherapy on cGAS-STING pathway activity in cancer cells, and how this response can be optimised. Chapter 5 will focus on the potential immunogenicity of this combination in syngeneic mouse tumour models.

4.1.1. Cytosolic dsDNA triggers the cGAS-STING pathway

Whether the source is a viral infection or DNA damage, the cGAS-STING pathway is initiated by the binding of dsDNA to cGAS in the cytoplasm, promoting a conformational change. This enables cGAS mediated generation of cGAMP, which in turn binds to STING on the ER membrane, promoting STING dimerisation and

translocation to the Golgi apparatus where it phosphorylates TBK1. IRF3 is recruited to and phosphorylated by TBK1, promoting IRF3 nuclear translocation wherein it promotes the transcription of IFNβ and inflammatory cytokines [104-106]. Once secreted, IFNβ binds IFNAR1 on cells, activating JAK-STAT mediated transcriptional regulation of ISGs, which are associated with an anti-viral and inflammatory response [111, 113]. A diagram showing the cGAS-STING pathway can be found in Figure 4.1 and is described further in Section 1.2.5.

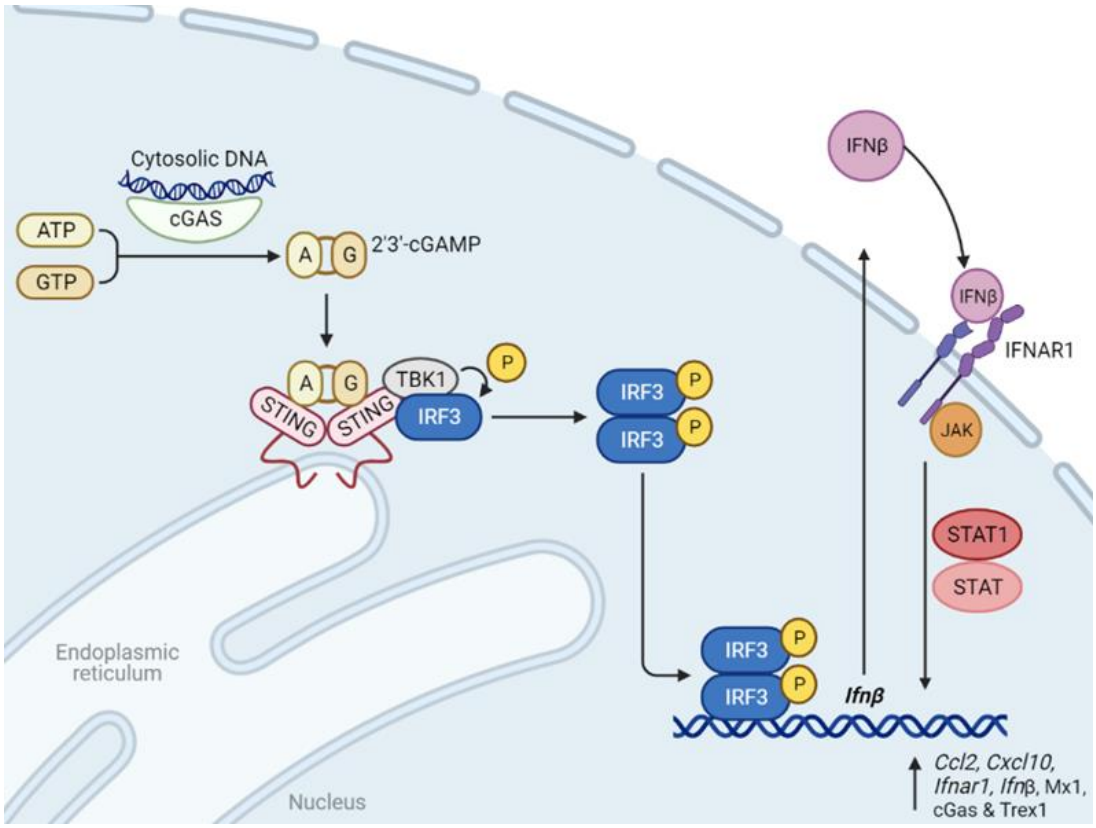

Figure 4.1. Illustration of cGAS-STING pathway and interferon stimulated gene expression.

The cGAS-STING pathway is triggered by the binding of cytosolic dsDNA to cGAS, which in turn catalyses the formation of cGAMP. cGAMP binds to STING on the endoplasmic reticulum resulting in TBK1 and then IRF3 phosphorylation. IRF3 homodimers enter the nucleus and promotes transcription of *Ifnβ*. Extracellular IFNβ binds to IFNAR1 and activates the JAK-STAT pathway which results in the transcription of interferon stimulated genes including *Ccl2, Cxcl10, Ifnar1, Ifnβ, Mx1, cGAS and Trex1.* Made in BioRender.

4.1.2. DNA damage provides a source of cytosolic dsDNA

The discovery that genotoxic stress also initiates the cGAS-STING pathway provides a clear link between the DNA damaging agents used in cancer therapy and the immune response. Following DNA damage, dsDNA becomes cytosolic by either leaking from the nucleus or in the form of micronuclei. During mitosis, damaged DNA can result in aberrant chromosomal segregation, forming small nuclear bodies which are distinct from the main nuclear body, these are micronuclei [118-120]. These nuclear bodies are unstable, and their degradation exposes dsDNA to cytosolic cGAS, triggering an IFNβ mediated inflammatory response [104-106] (further information can be found in Section 1.2.5.4).

While DNA damage is a trigger of the cGAS-STING pathway, the relationship between the degree of damage and pathway activity is not linear [83, 84, 101, 103, 131, 165]. A study by Demaria *et al* reported that while 30Gy and 3x8Gy regimens had similar efficacy in immunodeficient mice, in immunocompetent models, 3x8Gy improve primary tumour response, but could also elicit an abscopal effect [165]. This was because higher x-ray dose, 12Gy and above, increased expression of Trex1 which is an endonuclease that clears cytosolic dsDNA, preventing its binding to cGAS [83, 84, 131, 165]. Inhibition of HR due to ATM, BRCA1 or BRCA2 depletion and the use of PARPi have all been shown to increase cGAS-STING pathway activity [132-135]. The relationship between loss of NHEJ and cGAS-STING signalling however, is much less well defined. A recent study determined that treatment with radiotherapy and M3814 induced the formation of micronuclei and increase expression of genes associated with the cGAS-STING pathway [136]. More work is needed to better characterise and optimise this response.

4.1.3. Downregulation of the cGAS-STING pathway occurs in tumours

The link between genomic instability and increased innate immune response makes developing lesions more visible to immune system and therefore, loss of cGAS-STING pathway function in tumours cells is a means of immune evasion. Downregulation of cGAS-STING pathway activity is commonly observed in tumours. A study in human gastric cancer patients found 90.5% of patients to have lower levels of STING, which correlated with poorer prognosis [5]. STING is also downregulated in cancer cell lines of a wide variety of cancer types including prostate, lung, cervical and colorectal cancer [124, 130, 166]. In mouse studies, STING deficient tumours have lower levels of immune infiltration of tumours and fail to respond to immune checkpoint blockade [130]. The prevalence of cGAS-STING pathway downregulation limits the potential success of therapeutic approaches targeting this pathway. Consequently, the potential success of targeting the cGAS-STING pathway will benefit from stratification of patients to personalise treatment and strategies to restore cGAS-STING pathway functionality.

As discussed further in Section 1.2.5.5, there are multiple mechanisms regulating STING levels, including proteasomal degradation [167, 168], autophagy [169] and hypermethylation [6]. Of particular interest is hypermethylation as recent reports have indicated that the hypomethylating agent decitabine can restore cGAS-STING signalling in cancer and increase sensitivity to immunotherapy [129, 130]. Decitabine is currently approved by the FDA and EU for use in patients with AML [126-128]. More detail regarding decitabine can be found in section 1.2.5.6.

4.2. Research Aims

The aim of this Chapter is to determine the effect of DNA-PK inhibition and radiotherapy on cGAS-STING pathway activity in cancer. To do so, cGAS-STING pathway activity will be measured by quantifying cGAS positive micronuclei, gene expression of ISGs and secretion of IFNβ. Using KP.B6.F1 as an example of a STING deficient cancer, this Chapter will develop a therapeutic strategy to restore STING and thus, restore cGAS-STING pathway activity.

4.3. Results

4.3.1. Radiotherapy in mice increases expression of genes involved in the cGAS-STING pathway.

Following the findings by the Demaria lab in 2017 that 3 fractions of 8Gy RT (3x8Gy) elicited a favourable anti-tumour immune response due to activation of the cGAS-STING pathway[83], this regimen was investigated in the non-immunogenic NSCLC model, KP.B6.F1. KP.B6.F1 cells were injected intravenously to form orthotopic tumours in the lungs. Ten days later, mice were irradiated with 1x8Gy. This radiotherapy was performed using the Small Animal Research Platform (SARRP), using a CT scan of each mouse for accurate dose planning, and targeting. The platform enabled targeting of just the right lung, leaving the left lobes untouched, to investigate any abscopal effects. Mice were assigned to receive either 1x8Gy or 3x8Gy, with one day between each dose. The lungs and TDLNs were collected either 72 hours or one week after last dose of radiotherapy. In this tumour model, multiple tumour foci are formed in the lungs, rather than a single dissectible mass, therefore, the entire lungs and tumour draining lymph nodes (TDLNs) were harvested and processed into single cell suspension from which mRNA was extracted and analysed by qRT-PCR the gene expression of C*cl2, Cxcl10, Isg20, Mx1, Ifnβ, Ifnαr1, cGas* and *Trex1.* This experimental plan is shown in Figure 4.2.

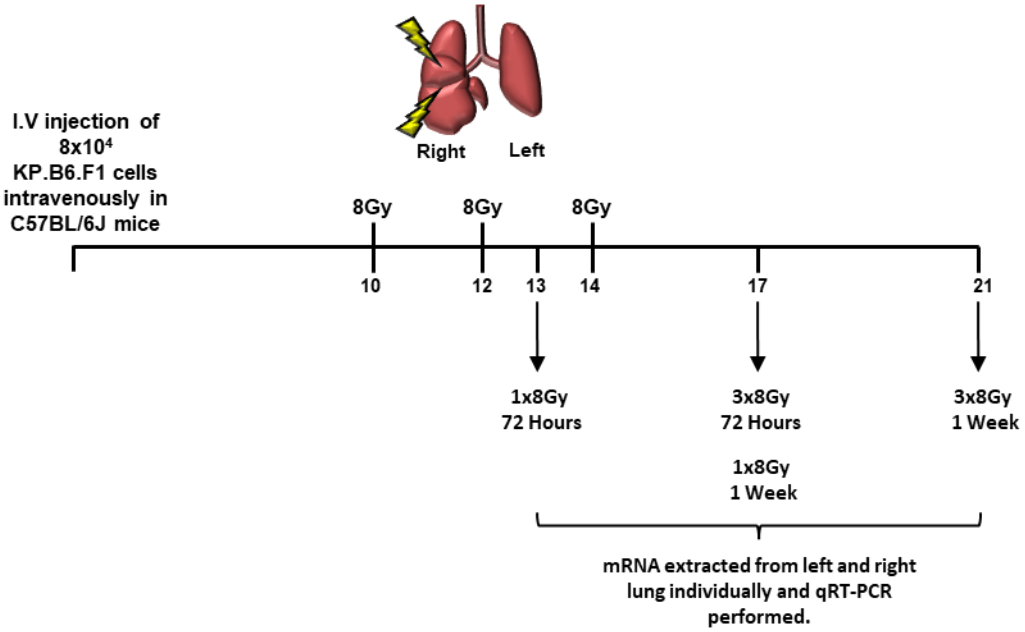

Figure 4. 2. Experimental plan for in vivo KP.B6.F1 radiotherapy experiment.

Illustration showing the experimental plan to compare the effects of 1x8Gy or 3x8Gy in KP.B6.F1 lung cancer mouse model.

Compared to untreated mice, there was a significant increase in *Ccl2 e*xpression in both the irradiated (7.5-fold)(Bonferroni's, p=0.0005) and non-irradiated lungs (5.9-fold)(Bonferroni's, p=0.0089) one week after treatment with 3x8Gy (Figure 4.3 A). The irradiated lung had significantly higher levels of *Ccl2* than those one week after treatment with 1x8Gy (Bonferroni's, p=0.0053), and 72 hours after 3x8Gy (Bonferroni's, p=0.0488). There was no significant difference between irradiated and non-irradiated lungs one week after 3x8Gy (Figure 4.3 A).

Interestingly, this effect was not observed in the expression of another chemokine, *Cxcl10* (Figure 4.3 B). Instead, there was a 2.9-fold increase in *Cxcl10* expression in irradiated lungs 72 hours following 1x8Gy treatment compared to untreated mice (Bonferroni's, p= 0.0023). This increase in *Cxcl10* expression was significantly greater than irradiated lungs of mice receiving 3x8Gy at both 72 hours (Bonferroni's, p=0.0207) and one week (Bonferroni's, p=0.0005)(Figure 4.3 B).

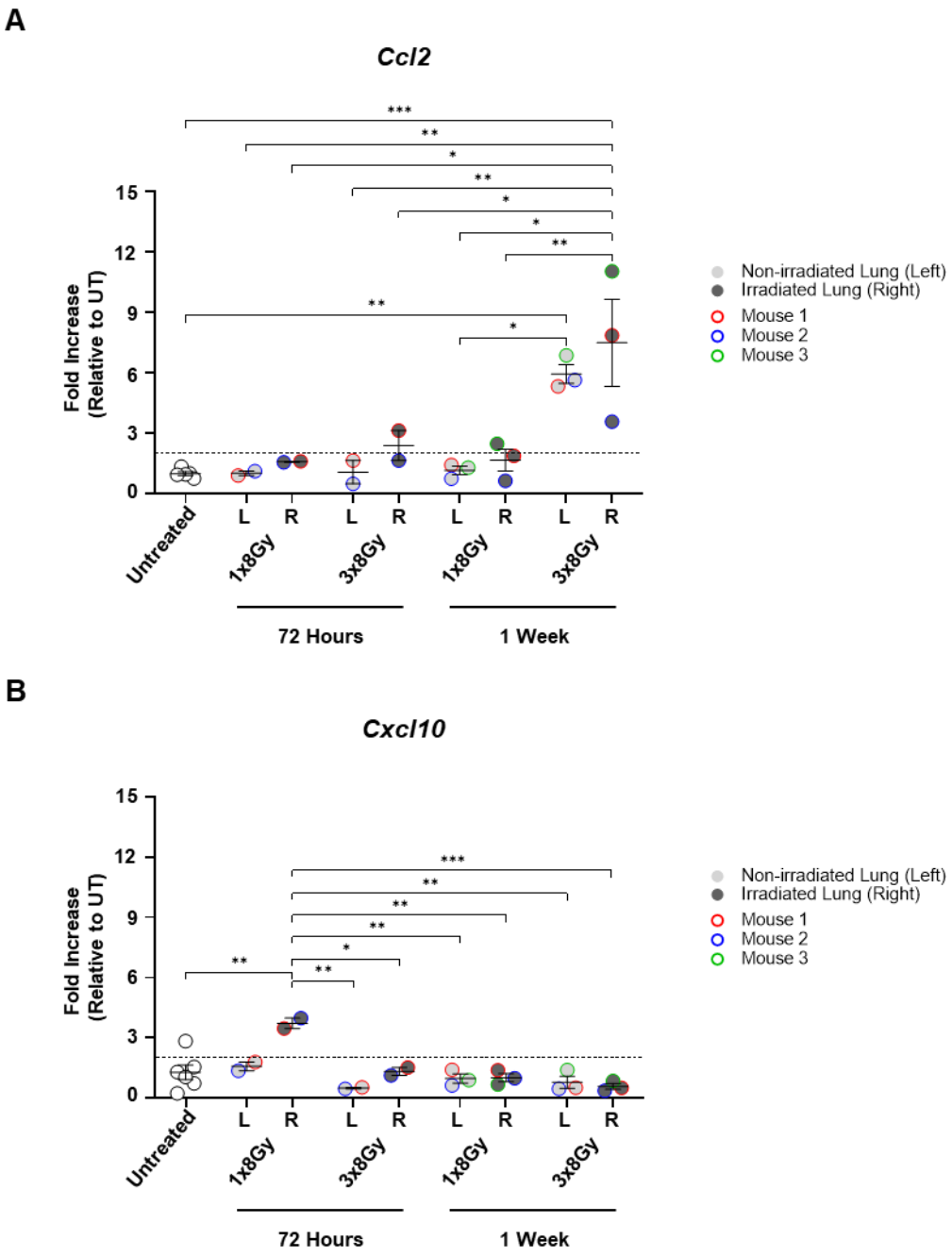

Figure 4. 3. Radiotherapy alters the expression of Ccl2 and Cxcl10 genes.

KP.B6.F1 lung cancer model were giving 1x8Gy or 3x8Gy using CT-guided radiotherapy to target only the right lung. Lung tissue was collected 72 hours or 1 week after last radiotherapy dose, mRNA extracted, and qRT-PCR performed to determine gene expression of *Ccl2* and *Cxcl10*. Data is shown for both lung and each individual mouse. Data from one independent experiment with 3 mice per group, except at 72 hours due to poor mRNA quality. Dashed line indicates a 2-fold increase. Average of all conditions analysed by one-way ANOVA followed by Bonferroni's multiple comparison test. Comparisons between left and right lung of same treatment conditions performed using two-way paired T test; *p<0.05, **p<0.01, ***p<0.001 ****p<0.0001.

Next, *Ifnβ* expression was investigated. IFNβ is an important product of the cGAS-STING pathway activity and plays vital role in recruitment and maturation of the innate immune arm [103]. Gene expression of *Ifnβ* was 6.8-fold higher in irradiated lungs 72 hours following treatment with 1x8Gy compared to untreated (Bonferroni's, p=0.0012)(Figure 4.4 A). There was no significant difference between the irradiated and non-irradiated lungs 72 hours post 1x8Gy. Gene expression of *Ifnαr1*, the receptor for *Ifnβ,* remained unchanged throughout treatment (Figure 4.4 B).

Additionally, the interferon stimulated genes (ISGs) were evaluated. Following successful binding of IFNβ to IFNAR1, these genes are upregulated [170]. The expression of two ISGs, *Isg20* and *Mx1,* were measured to determine cGAS-STING pathway activity (Figure 4.5 A&B). There was no change in the expression of *Isg20* in response to irradiation (Figure 4.5 A). There was, however, a significant 2.9-fold increase of *Mx1* gene expression in irradiated lungs 72 hours after 1x8Gy compared to untreated (Bonferroni's, p=0.0346)(Figure 4.5 B).

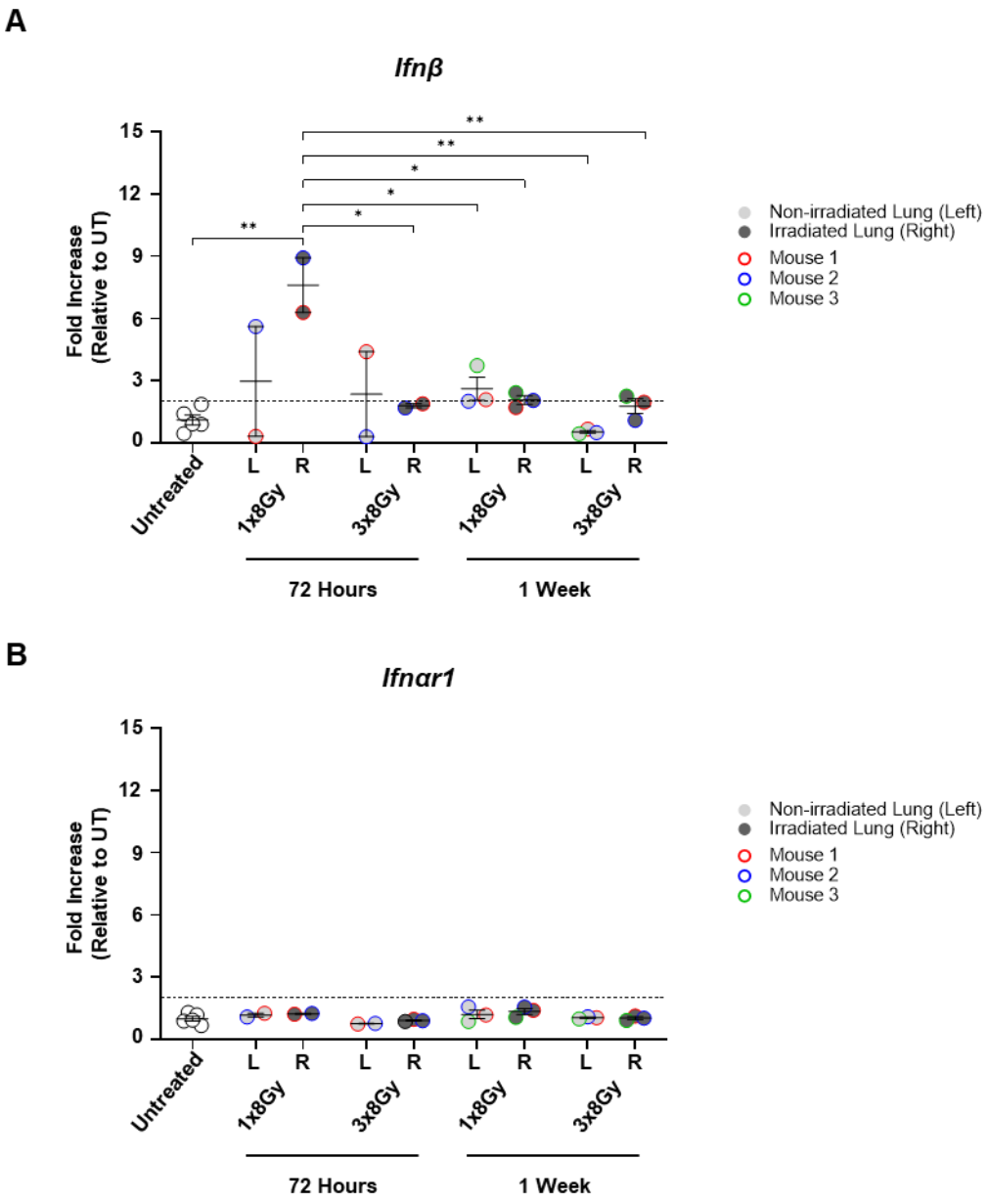

Figure 4. 4. Expression of Ifnβ increases 72 hours following 1x8Gy radiotherapy.

KP.B6.F1 lung cancer model were giving 1x8Gy or 3x8Gy using CT-guided radiotherapy to target only the right lung. Lung tissue was collected 72 hours or 1 week after last radiotherapy dose, mRNA extracted, and qRT-PCR performed to determine gene expression of *Ifnβ* and *Ifnar1*. Data is shown for both lung and each individual mouse. Data from one independent experiment with 3 mice per group, except at 72 hours due to poor mRNA quality. Dashed line indicates a 2-fold increase. Average of all conditions analysed by one-way ANOVA followed by Bonferroni's multiple comparison test. Comparisons between left and right lung of same treatment conditions performed using two-way paired T test; *p<0.05, **p<0.01, ***p<0.001 ****p<0.0001.

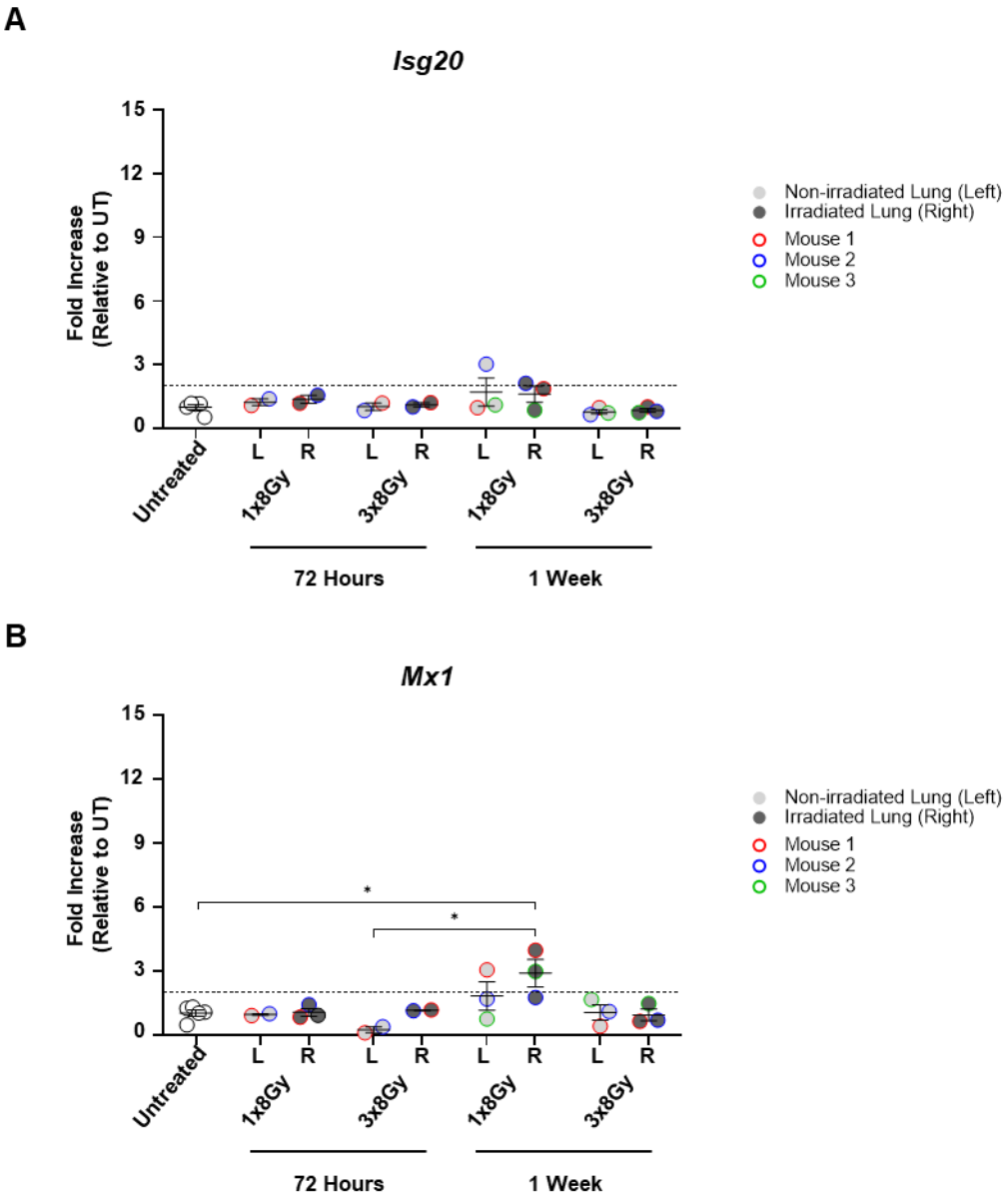

Figure 4. 5. Expression of Mx1 increases 1 week post 1x8Gy radiotherapy.

KP.B6.F1 lung cancer model were giving 1x8Gy or 3x8Gy using CT-guided radiotherapy to target only the right lung. Lung tissue was collected 72 hours or 1 week after last radiotherapy dose, mRNA extracted, and qRT-PCR performed to determine gene expression of *Isg20* and *Mx1*. Data is shown for both lung and each individual mouse. Data from one independent experiment with 3 mice per group, except at 72 hours due to poor mRNA quality. Dashed line indicates a 2-fold increase. Average of all conditions analysed by one-way ANOVA followed by Bonferroni's multiple comparison test. Comparisons between left and right lung of same treatment conditions performed using two-way paired T test; *p<0.05, **p<0.01, ***p<0.001 ****p<0.0001.

Gene expression of two important regulators of the cGAS-STING pathway were looked at (Figure 4.6 A&B). These were cGAS and the endonuclease Trex1, a negative regulator of the cGAS-STING pathway [83, 131]. One week following 3x8Gy treatment, there was a 2.9-fold increase in *cGas* expression – interestingly this occurred in the non-irradiated lung (Bonferroni's, p=0.0411). This elevated level of *cGas* gene expression in the non-irradiated lung was significantly greater than the irradiated lung of the same mouse (pair T-test, p=0.0495)(Figure 4.6 A).

In lungs receiving 1x8Gy, one week post treatment there was a 1.9-fold increase in *Trex1* gene expression compared to untreated (Bonferroni's, p=0.0295)(Figure 4.6 B). This was also a 2.1-fold increase compared to irradiated lungs receiving the higher dose, 3x8Gy, at the same timepoint (Bonferroni's, p=0.0344)(Figure 4.6 B).

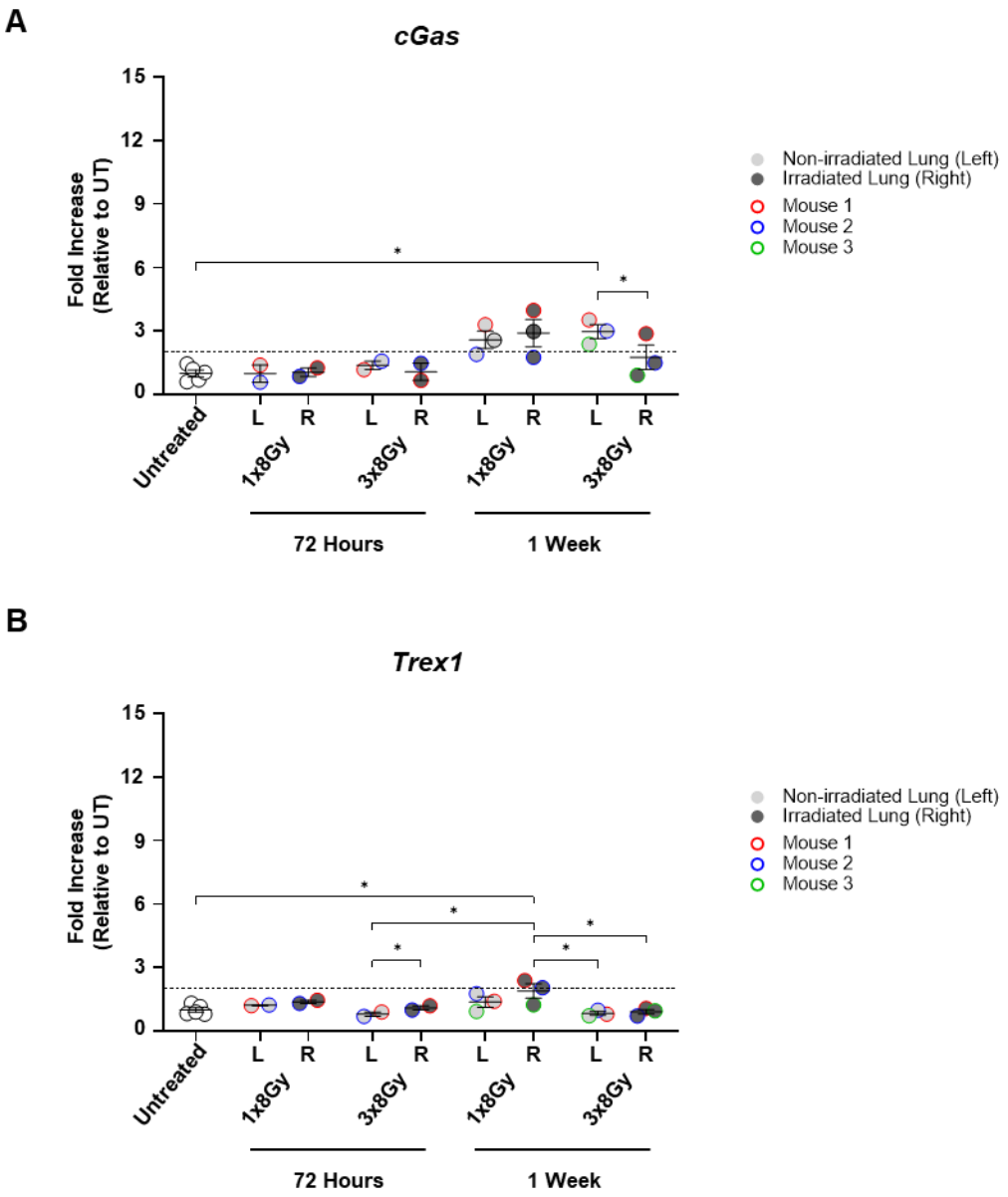

Figure 4. 6. Radiotherapy alters the expression of cGas and Trex1 genes.

KP.B6.F1 lung cancer model were giving 1x8Gy or 3x8Gy using CT-guided radiotherapy to target only the right lung. Lung tissue was collected 72 hours or 1 week after last radiotherapy dose, mRNA extracted, and qRT-PCR performed to determine gene expression of *cGas* and *Trex1*. Data is shown for both lung and each individual mouse. Data from one independent experiment with 3 mice per group, except at 72 hours due to poor mRNA quality. Dashed line indicates a 2-fold increase. Average of all conditions analysed by one-way ANOVA followed by Bonferroni's multiple comparison test. Comparisons between left and right lung of same treatment conditions performed using two-way paired T test; *p<0.05, **p<0.01, ***p<0.001 ****p<0.0001.

4.3.2. Treatment with M3814 and X-ray increases the formation of cGAS positive micronuclei in KP.B6.F1 cells.

The *in vivo* qRT-PCR experiment indicates there may be activation of the cGAS-STING pathway based on increased gene expression of *Ifnβ*, *Mx1, Ccl2* and *Cxcl10*. Previous work has shown that DNA damage in tumour cells can activate this pathway [101-103]. Due to the complexity of the tumour microenvironment, i*n vitro* assays were performed to better understand whether DNA damage induced by X-ray and DNA-PK inhibition may activate the cGAS-STING pathway. Aberrant mitosis due to DNA damage increases the formation of small nuclear bodies which are independent of the main nuclear body, these are micronuclei [15, 121]. These small, micronuclear bodies are unstable and as they begin to degrade, dsDNA is exposed to the cytoplasm and bind cGAS and activate the cGAS-STING pathway [118-120, 171]. To quantify micronuclei, an immunofluorescence was performed on KP.B6.F1 cells treated with 4Gy in combination with 0.5μM Nu7441 or 0.5μM M3814 for 24 hours. These cells were fixed and stained with phalloidin, to allow discrimination between different cells, Hoechst and cGAS. Using confocal microscopy, the number of micronuclei (MN) and whether they were cGAS positive or negative was quantified for each cell. In this experiment, only 4Gy was used as 8Gy alone induces excessive damage that the nuclear bodies cannot reliably be assessed. A micronucleus was defined as a nuclear body smaller than a third of the main nuclear body, and fully separate from the main nuclear body. An example of both a positive and negative micronucleus is shown in Figure 4.6 A.

The percentage of cells with at least one micronucleus was significantly influenced by X-ray treatment (two-way ANOVA, $p<0.0001$) and by the addition of DNA-PK inhibition (two-way ANOVA, $p=0.0495$)(Figure 4.7 B). There was also significant synergy between X-ray and DNA-PKi (two-way ANOVA, $p=0.0049$). Just 7.6% (±6.2) of untreated cells had one or more micronuclei which rose to 42.9% (±9.3) with 4Gy

alone (Bonferroni's, $p<0.0001$). Addition of M3814 to X-ray alone increased the percentage of MN positive cells by 17.6% (Bonferroni's, $p=0.0057$)(Figure 4.7 B).

The average number of micronuclei per micronucleated cell also significantly changed between treatment groups (Figure 4.7 C). Combination of DNA-PKi and X-ray was synergistic (two-way ANOVA, $p=0.0178$). Following treatment with 4Gy there were 1.7 (±0.2) MN per MN^+ cells which significantly increased to 2.2 (±0.1) with 4Gy+0.5μM M3814 (Bonferroni's, $p<0.018$)(Figure 4.7 C).

While the frequency of MN changed with treatment, so too did the frequency of $cGAS^+$ MN (Figure 4.7 D). Treatment with DNA-PKi and X-ray was synergistic (two-way ANOVA, $p=0.0376$). In 4Gy treated cells, 5% had a $cGAS^+$ MN. This rose significantly to 12.0% (±2.5) following 4Gy+0.5μM M3814 treatment (Bonferroni's, $p=0.0028$)(Figure 4.7 D). Representative images are shown in Figure 4.7 E. Together, these experiments determined that radiotherapy increased the formation of micronuclei and this was further increased with M3814. Considering evidence that the frequency of $cGAS^+$ increase, it was determined that treatment had the potential to trigger the cGAS-STING pathway.

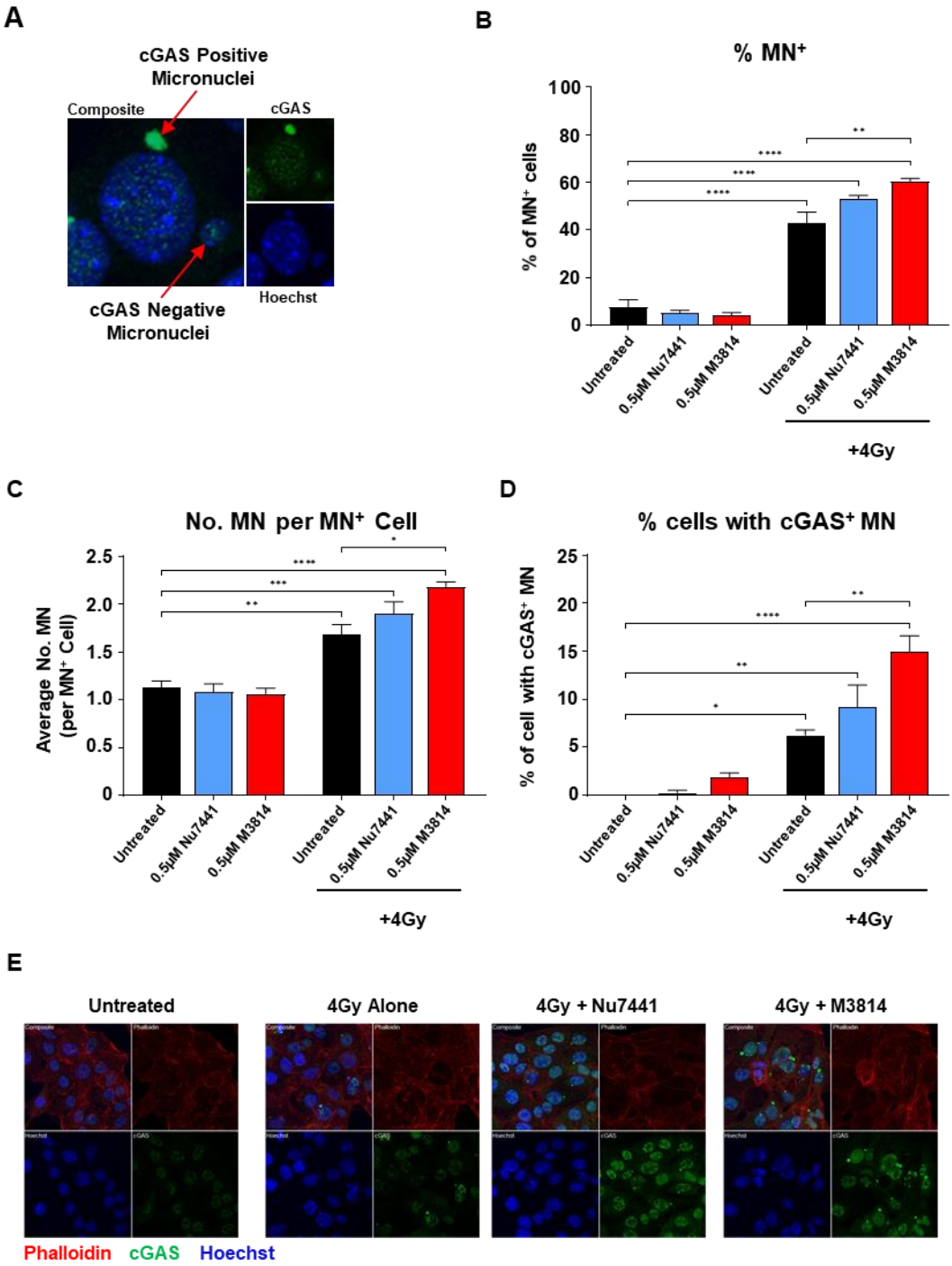

Figure 4. 7. Treatment with IR+DNA-PKi increases the frequency of micronuclei and cGAS+ micronuclei.

KP.B6.F1 cells were treated with 0.5μM Nu7441 or 0.5μM M3814 and one hour later 4Gy IR. Twenty-four hours later cells were fixed and stained using phalloidin, Hoechst and cGAS. Using confocal microscopy, images were obtained and the number of MN and cGAS$^+$ MN counted per cell. **(A)** Example of a cGAS$^+$ and cGAS$^-$ MN. **(B)** % of cells with ≥1 MN. **(C)** Average number of MN per MN$^+$ cell. **(D)** % of cells with ≥1 cGAS$^+$ MN. **(E)** Representative images. Data from three independent experiments presented as average±SEM and analysed by two-way ANOVA followed by Bonferroni's multiple comparison test: *p<0.05, **p<0.01, ***p<0.001 ****p<0.0001.

4.3.3. There is no increase in downstream cGAS-STING pathway activity.

The presence of cGAS$^+$ MN provides stimuli for cGAS-STING pathway activation. Therefore, evidence for downstream pathway activity was measured. To do so, qRT-PCR was performed to determine the gene expression of *Ifnβ, Ifnαr1* and *Sting* in KP.B6.F1 cells 24- and 48-hours following treatment with 4Gy, 8Gy or 12Gy. There was no change in the expression of any of these genes at either 24 or 48 hours (Figure 4.8 A&B). This experiment was repeated in CMT-167 cells (Figure 4.8 C&D). There was no significant change in the expression of *Ifnβ* or *Ifnαr1* at either 24 or 48 hours. The expression of *Sting*, however, was significantly influenced by X-ray treatment at both 24 hours (one-way ANOVA, p=0.0034) and 48 hours (one-way ANOVA, p=0.002). At 24 hours, 12Gy resulted in a 1.9-fold increase relative to untreated cells (Bonferroni's, p=0.0036). At 48 hours, there was a significant 1.6-fold increase with 8Gy treatment (Bonferroni's, p=0.0336) and a 1.9-fold increase with 12Gy (Bonferroni's, p=0.0172)(Figure 4.8 C&D). While these are statistically significant, these increases are small and the lack of changes to the other two genes, does not allow us to definitively confirm downstream activity of the cGAS-STING pathway.

Figure 4. 8. Radiotherapy increases Ifnβ, Ifnαr1 and Sting expression in CMT-167 but not KP.B6.F1 cells.

Next page. CMT-167 and KP.B6.F1 cells were treated with 4Gy, 8Gy or 12Gy IR. mRNA was collected 24 and 48 hours later and qRT-PCR performed to determine gene expression of *Ifnβ, Ifnαr1* and *Sting.* **(A)** 24 hours post X-ray in KP.B6.F1 cells. **(B)** 48 hours post X-ray in KP.B6.F1 cells. **(C)** 24 hours post X-ray in CMT-167 cells. **(D) 48** hours post X-ray in CMT-167 cells. Data from three independent experiments. Dashed line indicates a 2-fold increase. Average of all conditions analysed by one-way ANOVA followed by Bonferroni's multiple comparison test: *p<0.05, **p<0.01, ***p<0.001 ****p<0.0001.

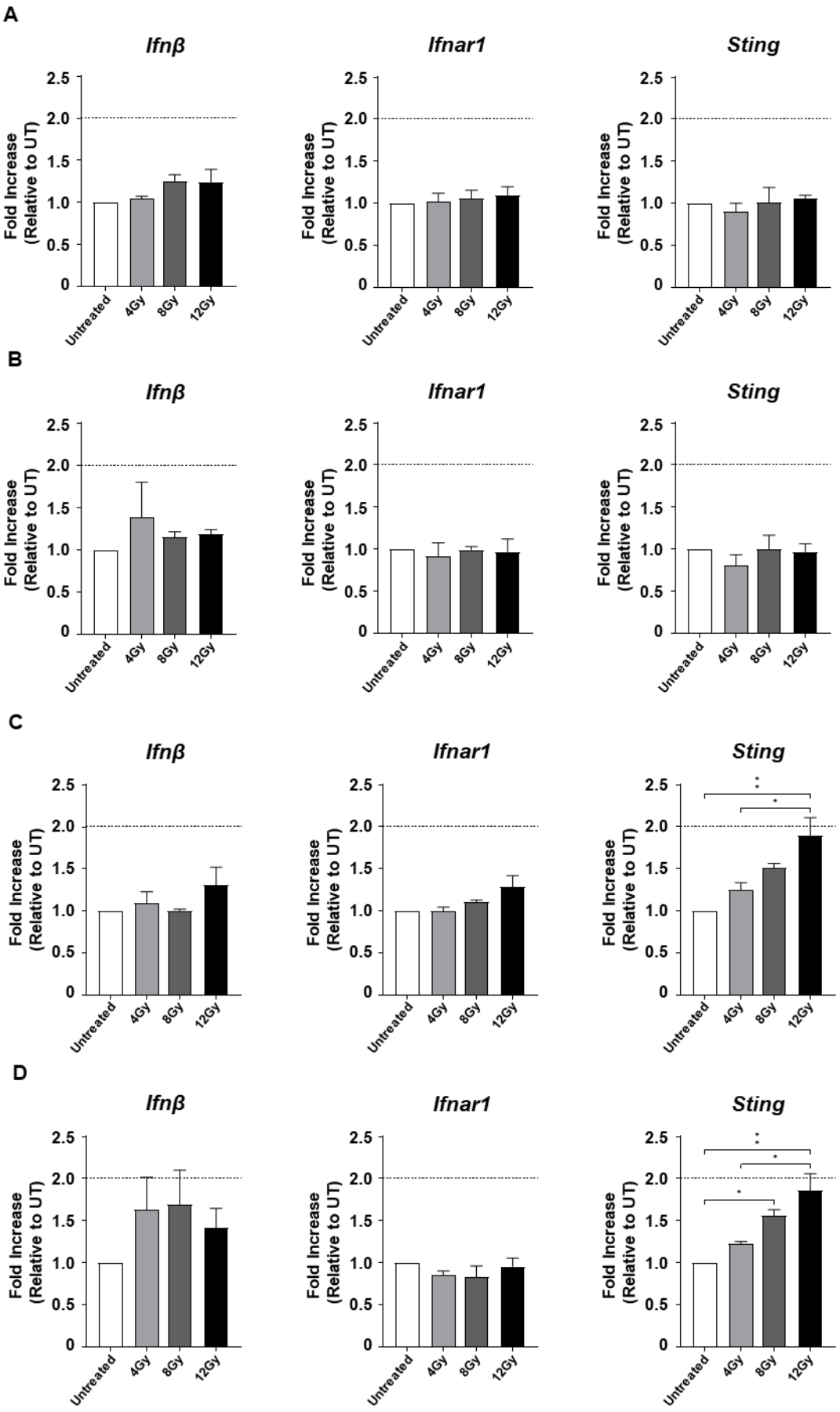
A
Ifnβ
Ifnar1
Sting
B
Ifnβ
Ifnar1
Sting
C
Ifnβ
Ifnar1
Sting
D
Ifnβ
Ifnar1
Sting
Fold Increase (Relative to UT)
0
0.5
1.0
1.5
2.0
2.5
Untreated
4Gy
8Gy
12Gy

4.3.4. Characterisation of cGAS-STING pathway in bone-marrow derived macrophages and murine cancer cell lines.

The disconnect between initiation of the cGAS-STING pathway, demonstrated by increased frequency of MN and $cGAS^+$ MN, and lack of evidence of downstream pathway activity as measured by qRT-PCR, required more investigation. To evaluate the cGAS-STING pathway transduction in cancer cells, cGAS-STING pathway activity in response to well-known stimulators of the pathway was analysed in bone-marrow derived macrophages (BMDMs) and a variety of murine cancer cells lines including B16, CMT-167, CT26, KP.B6.F1, LLC and MC38. These cells were transfected with cGAMP, interferon stimulatory DNA (ISD) or Polyinosinic:polycytidylic acid (Poly(I:C)). cGAMP directly activates the cGAS-STING pathway [172] and ISD provides cytosolic dsDNA to initiate the pathway [173]. Poly(I:C) is a synthetic dsRNA analogue which when detected in the cytoplasm by retinoic acid inducible gene 1 (RIG-1) or melanoma-differentiation-associated gene 5 (MAD5) results in upregulation of IFNβ [174, 175]. 24 hours after treatment, conditioned media was collected and IFNβ concentration measured using an ELISA. The resulting concentrations are shown for each cell line in Figure 4.9. There was a high degree of variation of response between the different cell lines. Importantly, none of the treatments elicited the release of IFNβ in KP.B6.F1 cells (Figure 4.9 D), and little in CMT-167 cells (Figure 4.9 B). Although there was a small amount of IFNβ secreted by CMT-167 cells in response to Poly(I:C) treatment which, although significantly greater than untreated, amounted to just 0.14pg/mL (±0.06)(Bonferroni's, $p=0.0018$). Of the six cell lines tested, CT26 and MC38 were the most responsive. The concentration of IFNβ in the conditioned media of CT26 cells increased in response to treatment with cGAMP, ISD and Poly(I:C), although only Poly(I:C) elicited a statistically significant increase relative to control of 1807pg/mL (±147.8)(Bonferroni's, $p<0.0001$)(Figure 4.9 C). Following treatment with ISD, MC38 released IFNβ to a concentration of 15.9pg/mL (±4.4), with cGAMP this was 7.6pg/mL

(±1.4) and Poly(I:C) this was 232.1pg/mL (±29.1), although only Poly(I:C) was statistically different to untreated cells (Bonferroni's, $p<0.0001$)(Figure 4.9 F). Based on this, KP.B6.F1 was classified as a cGAS-STING deficient cancer cell line and would therefore be unable to produce IFNβ despite evidence of $cGAS^{+}$ micronuclei as demonstrated in Figure 4.7.

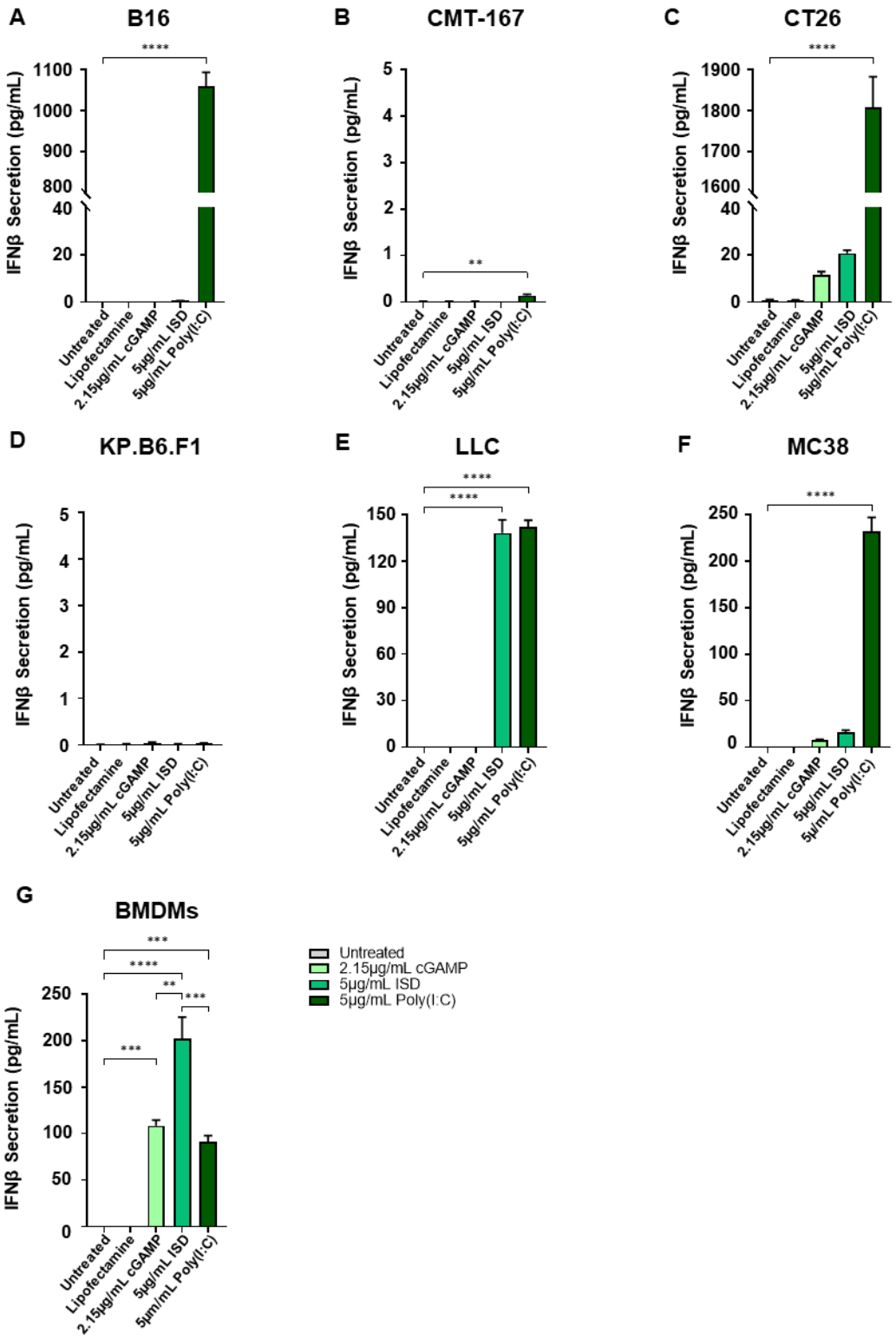

Figure 4. 9. There is variability of IFNβ release between different cancer cell lines following cGAS-STING pathway stimulation.

Cells were transfected with 2.15µg/mL cGAMP, 5µg/mL ISD or 5µg/mL Poly(I:C) for 24 hours. At which point conditioned media was collected and an ELISA performed to quantify IFNβ release. **(A)** B16 **(B)** CMT-167 **(C)** CT26 **(D)** KP.B6.F1 **(E)** LLC **(F)** MC38 **(G)** BMDMs. Data from three independent experiments presented as average±SEM and analysed by one-way ANOVA followed by Bonferroni's multiple comparison test: *p<0.05, **p<0.01, ***p<0.001 ****p<0.0001.

Developing mechanisms of immune evasion is a key turning point in tumorigenesis. Better understanding of how this may occur, with the aim of restoring visibility of cancer cells to the immune system is of interest. To better understand what may underpin the variation of cGAS-STING pathway activity between cancer cell lines, immunoblots were performed to quantify key components of the pathway (Figure 4.10)[176]. The proteins investigated were cGAS, STING, IRF3 and TBK1. First, the levels of cGAS and STING varied between cell lines. In LLC cells, cGAS was not detected, while KP.B6.F1 cells were STING deficient (Figure 4.10 A). There was also variation in the levels of IRF3 and TBK1 between the cell lines, although none were completely lacking (Figure 4.10 B&C).

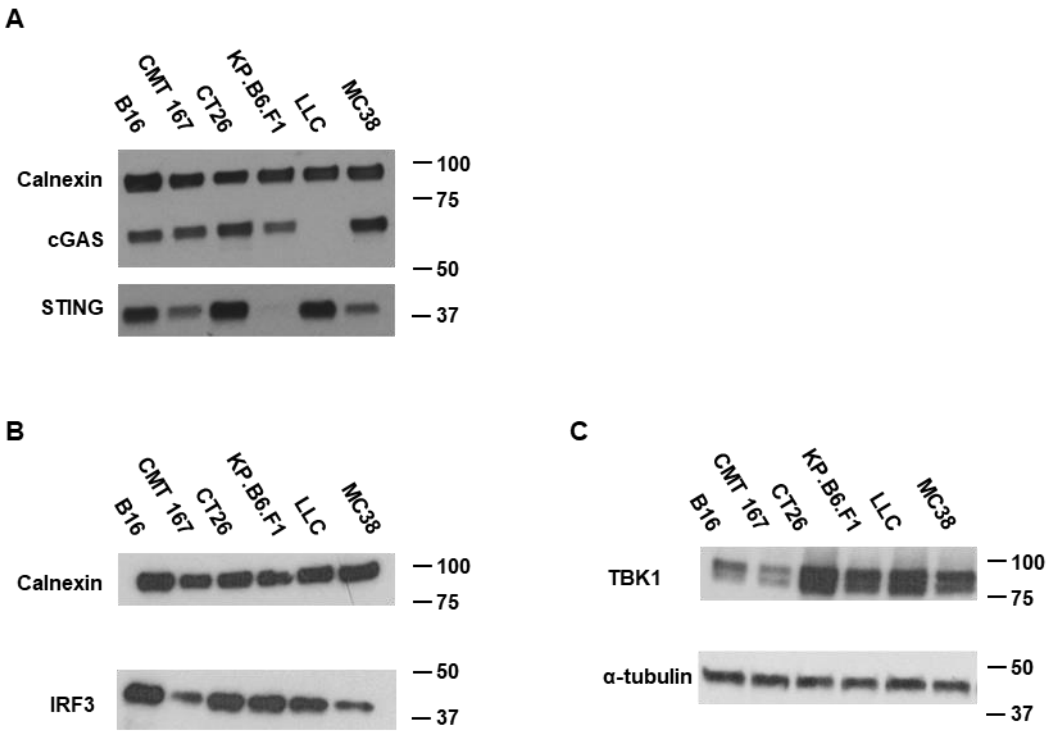

Figure 4. 10. KP.B6.F1 cells are STING deficient.

Immunoblot performed on murine cancer cell lines staining for **(A)** cGAS, STING and calnexin (loading control)(**B)** IRF-3 and calnexin (loading control)(**C)** TBK1 and α-tubulin (loading control). Blots are representative images of 3 biological repeats

4.3.5. Decitabine treatment restores STING and cGAS-STING pathway activity in KP.B6.F1 cells.

The lack of STING in KP.B6.F1 cells may explain its lack of IFNβ release despite treatment with cGAS-STING agonist. There is evidence for STING degradation by autophagy and the ubiquitin-proteasome pathway, or through reduced transcription due to promotor hypermethylation [129, 130, 177]. Therefore, experiments were conducted to determine whether inhibition of these mechanisms may restore STING levels in KP.B6.F1 cells. Bafilomycin, an autophagy inhibitor, and MG132, a proteasome inhibitor, had no effect on STING protein levels in a range of different concentrations and incubations times (Figure 4.11 A&B). The hypomethylating agent decitabine (DAC), however, restored STING levels in KP.B6.F1 (Figure 4.11 C&D). The greatest STING increase occurred with incubation of 100nM decitabine for 10 days and therefore, this treatment was chosen for further studies (Figure 4.11 D).

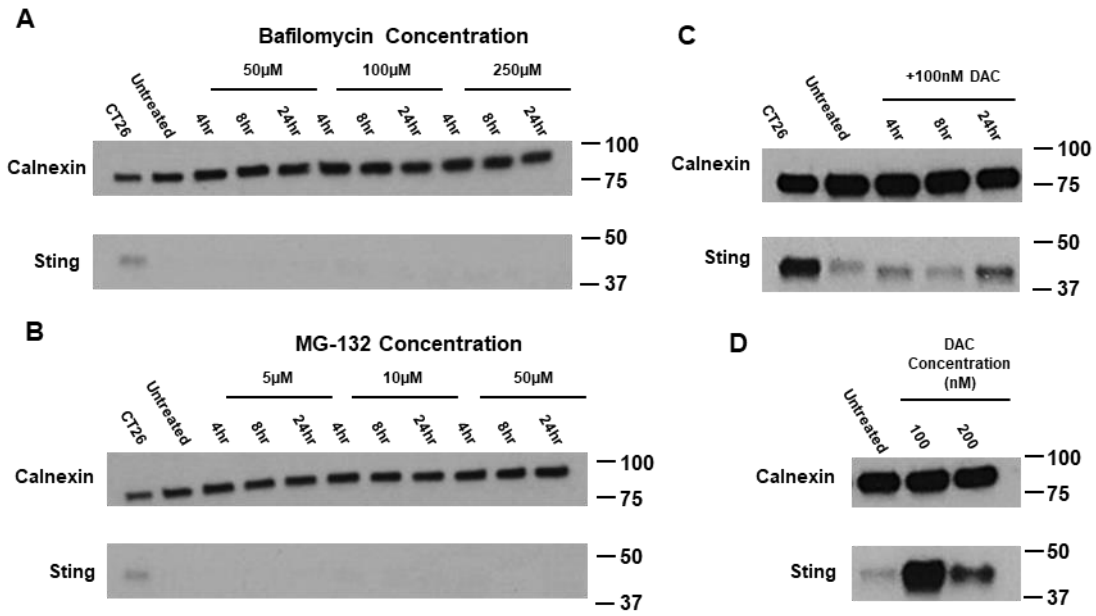

Figure 4. 11. Decitabine treatment restores STING protein levels in KP.B6.F1 cells.

Immunoblot staining for STING and calnexin (loading control) in response to different treatments. **(A)** 4, 8 or 24 hours of 50μM, 100μM or 250μM Bafilomycin. **(B)** 4, 8 or 24 hours of 5μM, 10μM or 50μM MG-132 **(C)** 4, 8 or 24 hours of 100nM decitabine **(D)** 10 days of 100nM or 200nM decitabine. Blots are representative images of 3 biological repeats.

A time course was performed with a range of DAC doses (25nM, 50nM, 100nM and 250nM) over 18 days determine the dynamics of STING increase in KP.B6.F1 cells and optimise conditions for further experiments. This was performed using an immunoblot, staining for STING and DNA methyltransferase 1 (DNMT1)(Figure 4.12). DNMT1 is an enzyme responsible for hypermethylation of genomic regions. DAC is a synthetic nucleic acid which is incorporated into DNA during replication [178]. When DNMT1 targets DAC in DNA for methylation DNA it is irreversibly bound and targeted for degradation [178, 179]. Therefore, DNMT1 levels provide a readout for DAC activity. With 100nM and 250nM treatment, DNMT1 initially decreases, at 10 days DNMT1 increased to similar levels to untreated (Figure 4.12 A). The largest increases were observed after 10 days of decitabine (Figure 4.12 B).

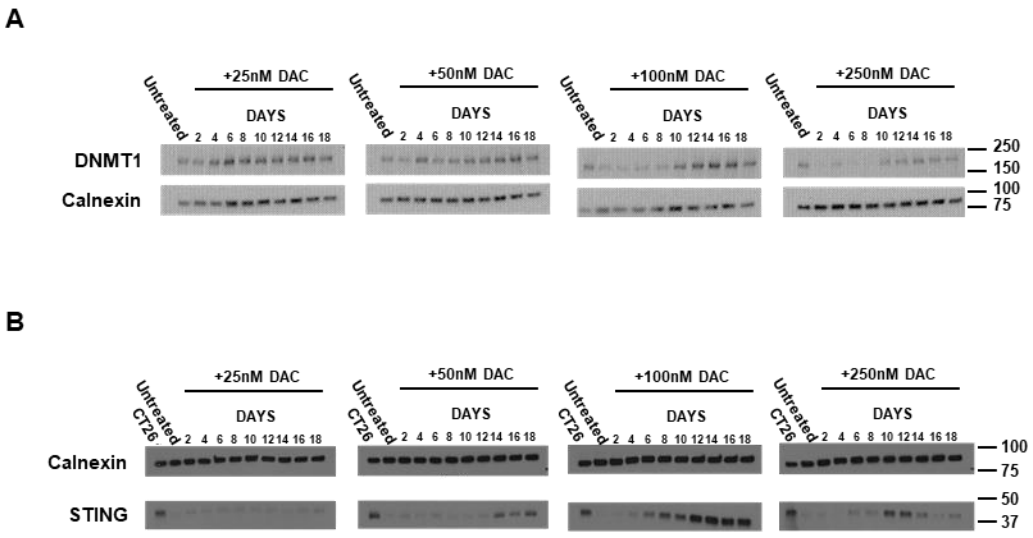

Figure 4. 12. Treatment with 100nM DAC reduces DNMT1 by day 8 at which point STING increases.

KP.B6.F1 cells were treated with 25nM, 50nM, 100nM or 250nM for 18 days. Lysate was collected every two days and an immunoblot performed to determine levels of **(A)** DNMT1 and calnexin (loading control)(**B)** STING and calnexin (loading control). Blots are representative images of 3 biological repeats.

DAC is an FDA approved treatment for CMML [127], and used off-label for the treatment of AML in elderly patients [126, 128]. Recently, DAC has been reported to have a synergistic effect in combination with immunotherapy [180]. This prompted further investigation into how the addition of DAC to X-ray and DNA-PKi may influence tumour cell immunogenicity.

A proliferation inhibition experiment was performed on cells treated with a range of decitabine doses to identify a non-toxic, STING restoring, dose. Treatment with 1000nM decitabine was highly toxic (Figure 4.13). All other doses initially decreased proliferation, which then began to increase shortly after. Cells treated with 50nM, 100nM and 250nM hit their lowest points at day six with a % proliferation relative to untreated of 73.7% (±1.3), 57.3% (±2.4) and 42.3% (±2.4), respectively. In cells treated with 50nM or 100nM decitabine, a normal level of proliferation was restored on day 12, whereas 250nM did not until day 18 (Figure 4.13). Therefore, treatment of 100nM decitabine for 10 days was selected as the optimum regimen to restore STING levels without excessive cytotoxicity.

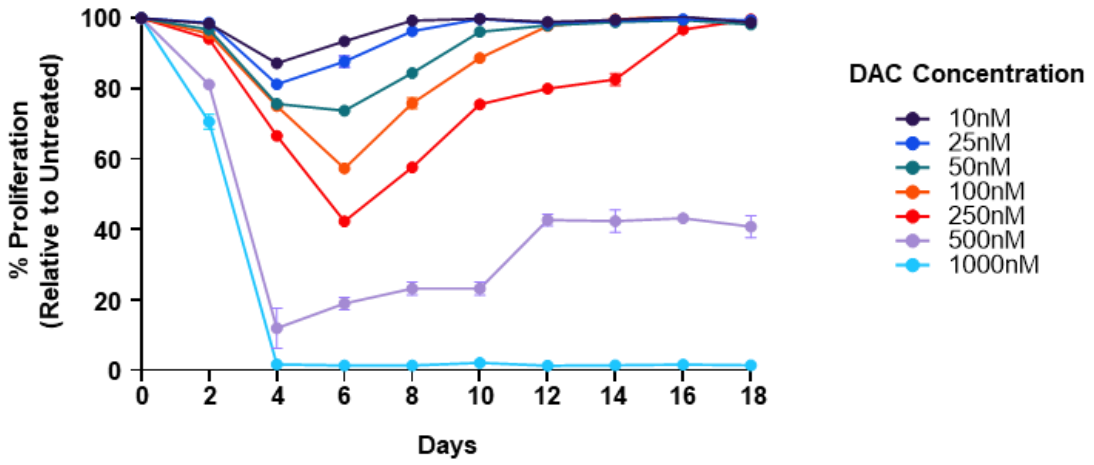

Figure 4. 13. Dose-dependent effect of decitabine (DAC) on KP.B6.F1 cell proliferation.

KP.B6.F1 cells were treated with 10nM, 25nM, 50nM, 100nM, 250nM, 500nM or 1000nM decitabine for 18 days. Every two days cells were collected and seeded in a 96 well plate for SRB staining after two days. Data from three independent experiments presented as average±SEM.

These experiments identified 100nM decitabine as an appropriate dose to restore STING protein levels in KP.B6.F1 cells without causing cytotoxicity, and therefore was selected to be used for further experiments. Following the finding that KP.B6.F1 cells did not release IFNβ following stimulation with cGAMP, ISD or Poly(I:C), the effect of 100nM decitabine treatment on response to cGAS-STING agonists was assessed (Figure 4.14). KP.B6.F1 cells were treated for 5 days with 100nM decitabine, at which point they were reseeded. After 24 hours, cells were transfected with cGAMP, ISD or Poly(I:C), conditioned media was collected 24 hours later, and an ELISA performed. As in Figure 4.8, KP.B6.F1 cells without decitabine, did not respond to cGAMP, ISD or Poly(I:C) treatment. On the other hand, KP.B6.F1 cells treated with 6 days of 100nM decitabine responded. Treatment with cGAMP in decitabine treated cells resulted in an IFNβ concentration of 4.5pg/mL (±1.9), which was significantly greater than both untreated cells and decitabine alone cells (Bonferroni's, $p=0.0189$ both). ISD induced IFNβ release to the concentration of 9.7pg/mL (±2.8). This too was significantly greater that untreated and decitabine alone cells (Bonferroni's, $p<0.0001$ both), but also greater than cGAMP treatment in DAC treated cells (Bonferroni's, $p=0.005$). The largest response was seen with Poly(I:C) treatment which increased the IFNβ concentration to 24.3pg/mL (±2.5). Again , this was significantly larger than untreated and decitabine alone cells (Bonferroni's, $p<0.0001$ both), but also higher than cGAMP (Bonferroni's, $p<0.0001$) or ISD (Bonferroni's, $p<0.001$) in decitabine treated cells (Figure 4.14).

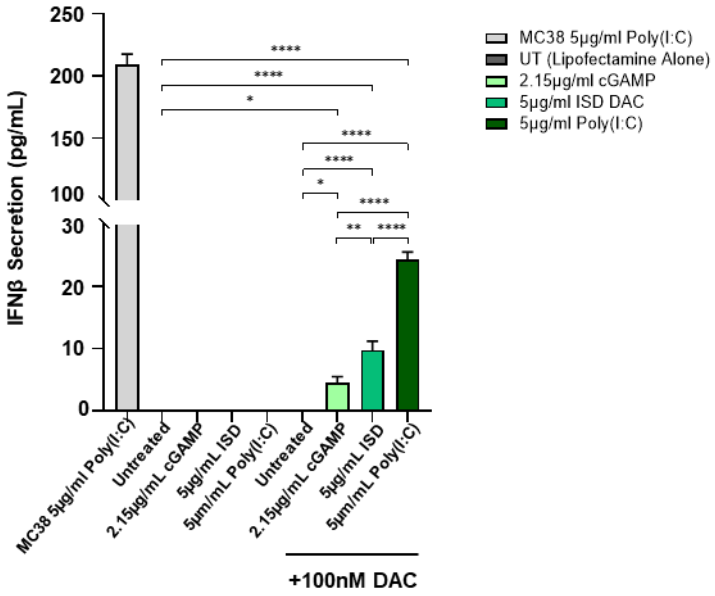

Figure 4. 14. Decitabine treated KP.B6.F1 cells release IFNβ in response to stimulation.

KP.B6.F1 cells were treated with 100nM DAC for 6 days, and then transfected with 2.15µg/mL cGAMP, 5µg/mL ISD or 5µg/mL Poly(I:C) for 24 hours. Finally, conditioned media was collected, and an ELISA performed to quantify IFNβ release. The induction of IFNβ secretion in MC38 cells was used as positive control. Data from three independent experiments presented as average±SEM and analysed by one-way ANOVA followed by Bonferroni's multiple comparison test: *p<0.05, **p<0.01, ***p<0.001 ****p<0.0001.

Following the determination that decitabine restored cGAS-STING pathway activity in the previously deficient KP.B6.F1, next cGAS-STING pathway activity was investigated in response to X-ray and M3814 treatment. This experiment was performed using MC38 cells, untreated KP.B6.F1 cells and decitabine-treated KP.B6.F1 cells. To determine pathway activity, gene expression of *IFNβ* was assessed by qRT-PCR 24 hours after treatment with 8Gy and 0.5µM M3814 (Figure 4.15). In MC38 cells, treatment with 8Gy alone increased *IFNβ* expression 2.6-fold (Bonferroni's, p=0.0089)(Figure 4.15 A). Treatment with 8Gy+0.5µM M3814 increased *IFNβ* expression further still to 4.2-fold greater than untreated. This was

significantly greater than both untreated (Bonferroni's, p<0.0001) and 8Gy alone (Bonferroni's, p=0.0065)(Figure 4.15 A).

In normal KP.B6.F1 treated cells, there was no change in the gene expression of *IFNβ* in response to treatment (Figure 4.15 B). However, in cells treated with 6 days of 100nM decitabine, treatment with 8Gy alone increased *IFNβ* gene expression 1.9-fold compared to control (Bonferroni's, p=0.008). Addition of 0.5μM M3814 to 8Gy increased this further to 2.2-fold greater than decitabine alone (Bonferroni's, p=0.0006)(Figure 4.15 B). This indicates that X-ray and X-ray in combination with M3814 activates the cGAS-STING pathway activity in MC38 and decitabine-treated KP.B6.F1 cells, but not untreated KP.B6.F1 cells.

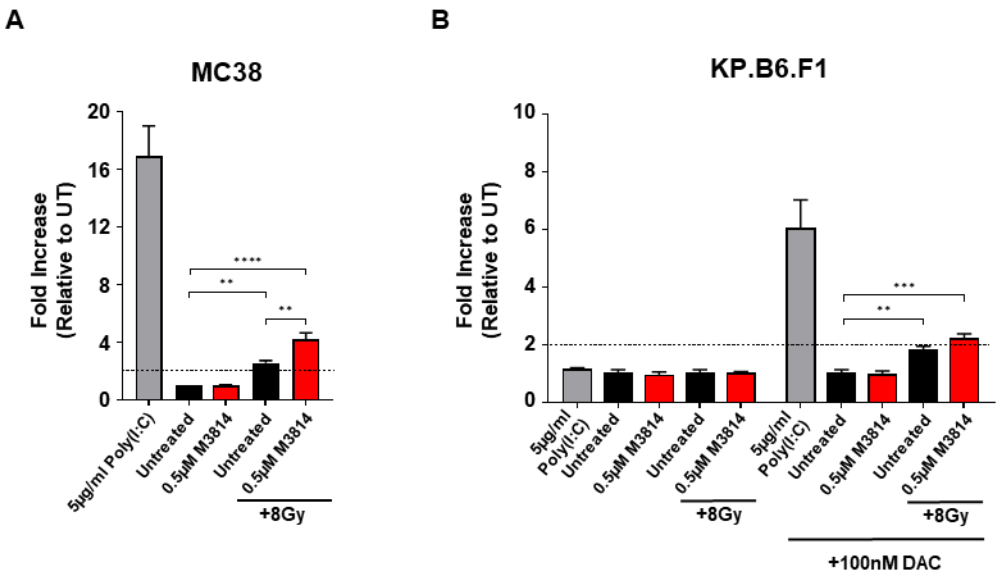

Figure 4. 15. MC38 and decitabine-treated KP.B6.F1 cells increase Ifnβ gene expression following treatment with IR+M3814.

Cells were treated with 0.5μM M3814 and one hour later with 8Gy. Twenty-four hours later, mRNA was extracted, and qRT-PCR was performed to determine gene expression of *Ifnβ* . **(A)** MC38 cells **(B)** KP.B6.F1 untreated cells and KP.B6.F1 cells after 6 days of 100nM decitabine. Data from three independent experiments. Dashed line indicates a 2-fold increase. Average of all conditions analysed by one-way ANOVA followed by Bonferroni's multiple comparison test: *p<0.05, **p<0.01, ***p<0.001 ****p<0.0001.

4.3.6. Decitabine treatment alters the surface levels of immunomodulatory molecules in KP.B6.F1 cells.

The previous work provides evidence that decitabine can restore cGAS-STING pathway activity in KP.B6.F1 cells. However, this effect is not STING specific. Decitabine hypomethylates CpG islands and therefore the effect of decitabine on gene expression of other immunomodulatory molecules was explored. These include those discussed in Chapter, 3: MHC Class I, MHC Class II and PD-L1. KP.B6.F1 cells were treated with 100nM decitabine for 5 days, at which point they were reseeded and 24 hours later treated with 1µg/mL IFNγ for a further 24 hours. At this point, cells were collected, and flow cytometry performed (Figure 4.16).

In untreated cells, addition of IFNγ significantly increased the frequency of MHC Class I^+ cells from 0.43% (±0.3) to 98.3% (±2.2)(Bonferroni's, $p<0.0001$)(Figure 4.16 A). IFNγ had a similar effect on decitabine treated cells, increasing the frequency of MHC Class I^+ cells from 38.5% (±3.6) to 97.0% (±2.3)(Bonferroni's, $p<0.0001$). While there was an increase in the percentage of MHC Class I^+ cells in decitabine treated KP.B6.F1 cells, this was only a small shift in the MFI of cells which was not statistically significant (Figure 4.16 A).

Next, MHC Class II was evaluated (Figure 4.16 B). In decitabine treated cells there was a significant increase in the frequency of MHC Class II^+ cells upon addition of IFNγ from 0.42% (±0.9) to 14.4% (±5.1)(Bonferroni's, $p=0.0004$). This was also greater than untreated cells treated with IFNγ (Bonferroni's, $p=0.0027$). The MFI of MHC Class II was also affected by treatment. While the frequency of MHC Class II^+ cells was not significantly changed in untreated cells upon addition of IFNγ, the MFI did (Bonferroni's, $p=0.0007$). Treatment with IFNγ also significantly increased the MFI in decitabine treated cells (Bonferroni's, $p<0.0001$). Furthermore, IFNγ combined with decitabine induced 1.6-fold higher MFI of MHC Class II than IFNγ treatment alone (Bonferroni's, $p=0.0324$)(Figure 4.16 B).

Finally, the surface levels of PD-L1 were assessed (Figure 4.16 C). The frequency of PD-L1$^+$ untreated cells increased from 1.5% (±0.3) to 99.5% (±0.4) upon addition of IFNγ (Bonferroni's, $p<0.0001$). In decitabine treated cells, the % of PD-L1$^+$ cells increase 2.4-fold from 40.5% (±1.1) to 98.9% (±0.4) upon addition of IFNγ (Bonferroni's, $p<0.0001$). There was a significant difference of 39.0% between untreated cells and those treated with decitabine alone (Bonferroni's, $p<0.0001$). The MFI of PD-L1 in untreated or decitabine alone treated cells remained low. Addition of IFNγ to decitabine treated cells increased the MFI 5.6-fold compared to decitabine alone (Bonferroni's, $p=0.0003$). Furthermore, PD-L1 MFI of IFNγ and decitabine treated cells showed a 3.0-fold increase relative to IFNγ alone (Bonferroni's, $p=0.0015$)(Figure 4.16 C).

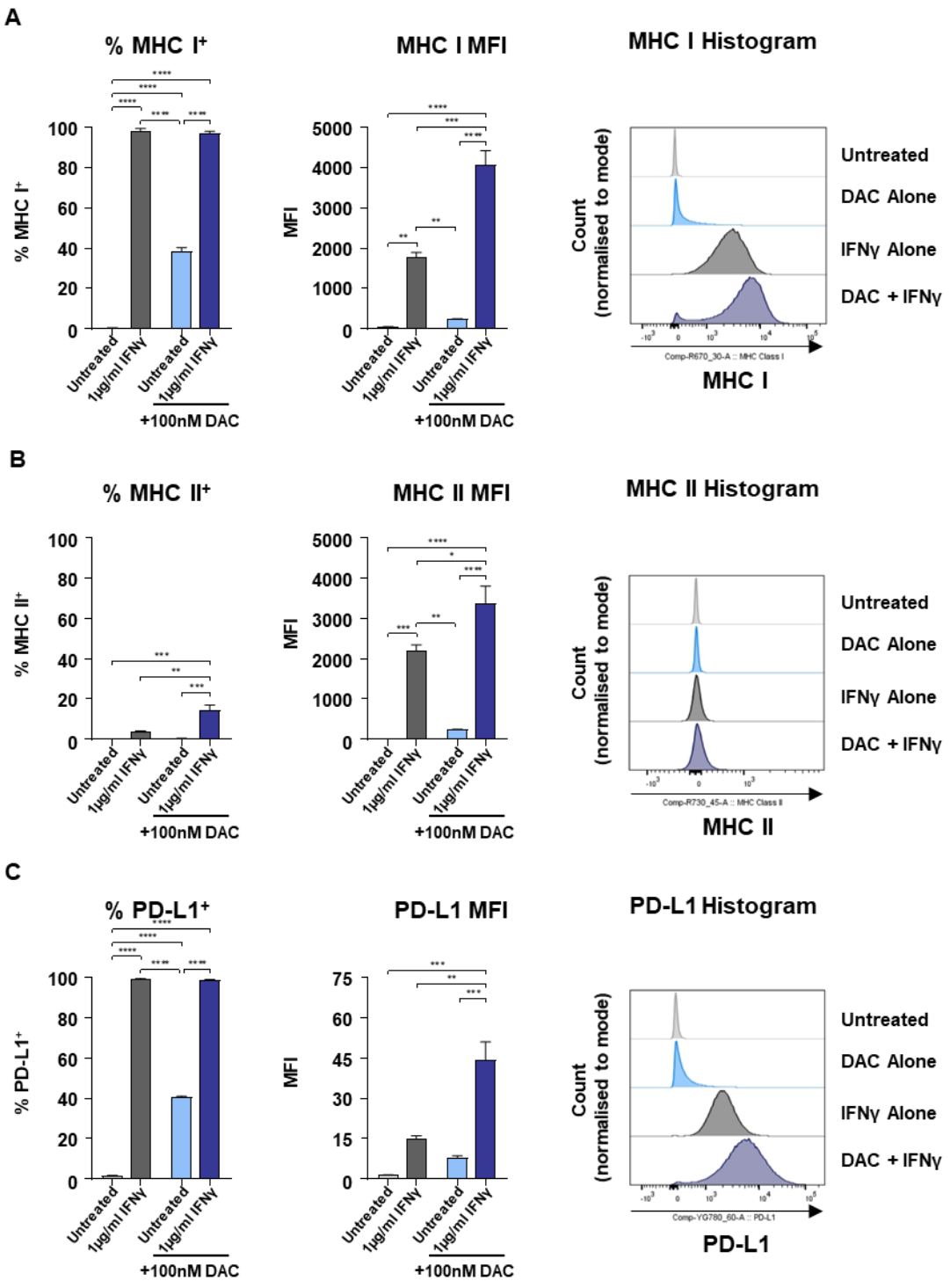

Figure 4. 16. Decitabine treated KP.B6.F1 cells have higher levels of MHC Class I, MHC Class II and PD-L1.

KP.B6.F1 cells were treated with 100nM decitabine for 6 days. 1µg/mL IFNγ was administered for 24 hours. Cells were collected and stained using conjugated antibodies and the % of viable cells and MFI calculated. The resulting histograms are also shown. The cells were stained for **(A)** MHC Class I **(B)** MHC Class II **(C)** PD-L1. Joint data of three independent experiments are presented as average±SEM and analysed by one-way ANOVA followed by Bonferroni's multiple comparison test: *p<0.05, **p<0.01, ***p<0.001 ****p<0.0001.

It has been shown that decitabine can increase the surface levels of other immunomodulatory molecules including CD40, CD80 and CD86 [181, 182]. Therefore, these were investigated (Figure 4.17).

CD40 is a co-stimulatory molecule typically found on antigen present cells (APCs) but can also be upregulated on tumour cells. In untreated cells, the % of $CD40^+$ cells were just 0.15% (±0.09)(Figure 4.17 A). This rose significantly to 3.4% (±0.8) in decitabine alone treated cells (Bonferroni's, p=0.0012). The MFI of CD40 was 2.2-fold greater in decitabine treated cells than untreated (Bonferroni's, p=0.0246)(Figure 4.17 A). CD80 is another marker typically found on APCs, it binds to CD28 and CTLA-4 on T cells to modulate their function and activity. The % of $CD80^+$ cells increased to 3.5% (±0.6) in decitabine treated cells compared to 0.1% (±0.1) in untreated cells (Bonferroni's, p=0.0091)(Figure 4.17 B). Addition of IFNγ to untreated cells had no significant influence on the % of $CD80^+$ cells, however its addition to decitabine treated cells increased the proportion of $CD80^+$ cells from 3.5% (±0.6) to 17.9% (±1.9)(Bonferroni's, p<0.0001). The MFI of CD80 in decitabine treated cells also increased 2.9-fold with the adding of IFNγ (Bonferroni's, p=0.0057). However, it is important to note that this increase produced a small shoulder in the CD80 histogram rather that a distinct bimodal population (Figure 4.17 B).

Like CD80, CD86 is normally expressed on APCs and binds to CD28 and CTLA-4, but with lower affinity. The frequency of $CD86^+$ cells increased from 0.14% (±0.1) in untreated cells to 5.1% (±1.1) in cells treated with decitabine (Bonferroni's, p=0.0037)(Figure 4.17 C). The difference between untreated cells and decitabine was also observed in their MFI, in which treatment with decitabine increase MFI 15.3-fold (Bonferroni's, p=0.0004)(Figure 4.17 C).

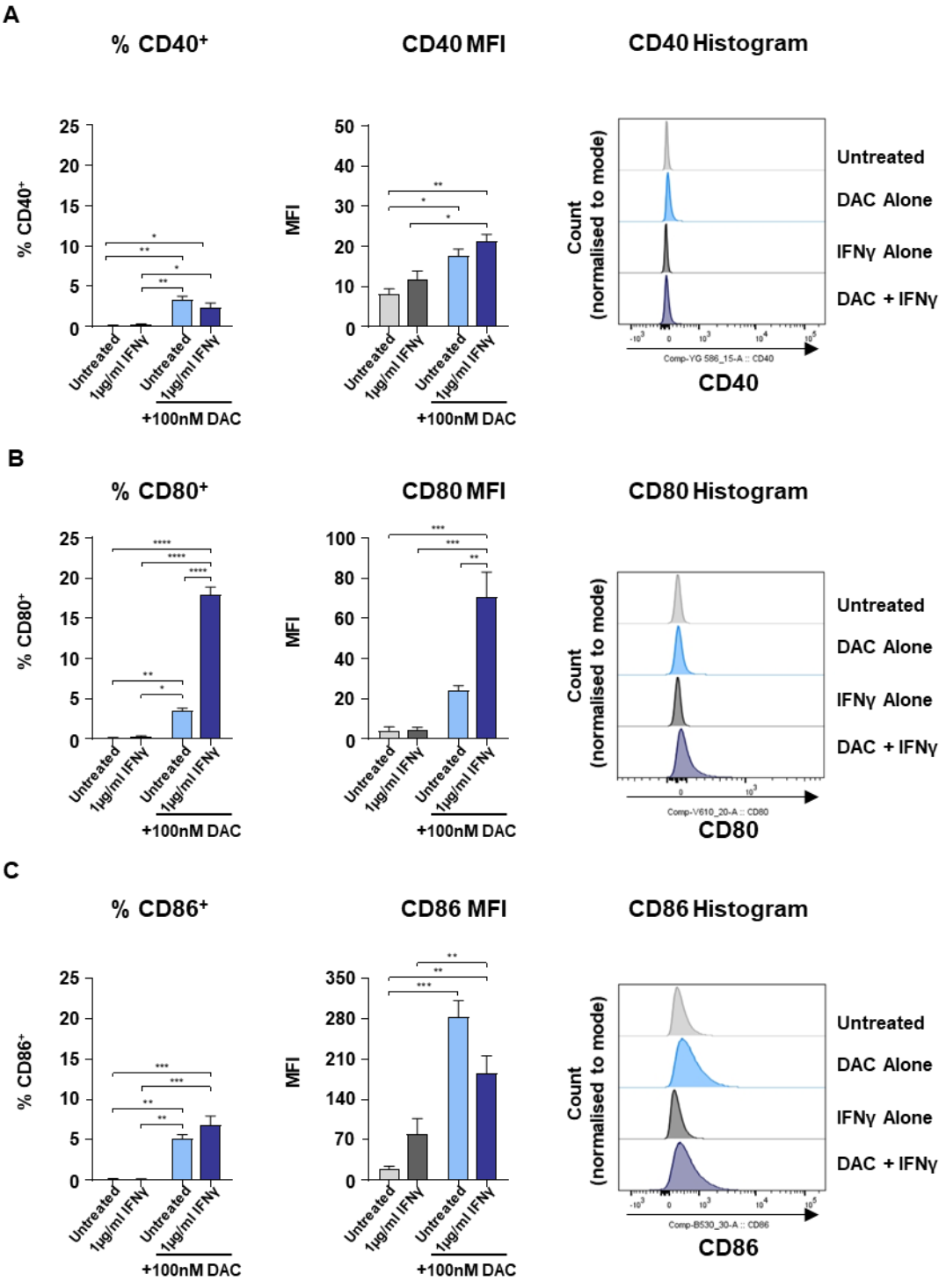

Figure 4. 17. Decitabine treated KP.B6.F1 cells have higher levels of CD40, CD80 and CD86.

KP.B6.F1 cells were treated with 100nM decitabine for 6 days. 1µg/mL IFNγ was administered for 24 hours. Cells were collected and stained using conjugated antibodies and the % of viable cells and MFI calculated. The resulting histograms are also shown. The cells were stained for **(A)** CD40 **(B)** CD80 **(C)** CD86. Joint data of three independent experiments are presented as average±SEM and analysed by one-way ANOVA followed by Bonferroni's multiple comparison test: *p<0.05, **p<0.01, ***p<0.001 ****p<0.0001.

4.4. Discussion

4.3.1. Radiotherapy of tumour-bearing lungs *in vivo* increases expression of genes associated with the cGAS-STING pathway

Initial *in vivo* experiments identified increased gene expression indicative of cGAS-STING pathway activity in lungs treated with radiotherapy. This included upregulation of *Cxcl10* and *Ifnβ* 72 hours after 1x8Gy, *Mx1* one week after 1x8Gy and *Ccl2* one week after 3x8Gy. These results are cohesive with that of the DeMaria study in which increased gene expression of *Ifnβ*, *Mx1*, *Ccl2*, and *Cxcl10* was observed 24 hours post 3x8Gy radiotherapy [83]. Furthermore, there are limitations of the tumour model used for this experiment. Tumour cells are injected into the tail vein where they enter circulation and colonise the lungs. This creates numerous tumour foci in the lungs, rather than a single dissectible mass. Therefore, qRT-PCR was performed with RNA obtained from single cell suspension of the entire lungs and therefore, is not exclusive to the tumour. This means that other cells, innate immune cells which are key providers of IFNβ, may be responsible for this increase in cGAS-STING gene expression rather than the cancer cells themselves.

4.3.2. The cGAS-STING pathway is downregulated in KP.B6.F1 cells.

To better understand what may be occurring in KP.B6.F1 cells following radiotherapy, experiments were then conducted *in vitro*. X-ray increased the formation of micronuclei from 7.6% in untreated cells up to 42.5% with 4Gy alone and further still to 52.9% with 4Gy+0.5μM M3814 (Figure 4.7 B). Additionally, the average number of these structures per cell increased from 1.1 in untreated to 2.2 following 4Gy+0.5μM M3814 treatment (Figure 4.7 C). These results indicate that addition of M3814 increases DNA damage in cells and could provide a source of cytosolic dsDNA.

The ability of radiotherapy to increase the formation of micronuclei has previously been demonstrated [171, 183-185]. Therefore, these findings indicate that the addition of M3814 to radiotherapy increases the level of DNA damage, resulting in

the formation of more micronuclei. Not only do these micronuclei bodies indicate DNA-damage, but they also provide a source of cytosolic dsDNA that cGAS can bind. This was supported by the finding that 7.4% of cells treated with 4Gy+0.5μM M3814 treatment had cGAS positive micronuclei (Figure 4.7 D). A recent study by Carr *et al* also found that addition of 1μM M3814 to 5Gy increased the frequency of cGAS positive micronuclei [136]. However, in the study by Carr *et al,* analysis of downstream signal transduction, including IRF3 and TBK1 phosphorylation, was also observed [136]. In contrast, here, despite apparent initiation of the cGAS-STING pathway, as indicated by $cGAS^{+}$ micronuclei, in KP.B6.F1 cells treated with M3814 and radiotherapy, there was no evidence of downstream cGAS-STING pathway activity, as measured by gene expression of ISGs and secretion of IFNβ (Figure 4.15 B & 4.8 respectively).

As the emerging picture of the role of cGAS-STING pathway in cancer develops, it has been demonstrated that downregulation of cGAS-STING is a method of immune evasion that tumours employ.

Therefore, the production of IFNβ in a range of murine cancer cell lines and BMDMs was analysed in response to cGAS-STING pathway agonists and Poly(I:C). This showed a high degree of variation in the response to cGAS-STING pathway agonist. Indeed, of the six cell lines investigated only half (CT26, LLC and MC38) released IFNβ in response to cGAS-STING pathway activation with ISD or cGAMP. Critically, KP.B6.F1 did not respond. Analysis of components of the cGAS-STING pathway using immunoblotting identified a deficiency of STING in KP.B6.F1 cells (Figure 4.10).

4.3.4. Decitabine increases the immunogenicity of KP.B6.F1 cancer cells

In this work, decitabine was shown to significantly increase STING expression in KP.B6.F1 cells. Following decitabine treatment, KP.B6.F1 cells treated with ISD, cGAMP and Poly(I:C) released IFNβ. This was a striking difference to cells not treated with decitabine, which had no detectable release of IFNβ (Figure 4.14). Following

treatment with 8Gy+0.5μM M3814, gene expression of *IFNβ* was increased 2-fold in decitabine treated KP.B6.F1 cells (Figure 4.15). Together, this work indicates that decitabine restores cGAS-STING pathway activity in the STING deficient KP.B6.F1 cell line and therefore, may increase immunogenicity.

As a hypomethylating agents, the effects of decitabine are not specific to the *STING* promotor region. Therefore, changes to the levels of other immunomodulatory molecules were also investigated. Decitabine treatment increased the frequency KP.B6.F1 cells positive for MHC Class I, MHC Class II, PD-L1, CD40, CD80 and CD86. However, while these populations grew there were only visible MFI shifts for MHC Class I, PD-L1 and CD86. In the context of increased IFNβ due to cGAS-STING pathway activity, increased expression of MHC Class I and CD86 could all combine to further improve dendritic cell antigen uptake. The increase in PD-L1 could point to a beneficial future combination of decitabine and therapies targeting the PD-1/PD-L1 axis. Indeed, a phase II clinical trial found that the addition of decitabine to cambrelizumab (anti-PD-1) increased remission rate compared to cambrelizumab alone [186]. Furthermore, a recent *in vivo* study using a triple negative breast cancer mouse model found the combination of decitabine and PD-1 inhibition to be synergistic due to reversed T cell exhaustion and improved T cell function. This study also observed increased *STING* expression, although this was not investigated further [129]. The effects of decitabine-induced STING restoration in combination with M3814 and radiotherapy *in vivo* will be explored in Chapter 5.

As Decitabine is an already FDA approved therapy with little toxicity, this could provide an exciting option to combine with DNA damaging treatments, such as radiotherapy and DNA-PKi, to mobilise an anti-tumour immune response. Based on the immunoblots (Figure 4.12), the effects of decitabine on DNMT1 appears to be transient, despite decitabine containing media being replenished. Over longer time periods it would be interesting to see whether increased STING is also transient. If

so, the timing between STING increase and activation of the cGAS-STING pathway will be important.

4.5. Conclusions

The results presented in this Chapter indicate that DNA-PK inhibition increases the ability of radiotherapy to trigger the cGAS-STING pathway. Most of the published work on the cGAS-STING pathway to date has used cell lines with proficient cGAS-STING pathways, however, as this Chapter shows, this is not representative of all tumours. Decitabine was identified as an agent which restored STING in KP.B6.F1 cells. Treatment of these STING deficient cells with decitabine, M3814 and 8Gy resulted in the production of IFNβ. This work, together with the results of Chapter 3, indicate that M3814 and radiotherapy is a beneficial combination which can increase the immunogenicity in cancer cells. Furthermore, in cancer cells lacking STING, this works suggests Decitabine could be an interesting addition to this combination. While this work indicates that this treatment regimen would be beneficial, *in vivo* experiments are required to determine the effects on the immune response. This will be addressed in Chapter 5.

5. Treatment with M3814, Radiotherapy and Decitabine Stimulates an *In Vivo* Immune Response

5.1. Introduction

The presented experiments provide evidence that M3814 not only radiosensitises cancer cells but that this cell death is accompanied by the release of DAMPs characteristic of ICD. Chapter 4 also demonstrated that this combination may increase tumour cell immunogenicity by increased release of IFNβ via the cGAS-STING pathway. In addition, a potential therapeutic strategy to restore cGAS-STING pathway in the STING deficient cell line KP.B6.F1 was also identified. However, while this work indicates that the combination may increase immunogenicity, this needs to be determined in the context of the immune system. In this Chapter, the effect of M3814, radiotherapy and decitabine on therapeutic efficacy and immune response will be assessed in immunocompetent, syngeneic mouse models.

As discussed in Section 1.2.1.1, successful immune clearance of a tumour requires the different components of the immune system. Figure 5.1 shows an illustration depicting this process. APCs, including DCs and macrophages, need to recognise and engulf the target cells. Once matured and activated, these cells need to present these antigens to complementary T cells in the lymph nodes. Once activated, $CD8^+$ T cells can travel to the tumour and eliminate target cells. As mentioned in more detail in Section 1.2.4, translocation of CRT to the cell surface membrane and release of HMGB1 are associated with ICD. Cell surface CRT binds to CD91 on APCs, promoting phagocytosis of the CRT-presenting cell, increased antigen processing and APC maturation [90-92]. Extracellular HMGB1 also stimulates APC cell maturation [96, 97]. Similarly, IFNβ increases dendritic cell activation and promotes upregulation of MHC molecules and co-stimulatory molecules [112, 187, 188]. IFNβ can also recruit inflammatory monocytes to the site of inflammation [189]. Together, these signals can alter the tumour immune microenvironment. To determine the

immune response to therapy, the immune compartments of tumours and tumour draining lymph nodes (TDLNs) will be characterised. Using high-dimensional flow cytometry, the identification of cell types and subsets will be determined, as will the expression of important immunomodulatory molecules including co-stimulatory and co-inhibitory molecules. Together, this will provide an important insight into the tumour immune microenvironment of treated mice. Where possible, mice with complete tumour control will be subject to a tumour rechallenge to validate whether tumour clearance was, in part, immune mediated. To evaluate the therapeutic efficacy of M3814, radiotherapy and decitabine, alone and in combination, tumour growth and long-term survival experiments will also be performed.

In combination with immune checkpoint inhibitors, fractionated radiotherapy has been demonstrated to induce a tumour specific adaptive immune arm response, resulting in both primary and abscopal tumour control [83, 84, 153]. However, in mouse models, radiotherapy induced abscopal tumour control is abrogated with STING loss [83, 103, 119]. As determined in Chapter 4, KP.B6.F1 is a STING deficient model, while MC38 is STING proficient. The effect of M3814 and radiotherapy in these models *in vivo* will be the focus. In addition, the ability of decitabine to restore STING in KP.B6.F1 *in vivo* will also be determined. Furthermore, the effect of adding decitabine to the combination therapy on both the therapeutic efficacy and immune response. Due to the prevalence of cGAS-STING loss in cancer, discussed further in Section 1.2.5.5, this could provide important insights into a potential therapeutic strategy in such tumours.

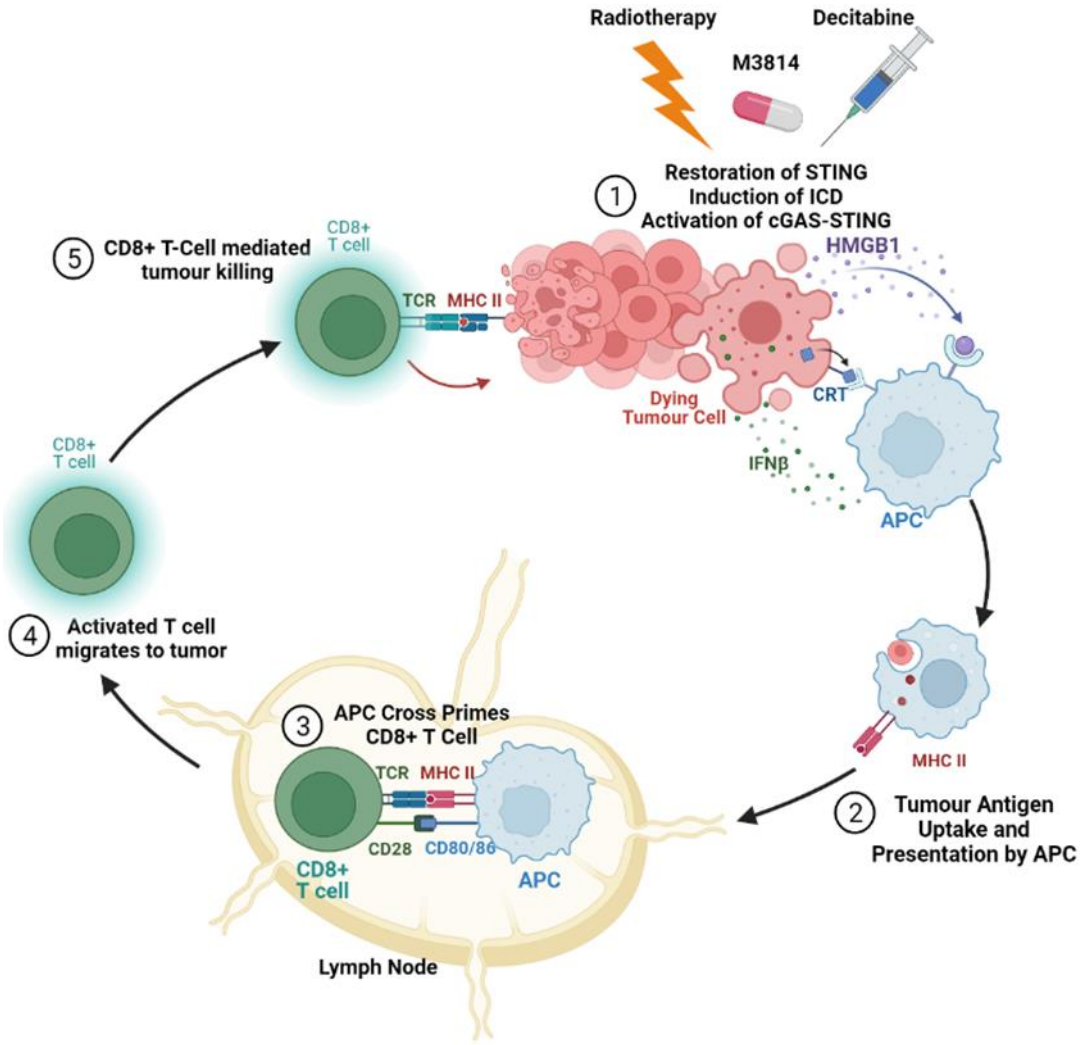

Figure 5. 1. Increase antigen presentation following treatment with radiotherapy, M3814 and decitabine.

Treatment with decitabine restores STING levels in KP.B6.F1. Treatment with radiotherapy and M3814 induce immunogenic cell death and initiate the cGAS-STING pathway. Together, this results in release of HMGB1, IFNβ and translocation of Calreticulin can may stimulate APCs to be recruited and increase uptake of tumour cells. APCs then process tumour material to present on their MHC Class II complex. APCs relocate to the lymph node when they can cross prime $CD8^+$ T cells. The resulting, activated T cells can travel to the tumour site and induce $CD8^+$ T Cell mediated tumour cell killing. Created in BioRender.

5.2. Research Aims

The aim of this Chapter is to assess how the *in vitro* findings from Chapters 3 and 4 translate into immunocompetent mouse models. To do so, mouse tumour models will be established using KP.B6.F1 and MC38 cells. First, the effect of *in vivo* decitabine treatment on STING expression in KP.B6.F1 cells will be explored. Following this, the therapeutic efficacy of decitabine, M3814 and radiotherapy will be determined by measuring tumour growth and mouse survival in KP.B6.F1 and MC38 tumour-bearing mice. To evaluate the immune response to the tumour response, high-dimensional flow cytometry will be performed to characterise the myeloid and lymphoid compartments within the tumour and tumour draining lymph nodes.

5.3. Results

5.3.1. Decitabine treatment *in vivo* increases STING levels and decreases DNMT1 in KP.B6.F1 tumours.

To better understand the immunological implications of combining IR, M3814 and decitabine, the therapeutic efficacy and immune response needs to be evaluated in an immunocompetent mouse model. First, the effect of decitabine on KP.B6.F1 tumour STING protein levels following decitabine treatment *in vivo* was investigated. It has previously been reported that five consecutive days of 1mg/kg decitabine, administered by intraperitoneal (I.P.) injection, induces hypomethylation [181]. Therefore, this dose was selected. C57BL/6 mice were injected with $5x10^5$ KP.B6.F1 cells subcutaneously and the resulting tumour allowed to grow for 5 days. At this point, mice received 1mg/kg decitabine via I.P. injection for five consecutive days. Mice were culled and tumours harvested on either day 10 (6 days after initiation of decitabine treatment) or day 15 (10 days after initiation of decitabine treatment) to enable comparisons between *in vivo* and *in vitro* experiments. The experimental plan is shown in Figure 5.1 A. Protein was extracted from the resulting tumours and western blot analyse was performed to determine DNMT1a and STING protein levels (Figure 5.2 B). In tumours collected 6 days after first decitabine dose, there was a clear loss of DNMT1, indicating decitabine mediated inhibition. By day 15 (10 days after first decitabine dose) DNMT1 levels returned to similar levels as untreated. In contrast, the levels of STING increased 10 days after decitabine treatment initiation (Figure 5.2 B). This demonstrated that the selected dose increased STING levels *in vivo*.

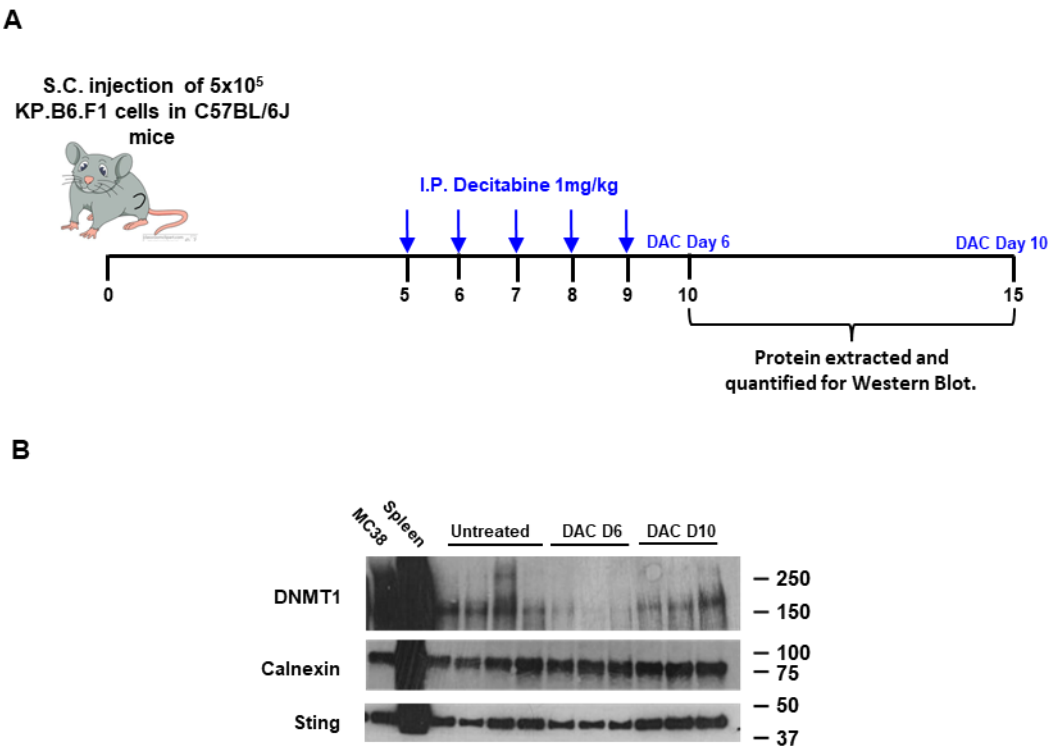

Figure 5. 2. Decitabine downregulates DNMT1 and upregulates STING in vivo.

Ten C57BL/6 mice were subcutaneously injected with 5x10^5 KP.B6.F1 cells. Five days later, 1mg/kg of decitabine was given for 5 consecutive days. On day 10, 3 treated mice and 2 untreated were culled and tumours obtained, on day 15 another 3 treated and 2 untreated were harvested. Protein was extracted from the tumours and western blot performs staining for DNMT1, STING and Calnexin (loading control). **(A)** Experimental plan **(B)** Western blot. Data from one experimental repeat.

5.3.2. Addition of decitabine to Radiotherapy+ M3814 improves KP.B6.F1 tumour control *in vivo.*

After determining that decitabine could increase STING expression, like that observed *in vitro*, the therapeutic efficacy of radiotherapy, M3814 and decitabine was assessed in the KP.B6.F1 tumour model. To do so, 5x10^5 KP.B6.F1 cells were injected subcutaneously. into the flank of C57BL/6 mice. On day 5, mice were given 1mg/kg decitabine via I.P. injection for five consecutive days. On day 10, mice were given 100mg/kg M3814 via oral gavage and one hour later 1x8Gy CT guided radiotherapy was administered using the SARRP. Tumours were measured three

times a week until the longest length exceeded 15mm or tumour volume exceed 600mm^3 . The experimental plan is shown in Figure 5.3.

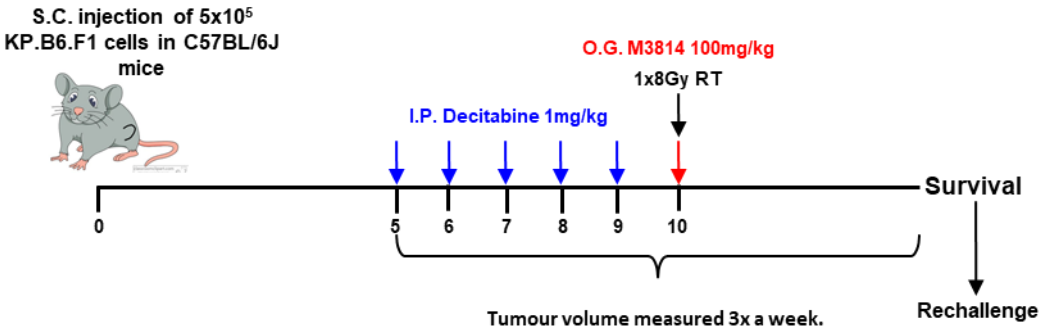

Figure 5. 3. Experimental plan for KP.B6.F1 in vivo survival experiment.

Illustration showing the experimental plan to compare the effects and combination of decitabine, radiotherapy and M3814 on KP.B6.F1 S.C. tumour growth and survival. Two independent experiments performed, with 5 mice per treatment group.

The resulting tumour growth and survival curves for the treatment groups are shown in Figure 5.4 A and B respectively. Radiotherapy had the biggest effect on tumour growth. For untreated mice, the median survival was 23 days, this significantly increased to 32 days with RT alone (Mantel-Cox, $p<0.0001$), 33.5 days with RT+M3814 (Mantel-Cox, $p<0.0001$), 30.5 day with RT+DAC (Mantel-Cox, $p=0.0001$) and the longest median survival of 37 days with RT+M3814+DAC (Mantel-Cox, $p<0.0001$)(Figure 5.3 B). No mice survived this experiment. However, the mouse with the longest survival, 49 days, weas treated with RT+DAC+M3814 group. The tumour growth curves of each individual mouse are shown in Figure 5.5.

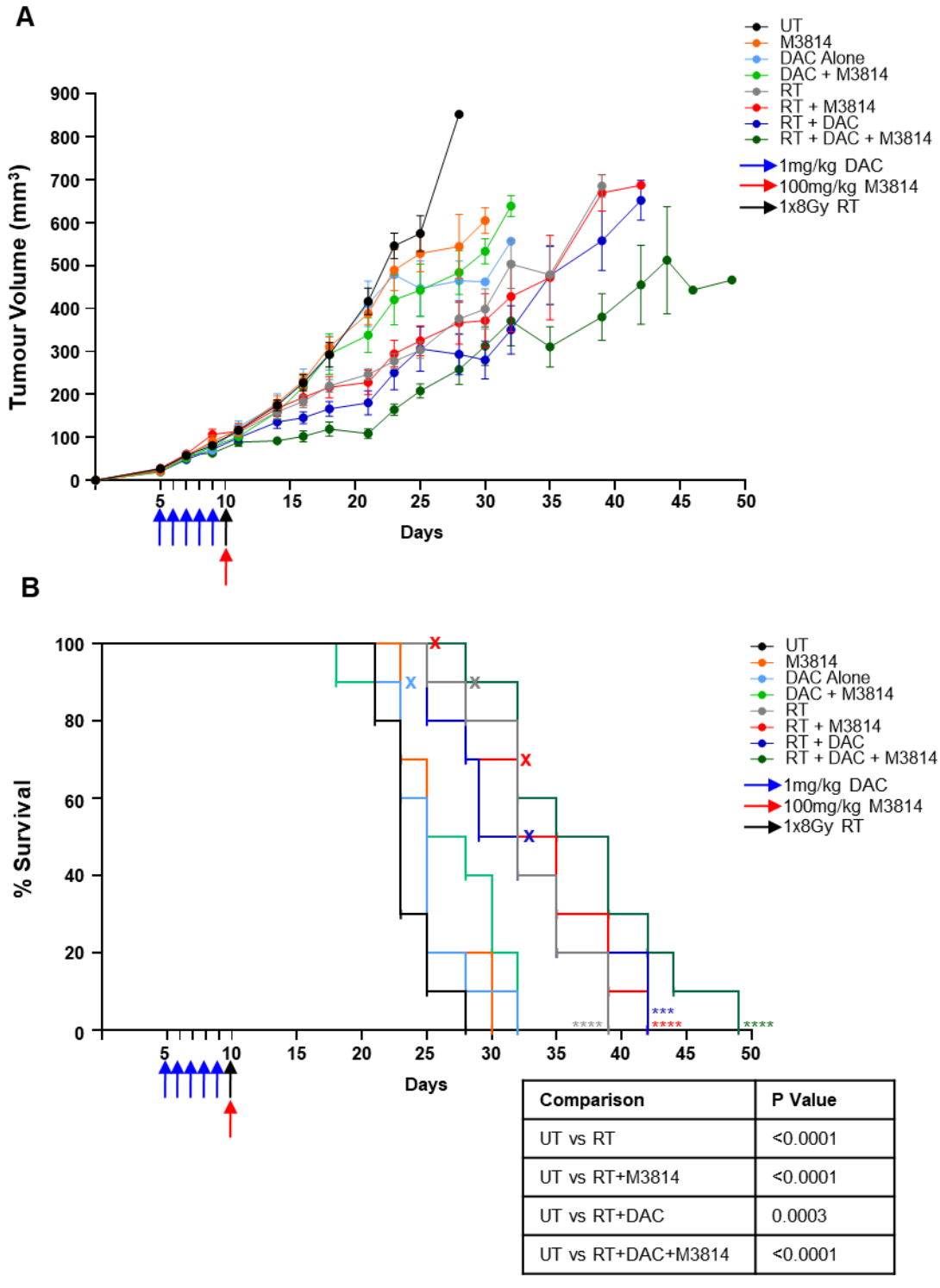

Comparison	P Value
UT vs RT	<0.0001
UT vs RT+M3814	<0.0001
UT vs RT+DAC	0.0003
UT vs RT+DAC+M3814	<0.0001

Figure 5. 4. Radiotherapy improves KP.B6.F1 tumour control in vivo.

C57BL/6 mice were inoculated with $5x10^5$ KP.B6.F1 cells via S.C. injection. On day 5, mice were treated with 1mg/kg DAC for 5 consecutive days. On day 10, 100mg/kg M3814 was administered via O.G. and one hour later mice were treated with CT guided 1x8Gy radiotherapy to the tumours. Tumour volume was recorded 3 times a week until mouse reached humane endpoint, tumour > $600mm^3$ or ulceration, at which point mouse was culled. **(A)** Average tumour growth curve. Data shown as average ±SEM of 10 mice per treatment group **(B)** Kaplan-Meier analysis of survival of initial experiment. X denotes where a mouse was sacrificed due to ulceration. Kaplan-Meier analysed by comparing each treatment group to Untreated using Mantel-Cox test, Significance adjusted for multiple corrections using Bonferroni method: $p<0.0125$.

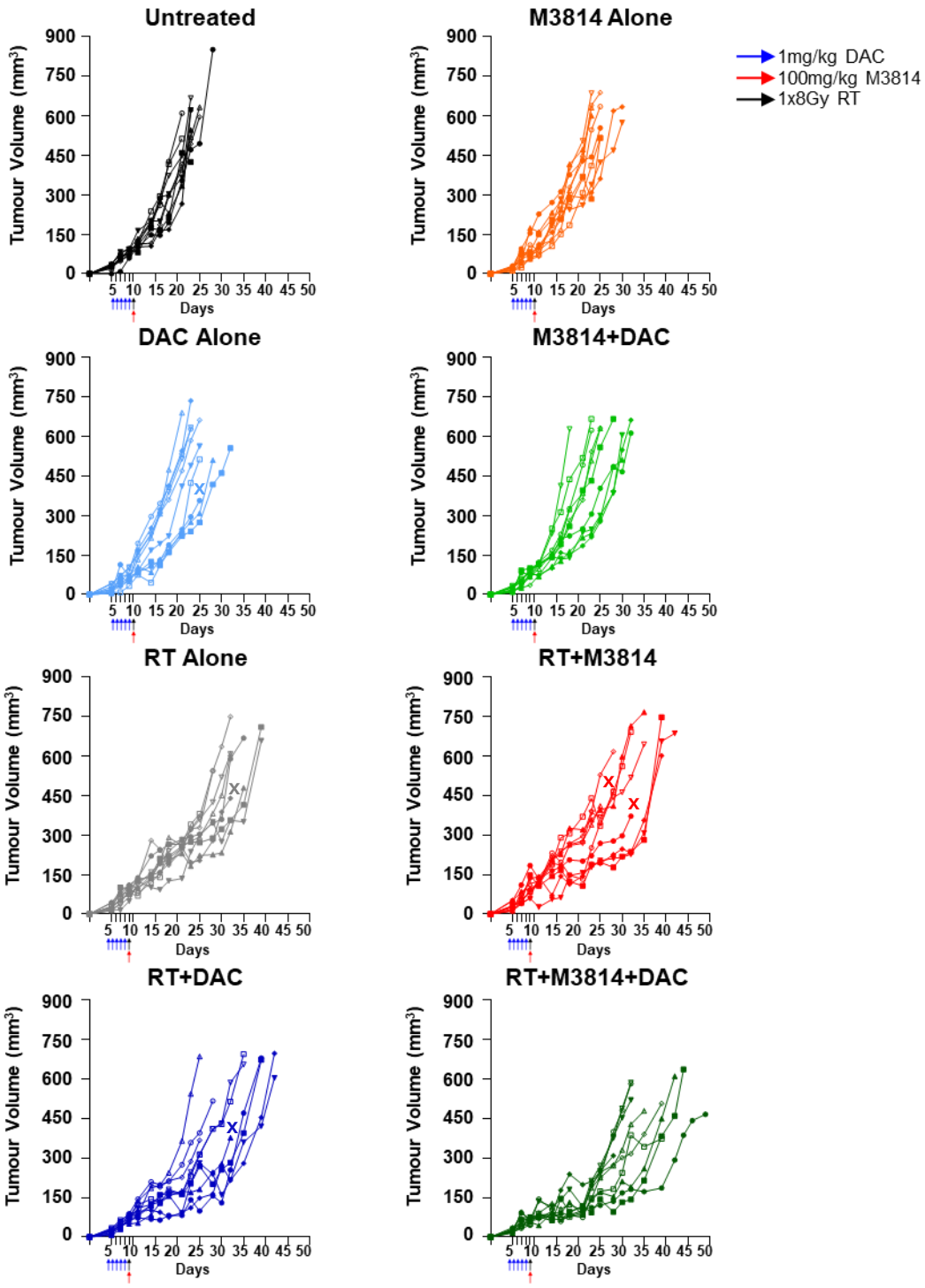

Figure 5. 5. Radiotherapy improves KP.B6.F1 tumour control in vivo – individual mouse data.

C57BL/6 mice were inoculated with 5x10^5 KP.B6.F1 cells via S.C. injection. On day 5, mice were treated with 1mg/kg DAC for 5 consecutive days. On day 10, 100mg/kg M3814 was administered via O.G. and one hour later mice were treated with CT guided 1x8Gy radiotherapy to the tumours. Tumour volume was recorded 3 times a week until mouse reached humane endpoint, tumour > 600mm^3 or ulceration, at which point mouse was culled. X denotes where a mouse was sacrificed due to ulceration. Tumour growth curves of individual mouse in each treatment group shown.

5.3.3. Combination of Radiotherapy and M3814 elicits MC38 tumour control *in vivo*, while addition of decitabine has little effect.

As determined in Chapter 4, unlike KP.B6.F1 which required decitabine treatment to enable cGAS-STING signalling, MC38 is already cGAS-STING functional. A recent article reported that radiotherapy, M3814 and bintrafusp alfa (targeting TGFβ and PD-L1) elicited abscopal tumour control in the MC38 model [136]. Therefore, the therapeutic efficacy of radiotherapy, M3814 and decitabine in MC38 was also investigated in MC38. C57BL/6 mice were injected with $5x10^5$ MC38 cells subcutaneously. After 6 days, when the tumour was palpable, mice were treated with 1mg/kg decitabine via I.P. injections for five consecutive days. On the day after the last decitabine treatment (day 11), mice were given 100mg/kg M3814 via oral gavage (O.G.). One hour following M3814 administration, mice were given 1x8Gy CT guided radiotherapy. Tumours were measured three times a week until the longest length exceeded 15mm or tumour volume exceed $600mm^3$ at which point the mouse was culled. If a mouse was tumour free for over 30 days, they were challenged on the contralateral flank with MC38 cells, and the resulting tumours measured. This experimental plan is shown in Figure 5.6.

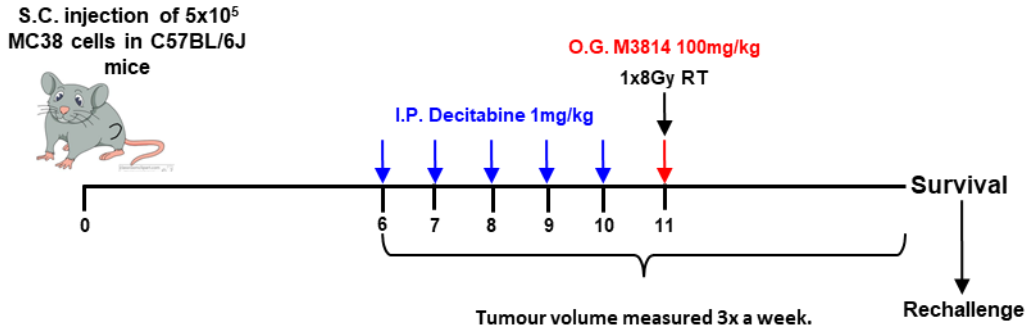

Figure 5. 6. Experimental plan for MC38 in vivo survival experiment.

Illustration showing the experimental plan to compare the effects and combination of decitabine, radiotherapy and M3814 on MC38 S.C. tumour growth and survival. Two independent experiments performed, with 5 mice per treatment group.

The resulting tumour volumes (calculated as the volume of an ellipsoid from height, depth, and width measurements) show a clear distinction from day 11 between mice receiving radiotherapy and those without (Figure 5.7 A). Those receiving radiotherapy however, had initial tumour control from day 11 until day 17 at which point, tumours in mice receiving RT alone, RT+DAC and RT+DAC+M3814 began to grow again. However, 30% of mice treated with RT+M3814 maintained tumour control to be tumour free (Figure 5.7 C). The individual mice curves also show that 40% of mice treated with RT+DAC+M3814 had prolonged tumour control, however, these mice did not remain tumour free (Figure 5.8). The median survival for mice significantly increased from 17 days in untreated mice to 26.5 with RT alone (Mantel-Cox, $p=0.0011$), 40 RT+M3814 (Mantel-Cox, $p<0.0001$), 25 RT+DAC (Mantel-Cox, $p=0.0003$) and 33 days RT+DAC+M3814 (Mantel-Cox, $p<0.0001$), respectively (Figure 5.6 B). Following 30 days tumour free, the three surviving RT+M3814 mice were rechallenged on the contralateral flank with MC38 cells. The tumours of all three mice were rejected and all three survived another 30 days tumour free (Figure 5.7 C).

Figure 5. 7. Radiotherapy improves MC38 tumour control in vivo and RT+M3814 leads to complete tumour control.

Next page. C57BL/6 mice were inoculated with $5x10^5$ MC38 cells via S.C. injection. On day 6, mice were treated with 1mg/kg DAC for 5 consecutive days. On day 11, 100mg/kg M3814 was administered via O.G. and one hour later mice were treated with CT guided 1x8Gy radiotherapy to the tumours. Tumour volume was recorded 3 times a week until mouse reached humane endpoint, tumour > $600mm^3$ or ulceration, at which point mouse was culled. After 30 days tumours free, mouse was rechallenged with $5x10^5$ MC38 cells on contralateral flank. **(A)** Average tumour growth curve. Data shown as average ±SEM of 10 mice per treatment group **(B)** Kaplan-Meier analysis of survival of initial experiment X denotes where a mouse was sacrificed due to ulceration. Kaplan-Meier analysed by comparing each treatment group to Untreated using Mantel-Cox test, Significance adjusted for multiple corrections using Bonferroni method: $p<0.0125$. **(C)** Kaplan-Meier analysis of surviving mice from B after rechallenge.

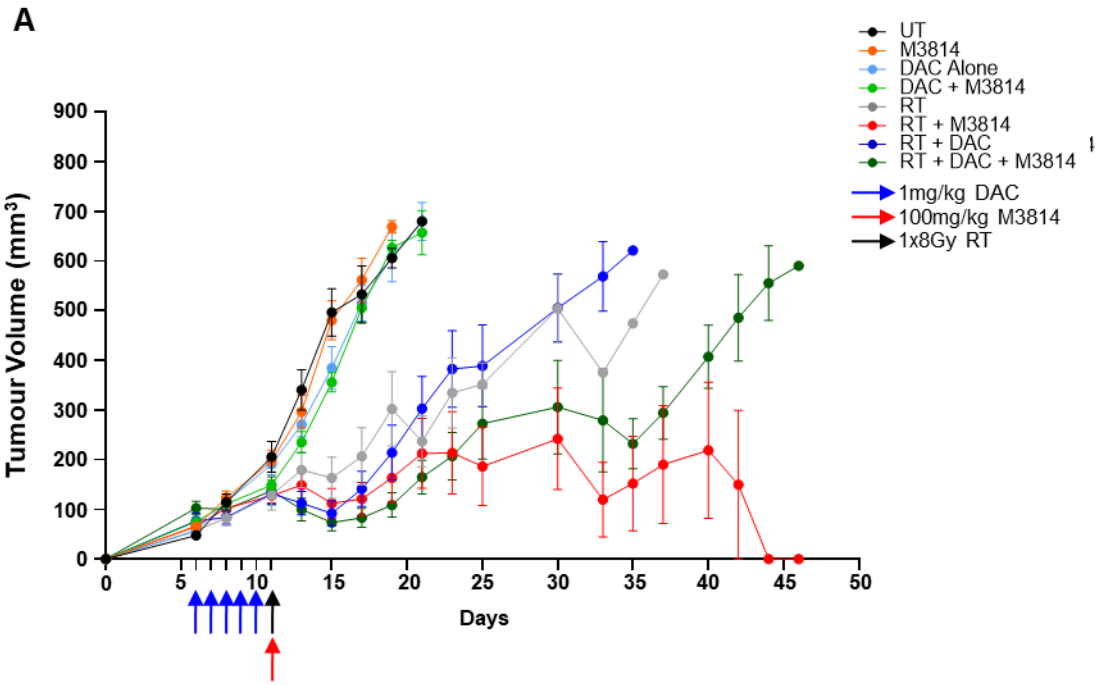

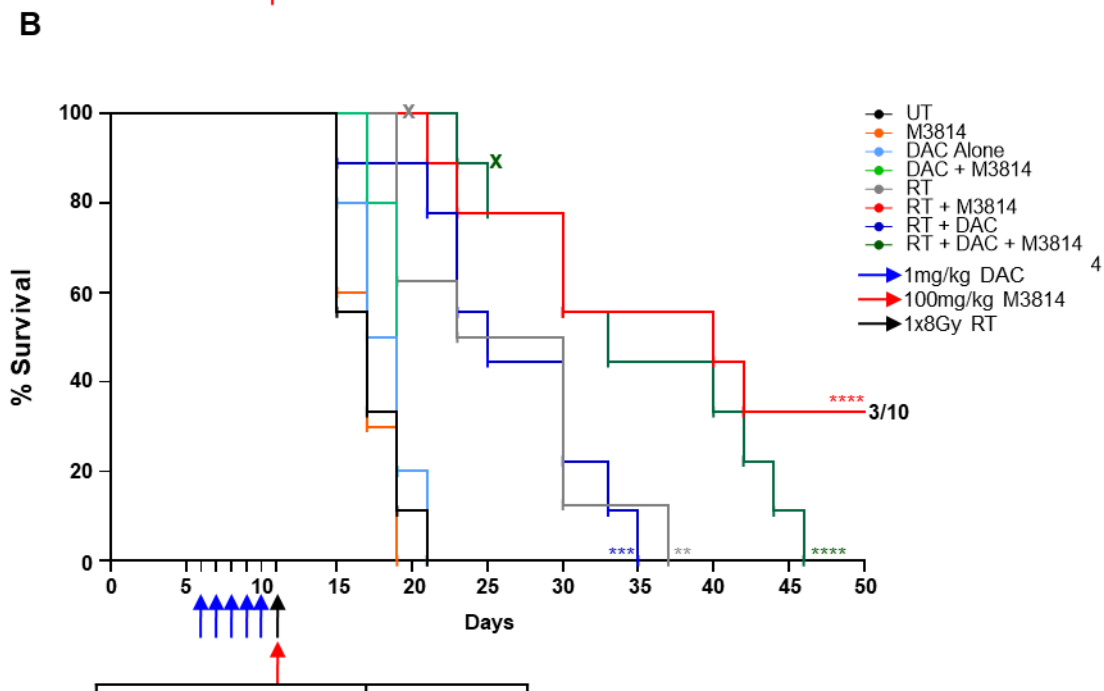

Comparison	P Value
UT vs RT	0.0011
UT vs RT+M3814	<0.0001
UT vs RT+DAC	0.0003
UT vs RT+DAC+M3814	<0.0001

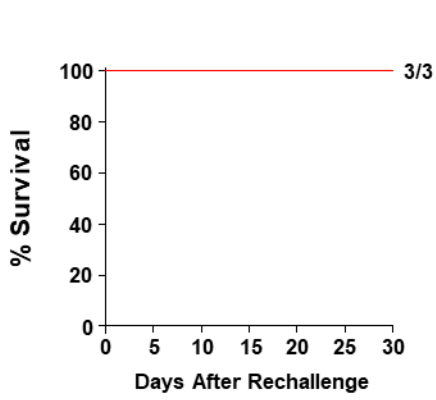

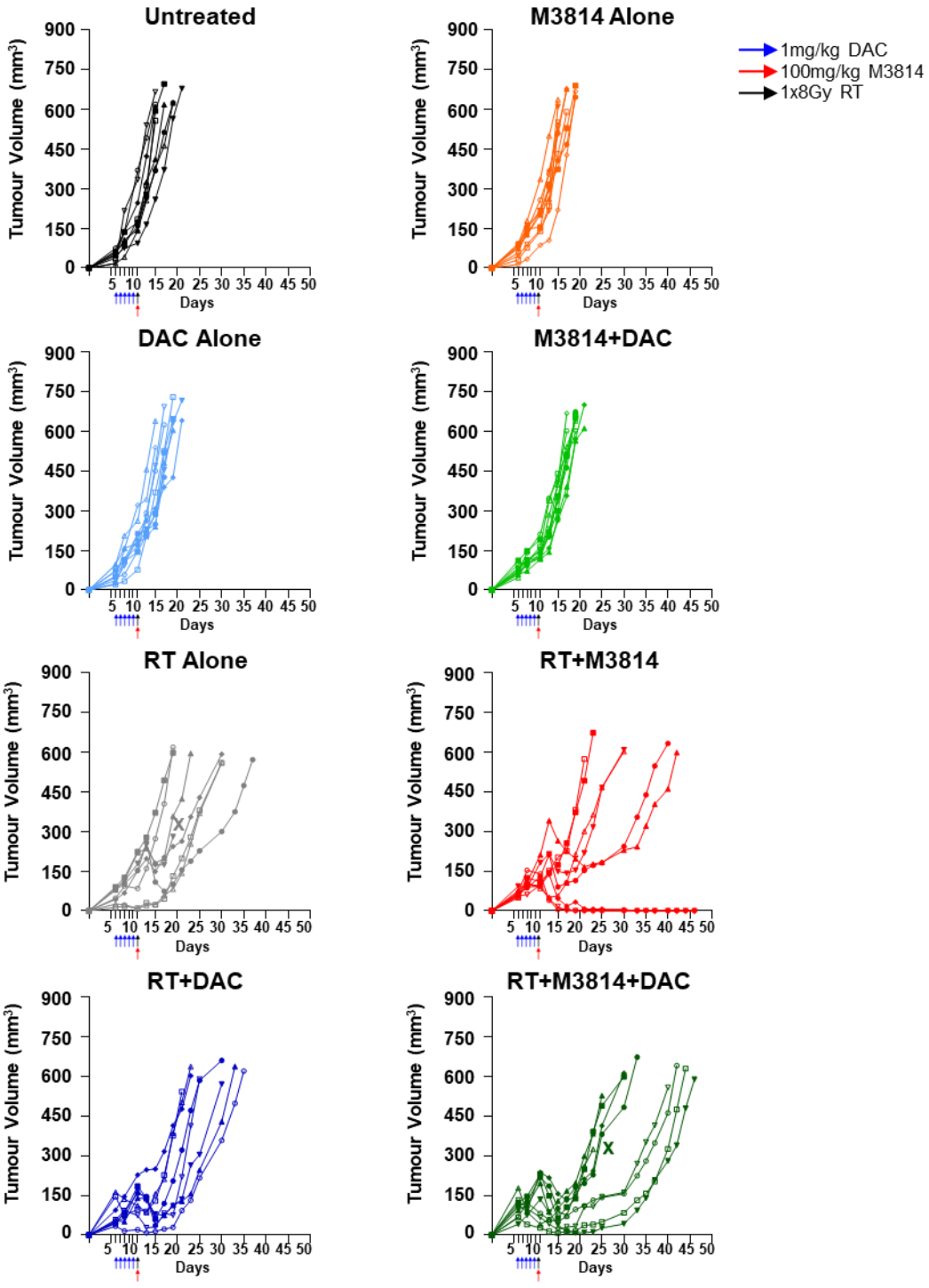

Figure 5. 8. Radiotherapy improves MC38 tumour control in vivo and RT+M3814 leads to complete tumour control - individual mice data.

C57BL/6 mice were inoculated with $5x10^5$ MC38 cells via S.C. injection. On day 6, mice were treated with 1mg/kg DAC for 5 consecutive days. On day 11, 100mg/kg M3814 was administered via O.G. and one hour later mice were treated with CT guided 1x8Gy radiotherapy to the tumours. Tumour volume was recorded 3 times a week until mouse reached humane endpoint, tumour > $600mm^3$ or ulceration, at which point mouse was culled. X denotes where a mouse was sacrificed due to ulceration. Tumour growth curves of individual mouse in each treatment group shown.

5.3.4. KP.B6.F1 tumours in mice treated with IR+M3814+DAC have an increased inflammatory tumour microenvironment.

Previous experiments indicate that treatment with radiotherapy and M3814 may increase immunogenicity through the induction of ICD and cGAS-STING pathway activity when combined with decitabine. Therefore, the tumour immune microenvironment was characterised KP.B6.F1 tumour-bear mice, treated with decitabine, radiotherapy and M3814. To do so, the same experimental procedure described in previous section was performed, however M3814 alone and DAC+M3814 were excluded. Reducing the number of samples ensured that samples could be processed quickly enough to preserve the data. Based on the tumour growth curves (Figure 5.4 A) day 18 was selected as the endpoint. On this day, the mice were culled. TDLNs and tumours were harvested and processed into a single cell suspension. Flow cytometry was performed using two antibody panels to characterise both the myeloid and lymphoid compartments. This experimental plan is shown in Figure 5.9.

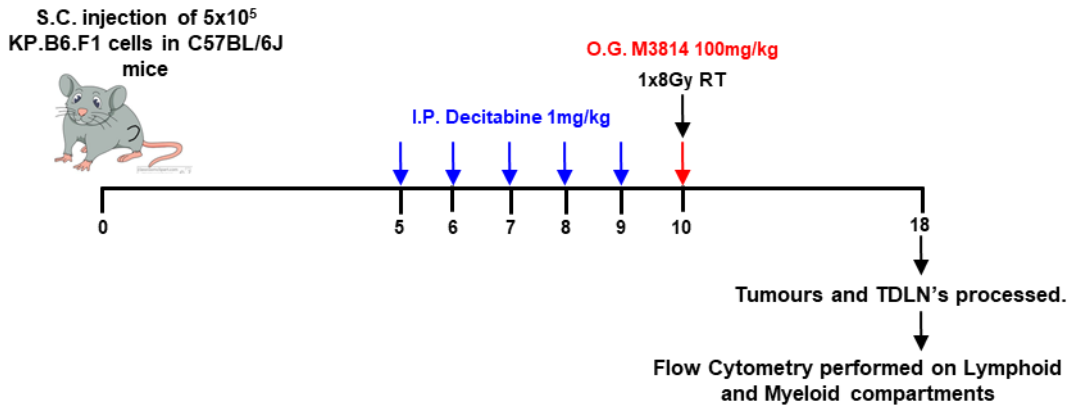

Figure 5. 9. Experimental plan for KP.B6.F1 in vivo functional experiment.

Illustration showing the experimental plan to compare the effects and combination of decitabine, radiotherapy and M3814 on the myeloid and lymphoid compartments of TDLNs and tumours. One experiment performed with 5 mice per treatment group (total 30 mice).

To analyse the different populations of cells, the t-distributed stochastic neighbour embedding (t-SNE) statistical method was used. This is a visualisation tool that applies an algorithm to the high-dimension single-cell flow cytometry data to create a

dot plot. Each dot represents a cell and its location relative to others indicates their similarity based on the expression of the selected markers. Similar cells group together and the profile of markers within the cluster can indicate what cell type that cluster contains [190]. The t-SNE plot were generated from a random selection of 5000 cells from each sample to ensure all populations were represented. To visualise how different treatments may affect clusters, samples were grouped together in their treatment groups.

First, the results for the lymphoid panel will be discussed. Figure 5.10 shows the resulting t-SNE plots of data concatenated from all tumour and T DLN samples from down sampled samples of all collected samples, both TIL's and TDLNs. These samples were preselected for living $CD45^{+}CD3^{+}$ cells. In Figure 5.10 the expression of each marker used for t-SNE clustering can be seen, which allows for the identification of cell subsets. Samples were concatenated into their treatment groups, rather than all together and t-SNE analysis was performed (Figure 5.10). Key T cell populations were identified, this includes Teffs ($CD4^{+}FoxP3^{-}$) , Tregs ($CD4^{+}FoxP3^{+}$), and $CD8^{+}$ t cells ($CD8^{+}$). There were two sub-populations of $CD8^{+}$ t cells, one of which was predominately found in the TDLNs and the other in tumours. These populations were labelled on the treatment group t-SNE plots (Figure 5.11). Figure 5.11 A shows t-SNE plots of different treatment groups in cells from TDLNs, whereas Figure 5.11 B shows data obtained from TILs.

Figure 5. 10. t-SNE map of combined TDLNs and TILs showing expression of lymphoid phenotypic markers.

Next page. C57BL/6 mice were inoculated with $5x10^{5}$ KP.B6.F1 cells via S.C. injection. On day 5, mice were treated with 1mg/kg DAC for 5 consecutive days. On day 10, 100mg/kg M3814 was administered via O.G. and one hour later mice were treated with CT guided 1x8Gy radiotherapy to the tumours. On day 18, TDLNs and tumours were collected, processed into single cell suspension, and stained using lymphoid phenotypic markers. Flow cytometry was performed and resulting data from all samples was down sampled and concatenated. T-SNE mapping was ran using the Barnes-Hut algorithm with 1000 iterations and a perplexity of 30. The fluorescence of markers used for t-SNE creation is shown on the resulting t-SNE plots.

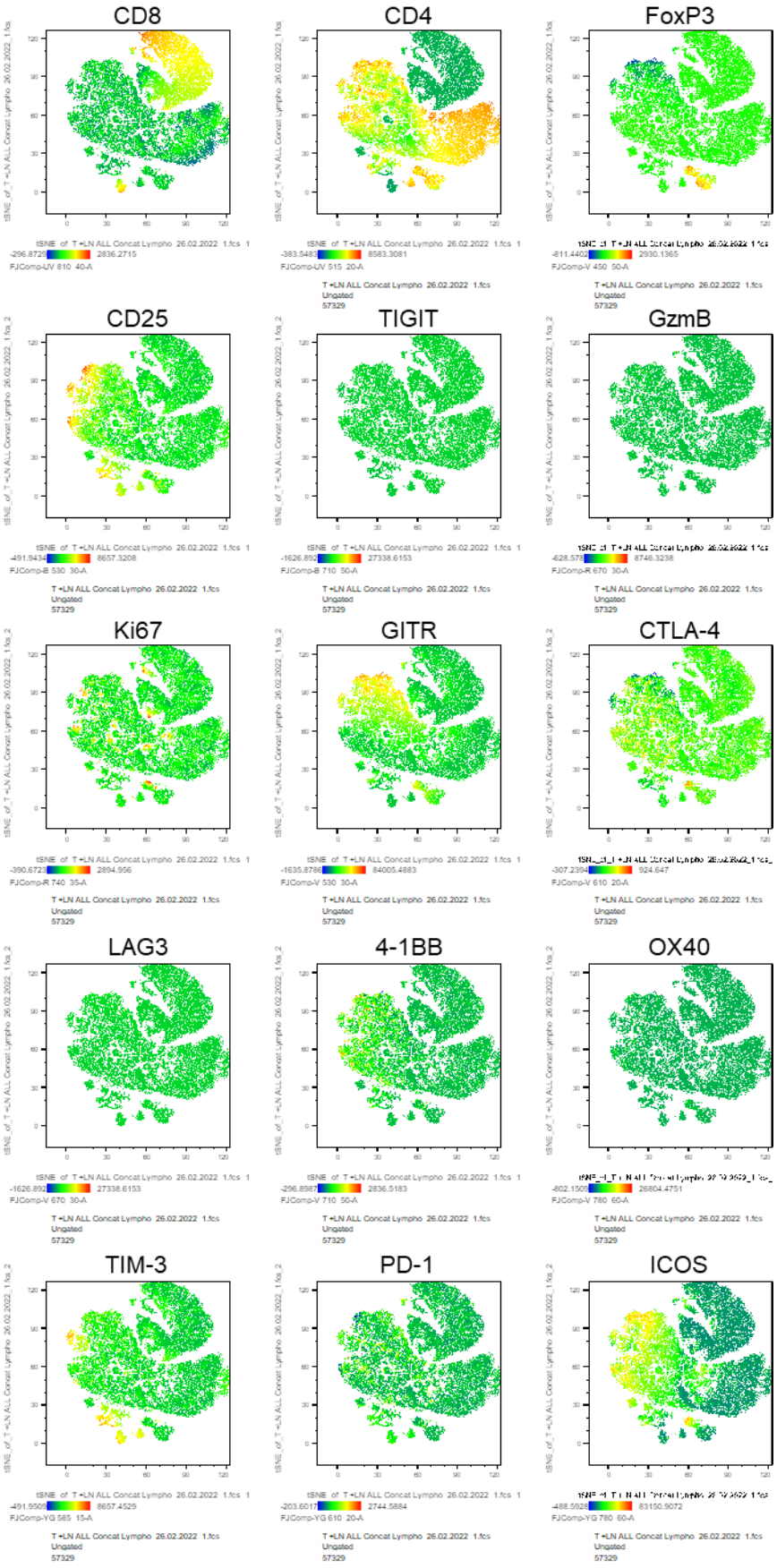
CD8
CD4
FoxP3
CD25
TIGIT
GzmB
Ki67
GITR
CTLA-4
LAG3
4-1BB
OX40
TIM-3
PD-1
ICOS

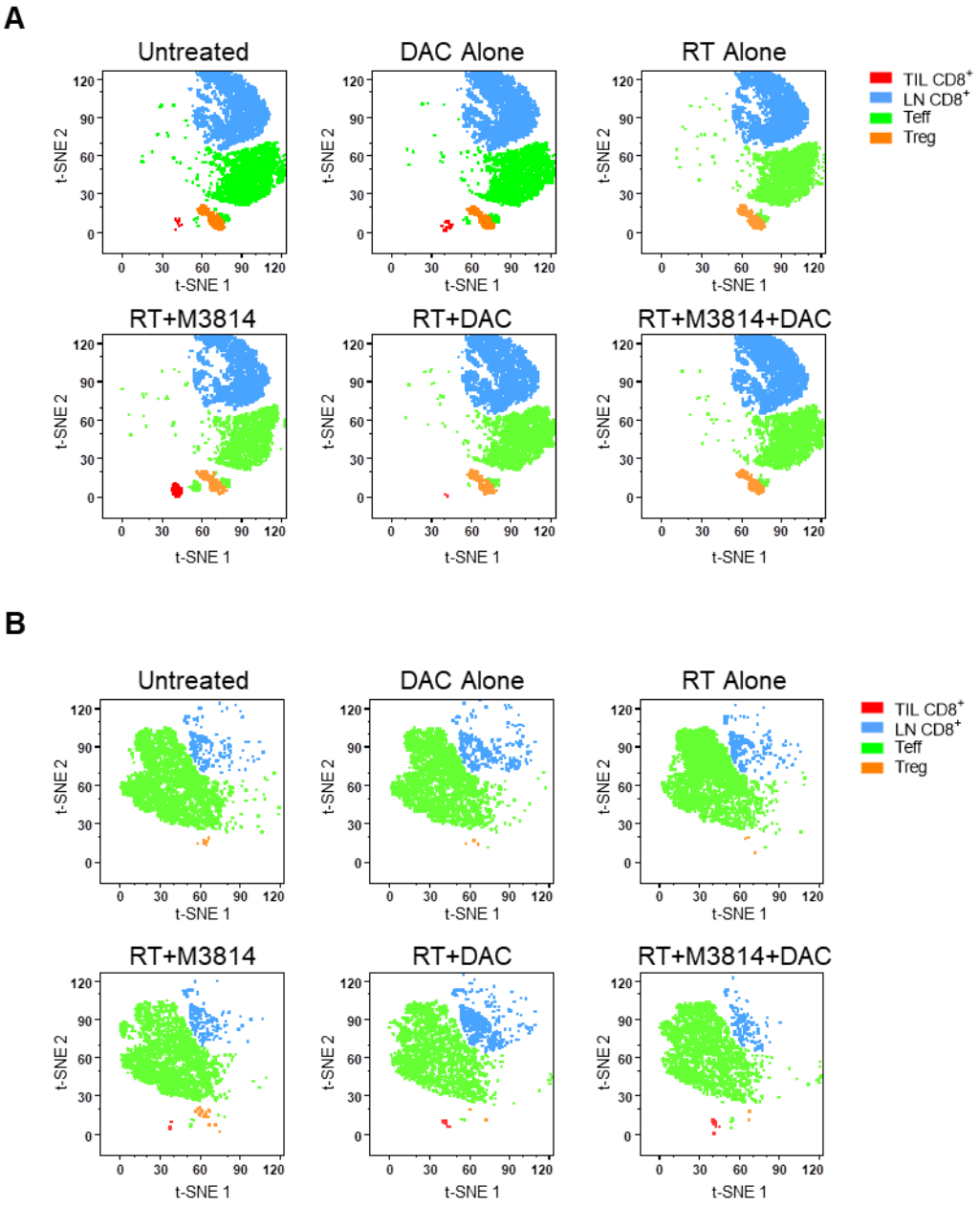

Figure 5. 11. Manual phenotypic gating on lymphoid t-SNE map of treatment groups.

C57BL/6 mice were inoculated with $5x10^5$ KP.B6.F1 cells via S.C. injection. On day 5, mice were treated with 1mg/kg DAC for 5 consecutive days. On day 10, 100mg/kg M3814 was administered via O.G. and one hour later mice were treated with CT guided 1x8Gy radiotherapy to the tumours. On day 18, TDLNs and tumours were collected, processed into single cell suspension, and stained using lymphoid phenotypic markers. Flow cytometry was performed and resulting data from all samples was down sampled and concatenated into treatment groups. T-SNE maps drawn for each treatment groups and Teffs, Tregs and $CD8^+$ drawn using manual gating. T-SNEs shown for **(A)** TDLNs **(B)** Tumours. T-SNE mapping was ran using the Barnes-Hut algorithm with 1000 iterations and a perplexity of 30. The fluorescence of markers used for t-SNE creation is shown on the resulting t-SNE plots.

To allow for quantification of T cell clusters, the algorithm FlowSOM (Self Organising Maps) was performed on the concatenated data of all samples identify clusters in an unsupervised manner. Using FlowSOM, 12 key clusters were identified. Mapping these clusters onto the previously generated t-SNE plots (Figure 5.12), allowed for verification that these clusters do indeed represent similar cell types (Figure 5.12 A). Using FlowSOM, a heatmap, shown in Figure 5.12 B, was generated to better understand how the clusters differentiated by the expression of the marker used. Using this heatmap, key populations of cells were identified. While visually there appears to be some differences between the clusters per treatment groups shown in Figure 5.11, unfortunately due to low cell numbers in some samples the decision was made not to quantify these clusters using this method. Instead, manual gating was performed to quantify the clusters of interest identified using FlowSOM.

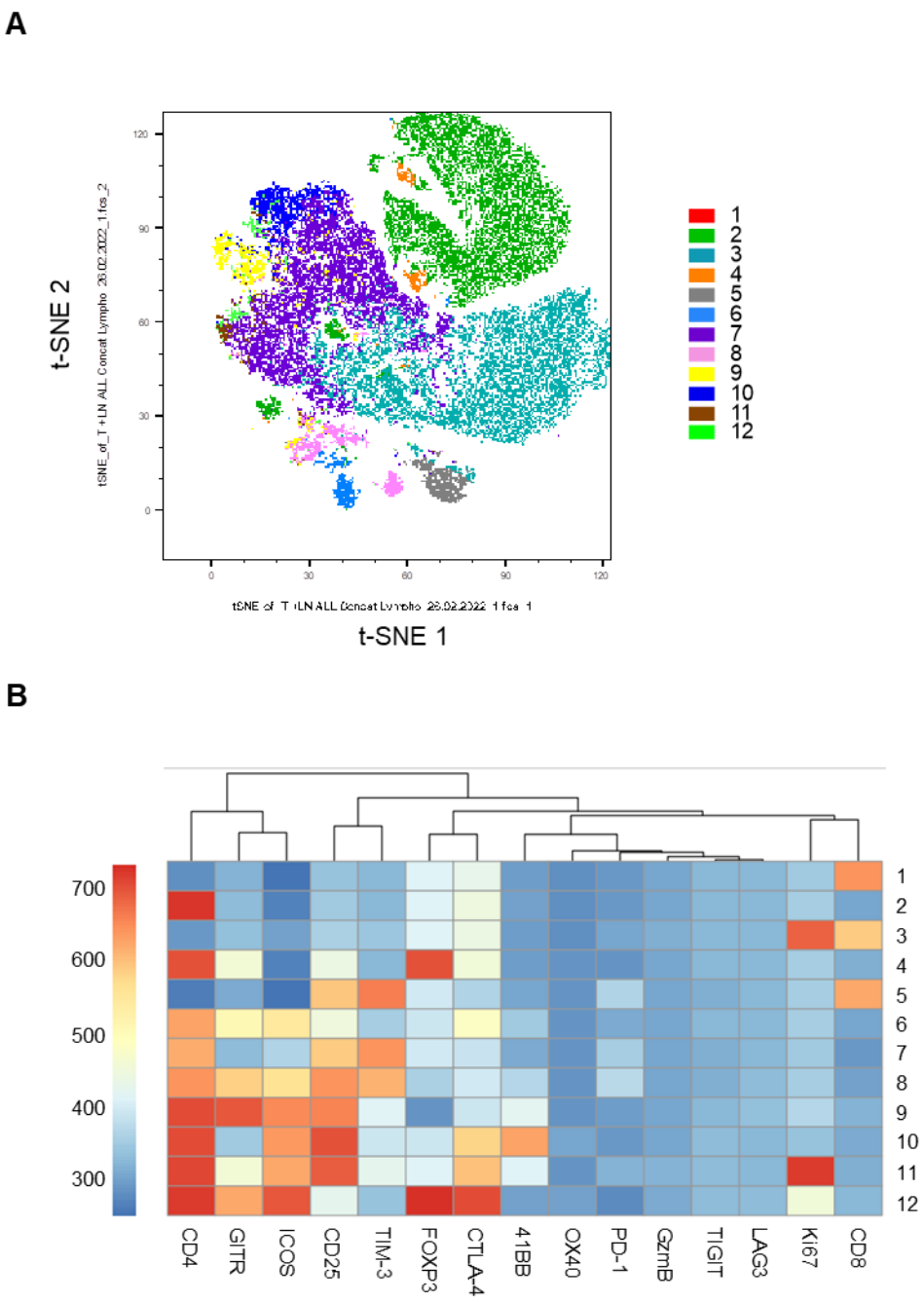

Figure 5. 12. FlowSOM analysis of lymphoid markers identifies 12 different cell populations.

C57BL/6 mice were inoculated with 5x10^5 KP.B6.F1 cells via S.C. injection. On day 5, mice were treated with 1mg/kg DAC for 5 consecutive days. On day 10, 100mg/kg M3814 was administered via O.G. and one hour later mice were treated with CT guided 1x8Gy radiotherapy to the tumours. On day 18, TDLNs and tumours were collected, processed into single cell suspension, and stained using lymphoid phenotypic markers. Flow cytometry was performed and resulting data from all samples was down sampled and concatenated. FlowSOM algorithm was performed with 18 meta-clusters. **(A)** Resulting FlowSOM populations plotted onto previously drawn t-SNE map **(B)** Heatmap showing expression of markers used for FlowSOM analysis per identified cluster.

5.3.4.1. Treatment with IR+M3814+DAC alters the tumour lymphoid compartment.

First, the main T cell subsets were quantified: Teffs ($CD3^+CD4^+Foxp3^-$), Tregs ($CD3^+CD4^+Foxp3^+$) and $CD8^+$ t cells ($CD3^+CD8^+$). In TDLNs, there was no significant change in the frequency of these groups between treatments (Figure 5.13). Within the $CD3^+$ population, Teff cells comprised between 40.3% to 43.5%, $CD8^+$ t cells

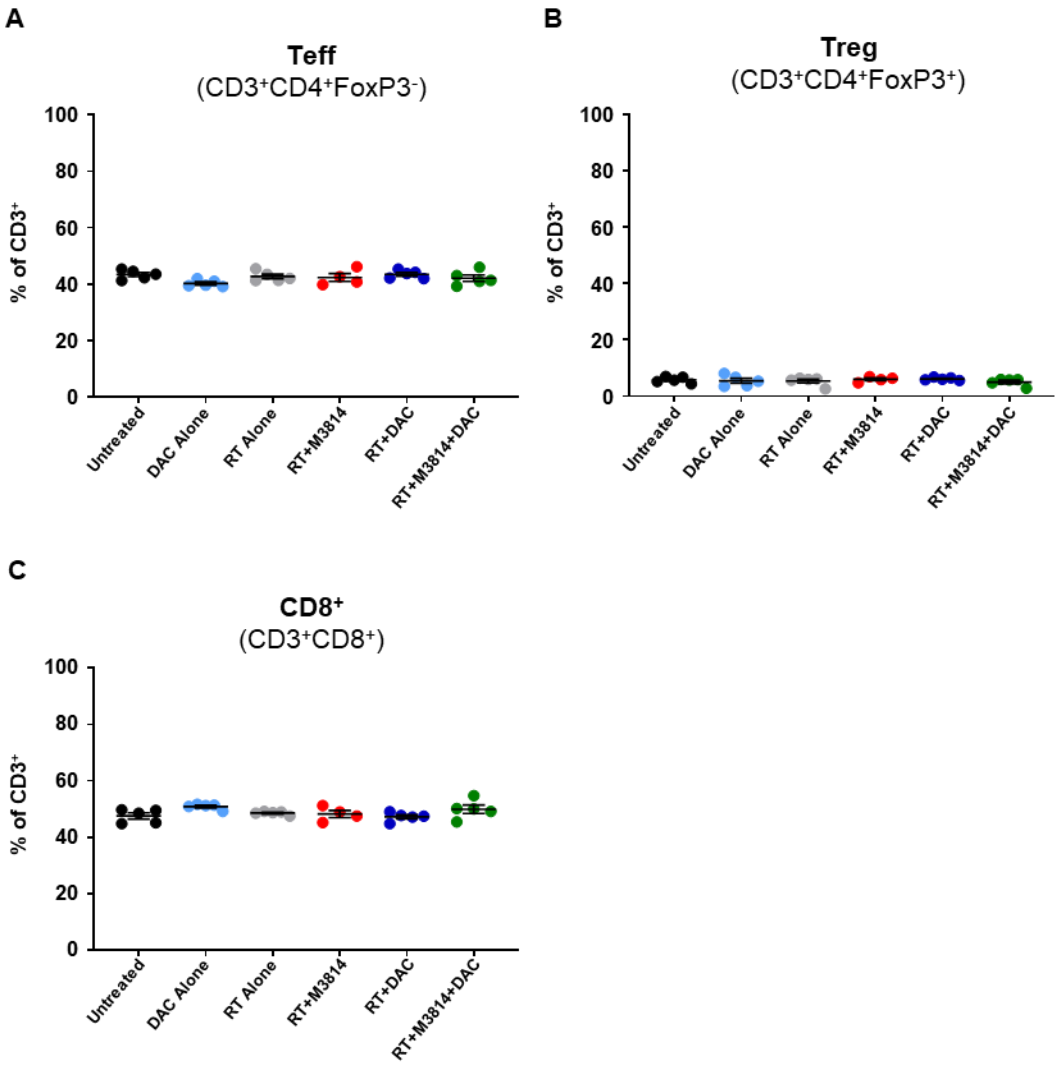

Figure 5. 13. The % of CD3+ that were Teff, Treg and CD8+ T cells remain unchanged with treatments in TDLNs.

C57BL/6 mice were inoculated with $5x10^5$ KP.B6.F1 cells via S.C. injection. On day 5, mice were treated with 1mg/kg DAC for 5 consecutive days. On day 10, 100mg/kg M3814 was administered via O.G. and one hour later mice were treated with CT guided 1x8Gy radiotherapy to the tumours. On day 18, TDLNs and tumours were collected, processed into single cell suspension, and flow cytometry performed using lymphoid panel. Manual gating performed to determine % of $CD45^+CD3^+$ cells in the TDLNs that were **(A)** Teffs **(B)** Tregs **(C)** $CD8^+$ T cells. Data shown as individual mice (5 per group) and average±SEM and analysed by one-way ANOVA followed by Bonferroni's multiple comparison test: *p<0.05, **p<0.01, ***p<0.001 ****p<0.0001.

contributed between 47.6% and 50.9%, while Tregs made up the small portion between 5% and 6% (Figure 5.13).

Within the tumours, the composition of $CD3^+$ cells in TILs differed from the TDLNs (Figure 5.14). Here, the majority were Teffs, making up 73.0% to 85.7% of $CD3^+$ cells. Between 2.5% and 11.8% were $CD8^+$ T cells, while Tregs contributed up to 2%

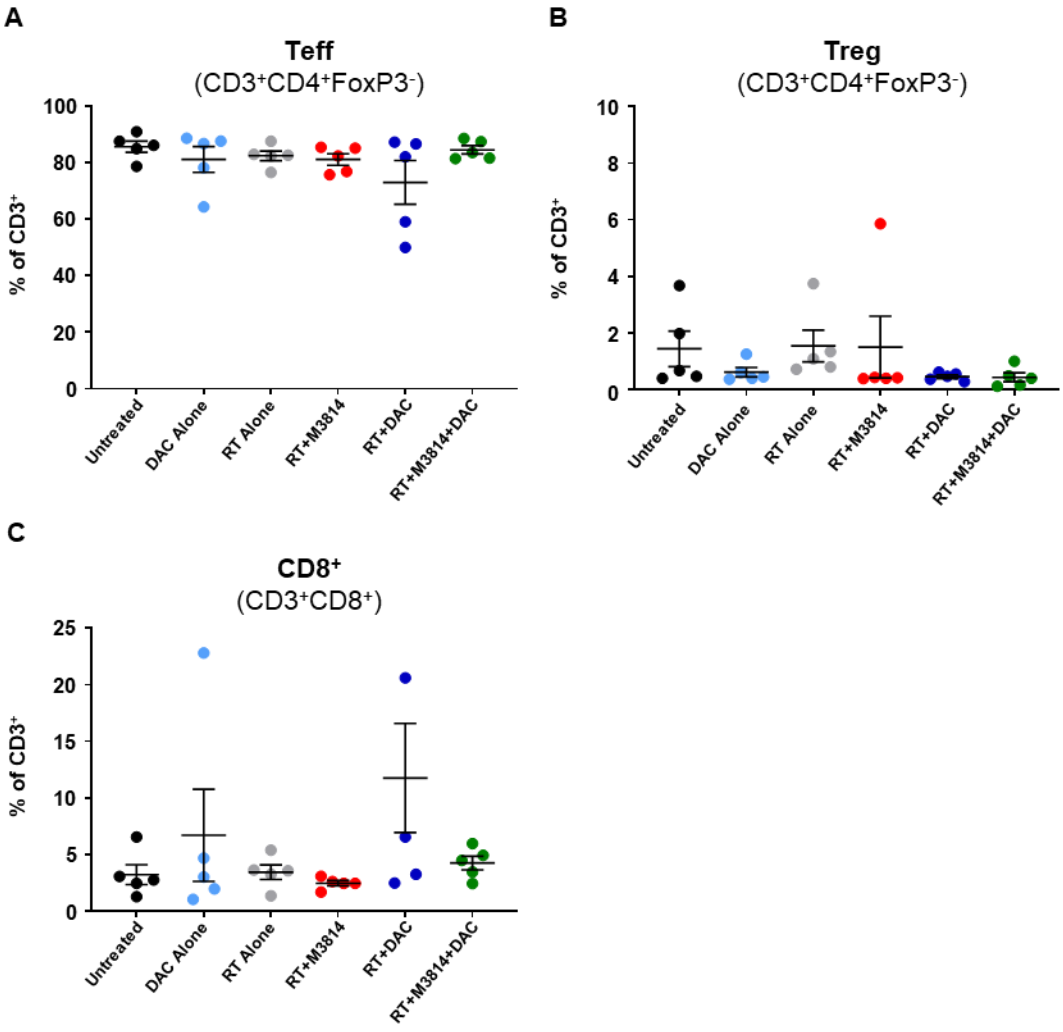

Figure 5. 14. The % of CD3+ that were Teff, Treg and CD8+ T cells remain unchanged with treatments in tumours.

C57BL/6 mice were inoculated with $5x10^5$ KP.B6.F1 cells via S.C. injection. On day 5, mice were treated with 1mg/kg DAC for 5 consecutive days. On day 10, 100mg/kg M3814 was administered via O.G. and one hour later mice were treated with CT guided 1x8Gy radiotherapy to the tumours. On day 18, TDLNs and tumours were collected, processed into single cell suspension, and flow cytometry performed using lymphoid panel. Manual gating performed to determine % of $CD45^+CD3^+$ cells in the tumour that were **(A)** Teffs **(B)** Tregs **(C)** $CD8^+$ T cells. Data shown as individual mice (5 per group) and average±SEM and analysed by one-way ANOVA followed by Bonferroni's multiple comparison test: *p<0.05, **p<0.01, ***p<0.001 ****p<0.0001.

(Figure 5.14). As seen in TDLNs, there was no significant changes to the frequency of any of these main cell types with treatment. The absolute number of each T cell type per gram of tumour were also not significantly altered by treatment (Figure 5.15).

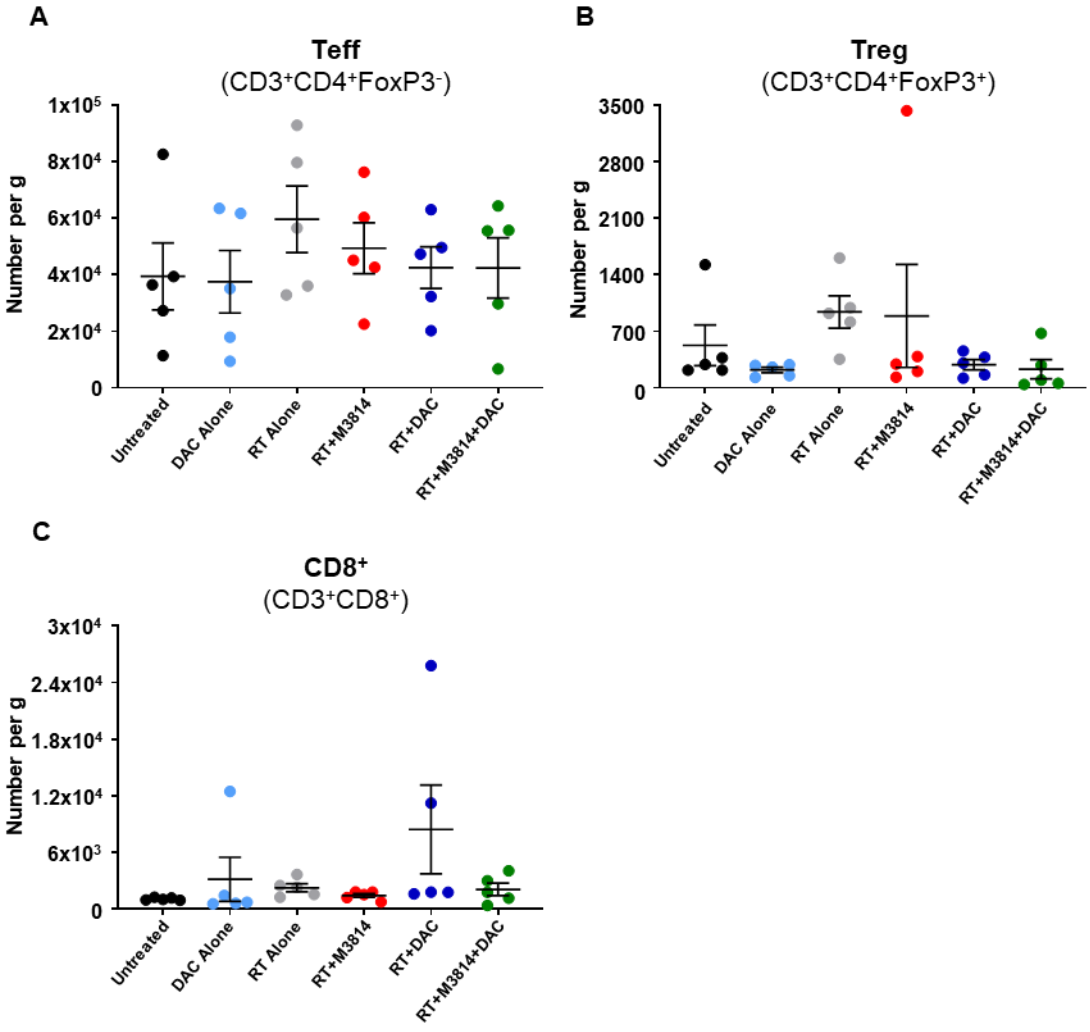

Figure 5. 15. Absolute number of Teff, Treg and CD8+ T cells remain unchanged with treatments in tumours.

C57BL/6 mice were inoculated with $5x10^5$ KP.B6.F1 cells via S.C. injection. On day 5, mice were treated with 1mg/kg DAC for 5 consecutive days. On day 10, 100mg/kg M3814 was administered via O.G. and one hour later mice were treated with CT guided 1x8Gy radiotherapy to the tumours. On day 18, TDLNs and tumours were collected, processed into single cell suspension, and flow cytometry performed using lymphoid panel. Manual gating performed to count the T cell subsets. Counts were then calculated per gram of tumour. **(A)** Teffs **(B)** Tregs **(C)** $CD8^+$ T cells. Data shown as individual mice (5 per group) and average±SEM and analysed by one-way ANOVA followed by Bonferroni's multiple comparison test: *p<0.05, **p<0.01, ***p<0.001 ****p<0.0001.

FlowSOM analysis identified 7 key Teff clusters including 2, 6, 7, 8, 9, 10 and 11. Cluster 2 cells were $CD4^+$ but negative for any other markers, indicating these are naïve $CD4^+$ T cells. CD25 and ICOS were key markers leading to differentiation of these clusters, therefore, three groups were focused upon. Those that were $ICOS^-CD25^+$ (cluster 6), $ICOS^+CD25^-$ (cluster 7) and those which were $ICOS^+CD25^+$ (clusters 8-11). ICOS is a co-stimulatory molecule that enhances Teff cell effector activity and cell proliferation [191]. CD25 is a receptor for Interleukin-2 (IL-2) and is typically regarded as an activation marker. As would be expected in the TDLNs, a place with little antigen exposure, the dominant Teff subset were the naïve Teffs ($ICOS^-CD25^-$) comprising between 89.9% (±7.8) in untreated mice to 94.0% (±2.2) in those given RT+M3814 (Figure 5.16 A). The smallest proportion were the most active group, $ICOS^+CD25^+$(Figure 5.16 D). There was no statistically significant change in the frequency of these groups between treatments.

Inside the tumours, the composition of Teffs was more affected by the treatments compared to those in the TDLNs (Figure 5.17). The minority of Teffs were naïve Teffs, with 3.5% in RT+DAC+M3814 and 16.1% in RT+DAC treated mice (Figure 5.17 A). Therefore, most cells consisted of active Teffs defined by the expression of either ICOS or CD25. There was no significant change in the frequency of naïve Teffs with treatments. However, the frequency of $ICOS^-CD25^+$ Teffs was significantly influenced by treatment groups (one-way ANOVA, p=0.0007). Untreated, DAC alone, RT alone, RT+M3814 treated mice had relatively similar sized $ICOS^-CD25^+$ Teff populations, however this fell in RT+DAC treated mice, and further still in RT+DAC+M3814 treated mice. The lowest proportion of $ICOS^-CD25^+$ Teffs were found in tumours of mice treated with RT+DAC+M3814 at 4.4% (±5.4) of Teffs (Figure 5.16 B). This was significantly less than in untreated mice at 20.2% (±3.3)(Bonferroni's, p=0.0022), DAC alone at 16.7% (±4.2)(Bonferroni's, p=0.0257), RT alone at 18.3% (±3.8)(Bonferroni's, p=0.0084) and RT+M3814 treated mice at

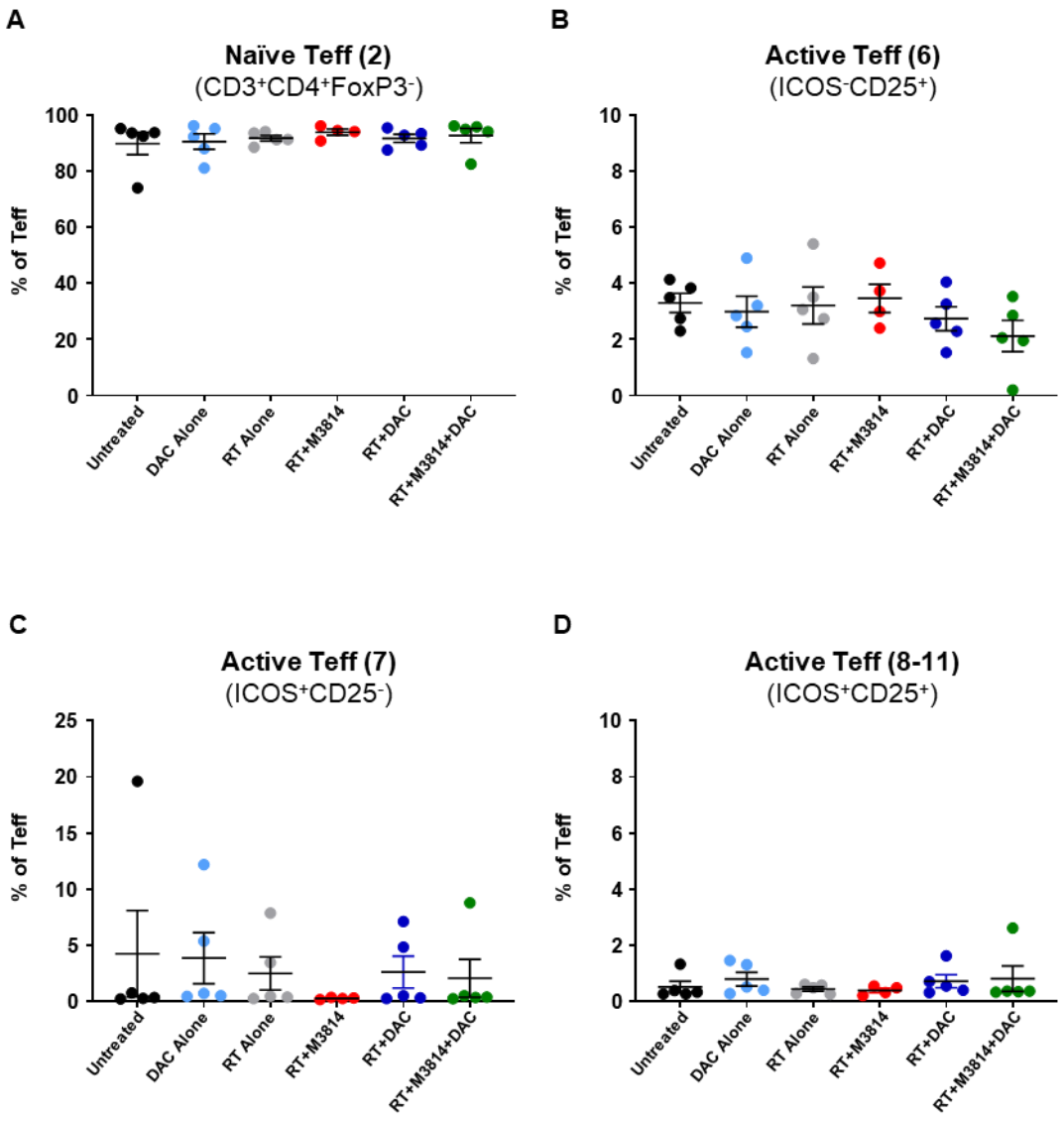

Figure 5. 16. Teff subsets remain unchanged with treatments in TDLNs.

C57BL/6 mice were inoculated with 5x10^5 KP.B6.F1 cells via S.C. injection. On day 5, mice were treated with 1mg/kg DAC for 5 consecutive days. On day 10, 100mg/kg M3814 was administered via O.G. and one hour later mice were treated with CT guided 1x8Gy radiotherapy to the tumours. On day 18, TDLNs and tumours were collected, processed into single cell suspension, and flow cytometry performed using lymphoid panel. Manual gating performed to determine % of Teffs in the TDLNs that were **(A)** Naïve **(B)** ICOS$^-$CD25$^+$ **(C)** ICOS$^+$CD25$^-$ **(D)** ICOS$^+$CD25$^+$. Data shown as individual mice (5 per group) and average±SEM and analysed by one-way ANOVA followed by Bonferroni's multiple comparison test: *p<0.05, **p<0.01, ***p<0.001 ****p<0.0001.

20.2% (±3.1)(Bonferroni's, p=0.0022). Treatment also had a significant effect on the proportion of ICOS$^+$CD25$^-$ Teffs (one-way ANOVA, p=0.0116)(Figure 5.17 C). While the frequency of ICOS$^-$CD25$^+$ Teffs fell in RT+DAC+M3814 treated mice, the opposite occurred in the ICOS$^+$CD25$^-$ Teff subset. In RT+DAC+M3814 treated mice this

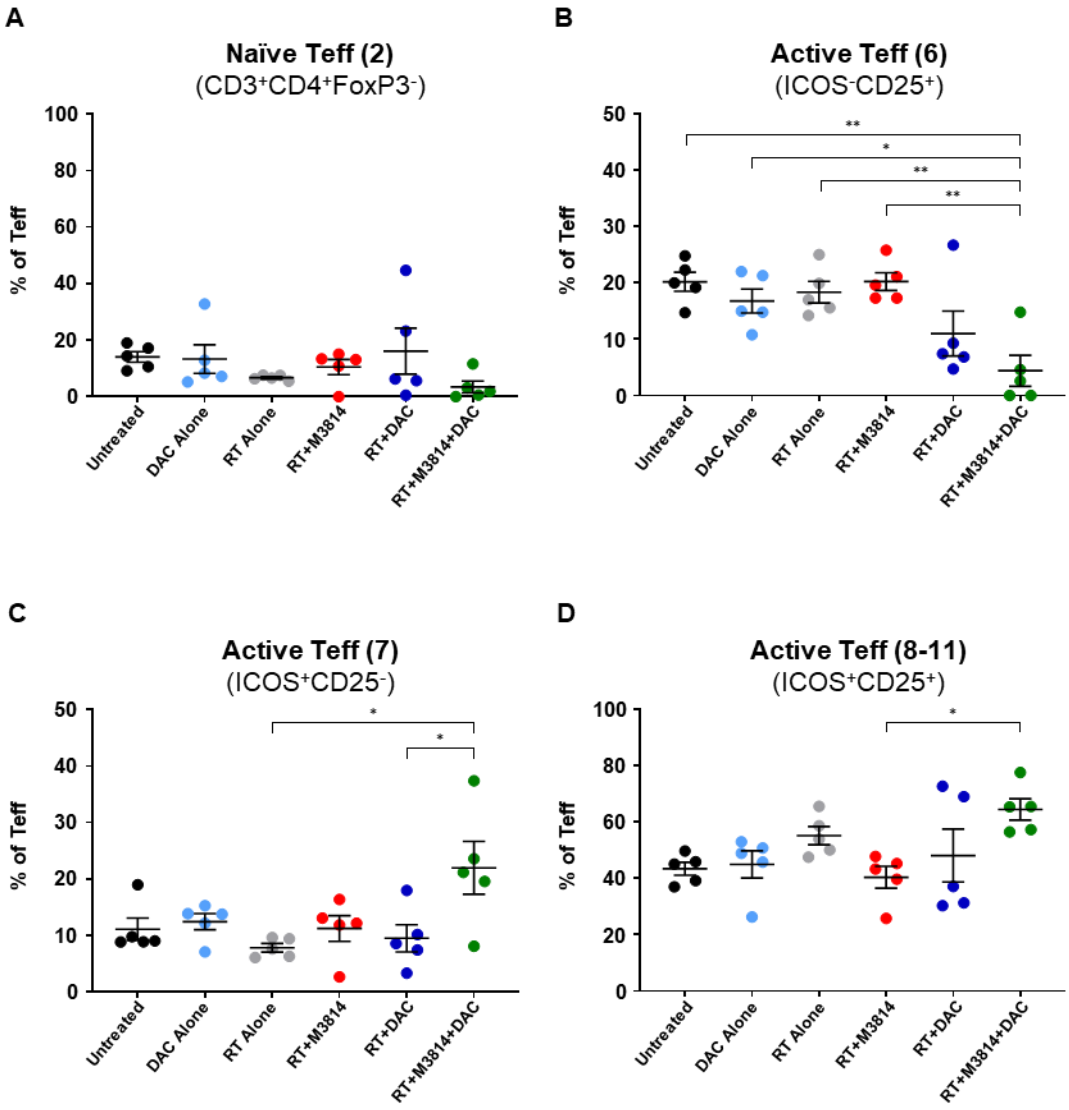

Figure 5. 17. Mice treated with RT+M3814+DAC have increased frequency of ICOS+CD25- and ICOS+CD25+ Teffs in tumours.

C57BL/6 mice were inoculated with 5x10^5 KP.B6.F1 cells via S.C. injection. On day 5, mice were treated with 1mg/kg DAC for 5 consecutive days. On day 10, 100mg/kg M3814 was administered via O.G. and one hour later mice were treated with CT guided 1x8Gy radiotherapy to the tumours. On day 18, TDLNs and tumours were collected, processed into single cell suspension, and flow cytometry performed using lymphoid panel. Manual gating performed to determine % of Teffs in the tumours that were **(A)** Naïve **(B)** ICOS$^-$CD25$^+$ **(C)** ICOS$^+$CD25$^-$ **(D)** ICOS$^+$CD25$^+$. Data shown as individual mice (5 per group) and average±SEM and analysed by one-way ANOVA followed by Bonferroni's multiple comparison test: *p<0.05, **p<0.01, ***p<0.001 ****p<0.0001.

increased to 22% (±9.2) from 7.9% (±1.5) in RT alone treated mice (Bonferroni's, p=0.0101) and 9.5% (±4.7) in RT+DAC treated mice (Bonferroni's, p=0.032). Finally, treatment also significantly affected the proportion of $ICOS^+CD25^+$ Teffs (one-way ANOVA, p=0.0282)(Figure 5.17 D). Similarly, to the $ICOS^+CD25^-$, the $ICOS^+CD25^+$ population is higher in the tumours of RT+DAC+M3814 treated mice at 64.5% (±7.5) - making up the majority of Teffs in RT+DAC+M3814 treated mice. This was significantly greater than RT+M3814 treated mice at 40.4% (±7.6) of Teffs (Bonferroni's, p=0.0416).

Next, the two clusters in the Treg subset were investigated (figure 5.18). These include cluster 4, which is negative for all markers and thus labelled as naïve, and cluster 12 in which cells were $GITR^+ICOS^+CTLA\text{-}4^+$, indicating they are active. In TDLNs, the majority of Tregs, between 56.2% (±6.4) in RT alone treated mice and 62.5% (±2.1) in untreated, fitted the naïve phenotype. The active Tregs made up between 16.0% (±2.7) in untreated to 23% (±6.1) in RT alone (Figure 5.18 A&B). In the tumours, the opposite was the case. The active Tregs made up a larger proportion of Tregs ranging between 15.3% (±12.7) in DAC alone treated mice to 28.5% (±19.3)in RT+DAC+M3814, while naïve spanned from 1.8% (±2.5) in untreated to 12.1% (±13.3) in RT+DAC treated mice (Figure 5.18 C&D). The proportion of either Treg subset remained unchanged with treatments in both the TDLNs and tumours. The final lymphocyte subset to be discussed are the $CD8^+$ T cells (Figure 5.18). Based on the FlowSOM analysis, two key populations were identified, a naïve population (cluster 1) and a $Ki67^+$ population (cluster 3). Ki67 is a marker of proliferation indicating that these $Ki67^+$ $CD8^+$ T cells are active and undergoing expansion. As previously seen the majority of $CD8^+$ T cells in the TDLNs were naïve ranging between 93.5% (±5.8) in untreated mice to 97.5% (±0.7) in those receiving RT+M3814 (Figure 5.18 A). Despite representing the minority of $CD8^+$ T cells, the frequency of $Ki67^+$ $CD8^+$ T cells was significantly altered by treatment (one-way

ANOVA, p<0.0001)(Figure 5.18 B). The largest proportion of Ki67^{+} CD8^{+} T cells occurred in mice receiving RT+DAC with 4.6% (±0.8) of CD8^{+} T cells. This was greater than untreated at 3.3% (±0.4)(Bonferroni's, p=0.0387), and DAC alone at 3.1% (±0.5)(Bonferroni's, p=0.0074), and RT+M3814 at 2.3% (±0.7)(Bonferroni's,

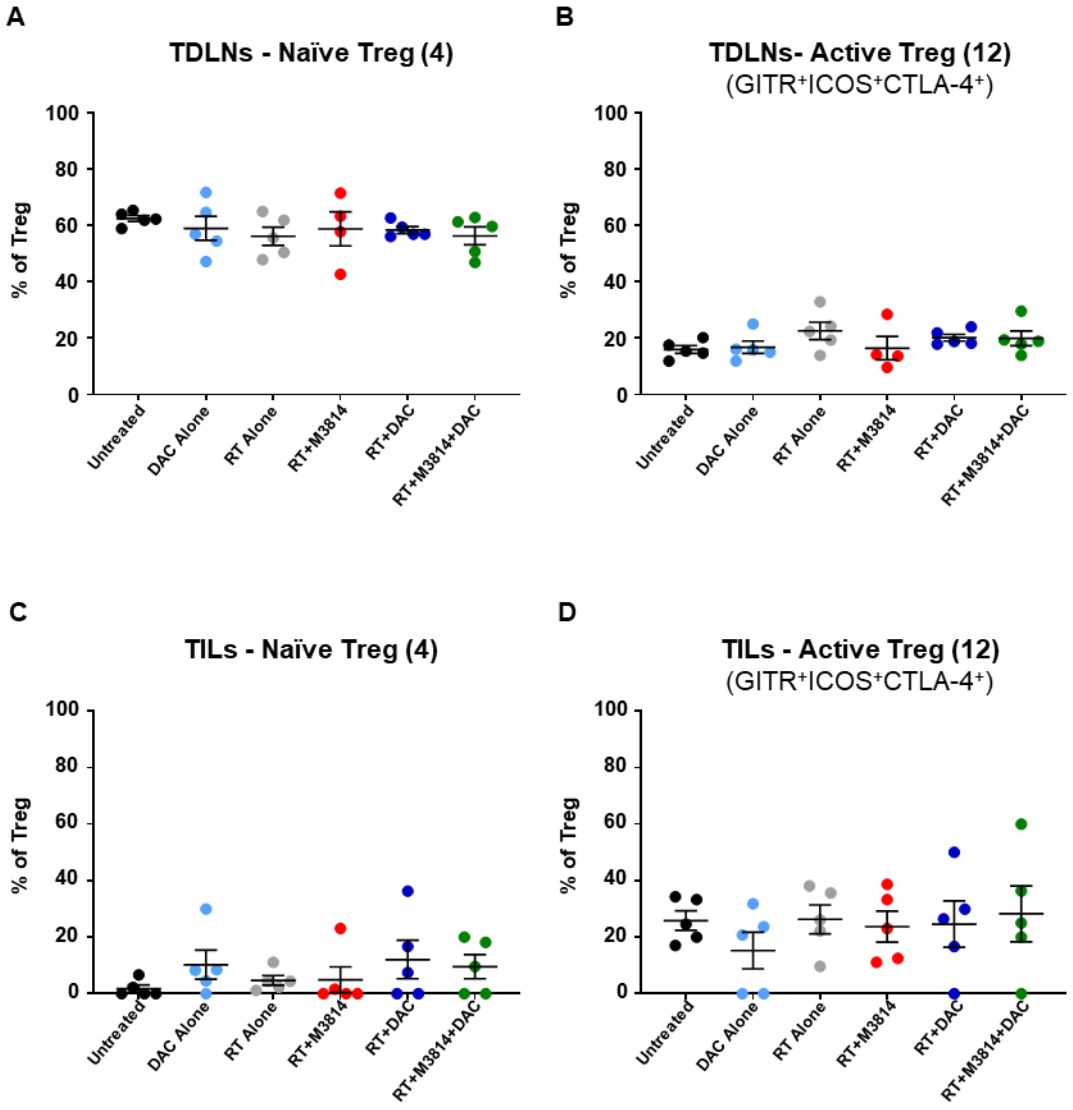

Figure 5. 18. Treg subsets remain unchanged with treatments in TDLNs and tumours.

C57BL/6 mice were inoculated with 5x10^{5} KP.B6.F1 cells via S.C. injection. On day 5, mice were treated with 1mg/kg DAC for 5 consecutive days. On day 10, 100mg/kg M3814 was administered via O.G. and one hour later mice were treated with CT guided 1x8Gy radiotherapy to the tumours. On day 18, TDLNs and tumours were collected, processed into single cell suspension, and flow cytometry performed using lymphoid panel. Manual gating performed to determine % of Tregs that were **(A)** Naïve in TDLNs **(B)** GITR^{+}ICOS^{+}CTLA-4^{+} in TDLNs **(C)** Naïve in tumours **(D)** GITR^{+}ICOS^{+}CTLA-4^{+} in tumours. Data shown as individual mice (5 per group) and average±SEM and analysed by one-way ANOVA followed by Bonferroni's multiple comparison test: *p<0.05, **p<0.01, ***p<0.001 ****p<0.0001.

p=0.0001) and in RT+DAC+M3814 treated mice at 2.7% (±0.2)(Bonferroni's, p=0.0005)(Figure 5.18 B).

Comparably to those seen in TDLNs, the $CD8^+$ T cells in the TIL population skewed towards the naïve phenotype (Figure 5.19 C&D). However, the proportion of naïve $CD8^+$ T cells was significantly influenced by the treatment received (one-way ANOVA, p=0.0041)(Figure 5.19 C). The lowest frequency of naïve $CD8^+$ T cells was 72.3% (±7.4) within the tumours of mice receiving RT+DAC+M3814. This was significantly less than the population size of 86.4% (±4.1) seen in tumours of mice treated with DAC alone (Bonferroni's, p=0.045), or 89.1% (±4.9) in those receiving RT alone (Bonferroni's, p=0.009). The reduction in naïve $CD8^+$ T cells frequency in mice treated with RT+DAC+M3814 was mirrored by an increase in the frequency of $Ki67^+$ $CD8^+$ T cells (Figure 5.19 D). Here, the $Ki67^+$ $CD8^+$ T cell population significantly rose from 9.4% (±5.3) in untreated mice (Bonferroni's, p=0.0352) and 7.9% (±5.6) in those treated with RT alone (Bonferroni's, p=0.0159) up to 25.1% (±6.4) upon RT+DAC+M3814 treatment.

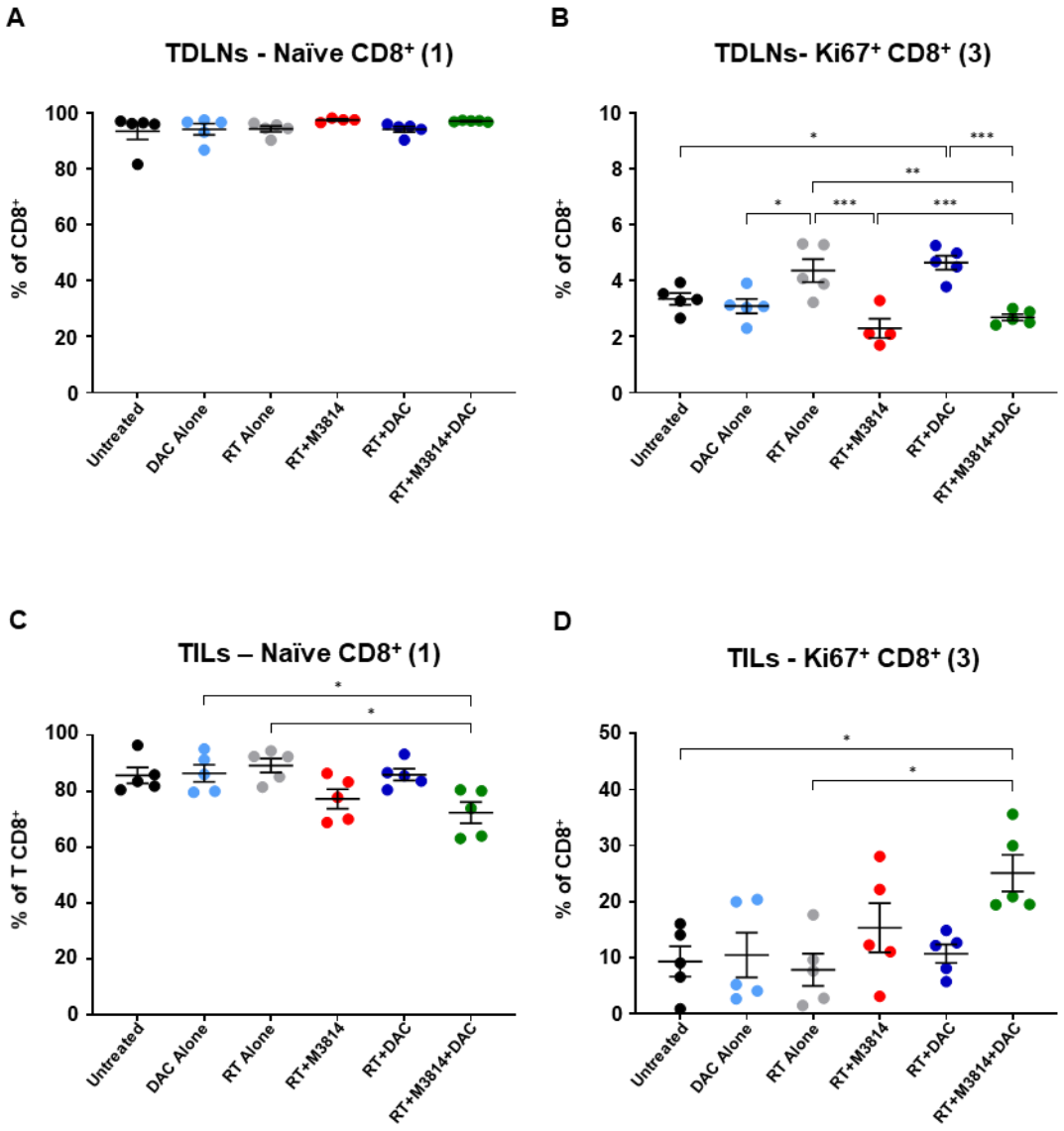

Figure 5. 19. CD8+ T cells in tumours are skewed towards an active phenotype.

C57BL/6 mice were inoculated with 5x10^5 KP.B6.F1 cells via S.C. injection. On day 5, mice were treated with 1mg/kg DAC for 5 consecutive days. On day 10, 100mg/kg M3814 was administered via O.G. and one hour later mice were treated with CT guided 1x8Gy radiotherapy to the tumours. On day 18, TDLNs and tumours were collected, processed into single cell suspension, and flow cytometry performed using lymphoid panel. Manual gating performed to determine % of CD8$^+$ T cells that were **(A)** Naïve in TDLNs **(B)** Ki67$^+$ in TDLNs **(C)** Naïve in tumours **(D)** Ki67$^+$ in tumours. Data shown as individual mice (5 per group) and average±SEM and analysed by one-way ANOVA followed by Bonferroni's multiple comparison test: *p<0.05, **p<0.01, ***p<0.001 ****p<0.0001.

5.3.4.2. Treatment with IR+M3814+DAC alters the tumour myeloid compartment.

Next, the myeloid compartment in both the tumours and TDLNs were characterised. Likewise, to the lymphoid compartment, t-SNE statistical analysis was performed on concatenated data from all samples. These samples were preselected as $CD45^+CD3^-CD19^+$. Figure 5.20 shows the expression of markers used mapped onto those resulting t-SNE plots. For example, cells in the region that is $CD68^+$ and $F4/80^+$ represent macrophages.

Samples were then concatenated into their treatment groups and t-SNE analysis was repeated for each group (Figure 5.21). Key cell populations, based on their expression of markers, were identified, and labelled on the t-SNE plots (Figure 21). These include monocytes, dendritic cells (DCs), NK Cells, macrophages, and granulocytes. There was also a population of cells that were $CD11b^+$ only. Figure 5.20 A shows t-SNE plots of different treatment groups in cells obtained from TDLNs, whereas Figure 5.21 B shows data obtained from tumours. This shows key differences between the populations of cells within the TDLNs and tumours, such as much more monocytes and the presence of macrophages in tumours. There are also differences in composition of cells between treatment groups, however, as mentioned in the lymphoid analysis a few samples had low cell numbers and so, cells were manually gated for quantification.

Figure 5. 20. t-SNE map of combined TDLNs and tumours showing expression of myeloid phenotypic markers.

Next page. C57BL/6 mice were inoculated with $5x10^5$ KP.B6.F1 cells via S.C. injection. On day 5, mice were treated with 1mg/kg DAC for 5 consecutive days. On day 10, 100mg/kg M3814 was administered via O.G. and one hour later mice were treated with CT guided 1x8Gy radiotherapy to the tumours. On day 18, TDLNs and tumours were collected, processed into single cell suspension, and stained using myeloid phenotypic markers. Flow cytometry was performed and resulting data from all samples was down sampled and concatenated. T-SNE mapping was ran using the Barnes-Hut algorithm with 1000 iterations and a perplexity of 30. The fluorescence of markers used for t-SNE creation is shown on the resulting t-SNE plots.

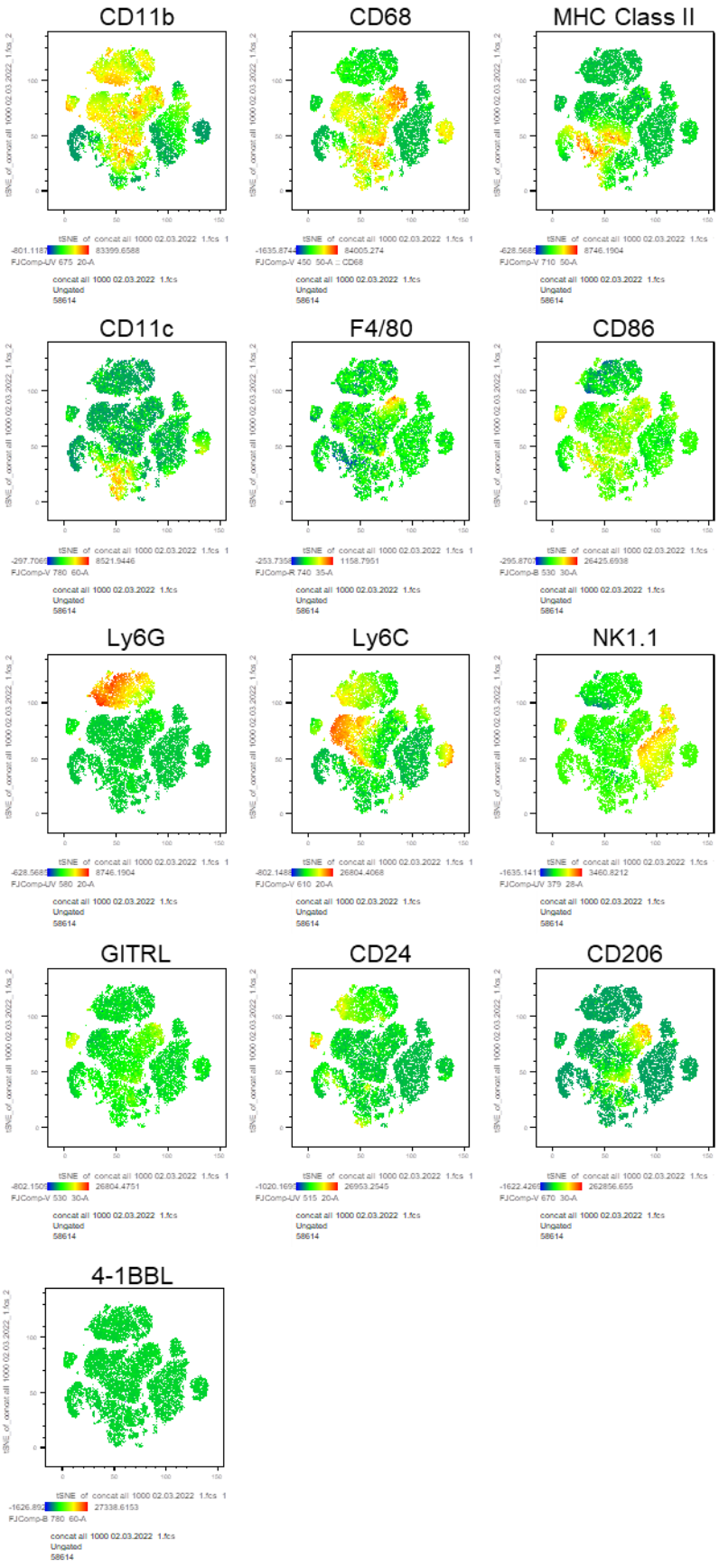
CD11b
CD68
MHC Class II
CD11c
F4/80
CD86
Ly6G
Ly6C
NK1.1
GITRL
CD24
CD206
4-1BBL

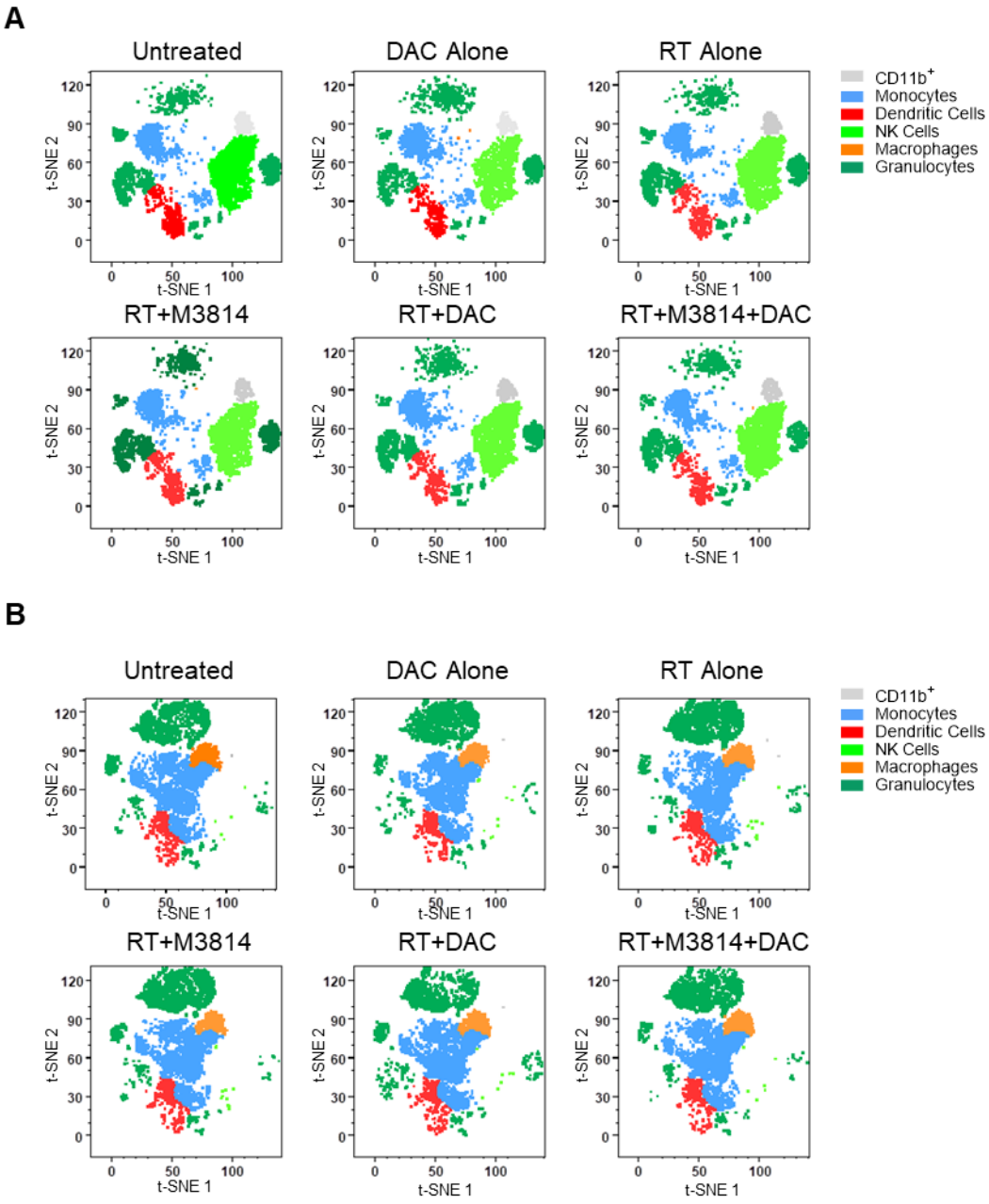

Figure 5. 21. Manual phenotypic gating on myeloid t-SNE map of treatment groups.

C57BL/6 mice were inoculated with $5x10^5$ KP.B6.F1 cells via S.C. injection. On day 5, mice were treated with 1mg/kg DAC for 5 consecutive days. On day 10, 100mg/kg M3814 was administered via O.G. and one hour later mice were treated with CT guided 1x8Gy radiotherapy to the tumours. On day 18, TDLNs and tumours were collected, processed into single cell suspension, and stained using myeloid phenotypic markers. Flow cytometry was performed and resulting data from all samples was down sampled and concatenated into treatment groups. T-SNE maps drawn for each treatment groups and monocytes, dendritic cells, NK cells and granulocytes drawn using manual gating. T-SNEs shown for **(A)** TDLNs **(B)** Tumours. T-SNE mapping was ran using the Barnes-Hut algorithm with 1000 iterations and a perplexity of 30. The fluorescence of markers used for t-SNE creation is shown on the resulting t-SNE plots.

The FlowSOM algorithm was performed, and 19 clusters were identified. These were mapped onto the t-SNE plot in Figure 5.22 A to show how the clusters may be related. A heatmap showing the expression of the markers for each cluster is shown in Figure 5.22 B. Manual gating was guided by the clusters generated by this algorithm.

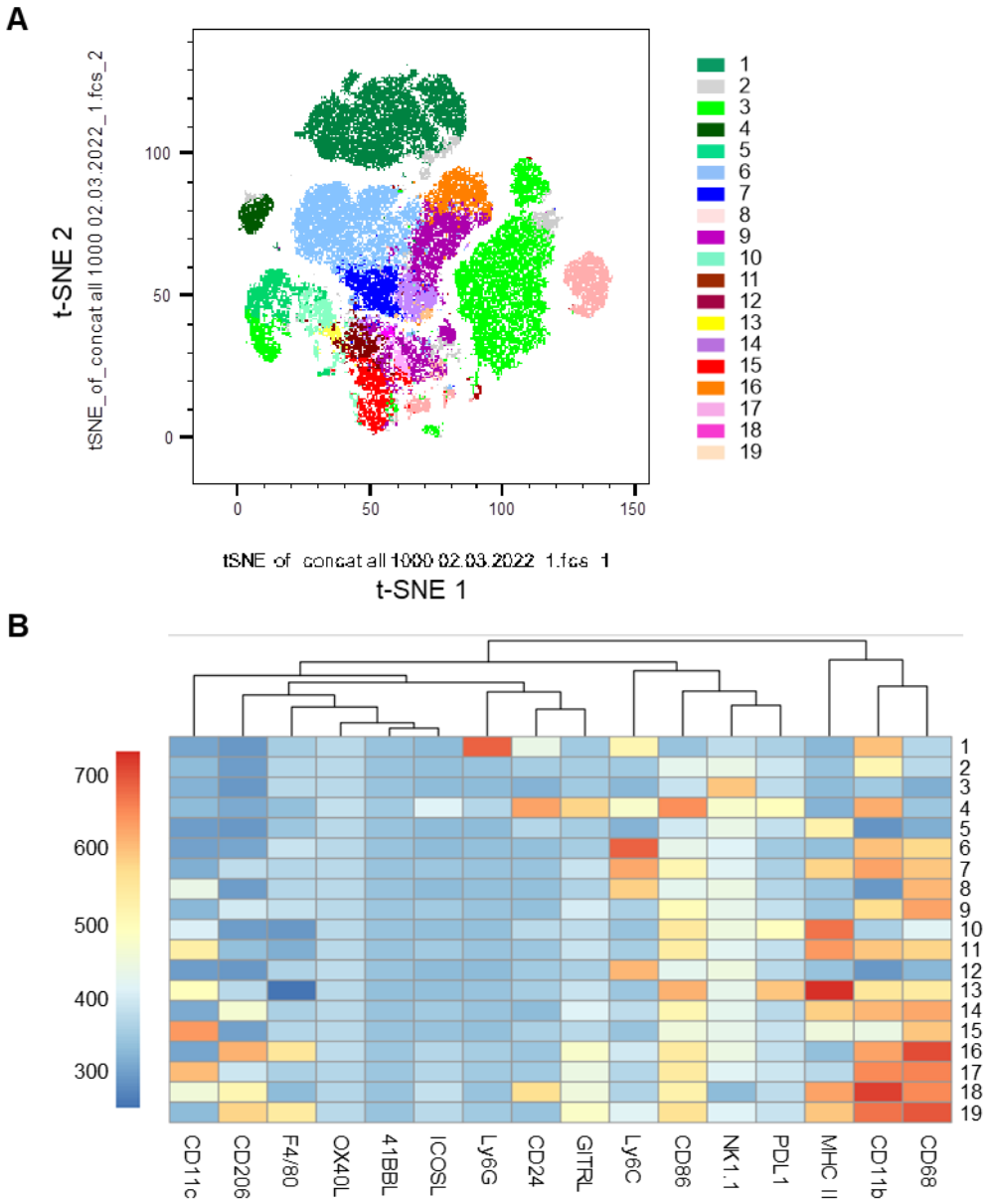

Figure 5. 22. FlowSOM analysis of myeloid markers identifies 19 cell populations.

C57BL/6 mice were inoculated with 5x10^5 KP.B6.F1 cells via S.C. injection. On day 5, mice were treated with 1mg/kg DAC for 5 consecutive days. On day 10, 100mg/kg M3814 was administered via O.G. and one hour later mice were treated with CT guided 1x8Gy radiotherapy to the tumours. On day 18, TDLNs and tumours were collected, processed into single cell suspension, and stained using myeloid phenotypic markers. Flow cytometry was performed and resulting data from all samples was down sampled and concatenated. FlowSOM algorithm was performed with 18 meta-clusters. **(A)** Resulting FlowSOM populations plotted onto previously drawn t-SNE map **(B)** Heatmap showing expression of markers used for FlowSOM analysis per identified cluster.

First, the frequency of four main cell populations were quantified. These included monocytes ($CD68^+CD11b^+CD11c^-F4/80^-$), macrophages ($CD68^+CD11b^+CD11c^-F4/80^+$), DCs ($CD11c^+$MHC II^+CD68^-) and granulocytes ($CD11b^+Ly6G^+$). Within the myeloid compartments in the TDLNs, monocytes made up the largest share (Figure 5.23). The percentage of monocytes ranged from the lowest in RT alone treated mice with 17.2% (±4.6) up to DAC alone treated cells with 25.2% (±6.0)(Figure 5.23 A). Within the TDLNs, macrophages made up a small proportion of $CD45^+CD3^-CD19^-$ cells, all below 0.5% (Figure 5.23 B). Only a small proportion of cells were determined to be DCs, ranging between 0.92 and 2.1% (Figure 5.22 C). Neither the monocytes, macrophages nor DCs population sizes were significantly affected by treatment (Figure 5.23 A-C). The proportion of granulocytes in TDLNs however, were significantly alters by treatments (one-way ANOVA, p=0.0185). The largest granulocyte population was observed in mice treated with DAC alone, at 12.0% (±3.4). This was significantly larger than in untreated mice at 4.9% (±1.9)(Bonferroni's, p=0.0349) and RT alone with 4.8% (±0.6)(Bonferroni's, p=0.0331)(Figure 5.23 D).

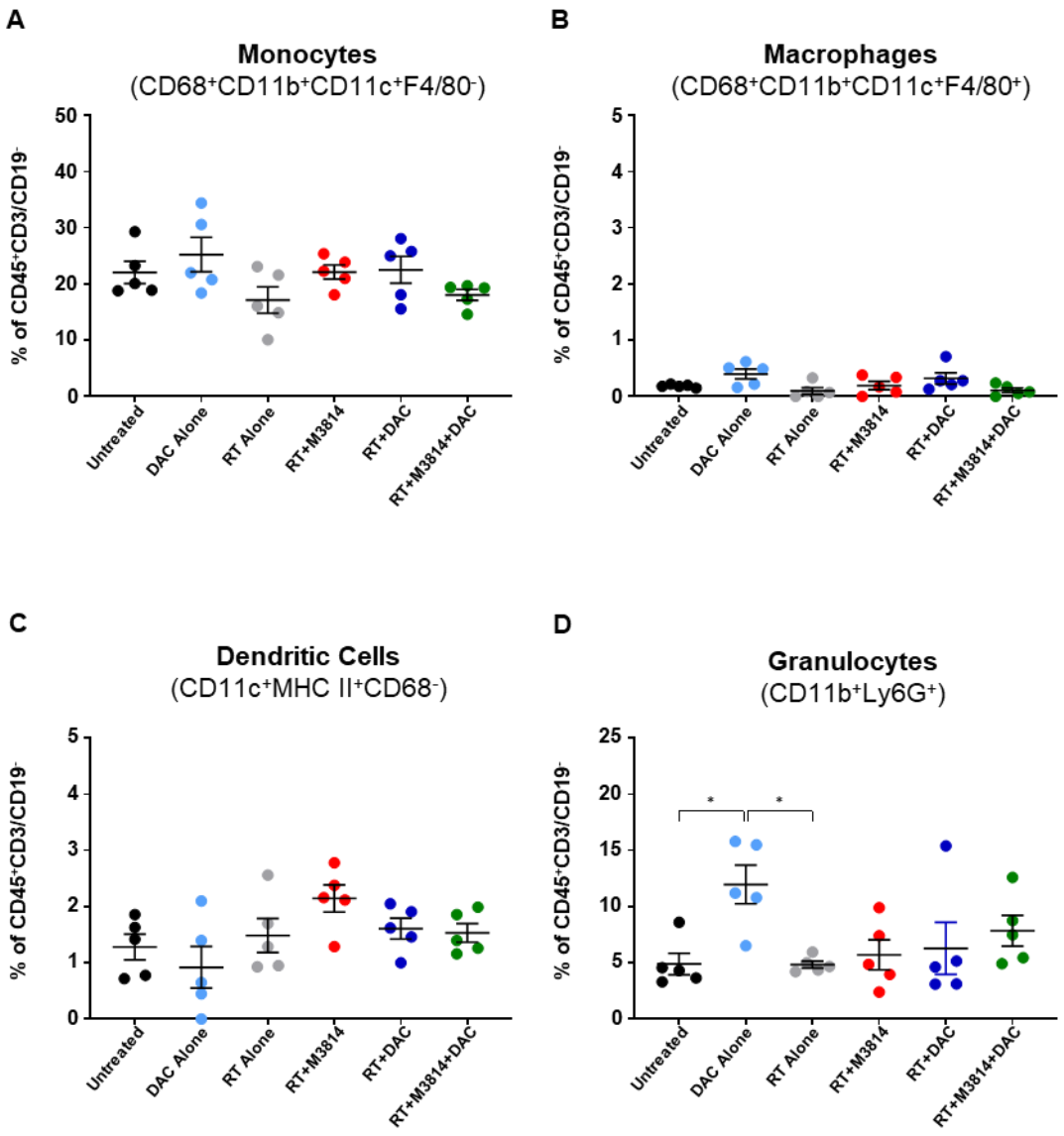

Figure 5. 23. Frequency of granulocytes increases in TDLNs of mice treated with DAC alone.

C57BL/6 mice were inoculated with 5x10^5 KP.B6.F1 cells via S.C. injection. On day 5, mice were treated with 1mg/kg DAC for 5 consecutive days. On day 10, 100mg/kg M3814 was administered via O.G. and one hour later mice were treated with CT guided 1x8Gy radiotherapy to the tumours. On day 18, TDLNs and tumours were collected, processed into single cell suspension, and flow cytometry performed using myeloid panel. Manual gating performed to determine % of CD45$^+$CD3$^-$CD19$^-$ cells in TDLNs that were **(A)** monocytes **(B)** macrophages **(C)** dendritic cells **(D)** granulocytes. Data shown as individual mice (5 per group) and average±SEM and analysed by one-way ANOVA followed by Bonferroni's multiple comparison test: *p<0.05, **p<0.01, ***p<0.001 ****p<0.0001.

Within tumours, the monocyte population was significantly influenced by treatment (one-way ANOVA, p=0.0465)(Figure 5.24 A). The % of monocytes fell from 43.2% (±6.3) of $CD45^+CD3^-CD19^-$ cells in untreated mice to 39.9% (±4.4) in RT alone treated mice. There was then a significant increase of 12.8% from RT alone to RT+DAC+M3814 treated mice at 52.7% (±3.2)(Bonferroni's, p=0.0425)(Figure 5.24 A). The population of macrophages were also significantly different between the treatment groups (one-way ANOVA, p=0.0004)(Figure 5.24 B). The largest % of macrophages occurred in mice treated with RT+DAC+M3814, with 13.8% (±2.8). This was significantly greater than the 6.8% (±1.7) in mice treated with RT alone (Bonferroni's, p=0.0016), 5.7% (±0.8) with RT+M3814 alone (Bonferroni's, p=0.0386), and 8.7% (±2.1) in the RT+DAC group (Bonferroni's, p=0.0386)(Figure 5.24 B). The % of $CD45^+CD3^-CD19^-$ cells that were DCs remained low in tumours, all were below 1% and did not significantly change between treatment groups (Figure 5.24 C). Granulocytes represented between 21.7% (±6.6) in RT+DAC treated mice and 37.0% (±6.6) in RT alone but did not significantly differ between treatment groups (Figure 5.24 D).

Next, the key clusters identified by FlowSOM within the monocyte population were investigated (Figure 5.25). Expression of Ly6C played a significant role in separating monocyte clusters and can be used to identify two important types of monocytes [192, 193]. Those that are $Ly6C^-$ are known as patrolling monocytes while those that are $Ly6C^-$ are inflammatory monocytes which circulate the peripheral blood until they are recruited to sites of inflammation. Clusters 6 and 7 are inflammatory monocytes, whereas clusters 9, 14 and 18 are patrolling monocytes. MHC Class II expression further separated these populations. There is evidence to suggest that monocytes with increased MHC Class II may go onto differentiate into monocyte derived DCs (moDCs) and these were termed 'intermediate' [194]. $Ly6C^+$MHC II^- monocytes were termed 'inflammatory' and represent cluster 6. $Ly6C^+$MHC II^+ are 'inflammatory

intermediate' which included cluster 7. Ly6C$^-$MHC II$^-$ monocytes are 'patrolling' monocytes and include cluster 9. Finally, Ly6C$^-$MHC II$^+$ monocytes are 'patrolling intermediate' and include clusters 14 and 18 (Figure 5.25).

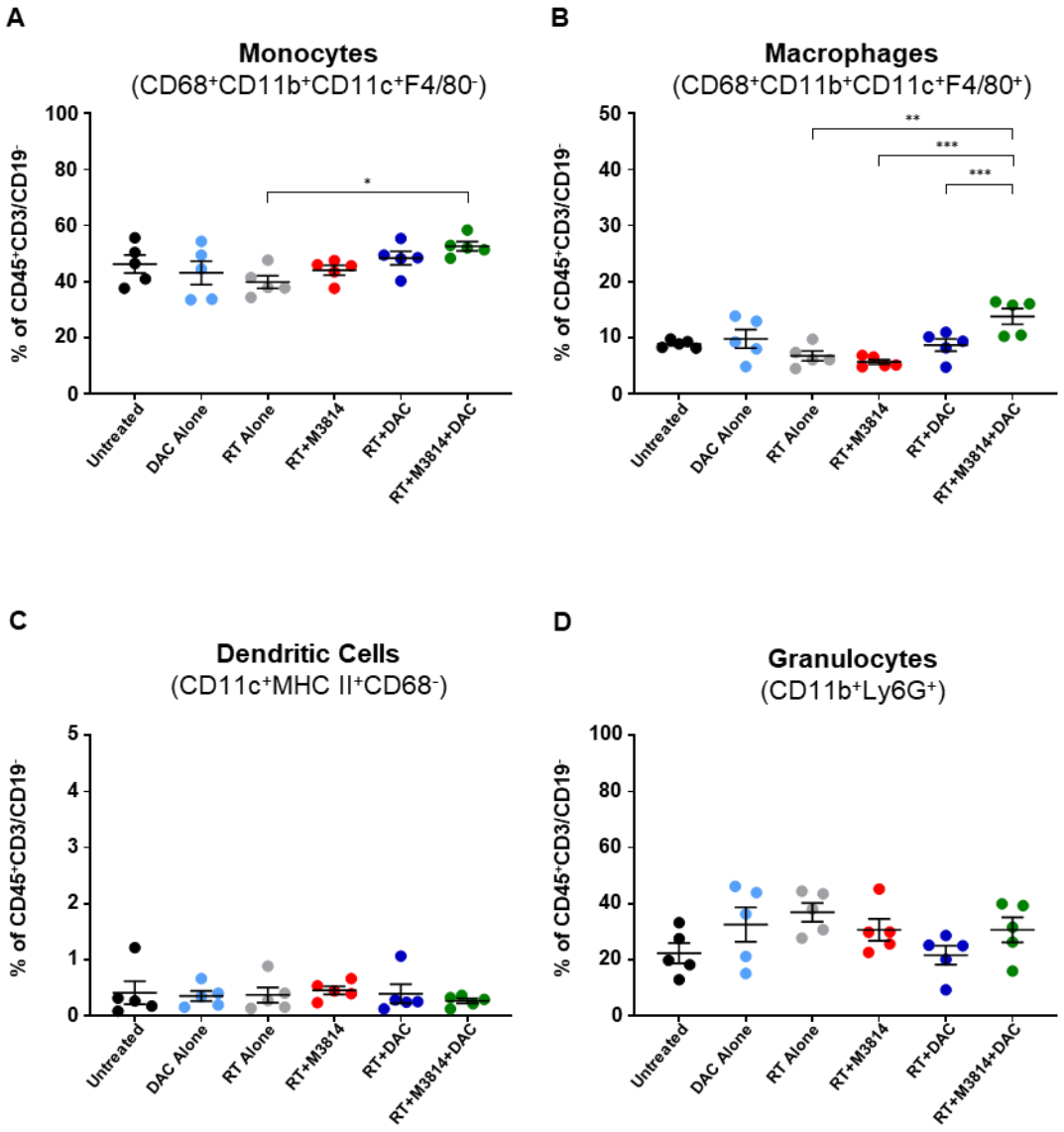

Figure 5. 24. The frequency of monocytes in tumours increases in mice treated with RT+M3814+DAC.

C57BL/6 mice were inoculated with 5x10^5 KP.B6.F1 cells via S.C. injection. On day 5, mice were treated with 1mg/kg DAC for 5 consecutive days. On day 10, 100mg/kg M3814 was administered via O.G. and one hour later mice were treated with CT guided 1x8Gy radiotherapy to the tumours. On day 18, TDLNs and tumours were collected, processed into single cell suspension, and flow cytometry performed using myeloid panel. Manual gating performed to determine % of CD45$^+$CD3$^-$CD19$^-$ cells in tumours that were **(A)** monocytes **(B)** macrophages **(C)** dendritic cells **(D)** granulocytes. Data shown as individual mice (5 per group) and average±SEM and analysed by one-way ANOVA followed by Bonferroni's multiple comparison test: *p<0.05, **p<0.01, ***p<0.001 ****p<0.0001.

Due to their role in being recruited to tissue in response to inflammation, these subsets will be discussed only in the context of the tumour, rather than within the TDLNs. The frequency of inflammatory monocytes (Ly6C^{+}MHC II^{-}) was significantly affected by the treatment administered (one-way ANOVA, p=0.0024)(Figure 5.25 A). This population of cells was greatest in untreated mice, at 30.9% (±5.4) of monocytes. This significantly fell with RT treatment to make up 19.6% (±2.7) of monocytes (Bonferroni's, p=0.0016). RT alone had the smallest proportion of inflammatory intermediate monocytes. This was significantly lower than DAC alone at 27.9% (±3.0) (Bonferroni's, p=0.0377) and RT+M3814 with 28.0% (±2.4)(Bonferroni's, p=0.0334)(Figure 5.25 A). The frequency of inflammatory intermediate monocytes was also significantly different between treatment groups (one-way ANOVA, p=0.0001)(Figure 5.25 B). The % of monocytes which were Ly6C^{+}MHC II^{+} remained similar between untreated, DAC alone, RT alone and RT+M3814. However, there was a significant increased from 15.5% (±3.0) in untreated mice to 23.3% (±2.8) in RT+DAC treated mice (Bonferroni's, p=0.0241). This increased further still with RT+DAC+M3814 to 27.2% (±2.4). This proportion was significantly greater than untreated at 15.5% (±3.0)(Bonferroni's, p=0.0003), DAC alone with 17.8% (±3.0)(Bonferroni's, p=0.004), RT alone with 19% (±2.7)(Bonferroni's, p=0.0157) and RT+M3814 with 16.5% (±2.4)(Bonferroni's, p=0.0009)(Figure 5.25 B).

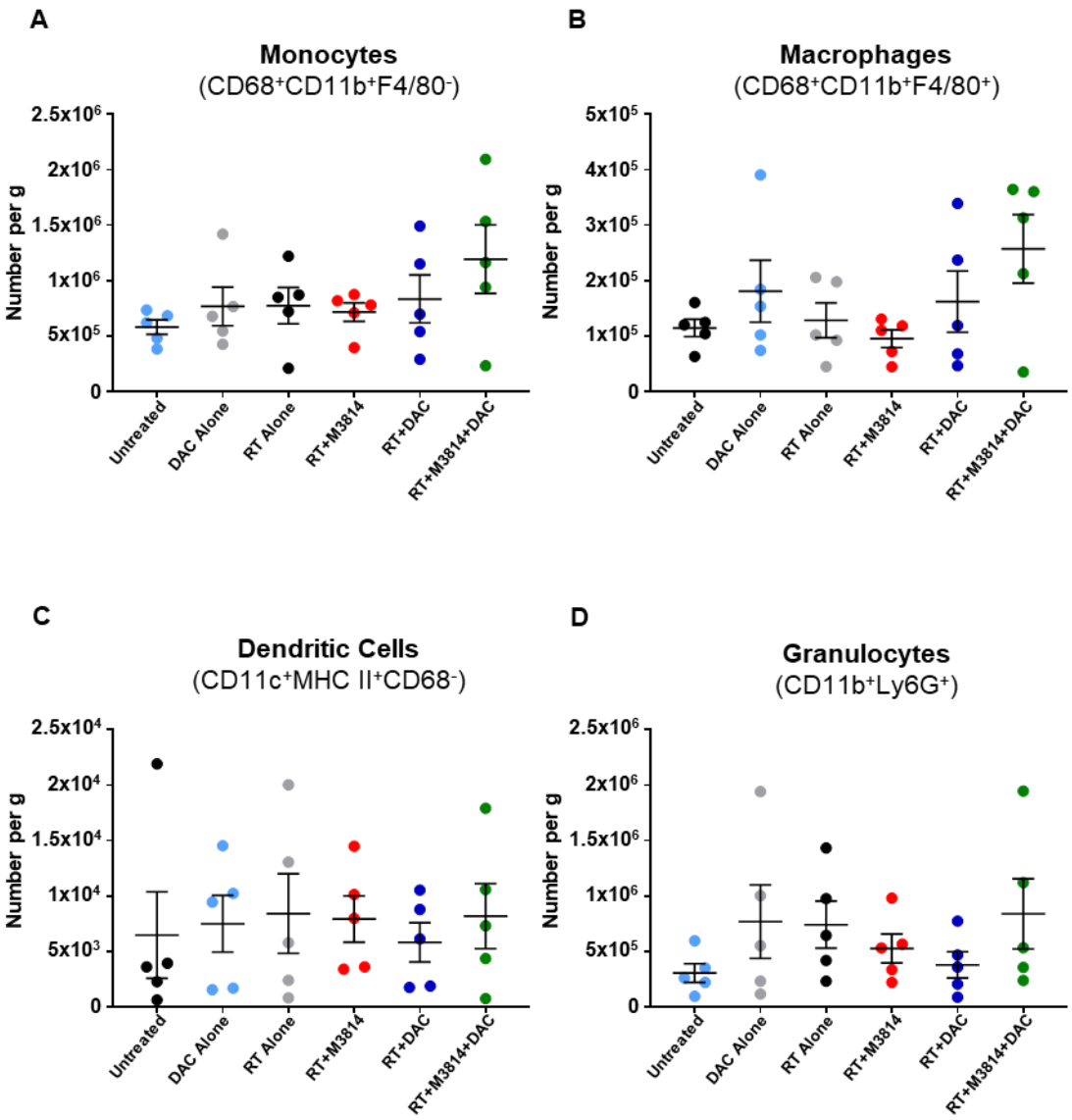

Figure 5. 25. The number of monocytes, macrophages, Dendritic cells, and Granulocytes remains unchanged with treatment.

C57BL/6 mice were inoculated with $5x10^5$ KP.B6.F1 cells via S.C. injection. On day 5, mice were treated with 1mg/kg DAC for 5 consecutive days. On day 10, 100mg/kg M3814 was administered via O.G. and one hour later mice were treated with CT guided 1x8Gy radiotherapy to the tumours. On day 18, TDLNs and tumours were collected, processed into single cell suspension, and flow cytometry performed using myeloid panel. Manual gating performed to count the T cell subsets. Counts were then calculated per gram of tumour. **(A)** monocytes **(B)** macrophages **(C)** dendritic cells **(D)** granulocytes. Data shown as individual mice (5 per group) and average±SEM and analysed by one-way ANOVA followed by Bonferroni's multiple comparison test: *p<0.05, **p<0.01, ***p<0.001 ****p<0.0001.

Patrolling monocytes was also significantly influenced by treatment group (one-way ANOVA, p=0.0084)(Figure 5.26 C). The largest % of patrolling monocytes occurred in tumours of mice treated with RT alone, contributing 39.7% (±6.0) of monocytes. This was significantly more than that seen in the RT+DAC+M3814 treatment group,

which was 28.2% (±4.0)(Bonferroni's, p=0.0099)(Figure 5.26 C). There was no significant change in the population of patrolling intermediate monocytes (Figure 5.26 D).

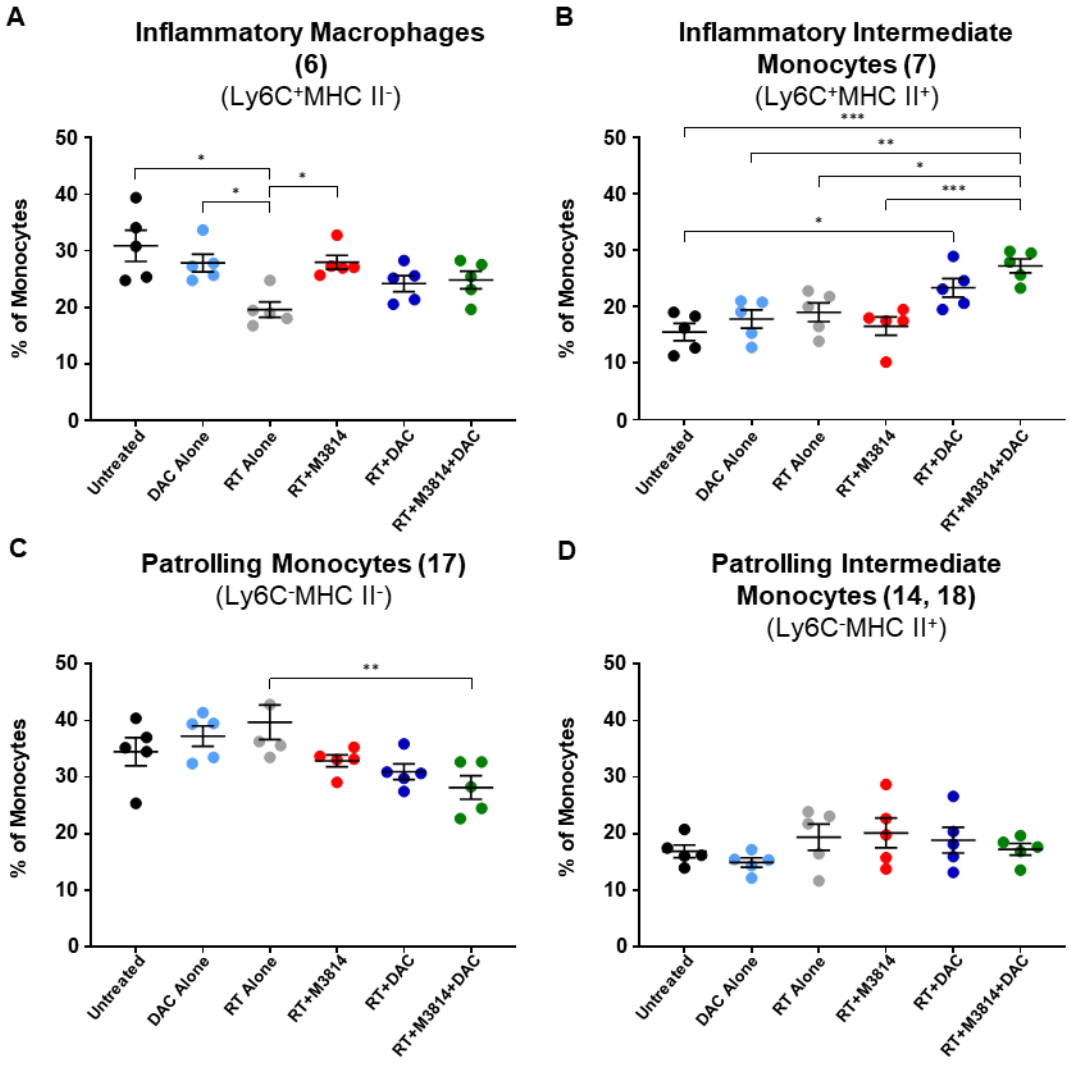

Figure 5. 26. The monocyte population in tumours of mice treated with RT+M3814+DAC is skewed towards an inflammatory intermediate phenotype.

C57BL/6 mice were inoculated with $5x10^5$ KP. B6.F1 cells via S.C. injection. On day 5, mice were treated with 1mg/kg DAC for 5 consecutive days. On day 10, 100mg/kg M3814 was administered via O.G. and one hour later mice were treated with CT guided 1x8Gy radiotherapy to the tumours. On day 18, TDLNs and tumours were collected, processed into single cell suspension, and flow cytometry performed using myeloid panel. Manual gating performed to determine % of monocytes in tumours that were **(A)** $Ly6C^+MHC\ II^-$ **(B)** $Ly6C^+MHC\ II^+$ **(C)** $Ly6C^-MHC\ II^-$ **(D)** $Ly6C^+MHC\ II^+$. Data shown as individual mice (5 per group) and average±SEM and analysed by one-way ANOVA followed by Bonferroni's multiple comparison test: *p<0.05, **p<0.01, ***p<0.001 ****p<0.0001.

Next, the macrophage subsets were examined. The FlowSOM analysis (Figure 5.22) identified two macrophage clusters: 16 and 19. Both were CD206 positive which is associated with tumour associated macrophages. One of these, 19, was also positive for MHC Class II meaning this population has an M1 phenotype. These are macrophages involved in detecting and eliminating threats cells and antigen presentation, making them more closely associated with an anti-tumour phenotype. On the other hand, cluster 16 was MHC Class II negative, implying it lies closer to the M2 end of the macrophage polarisation spectrum. These macrophages are important for wound healing and inducing cell proliferation, making them pro-tumour [195]. Again, this analysis will be focused on the tumours. Macrophages in tumours of mice treated with RT+DAC or RT+DAC+M3814 were more skewed towards the M1 phenotype than untreated, DAC alone, RT alone or RT+M3814 (Figure 5.27). The frequency of M1 macrophages was significantly influenced by treatment (one-way ANOVA, p=0.0002)(Figure 5.28 A). The % of macrophages with the M1 phenotypes in RT+DAC tumours was 29.1% (±4.3) which was significantly greater than untreated at 18.7% (±5.7)(Bonferroni's, p=0.0451), DAC alone 14.5% (±3.1)(Bonferroni's, p=0.0017), RT alone at 16.3% (±5.1)(Bonferroni's, p=0.0072) and RT+M3814 at 15.7% (±4.1)(Bonferroni's, p=0.0043). RT+DAC+M3814 had a similar proportion of M1 macrophages to RT+DAC, 26.9% (±3.4). This was significantly greater than DAC alone (Bonferroni's, p=0.0101), RT alone (Bonferroni's, p=0.0418) and RT+M3814 (Bonferroni's, p=0.0252)(Figure 5.27 A).

The M2 population was also significantly affected by treatment (one-way ANOVA, 0.0001)(Figure 5.27 B). As macrophages skewed towards M1 in RT+DAC and RT+DAC+M3814 treated mice, the proportion of M2 fell. In RT+DAC treated mice, the proportion of M2 macrophages was the lowest, at 67.9% (±4.2). This was significantly less than untreated at 78.7% (±5.4)(Bonferroni's, p=0.0278), DAC alone at 82.5% (±3.7)(Bonferroni's, p=0.0013), RT alone at 82% (±4.7)(Bonferroni's,

p=0.0029) and RT+M3814 81.0% (±4.2)(Bonferroni's, p=0.0045). In RT+DAC+M3814 treated mice, the M2 population fell to 70.7% (±3.2) which was significantly less than DAC alone (Bonferroni's, p=0.0129), RT alone (Bonferroni's, p=0.0278) and RT+M3814 (Bonferroni's, p=0.0427)(Figure 5.27 B).

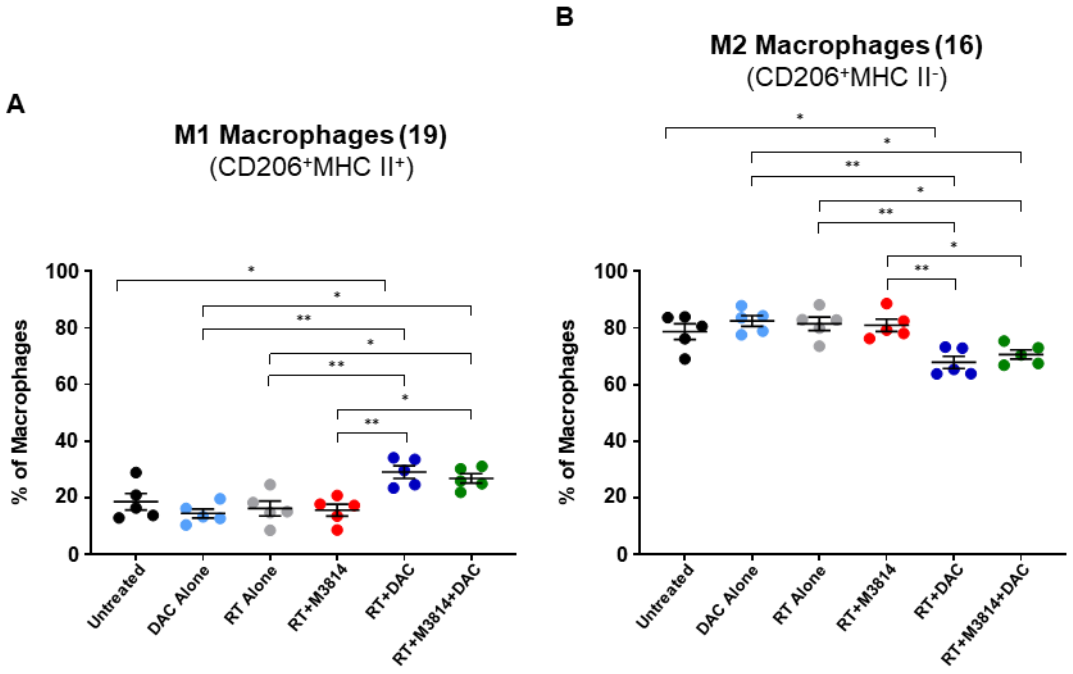

Figure 5. 27. The macrophage population in tumours of mice treated with RT+M3814+DAC is skewed towards an M1 phenotype.

C57BL/6 mice were inoculated with $5x10^5$ KP.B6.F1 cells via S.C. injection. On day 5, mice were treated with 1mg/kg DAC for 5 consecutive days. On day 10, 100mg/kg M3814 was administered via O.G. and one hour later mice were treated with CT guided 1x8Gy radiotherapy to the tumours. On day 18, TDLNs and tumours were collected, processed into single cell suspension, and flow cytometry performed using myeloid panel. Manual gating performed to determine % of macrophages in tumours that were **(A)** $CD206^+MHC\ II^+$ **(B)** $CD206^+MHC\ II^-$. Data shown as individual mice (5 per group) and average±SEM and analysed by one-way ANOVA followed by Bonferroni's multiple comparison test: *p<0.05, **p<0.01, ***p<0.001 ****p<0.0001.

The final cell type to be examined is the dendritic cell. The FlowSOM algorithm pointed to clusters 11, 13 and 15 (Figure 5.22). Cluster 13 is $CD11c^+PD\text{-}L1^+CD11b^+MHC\ II^{high}CD86^{high}$ while clusters 11 and 15 are $CD11c^+PD\text{-}L1^-CD11b^-MHC\ II^{int}CD86^{int}$. Cluster 13 is indicative of a mature dendritic cell and PD-L1 is

upregulated on dendritic cells in response to $CD8^+$ T cell activation. Therefore, cluster 13 was termed ‘mature’ DC, while clusters 11 and 15 were deemed ‘immature’ DCs.

In the TDLNs, there was no significant difference in the proportion of immature or mature DCs in response to treatment (Figure 5.28 A&B). There did appear to be a trend increase from an average of 40.7% (±13.5) of mature DCs in untreated mice increasing to 50.6% (±9.4) in those treated with RT+DAC+M3814, however again, this was not significant, likely due to the large degree of variation (Figure 5.28 B).

In tumours, the proportion of DCs in the immature category was significantly different between treatment groups (one-way ANOVA, p=0.025)(Figure 5.28 C). The % of DCs which were immature in RT+DAC treated mice was 20.9% (±9.5). This was significantly lower than untreated with 40.2% (±13.5) of DCs being immature (Bonferroni’s, p=0.0305), DAC alone with 49.1% (±6.6)(Bonferroni’s, p=0.0005) and RT+M3814 at 40.9% (±6.8)(Bonferroni’s, p=0.0218). In RT+DAC+M3814 treated mice, 28.0% (±8.1) of DCs were immature, this was significantly lower than with DAC alone (Bonferroni’s, p=0.0136)(Figure 5.28 C). The proportion of DCs which were in the mature population was significantly influenced by treatment (one-way ANOVA, p=0.0488)(Figure 5.28 D). The largest proportion was 59.9% (±13.6) of DCs and was observed in RT+DAC treated mice. This was significantly larger than DAC alone treated mice with 29.6% (±4.9) of DCs being mature (Bonferroni’s, p=0.0051). RT+DAC+M3814 also appeared to increase, however, this was not significant (Figure 5.28 D).

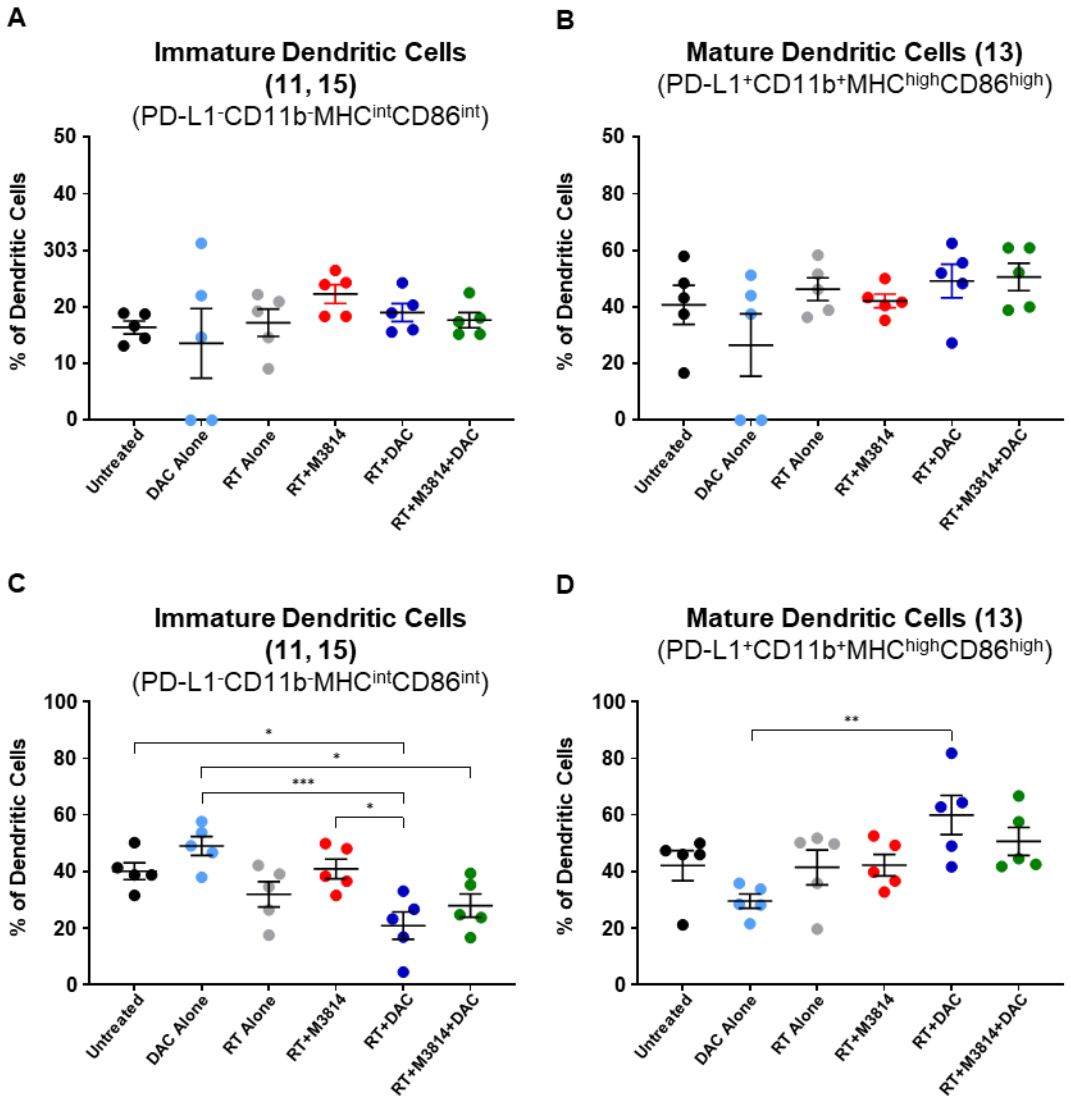

Figure 5. 28. The dendritic cell population in tumours of mice treated with DAC alone is skewed towards a more mature phenotype.

C57BL/6 mice were inoculated with 5x10^5 KP.B6.F1 cells via S.C. injection. On day 5, mice were treated with 1mg/kg DAC for 5 consecutive days. On day 10, 100mg/kg M3814 was administered via O.G. and one hour later mice were treated with CT guided 1x8Gy radiotherapy to the tumours. On day 18, TDLNs and tumours were collected, processed into single cell suspension, and flow cytometry performed using myeloid panel. Manual gating performed to determine % of dendritic cells in tumours that were **(A)** TDLNs PD-L1$^-$CD11b$^-$MHC II^{int}CD86$^-$ **(B)** TDLNs PD-L1$^+$CD11b$^+$MHC II^{high}CD86$^+$ **(C)** Tumour PD-L1$^-$CD11b$^-$MHC II^{int}CD86$^-$ **(D)** Tumour PD-L1$^+$CD11b$^+$MHC II^{high}CD86$^+$. Data shown as individual mice (5 per group) and average±SEM and analysed by one-way ANOVA followed by Bonferroni's multiple comparison test: *p<0.05, **p<0.01, ***p<0.001 ****p<0.0001.

5.4. Discussion

5.4.1. Addition of decitabine to radiotherapy and M3814 has differential effects on KP.B6.F1 and MC38 tumour growth *in vivo.*

Using the MC38 tumour model, addition of either M3814 alone or DAC+M3814 to 8Gy improved tumour control and prolonged mouse survival (Figure 5.6). RT+M3814 was the optimal treatment group, with a 30% survival rate. Of these three mice, all rejected subsequent tumour rechallenge indicating that successful treatment of the original tumour had also primed an anti-tumour immune response offering the mouse systemic tumour protection. As only mice from this group survived, we cannot know whether other treatments, such as radiotherapy alone, may have also engaged the immune system.

In the KP.B6.F1 tumour model, addition of M3814 alone to 8Gy offered no improvement to tumours control (Figure 5.3). Addition of both DAC+M3814 to 8Gy however, did improve tumour control and prolong mouse survival compared to radiotherapy alone. While survival was prolonged, there were no survivors, preventing a rechallenge. While the MC38 experiment did have three survivors, these were limited to one treatment group. To offer better insight into both experiments, titration experiments of MC38 and KP.B6.F1 cells could be performed to increase the likelihood of survivors, and thus provide more opportunities for tumour rechallenge. The involvement of the immune system in the efficacy of the treatments in either model could also be determined either by using immunodeficient mice or knocking out $CD8^+$ T cells.

Previous reports have demonstrated that upon addition to radiotherapy, M3814 improves tumour control and prolongs overall survival in multiple immunodeficient human xenograft tumour models including head and neck (FaDU)[69], NSCLC (NCI-H460)[69] and cervical (HeLA) [68]. There is however, only one published study showing efficacy in an immunocompetent model, MC38 [136]. This paper, as well as

the previously mentioned studies, combined daily administered M3814 alongside 5 consecutive days of 2Gy radiotherapy. Like the experiment presented in this paper, despite using a significantly different radiotherapy and M3814 regimen, M3814 in combination with radiotherapy improved tumour control and prolonged survival. Addition of bintrafusp alfa (bifunctional fusion protein targeting TGFβ and PD-L1) improved this effect and elicited abscopal control, indicating engagement of the adaptive immune arm. This is in accordance with the findings presented here. In contrast, KP.B6.F1 did not benefit from addition of M3814 alone to radiotherapy, and therefore, the improved tumour control with decitabine may provide an important insight into its potential application in the future.

5.4.2. KP.B6.F1 tumours in mice treated with RT+M3814+DAC have an increased inflammatory tumour microenvironment.

While the frequency and count of Teff, Tregs and $CD8^+$ cells in the $CD3^+$ population remained unchanged with treatment, the subsets within these groups were altered. With RT+DAC+M3814 treatment, the frequency of $ICOS^+$ cells significantly increased ($ICOS^+CD25^-$ and $ICOS^+CD25^+$) within the tumours. ICOS is upregulated in T cells following antigen activation and provides a co-stimulatory signal. This signal increases cell proliferation and the release of cytokines [191]. This effect was limited to the tumours.

The frequency of $CD8^+$ T cell subpopulations also changed with treatment. The two key subsets identified were the naïve $CD8^+$ and $Ki67^+CD8^+$ cells. In the TDLNs, RT and RT+DAC increased the $Ki67^+$ $CD8^+$, however, it is important to know that these remained a small proportion of the $CD8^+$ T cell population. In contrast, within the tumours there was a significant increase in $Ki67^+CD8^+$ T cells following RT+DAC+M3814 treatment. This made up 25.1% of $CD8^+$ T cells, 2.7-fold greater than in untreated. Ki67 is a marker of proliferation, indicating that these cells are active and undergoing proliferation. However, in the absence of Granzyme B staining,

it cannot be determined whether these are cytotoxic. Along with the increase in active Teff cells, this gives the picture of a more active TIME than those observed in the untreated tumours.

There were also changes to the myeloid compartments with treatments. The frequency of monocytes and macrophages was greatest in the tumours of mice treated with RT+DAC+M3814. Interestingly, CCL2 gene expression, a key chemokine which promotes long range recruitment of monocytes, was found to be upregulated *in vivo* in response to radiotherapy. While the tumour model was different, in the lung rather than subcutaneously injected, it would be interesting to investigate this further. The counts per gram also appeared to increase but there was large degree of variability between mice. This increase in the monocyte population was shown to be driven by an increase in inflammatory monocytes ($Ly6C^+$). More specifically, there was an increase in $Ly6C^+$MHC Class II^+ monocytes indicating that not only has been recruitment of monocytes to the tumours, but they may be transitioning into macrophages [193]. It is reported that these inflammatory monocytes transition into a more M1 like macrophages, whereas those derives from patrolling monocytes are more associated with an M2 phenotype [196]. Indeed, while most TAMs had a more M2-like phenotype (MHC Class II low), treatment with RT+DAC and RT+DAC+M3814 pushed this skew closer to the M1 phenotype than in untreated.

IFN-β is an important driver of DC maturation and activation. There was a significant decrease in immature DCs with either RT+DAC or RT+DAC+M3814. In RT+DAC treated tumours, this was mirrored by a significant increase in mature DCs, however, although there was an increase with RT+DAC+M3814 it was not significant.

As shown in Figure 5.1, treatment with decitabine restored STING protein levels in KP.B6.F1 tumours. Based on the evidence provided in Chapter 4 it is reasonable to hypothesise that this may restore cGAS-STING pathway. Furthermore, as was demonstrated in Chapter 4, radiotherapy and M3814 can increase the formation of

cGAS positive micronuclei, triggering the cGAS-STING pathway and resulting in the release of IFN-β. To assess whether these *in vitro* findings may translate to release of the immunostimulatory IFN-β *in vivo*, more work need to be done. This would include determining pathway activity of cGAS-STING in tumour tissue. The imaging of sections from tumour tissue collected during these experiments would enable quantification of cGAS puncta and micronuclei, offering an insight into cGAS-STING pathway activity in these tumours followed by treatment [197].

6. Summary and Outlook

Initially, radiotherapy is often an effective treatment for cancer. However, resistance and disease recurrence limit this success. Strategies to sensitise tumours to radiotherapy and improve response decrease risk of relapse. This thesis provides evidence that pharmacological inhibition of DNA-PK with M3814 has the potential to do so both by cancer cell intrinsic mechanisms and through increasing tumour immunogenicity.

Following the induction of double strand breaks, rapidly proliferating cancer cells with a dysregulated DNA damage response rely heavily on DNA-PK to quickly resolve the breaks, failure to do so results in cell death making them vulnerable to DNA-PK inhibition. The radiosensitising effect of DNA-PK inhibitor has culminated in the development of multiple generations of DNA-PK inhibitors, the latest of which are the subject of investigation in clinical trials (Table 1.1). The DNA-PKi focused on in this thesis, M3814, was shown in Chapter 3 to sensitise a panel of six different of cancer cell lines, supporting previous reports of M3814 as a potent radiosensitising agent [67-69, 136, 156, 157]. In contrast, the effects of DNA-PK inhibition on radiotherapy treated cancer cells in the context of the tumour immune microenvironment is much less understood. Given the use of M3814 in clinical trials, insights into these immunological outcomes are timely and critical.

This thesis indicates that the treatment of the immunogenically cold KP.B6.F1 cell line with combination of M3814 and radiotherapy increases the release of immunostimulatory signals. First, Chapter 3 demonstrates that the cell death induced by radiotherapy and M3814 treatment is accompanied with the release of DAMPs which are characteristic of ICD, including HMGB1 secretion and translocation of CRT to the cell surface membrane. Radiotherapy alone has been previously demonstrated to increase ICD in cells [91, 100, 164], however, this work shows for the first time that addition of DNA-PKi, and to a greater extent M3814, exacerbates this effect.

Furthermore, the work in this thesis provides evidence that DNA damage induced by radiotherapy and M3814 has the potential to initiate the cGAS-STING pathway, resulting in the production and release of IFNβ. Treatment with radiotherapy induced the formation of cGAS positive micronuclei, which was increased further with M3814. This indicates that treatment is sufficient to provide the cytosolic dsDNA necessary to trigger the cGAS-STING pathway. In MC38, treatment with radiotherapy and M3814 was sufficient to promote gene expression of *Ifnβ*, corroborating a recent study [136]. In contrast to MC38, and despite evidence of pathway initiation, treated KP.B6.F1 cells showed no evidence of downstream cGAS-STING pathway activity. This was the case despite treatment with potent cGAS-STING pathway agonists indicating KP.B6.F1 lack a functional cGAS-STING response. In recent years, strategies to activate the cGAS-STING pathway in cancer has been the subject of intense research. However, loss of cGAS-STING pathway functionality occurs frequently in cancer, limiting the translation and success of such approaches in the clinic. The discovery that KP.B6.F1 was STING deficient presented the opportunity to investigate how the effects of radiotherapy and M3814 could be optimised in a model which is representative of cGAS-STING deficient tumours. The differences between MC38 and KP.B6.F1 were also apparent *in vivo*. Treatment with radiotherapy and M3814 cured 30% of mice and provided protection from tumour rechallenge, providing functional validation of a tumour-specific immune response. In KP.B6.F1 tumours however, M3814 treatment did little to radiosensitise tumours. Addition of decitabine prolonged survival, however, as no mice were cured protection against rechallenge could not be tested. Characterisation of the myeloid and lymphoid compartments found increased tumour infiltration of $Ki67^{+}CD8^{+}$ T cells, inflammatory monocytes, M1 macrophages and mature dendritic cells. In line with the *in vitro* experiments presented in this thesis, this indicates that this combination therapy increased immunogenicity of an immunogenically cold tumour model, KP.B6.F1. Taken together, these findings indicate that radiotherapy and M3814 may increase the

release of immunogenicity in stimulatory signal through the induction of ICD and cGAS-STING. In addition to this, this work proposes decitabine as a potential therapeutic strategy for patients lacking cGAS-STING pathway functionality. Treatment with low-dose decitabine increased STING expression and restored the cGAS-STING pathway. Decitabine treated cells responded to cGAS-STING pathway agonists to produce IFNβ and, like MC38, treatment with radiotherapy and M3814 increased *Ifnβ* gene expression. Figure 6.1 shows a graphical summary of the findings of this thesis

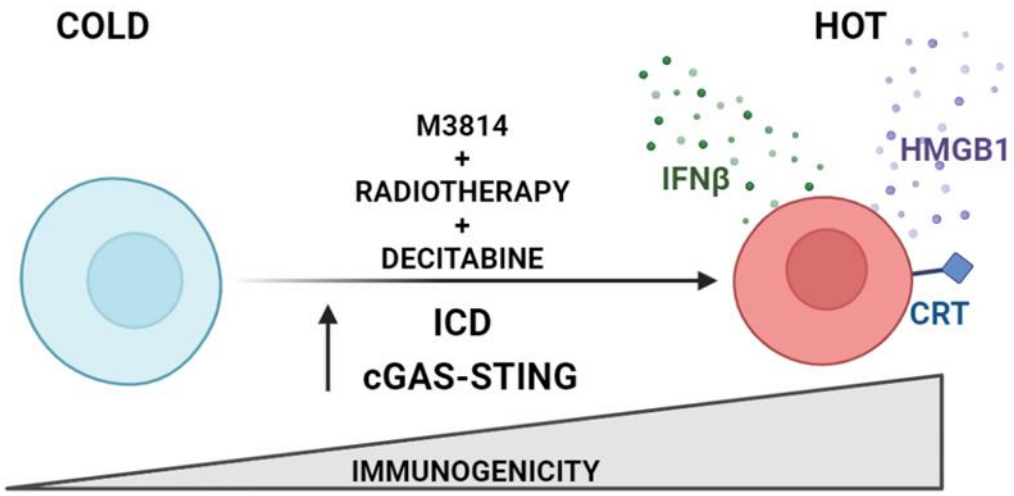

Figure 6. 1. Treatment with Radiotherapy, M3814 and decitabine increases tumour cell immunogenicity.

Treatment with radiotherapy and M3814 induce immunogenic cell death and initiate the cGAS-STING pathway. In the STING deficient model KP.B6.F1, decitabine restores cGAS-STING pathway activity, further increasing immunogenicity. Created in BioRender.

This thesis provides evidence that M3814 increases sensitivity to radiotherapy both by cancer-cell intrinsic mechanism and through increased immunogenicity of cells, it also presents decitabine as an interesting therapeutic approach to restore cGAS-SITNG pathway functionality in STING deficient tumours. While this provides important insight, it raises many questions for future research. Further work is needed

to validate the proposed mechanisms of increased immunogenicity *in vivo* and to demonstrate whether these findings can be applied to other cancer models. As different radiotherapy regimens have profoundly different effects on both tumour control and on tumour immunogenicity, it would be important to optimise therapy regimens. To build upon the findings that radiotherapy and M3814 increase tumour cell immunogenicity, it would also be of interest to determine how the resulting DNA damage may affect the generation of neoantigens and whether what effect this may also have on the visibility of tumour cells.

While the result from this thesis opens the door for multiple lines of investigation in the laboratory, they also provide directly translational advance. In particular, the findings that low-dose decitabine can restore cGAS-STING functionality is of particular interest. Decitabine is already approved by the FDA for the treatment of acute myeloid leukaemia (AML) and chronic myeloid leukaemia (CML) in elderly patients due to its low toxicity and more recently has been shown to increase response to immune checkpoint blockade in both syngeneic tumour models [129] and in a Phase II clinical trial investigating the combination of low-dose decitabine and anti-PD-1 in patients with non-Hodgkin's lymphoma [186]. The work presented in this thesis presents the case for combination with DNA damaging agents which can trigger the cGAS-STING pathway and furthers the case for investigation of decitabine as an immunomodulatory agent in cancer therapy.

References

1. Sung, H., et al., *Global Cancer Statistics 2020: GLOBOCAN Estimates of Incidence and Mortality Worldwide for 36 Cancers in 185 Countries.* CA Cancer J Clin, 2021. **71**(3): p. 209-249.
2. Bray, F., et al., *The ever-increasing importance of cancer as a leading cause of premature death worldwide.* Cancer, 2021. **127**(16): p. 3029-3030.
3. Bray, F., et al., *Global cancer transitions according to the Human Development Index (2008-2030): a population-based study.* Lancet Oncol, 2012. **13**(8): p. 790-801.
4. Foreman, K.J., et al., *Forecasting life expectancy, years of life lost, and all-cause and cause-specific mortality for 250 causes of death: reference and alternative scenarios for 2016-40 for 195 countries and territories.* Lancet, 2018. **392**(10159): p. 2052-2090.
5. Song, S., et al., *Decreased expression of STING predicts poor prognosis in patients with gastric cancer.* Scientific Reports, 2017. **7**(1): p. 39858.
6. Konno, H., et al., *Suppression of STING signaling through epigenetic silencing and missense mutation impedes DNA damage mediated cytokine production.* Oncogene, 2018. **37**(15): p. 2037-2051.
7. Hanahan, D., *Hallmarks of Cancer: New Dimensions.* Cancer Discovery, 2022. **12**(1): p. 31-46.
8. Negrini, S., V.G. Gorgoulis, and T.D. Halazonetis, *Genomic instability--an evolving hallmark of cancer.* Nat Rev Mol Cell Biol, 2010. **11**(3): p. 220-8.
9. Jackson, S.P. and J. Bartek, *The DNA-damage response in human biology and disease.* Nature, 2009. **461**(7267): p. 1071-8.
10. Ciccia, A. and S.J. Elledge, *The DNA damage response: making it safe to play with knives.* Mol Cell, 2010. **40**(2): p. 179-204.
11. Chatterjee, N. and G.C. Walker, *Mechanisms of DNA damage, repair, and mutagenesis.* Environ Mol Mutagen, 2017. **58**(5): p. 235-263.
12. Swift, L.H. and R.M. Golsteyn, *Genotoxic anti-cancer agents and their relationship to DNA damage, mitosis, and checkpoint adaptation in proliferating cancer cells.* Int J Mol Sci, 2014. **15**(3): p. 3403-31.
13. Tuduri, S., et al., *Topoisomerase I suppresses genomic instability by preventing interference between replication and transcription.* Nat Cell Biol, 2009. **11**(11): p. 1315-24.
14. Kang, Z.J., et al., *The Philadelphia chromosome in leukemogenesis.* Chin J Cancer, 2016. **35**: p. 48.
15. Fenech, M., et al., *Molecular mechanisms of micronucleus, nucleoplasmic bridge and nuclear bud formation in mammalian and human cells.* Mutagenesis, 2011. **26**(1): p. 125-32.
16. Fackenthal, J.D. and O.I. Olopade, *Breast cancer risk associated with BRCA1 and BRCA2 in diverse populations.* Nat Rev Cancer, 2007. **7**(12): p. 937-48.
17. Pearl, L.H., et al., *Therapeutic opportunities within the DNA damage response.* Nat Rev Cancer, 2015. **15**(3): p. 166-80.
18. Olivier, M., M. Hollstein, and P. Hainaut, *TP53 mutations in human cancers: origins, consequences, and clinical use.* Cold Spring Harb Perspect Biol, 2010. **2**(1): p. a001008.
19. Ding, L., et al., *Somatic mutations affect key pathways in lung adenocarcinoma.* Nature, 2008. **455**(7216): p. 1069-75.
20. Lord, C.J. and A. Ashworth, *The DNA damage response and cancer therapy.* Nature, 2012. **481**(7381): p. 287-94.

21. Li, L.-y., et al., *DNA Repair Pathways in Cancer Therapy and Resistance.* Frontiers in Pharmacology, 2021. **11**.
22. O'Connor, M.J., *Targeting the DNA Damage Response in Cancer.* Mol Cell, 2015. **60**(4): p. 547-60.
23. Cannan, W.J. and D.S. Pederson, *Mechanisms and Consequences of Double-Strand DNA Break Formation in Chromatin.* J Cell Physiol, 2016. **231**(1): p. 3-14.
24. Rothkamm, K. and M. Löbrich, *Evidence for a lack of DNA double-strand break repair in human cells exposed to very low x-ray doses.* Proc Natl Acad Sci U S A, 2003. **100**(9): p. 5057-62.
25. Shibata, A., et al., *Factors determining DNA double-strand break repair pathway choice in G2 phase.* Embo j, 2011. **30**(6): p. 1079-92.
26. Blackford, A.N. and S.P. Jackson, *ATM, ATR, and DNA-PK: The Trinity at the Heart of the DNA Damage Response.* Mol Cell, 2017. **66**(6): p. 801-817.
27. Mao, Z., et al., *Comparison of nonhomologous end joining and homologous recombination in human cells.* DNA Repair (Amst), 2008. **7**(10): p. 1765-71.
28. Beucher, A., et al., *ATM and Artemis promote homologous recombination of radiation-induced DNA double-strand breaks in G2.* Embo j, 2009. **28**(21): p. 3413-27.
29. Pannunzio, N.R., G. Watanabe, and M.R. Lieber, *Nonhomologous DNA end-joining for repair of DNA double-strand breaks.* J Biol Chem, 2018. **293**(27): p. 10512-10523.
30. An, J., et al., *DNA-PKcs plays a dominant role in the regulation of H2AX phosphorylation in response to DNA damage and cell cycle progression.* BMC Molecular Biology, 2010. **11**(1): p. 18.
31. Kinner, A., et al., *Gamma-H2AX in recognition and signaling of DNA double-strand breaks in the context of chromatin.* Nucleic Acids Res, 2008. **36**(17): p. 5678-94.
32. Liu, J., et al., *Structural mechanism of the phosphorylation-dependent dimerization of the MDC1 forkhead-associated domain.* Nucleic Acids Res, 2012. **40**(9): p. 3898-912.
33. Marini, F., et al., *Regulation of DNA Double Strand Breaks Processing: Focus on Barriers.* Front Mol Biosci, 2019. **6**: p. 55.
34. Williams, R.S., J.S. Williams, and J.A. Tainer, *Mre11-Rad50-Nbs1 is a keystone complex connecting DNA repair machinery, double-strand break signaling, and the chromatin template.* Biochem Cell Biol, 2007. **85**(4): p. 509-20.
35. Godin, S.K., M.R. Sullivan, and K.A. Bernstein, *Novel insights into RAD51 activity and regulation during homologous recombination and DNA replication.* Biochem Cell Biol, 2016. **94**(5): p. 407-418.
36. Wright, W.D., S.S. Shah, and W.D. Heyer, *Homologous recombination and the repair of DNA double-strand breaks.* J Biol Chem, 2018. **293**(27): p. 10524-10535.
37. Greene, E.C., *DNA Sequence Alignment during Homologous Recombination.* J Biol Chem, 2016. **291**(22): p. 11572-80.
38. Beck, C., et al., *Poly(ADP-ribose) polymerases in double-strand break repair: focus on PARP1, PARP2 and PARP3.* Exp Cell Res, 2014. **329**(1): p. 18-25.
39. Kragelund, B.B., et al., *The Ku70/80 ring in Non-Homologous End-Joining: easy to slip on, hard to remove.* Front Biosci (Landmark Ed), 2016. **21**: p. 514-27.
40. Myler, L.R., et al., *Single-Molecule Imaging Reveals How Mre11-Rad50-Nbs1 Initiates DNA Break Repair.* Mol Cell, 2017. **67**(5): p. 891-898.e4.

41. Mari, P.O., et al., *Dynamic assembly of end-joining complexes requires interaction between Ku70/80 and XRCC4.* Proc Natl Acad Sci U S A, 2006. **103**(49): p. 18597-602.
42. Sibanda, B.L., D.Y. Chirgadze, and T.L. Blundell, *Crystal structure of DNA-PKcs reveals a large open-ring cradle comprised of HEAT repeats.* Nature, 2010. **463**(7277): p. 118-21.
43. Chan, D.W., et al., *Autophosphorylation of the DNA-dependent protein kinase catalytic subunit is required for rejoining of DNA double-strand breaks.* Genes Dev, 2002. **16**(18): p. 2333-8.
44. Chen, B.P., et al., *Cell cycle dependence of DNA-dependent protein kinase phosphorylation in response to DNA double strand breaks.* J Biol Chem, 2005. **280**(15): p. 14709-15.
45. Farber-Katz, Suzette E., et al., *DNA Damage Triggers Golgi Dispersal via DNA-PK and GOLPH3.* Cell, 2014. **156**(3): p. 413-427.
46. Chang, H.H.Y., et al., *Non-homologous DNA end joining and alternative pathways to double-strand break repair.* Nat Rev Mol Cell Biol, 2017. **18**(8): p. 495-506.
47. Ishida, N., et al., *Ubiquitylation of Ku80 by RNF126 Promotes Completion of Nonhomologous End Joining-Mediated DNA Repair.* Mol Cell Biol, 2017. **37**(4).
48. Chen, H.H.W. and M.T. Kuo, *Improving radiotherapy in cancer treatment: Promises and challenges.* Oncotarget, 2017. **8**(37): p. 62742-62758.
49. Arcaro, A. and M.P. Wymann, *Wortmannin is a potent phosphatidylinositol 3-kinase inhibitor: the role of phosphatidylinositol 3,4,5-trisphosphate in neutrophil responses.* Biochem J, 1993. **296 (Pt 2)**(Pt 2): p. 297-301.
50. Vlahos, C.J., et al., *A specific inhibitor of phosphatidylinositol 3-kinase, 2-(4-morpholinyl)-8-phenyl-4H-1-benzopyran-4-one (LY294002).* J Biol Chem, 1994. **269**(7): p. 5241-8.
51. Elliott, S.L., et al., *Mitoxantrone in combination with an inhibitor of DNA-dependent protein kinase: a potential therapy for high risk B-cell chronic lymphocytic leukaemia.* Br J Haematol, 2011. **152**(1): p. 61-71.
52. Yanai, M., et al., *DNA-PK Inhibition by NU7441 Enhances Chemosensitivity to Topoisomerase Inhibitor in Non-Small Cell Lung Carcinoma Cells by Blocking DNA Damage Repair.* Yonago Acta Med, 2017. **60**(1): p. 9-15.
53. Dong, J., et al., *Inactivation of DNA-PK by knockdown DNA-PKcs or NU7441 impairs non-homologous end-joining of radiation-induced double strand break repair.* Oncol Rep, 2018. **39**(3): p. 912-920.
54. Ciszewski, W.M., et al., *DNA-PK inhibition by NU7441 sensitizes breast cancer cells to ionizing radiation and doxorubicin.* Breast Cancer Res Treat, 2014. **143**(1): p. 47-55.
55. Zhao, Y., et al., *Preclinical evaluation of a potent novel DNA-dependent protein kinase inhibitor NU7441.* Cancer Res, 2006. **66**(10): p. 5354-62.
56. Harnor, S.J., A. Brennan, and C. Cano, *Targeting DNA-Dependent Protein Kinase for Cancer Therapy.* ChemMedChem, 2017. **12**(12): p. 895-900.
57. Damia, G., *Targeting DNA-PK in cancer.* Mutat Res, 2020. **821**: p. 111692.
58. van Bussel, M.T.J., et al., *A first-in-man phase 1 study of the DNA-dependent protein kinase inhibitor peposertib (formerly M3814) in patients with advanced solid tumours.* Br J Cancer, 2021. **124**(4): p. 728-735.
59. Munster, P., et al., *First-In-Human Phase I Study Of A Dual mTOR Kinase And DNA-PK Inhibitor (CC-115) In Advanced Malignancy.* Cancer Manag Res, 2019. **11**: p. 10463-10476.
60. Liang, S., et al., *Structural insights into inhibitor regulation of the DNA repair protein DNA-PKcs.* Nature, 2022. **601**(7894): p. 643-648.

61. Wise, H.C., et al., *Activity of M3814, an Oral DNA-PK Inhibitor, In Combination with Topoisomerase II Inhibitors in Ovarian Cancer Models.* Scientific Reports, 2019. **9**(1): p. 18882.
62. Chao, O.S. and O.B. Goodman, Jr., *DNA-PKc inhibition overcomes taxane resistance by promoting taxane-induced DNA damage in prostate cancer cells.* Prostate, 2021. **81**(14): p. 1032-1048.
63. Wise, H.C., et al., *Activity of M3814, an Oral DNA-PK Inhibitor, In Combination with Topoisomerase II Inhibitors in Ovarian Cancer Models.* Sci Rep, 2019. **9**(1): p. 18882.
64. Wang, M., et al., *DNA-PK inhibition by M3814 enhances chemosensitivity in non-small cell lung cancer.* Acta Pharm Sin B, 2021. **11**(12): p. 3935-3949.
65. Haines, E., et al., *DNA-PK inhibitor peposertib enhances p53-dependent cytotoxicity of DNA double-strand break inducing therapy in acute leukemia.* Sci Rep, 2021. **11**(1): p. 12148.
66. Carr, M.I., et al., *DNA-PK Inhibitor, M3814, as a New Combination Partner of Mylotarg in the Treatment of Acute Myeloid Leukemia.* Frontiers in Oncology, 2020. **10**.
67. Smithson, M., et al., *Inhibition of DNA-PK may improve response to neoadjuvant chemoradiotherapy in rectal cancer.* Neoplasia, 2022. **25**: p. 53-61.
68. Gordhandas, S.B., et al., *Pre-clinical activity of the oral DNA-PK inhibitor, peposertib (M3814), combined with radiation in xenograft models of cervical cancer.* Sci Rep, 2022. **12**(1): p. 974.
69. Zenke, F.T., et al., *Pharmacologic Inhibitor of DNA-PK, M3814, Potentiates Radiotherapy and Regresses Human Tumors in Mouse Models.* Mol Cancer Ther, 2020. **19**(5): p. 1091-1101.
70. Dunn, G.P., et al., *Cancer immunoediting: from immunosurveillance to tumor escape.* Nat Immunol, 2002. **3**(11): p. 991-8.
71. Finn, O.J., *A Believer's Overview of Cancer Immunosurveillance and Immunotherapy.* J Immunol, 2018. **200**(2): p. 385-391.
72. Schreiber, R.D., L.J. Old, and M.J. Smyth, *Cancer immunoediting: integrating immunity's roles in cancer suppression and promotion.* Science, 2011. **331**(6024): p. 1565-70.
73. Galon, J., et al., *Type, density, and location of immune cells within human colorectal tumors predict clinical outcome.* Science, 2006. **313**(5795): p. 1960-4.
74. Camus, M., et al., *Coordination of intratumoral immune reaction and human colorectal cancer recurrence.* Cancer Res, 2009. **69**(6): p. 2685-93.
75. Mittal, D., et al., *New insights into cancer immunoediting and its three component phases--elimination, equilibrium and escape.* Curr Opin Immunol, 2014. **27**: p. 16-25.
76. Galon, J. and D. Bruni, *Approaches to treat immune hot, altered and cold tumours with combination immunotherapies.* Nat Rev Drug Discov, 2019. **18**(3): p. 197-218.
77. Mlecnik, B., et al., *Histopathologic-based prognostic factors of colorectal cancers are associated with the state of the local immune reaction.* J Clin Oncol, 2011. **29**(6): p. 610-8.
78. Lugade, A.A., et al., *Local radiation therapy of B16 melanoma tumors increases the generation of tumor antigen-specific effector cells that traffic to the tumor.* J Immunol, 2005. **174**(12): p. 7516-23.
79. Lee, Y., et al., *Therapeutic effects of ablative radiation on local tumor require CD8+ T cells: changing strategies for cancer treatment.* Blood, 2009. **114**(3): p. 589-95.
80. Gupta, A., et al., *Radiotherapy promotes tumor-specific effector CD8+ T cells via dendritic cell activation.* J Immunol, 2012. **189**(2): p. 558-66.

81. Takeshima, T., et al., *Local radiation therapy inhibits tumor growth through the generation of tumor-specific CTL: its potentiation by combination with Th1 cell therapy.* Cancer Res, 2010. **70**(7): p. 2697-706.
82. Yoshimoto, Y., et al., *Radiotherapy-induced anti-tumor immunity contributes to the therapeutic efficacy of irradiation and can be augmented by CTLA-4 blockade in a mouse model.* PLoS One, 2014. **9**(3): p. e92572.
83. Vanpouille-Box, C., et al., *DNA exonuclease Trex1 regulates radiotherapy-induced tumour immunogenicity.* Nat Commun, 2017. **8**: p. 15618.
84. Dewan, M.Z., et al., *Fractionated but not single-dose radiotherapy induces an immune-mediated abscopal effect when combined with anti-CTLA-4 antibody.* Clin Cancer Res, 2009. **15**(17): p. 5379-88.
85. Filatenkov, A., et al., *Ablative Tumor Radiation Can Change the Tumor Immune Cell Microenvironment to Induce Durable Complete Remissions.* Clin Cancer Res, 2015. **21**(16): p. 3727-39.
86. Postow, M.A., et al., *Immunologic correlates of the abscopal effect in a patient with melanoma.* N Engl J Med, 2012. **366**(10): p. 925-31.
87. Kepp, O., et al., *The immunogenicity of tumor cell death.* Curr Opin Oncol, 2009. **21**(1): p. 71-6.
88. Kroemer, G., et al., *Immunogenic cell death in cancer therapy.* Annu Rev Immunol, 2013. **31**: p. 51-72.
89. Panaretakis, T., et al., *The co-translocation of ERp57 and calreticulin determines the immunogenicity of cell death.* Cell Death Differ, 2008. **15**(9): p. 1499-509.
90. Schcolnik-Cabrera, A., et al., *Calreticulin in phagocytosis and cancer: opposite roles in immune response outcomes.* Apoptosis, 2019.
91. Obeid, M., et al., *Calreticulin exposure is required for the immunogenicity of gamma-irradiation and UVC light-induced apoptosis*, in *Cell Death Differ*. 2007: England. p. 1848-50.
92. Gardai, S.J., et al., *Cell-Surface Calreticulin Initiates Clearance of Viable or Apoptotic Cells through trans-Activation of LRP on the Phagocyte.* Cell, 2005. **123**(2): p. 321-334.
93. Nagata, S., *Apoptosis and Clearance of Apoptotic Cells.* Annu Rev Immunol, 2018. **36**: p. 489-517.
94. Segawa, K., et al., *Caspase-mediated cleavage of phospholipid flippase for apoptotic phosphatidylserine exposure.* Science, 2014. **344**(6188): p. 1164-8.
95. Adinolfi, E., et al., *The P2X7 receptor: A main player in inflammation.* Biochem Pharmacol, 2018. **151**: p. 234-244.
96. Apetoh, L., et al., *Toll-like receptor 4-dependent contribution of the immune system to anticancer chemotherapy and radiotherapy.* Nat Med, 2007. **13**(9): p. 1050-9.
97. Li, G., X. Liang, and M. Lotze, *HMGB1: The Central Cytokine for All Lymphoid Cells.* Frontiers in Immunology, 2013. **4**.
98. Li, X., *The inducers of immunogenic cell death for tumor immunotherapy.* Tumori, 2018. **104**(1): p. 1-8.
99. Bezu, L., et al., *Combinatorial strategies for the induction of immunogenic cell death.* Front Immunol, 2015. **6**: p. 187.
100. Golden, E.B., et al., *Radiation fosters dose-dependent and chemotherapy-induced immunogenic cell death.* Oncoimmunology, 2014. **3**: p. e28518.
101. Wilkins, A.C., et al., *The immunological consequences of radiation-induced DNA damage.* J Pathol, 2019. **247**(5): p. 606-614.
102. Burnette, B.C., et al., *The efficacy of radiotherapy relies upon induction of type i interferon-dependent innate and adaptive immunity.* Cancer Res, 2011. **71**(7): p. 2488-96.

103. Deng, L., et al., *STING-Dependent Cytosolic DNA Sensing Promotes Radiation-Induced Type I Interferon-Dependent Antitumor Immunity in Immunogenic Tumors.* Immunity, 2014. **41**(5): p. 843-52.
104. Bose, D., *cGAS/STING Pathway in Cancer: Jekyll and Hyde Story of Cancer Immune Response.* Int J Mol Sci, 2017. **18**(11).
105. Li, T. and Z.J. Chen, *The cGAS-cGAMP-STING pathway connects DNA damage to inflammation, senescence, and cancer.* J Exp Med, 2018. **215**(5): p. 1287-1299.
106. Chen, Q., L. Sun, and Z.J. Chen, *Regulation and function of the cGAS-STING pathway of cytosolic DNA sensing.* Nat Immunol, 2016. **17**(10): p. 1142-9.
107. Li, X., et al., *Cyclic GMP-AMP synthase is activated by double-stranded DNA-induced oligomerization.* Immunity, 2013. **39**(6): p. 1019-31.
108. Andreeva, L., et al., *cGAS senses long and HMGB/TFAM-bound U-turn DNA by forming protein-DNA ladders.* Nature, 2017. **549**(7672): p. 394-398.
109. Du, M. and J. Chen Zhijian, *DNA-induced liquid phase condensation of cGAS activates innate immune signaling.* Science, 2018. **361**(6403): p. 704-709.
110. Pestka, S., C.D. Krause, and M.R. Walter, *Interferons, interferon-like cytokines, and their receptors.* Immunol Rev, 2004. **202**: p. 8-32.
111. Ivashkiv, L.B. and L.T. Donlin, *Regulation of type I interferon responses.* Nature Reviews Immunology, 2014. **14**(1): p. 36-49.
112. Fuertes, M.B., et al., *Host type I IFN signals are required for antitumor CD8+ T cell responses through CD8{alpha}+ dendritic cells.* J Exp Med, 2011. **208**(10): p. 2005-16.
113. McNab, F., et al., *Type I interferons in infectious disease.* Nature Reviews Immunology, 2015. **15**(2): p. 87-103.
114. Amouzegar, A., et al., *STING Agonists as Cancer Therapeutics.* Cancers (Basel), 2021. **13**(11).
115. Roberts, Z.J., L.-M. Ching, and S.N. Vogel, *IFN-β-Dependent Inhibition of Tumor Growth by the Vascular Disrupting Agent 5,6-Dimethylxanthenone-4-Acetic Acid (DMXAA).* Journal of Interferon & Cytokine Research, 2008. **28**(3): p. 133-139.
116. Jassar, A.S., et al., *Activation of tumor-associated macrophages by the vascular disrupting agent 5,6-dimethylxanthenone-4-acetic acid induces an effective CD8+ T-cell-mediated antitumor immune response in murine models of lung cancer and mesothelioma.* Cancer Res, 2005. **65**(24): p. 11752-61.
117. Conlon, J., et al., *Mouse, but not Human STING, Binds and Signals in Response to the Vascular Disrupting Agent 5,6-Dimethylxanthenone-4-Acetic Acid.* The Journal of Immunology, 2013. **190**(10): p. 5216.
118. de Oliveira Mann, C.C. and P.J. Kranzusch, *cGAS Conducts Micronuclei DNA Surveillance.* Trends Cell Biol, 2017. **27**(10): p. 697-698.
119. Harding, S.M., et al., *Mitotic progression following DNA damage enables pattern recognition within micronuclei.* Nature, 2017. **548**(7668): p. 466-470.
120. Mackenzie, K.J., et al., *cGAS surveillance of micronuclei links genome instability to innate immunity.* Nature, 2017. **548**(7668): p. 461-465.
121. Crasta, K., et al., *DNA breaks and chromosome pulverization from errors in mitosis.* Nature, 2012. **482**(7383): p. 53-8.
122. Hintzsche, H., et al., *Fate of micronuclei and micronucleated cells.* Mutat Res, 2017. **771**: p. 85-98.
123. Bhatia, A. and Y. Kumar, *Cancer cell micronucleus: an update on clinical and diagnostic applications.* APMIS, 2013. **121**(7): p. 569-581.

124. Xia, T., et al., *Deregulation of STING Signaling in Colorectal Carcinoma Constrains DNA Damage Responses and Correlates With Tumorigenesis.* Cell Rep, 2016. **14**(2): p. 282-97.
125. Nishiyama, A. and M. Nakanishi, *Navigating the DNA methylation landscape of cancer.* Trends in Genetics, 2021. **37**(11): p. 1012-1027.
126. Malik, P. and A.F. Cashen, *Decitabine in the treatment of acute myeloid leukemia in elderly patients.* Cancer management and research, 2014. **6**: p. 53-61.
127. Dhillon, S., *Decitabine/Cedazuridine: First Approval.* Drugs, 2020. **80**(13): p. 1373-1378.
128. Filì, C., et al., *Efficacy and toxicity of Decitabine in patients with acute myeloid leukemia (AML): A multicenter real-world experience.* Leuk Res, 2019. **76**: p. 33-38.
129. Wu, S.-Y., et al., *MYC suppresses STING-dependent innate immunity by transcriptionally upregulating DNMT1 in triple-negative breast cancer.* Journal for ImmunoTherapy of Cancer, 2021. **9**(7): p. e002528.
130. Kitajima, S., et al., *Suppression of STING Associated with LKB1 Loss in KRAS-Driven Lung Cancer.* Cancer Discov, 2019. **9**(1): p. 34-45.
131. Erdal, E., et al., *A prosurvival DNA damage-induced cytoplasmic interferon response is mediated by end resection factors and is limited by Trex1.* Genes Dev, 2017. **31**(4): p. 353-369.
132. Härtlova, A., et al., *DNA Damage Primes the Type I Interferon System via the Cytosolic DNA Sensor STING to Promote Anti-Microbial Innate Immunity.* Immunity, 2015. **42**(2): p. 332-343.
133. Heijink, A.M., et al., *BRCA2 deficiency instigates cGAS-mediated inflammatory signaling and confers sensitivity to tumor necrosis factor-alpha-mediated cytotoxicity.* Nature Communications, 2019. **10**(1): p. 100.
134. Pantelidou, C., et al., *PARP Inhibitor Efficacy Depends on CD8(+) T-cell Recruitment via Intratumoral STING Pathway Activation in BRCA-Deficient Models of Triple-Negative Breast Cancer.* Cancer Discov, 2019. **9**(6): p. 722-737.
135. Chabanon, R.M., et al., *PARP inhibition enhances tumor cell-intrinsic immunity in ERCC1-deficient non-small cell lung cancer.* J Clin Invest, 2019. **129**(3): p. 1211-1228.
136. Carr, M.I., et al., *DNA-PK Inhibitor Peposertib Amplifies Radiation-Induced Inflammatory Micronucleation and Enhances TGFβ/PD-L1 Targeted Cancer Immunotherapy.* Mol Cancer Res, 2022.
137. Wang, Y., G. Ghosh, and E.A. Hendrickson, *Ku86 represses lethal telomere deletion events in human somatic cells.* Proc Natl Acad Sci U S A, 2009. **106**(30): p. 12430-5.
138. Sharma, A., K. Singh, and A. Almasan, *Histone H2AX phosphorylation: a marker for DNA damage.* Methods Mol Biol, 2012. **920**: p. 613-26.
139. Urushihara, Y., et al., *DNA-PK inhibition causes a low level of H2AX phosphorylation and homologous recombination repair in Medaka (Oryzias latipes) cells.* Biochemical and Biophysical Research Communications, 2012. **429**(3): p. 131-136.
140. Halberg, N., et al., *PITPNC1 Recruits RAB1B to the Golgi Network to Drive Malignant Secretion.* Cancer Cell, 2016. **29**(3): p. 339-353.
141. Buschman, M.D., M. Xing, and S.J. Field, *The GOLPH3 pathway regulates Golgi shape and function and is activated by DNA damage.* Front Neurosci, 2015. **9**: p. 362.
142. Dippold, H.C., et al., *GOLPH3 bridges phosphatidylinositol-4- phosphate and actomyosin to stretch and shape the Golgi to promote budding.* Cell, 2009. **139**(2): p. 337-51.

143. Bui, S., et al., *Adaptation of the Golgi Apparatus in Cancer Cell Invasion and Metastasis.* Frontiers in Cell and Developmental Biology, 2021. **9**.
144. Sechi, S., et al., *Oncogenic Roles of GOLPH3 in the Physiopathology of Cancer.* Int J Mol Sci, 2020. **21**(3).
145. Petrosyan, A., *Onco-Golgi: Is Fragmentation a Gate to Cancer Progression?* Biochem Mol Biol J, 2015. **1**(1).
146. Nakamura, K., et al., *Inhibition of DNA-PK with AZD7648 Sensitizes Tumor Cells to Radiotherapy and Induces Type I IFN-Dependent Durable Tumor Control.* Clin Cancer Res, 2021. **27**(15): p. 4353-4366.
147. Garrido, F., et al., *The urgent need to recover MHC class I in cancers for effective immunotherapy.* Curr Opin Immunol, 2016. **39**: p. 44-51.
148. Johnsen, A.K., et al., *Deficiency of transporter for antigen presentation (TAP) in tumor cells allows evasion of immune surveillance and increases tumorigenesis.* J Immunol, 1999. **163**(8): p. 4224-31.
149. Tumeh, P.C., et al., *PD-1 blockade induces responses by inhibiting adaptive immune resistance.* Nature, 2014. **515**(7528): p. 568-71.
150. Lhuillier, C., et al., *Radiation therapy and anti-tumor immunity: exposing immunogenic mutations to the immune system.* Genome Med, 2019. **11**(1): p. 40.
151. Reits, E.A., et al., *Radiation modulates the peptide repertoire, enhances MHC class I expression, and induces successful antitumor immunotherapy.* J Exp Med, 2006. **203**(5): p. 1259-71.
152. Sato, H., et al., *DNA double-strand break repair pathway regulates PD-L1 expression in cancer cells.* Nat Commun, 2017. **8**(1): p. 1751.
153. Dovedi, S.J., et al., *Fractionated Radiation Therapy Stimulates Antitumor Immunity Mediated by Both Resident and Infiltrating Polyclonal T-cell Populations when Combined with PD-1 Blockade.* Clin Cancer Res, 2017. **23**(18): p. 5514-5526.
154. Tsai, A.K., et al., *A Multikinase and DNA-PK Inhibitor Combination Immunomodulates Melanomas, Suppresses Tumor Progression, and Enhances Immunotherapies.* Cancer Immunol Res, 2017. **5**(9): p. 790-803.
155. Brown, J.S., R. Sundar, and J. Lopez, *Combining DNA damaging therapeutics with immunotherapy: more haste, less speed.* Br J Cancer, 2018. **118**(3): p. 312-324.
156. Zenke, F.T., et al., *M3814, a novel investigational DNA-PK inhibitor: enhancing the effect of fractionated radiotherapy leading to complete regression of tumors in mice*. 2016, AACR.
157. Sun, Q., et al., *Therapeutic Implications of p53 Status on Cancer Cell Fate Following Exposure to Ionizing Radiation and the DNA-PK Inhibitor M3814.* Mol Cancer Res, 2019. **17**(12): p. 2457-2468.
158. Galluzzi, L., et al., *Immunogenic cell death in cancer and infectious disease.* Nat Rev Immunol, 2017. **17**(2): p. 97-111.
159. Permata, T.B.M., et al., *Base excision repair regulates PD-L1 expression in cancer cells.* Oncogene, 2019. **38**(23): p. 4452-4466.
160. Wan, S., et al., *Chemotherapeutics and radiation stimulate MHC class I expression through elevated interferon-beta signaling in breast cancer cells.* PLoS One, 2012. **7**(3): p. e32542.
161. Sharma, A., et al., *γ-Radiation Promotes Immunological Recognition of Cancer Cells through Increased Expression of Cancer-Testis Antigens In Vitro and In Vivo.* PLOS ONE, 2011. **6**(11): p. e28217.
162. Panaretakis, T., et al., *The co-translocation of ERp57 and calreticulin determines the immunogenicity of cell death.*
163. Mukherjee, S., et al., *Fragmentation of the Golgi apparatus: an early apoptotic event independent of the cytoskeleton.* Traffic, 2007. **8**(4): p. 369-78.

164. Huang, Y., et al., *Comparison of the effects of photon, proton and carbon-ion radiation on the ecto-calreticulin exposure in various tumor cell lines.* Annals of Translational Medicine, 2019. **7**(20): p. 542.
165. Vanpouille-Box, C., S.C. Formenti, and S. Demaria, *TREX1 dictates the immune fate of irradiated cancer cells.* Oncoimmunology, 2017. **6**(9): p. e1339857.
166. Suter, M.A., et al., *cGAS–STING cytosolic DNA sensing pathway is suppressed by JAK2-STAT3 in tumor cells.* Scientific Reports, 2021. **11**(1): p. 7243.
167. Wang, Y., et al., *TRIM30α Is a Negative-Feedback Regulator of the Intracellular DNA and DNA Virus-Triggered Response by Targeting STING.* PLoS Pathog, 2015. **11**(6): p. e1005012.
168. Wang, Q., et al., *The E3 ubiquitin ligase AMFR and INSIG1 bridge the activation of TBK1 kinase by modifying the adaptor STING.* Immunity, 2014. **41**(6): p. 919-33.
169. Konno, H., K. Konno, and G.N. Barber, *Cyclic dinucleotides trigger ULK1 (ATG1) phosphorylation of STING to prevent sustained innate immune signaling.* Cell, 2013. **155**(3): p. 688-98.
170. Wu, J., et al., *Interferon-Independent Activities of Mammalian STING Mediate Antiviral Response and Tumor Immune Evasion.* Immunity, 2020. **53**(1): p. 115-126.e5.
171. Durante, M. and S.C. Formenti, *Radiation-Induced Chromosomal Aberrations and Immunotherapy: Micronuclei, Cytosolic DNA, and Interferon-Production Pathway.* Frontiers in Oncology, 2018. **8**.
172. Sun, L., et al., *Cyclic GMP-AMP synthase is a cytosolic DNA sensor that activates the type I interferon pathway.* Science, 2013. **339**(6121): p. 786-91.
173. Ishikawa, H. and G.N. Barber, *STING is an endoplasmic reticulum adaptor that facilitates innate immune signalling.* Nature, 2008. **455**(7213): p. 674-678.
174. Yoneyama, M., et al., *The RNA helicase RIG-I has an essential function in double-stranded RNA-induced innate antiviral responses.* Nature Immunology, 2004. **5**(7): p. 730-737.
175. Kato, H., et al., *Differential roles of MDA5 and RIG-I helicases in the recognition of RNA viruses.* Nature, 2006. **441**(7089): p. 101-105.
176. Decout, A., et al., *The cGAS–STING pathway as a therapeutic target in inflammatory diseases.* Nature Reviews Immunology, 2021. **21**(9): p. 548-569.
177. Chiappinelli, K.B., et al., *Inhibiting DNA Methylation Causes an Interferon Response in Cancer via dsRNA Including Endogenous Retroviruses.* Cell, 2015. **162**(5): p. 974-986.
178. Stresemann, C. and F. Lyko, *Modes of action of the DNA methyltransferase inhibitors azacytidine and decitabine.* Int J Cancer, 2008. **123**(1): p. 8-13.
179. Gnyszka, A., Z. JastrzĘBski, and S. Flis, *DNA Methyltransferase Inhibitors and Their Emerging Role in Epigenetic Therapy of Cancer.* Anticancer Research, 2013. **33**(8): p. 2989.
180. Wong, K.K., R. Hassan, and N.S. Yaacob, *Hypomethylating Agents and Immunotherapy: Therapeutic Synergism in Acute Myeloid Leukemia and Myelodysplastic Syndromes.* Frontiers in Oncology, 2021. **11**.
181. Wang, L.X., et al., *Low dose decitabine treatment induces CD80 expression in cancer cells and stimulates tumor specific cytotoxic T lymphocyte responses.* PLoS One, 2013. **8**(5): p. e62924.
182. Son, C.-H., et al., *Combination treatment with decitabine and ionizing radiation enhances tumor cells susceptibility of T cells.* Scientific Reports, 2016. **6**(1): p. 32470.

183. Kobayashi, D., et al., *Induction of Micronuclei in Cervical Cancer Treated with Radiotherapy.* J Pers Med, 2020. **10**(3).
184. Kirsch-Volders, M., et al., *Report from the In Vitro Micronucleus Assay Working Group.* Environmental and Molecular Mutagenesis, 2000. **35**(3): p. 167-172.
185. Pinto, M.M., N.F. Santos, and A. Amaral, *Current status of biodosimetry based on standard cytogenetic methods.* Radiat Environ Biophys, 2010. **49**(4): p. 567-81.
186. Nie, J., et al., *Addition of Low-Dose Decitabine to Anti-PD-1 Antibody Camrelizumab in Relapsed/Refractory Classical Hodgkin Lymphoma.* J Clin Oncol, 2019. **37**(17): p. 1479-1489.
187. Diamond, M.S., et al., *Type I interferon is selectively required by dendritic cells for immune rejection of tumors.* J Exp Med, 2011. **208**(10): p. 1989-2003.
188. Lorenzi, S., et al., *Type I IFNs control antigen retention and survival of CD8α(+) dendritic cells after uptake of tumor apoptotic cells leading to cross-priming.* J Immunol, 2011. **186**(9): p. 5142-50.
189. Lee, P.Y., et al., *Type I interferon modulates monocyte recruitment and maturation in chronic inflammation.* Am J Pathol, 2009. **175**(5): p. 2023-33.
190. Saeys, Y., S. Van Gassen, and B.N. Lambrecht, *Computational flow cytometry: helping to make sense of high-dimensional immunology data.* Nature Reviews Immunology, 2016. **16**(7): p. 449-462.
191. Sanmamed, M.F., et al., *Agonists of Co-stimulation in Cancer Immunotherapy Directed Against CD137, OX40, GITR, CD27, CD28, and ICOS.* Seminars in Oncology, 2015. **42**(4): p. 640-655.
192. Kratofil, R.M., P. Kubes, and J.F. Deniset, *Monocyte Conversion During Inflammation and Injury.* Arteriosclerosis, Thrombosis, and Vascular Biology, 2017. **37**(1): p. 35-42.
193. Olingy, C.E., H.Q. Dinh, and C.C. Hedrick, *Monocyte heterogeneity and functions in cancer.* Journal of leukocyte biology, 2019. **106**(2): p. 309-322.
194. Menezes, S., et al., *The Heterogeneity of Ly6Chi Monocytes Controls Their Differentiation into iNOS+ Macrophages or Monocyte-Derived Dendritic Cells.* Immunity, 2016. **45**(6): p. 1205-1218.
195. Zhou, J., et al., *Tumor-Associated Macrophages: Recent Insights and Therapies.* Frontiers in Oncology, 2020. **10**.
196. Italiani, P. and D. Boraschi, *From Monocytes to M1/M2 Macrophages: Phenotypical vs. Functional Differentiation.* Frontiers in Immunology, 2014. **5**.
197. Vicencio, J.M., et al., *Osimertinib and anti-HER3 combination therapy engages immune dependent tumor toxicity via STING activation in trans.* Cell Death Dis, 2022. **13**(3): p. 274.